Quasi-ductile mechanisms in porous liquid-phase sintered alumina induced by Hertzian contact.

Citation

DiGiovanni, Anthony Albert. *Quasi-Ductile Mechanisms in Porous Liquid-Phase Sintered Alumina Induced by Hertzian Contact.* 1999, https://preserve.lehigh.edu/lehigh-scholarship/graduate-publications-theses-dissertations/theses-dissertations/quasi-ductile.

INFORMATION TO USERS

This manuscript has been reproduced from the microfilm master. UMI films the text directly from the original or copy submitted. Thus, some thesis and dissertation copies are in typewriter face, while others may be from any type of computer printer.

The quality of this reproduction is dependent upon the quality of the copy submitted. Broken or indistinct print, colored or poor quality illustrations and photographs, print bleedthrough, substandard margins, and improper alignment can adversely affect reproduction.

In the unlikely event that the author did not send UMI a complete manuscript and there are missing pages, these will be noted. Also, if unauthorized copyright material had to be removed, a note will indicate the deletion.

Oversize materials (e.g., maps, drawings, charts) are reproduced by sectioning the original, beginning at the upper left-hand corner and continuing from left to right in equal sections with small overlaps. Each original is also photographed in one exposure and is included in reduced form at the back of the book.

Photographs included in the original manuscript have been reproduced xerographically in this copy. Higher quality 6" x 9" black and white photographic prints are available for any photographs or illustrations appearing in this copy for an additional charge. Contact UMI directly to order.

UMI®

Bell & Howell Information and Learning
300 North Zeeb Road, Ann Arbor, MI 48106-1346 USA
800-521-0600

Reproduced with permission of the copyright owner. Further reproduction prohibited without permission.

QUASI-DUCTILE MECHANISMS IN POROUS LIQUID PHASE SINTERED ALUMINA INDUCED BY HERTZIAN CONTACT

By

Anthony A. DiGiovanni

Presented to the Graduate and Research Committee

of Lehigh University

in Candidacy for the Degree of

Doctor of Philosophy

in

Materials Science and Engineering

Lehigh University

May 1999

UMI
300 North Zeeb Road
Ann Arbor, MI 48103

CERTIFICATE OF APPROVAL

Approved and recommended for acceptance as a dissertation in partial fulfillment of the requirements for the degree of Doctor of Philosophy.

5-6-99
(Date)

Helen Chan

Martin P. Harmer
Professors in Charge

Accepted 5-4-99
(Date)

Committee Members:

Helen Chan
Dr. Helen M. Chan (Chair)

Martin P. Harmer
Dr. Martin P. Harmer (Co-Chair)

Dr. Raymond A. Pearson

Dr. Herman F. Nied

No pessimist ever discovered the secrets of the stars,
or sailed to an uncharted land, or opened a
new heaven to the human spirit.

-- Helen Keller --

ACKNOWLEDGMENTS

First, I would like to thank my faculty advisors, Drs. Helen M. Chan and Martin P. Harmer, for their support and guidance during the course of this research. I would also like to thank the other members of my thesis committee, Dr. Ray Pearson (Materials Science, Lehigh) for his support and Dr. Herman Nied (Mechanics, Lehigh), for his knowledge of fracture mechanics and expertise in finite elements.

Further thanks go to Dr. Jan Tullis, Brown University, for her help in understanding the fundamentals of rock mechanics and conducting related experiments on our materials. In addition, I would like to acknowledge Dr. Brian Lawn, NIST, for his useful comments and suggestions. I would also like to thank Terry Anderson of Coors Ceramics and Dan Tipsord (formerly of Coors Ceramics) for providing me with substrates and useful information regarding their products.

It is my distinct pleasure to have worked with and been influenced by many outstanding members from institutions in the vast engineering and related sciences prior to and during my tenure at Lehigh University. My studies could not have been completed without the expertise and wisdom of the following people (LU): A. Benscotter (metallography/ ceramography); D. Ackland and K. Repa (electron microscopy), G. Kozma (Instron repair and support); J. Williams (machining all kinds of crazy things on short notice); A. Pressler (photography); P. Newhart, M. Mattie, S. Coe, V. Newhard, J. DiClimente, K. Kennery, K. Fox and especially C. Sottosanti (administrative).

To my fellow graduate students I will be always indebted for their patience, kindness, friendship and assistance in teaching me about many things, both technical and non-technical alike. In particular I would like to thank G. Thompson, G. Lucadamo, B.

Schorr, D. Carpenter and M. Watson for having the patience to live with me at various stages and for their endless help in the lab. I would also like to thank the members of "Team Marder" for helping me to understand the world of metals. Thanks go to: B. Lindsley, B. Levin, K. Luer, S. Banovic, D. Susan, C. Kusko, J. Nawrocki, Dr. J. Dupont, and D. Puerta. Other graduate students I with to thank are: J. Goodelle, H. Ha, L. An, S. Gaus, J. Albuquerque, A. Khan, P. Sheedy, J. Cho, I. Chou, V. Keast, J. Kim, C. Palanduz, A. Scotch, W. Dong, S. Saha as well as Drs. A. M. Thompson, L. Stearns, J. Alves and M. Raymond, for a variety of experiences we have shared.

I am especially indebted to B. Yildrim who donated much of his time to help me understand the finer points of mechanics and for keeping the FEM software running! Additional acknowledgements go to those students who proof read various parts of my dissertation: K. Luer, A. Scotch, M. Watson, P. Sheedy, A. Khan, H. Ha

Very special thanks go to my parents, my sisters and the rest of my immediate family who have always supported my education and have had the patience to endure its course. The same may be said for the very good friends I have made over the years, especially PD, CR, and MC. Thank you gentlemen!

TABLE OF CONTENTS

LIST OF FIGURES

LIST OF TABLES

LIST OF SYMBOLS AND ABBREVIATIONS

Symbols

σ	nominal or engineering stress
ε	nominal or engineering strain
E	Young's modulus
Y	yield stress
s	arbitrary distance between two points
σ_1, σ_2, σ_3	principal stresses where $\sigma_1 > \sigma_2 > \sigma_3$
ν	Poisson's ratio
s_{xx}, s_{yy}, s_{zz}	arbitrary stresses in the x,y,z coordinate system
τ	shear stress
A	an arbitrary constant
m	exponent in a power law relation $0 < m < 1$
P	applied load (N)
a	Hertzian contact area radius, also a normalized crack length coordinate
E*	composite modulus of the Hertzian indenter and substrate
R	radius of the Hertzian indenter, also the radius of a pore
k	an alternate unitless constant used in representing the Hertzian relation
P_o, p_o	peak indentation pressure
P	arbitrary indentation pressure, more commonly the value of porosity in the system
r	variable in coordinate direction, r
P_m	mean or average indentation stress
σ_r, σ_θ, σ_z	arbitrary stresses in the r,θ,z coordinate system
z	variable in coordinate direction, z
u	positional constant for Hertzian stress equations
γ_s	surface energy of a crack per unit area
K_1	mode 1 stress intensity factor
f	geometric stress magnification factor

l	flaw or crack size
K_{Ic}, T_o	mode 1 material fracture toughness
σ_c	critical failure stress
G_c	critical strain energy release rate
E'	a substitutional variable for the elastic modulus, changes for plane strain or plane stress
zz	tensile stress in spherical coordinates
rr	radial stress in spherical coordinates
$\theta\theta$	surface tangential stress of a sphere
$\phi\phi$	surface tangential stress of a sphere, normal to $\theta\theta$
p_2, p_1	remotely applied compressive stresses, $p_1 > p_2$ (+ is compressive)
θ	variable in angular coordinate direction, θ
N	number of cracks
F	geometric stress magnification function
λ	ratio of principle compressive stresses, σ_3/σ_1
L	ratio of flaw size, l to pore radius R
b/c	ratio of pore spacing in the x-y directions, from Isida (1987)
c/a	ratio of pore center to center distance, c, to the pore radius 'a'
P_c	the critical load to induce ring/cone cracking
c_o	minimum initial flaw size
c_i	initial flaw size
c_c	growth of flaw into ring crack of length, c_c
c_f	final cone crack pop in length
P'	applied load to initiate c_o to grow into a ring crack
P''	applied load to grow ring crack to size c_c
P'''	applied load to initiate cone cracking
S	net shear stress along a twin fault
μ	coefficient of friction
H_v	Vickers hardness

H_o	initial Vickers hardness
B	an experimentally determined constant
σ	empirically determined strength
σ_o	initial strength value
ν_o	initial Poisson's ratio
$\sigma_{\theta\theta}$	angular stress around a pore
σ_{rr}	radial stress around a pore
$\sigma_{r\theta}$	shear stress around a pore
N	½ the nearest neighbor distance between pores
A%	area percent or 2D porosity
n	normalized distance representing pore separation
c	flaw size
d	ratio of flaw size to contact area, *a*
ξ	unitless stress magnification constant determined from FEM
K_{Ic}^{gb}	grain boundary fracture toughness

Abbreviations

2D = two dimensional
3D = three dimensional
FEG = field emission gun
FEM = finite element modeling
LEFM = linear elastic fracture mechanics
LOM = light optical microscopy
LPS = liquid phase sintered
NND = nearest neighbor direction
PBC = periodic boundary conditions
PLPS = porous liquid phase sintered
PPI = pre- and post-indentation
SEM = scanning electron microscopy
SQP = square quarter-pore
TEM = transmission electron microscopy

ABSTRACT

Hertzian indentation has been effective in evaluating material response and deformation behavior through single and repeated contacts of a hard sphere into a representative bulk sample in laboratory conditions. Using this technique, the macroscopic and microscopic deformation characteristics of a commercial alumina substrate were evaluated. Significant 'quasi-ductile' behavior was observed, not unlike that observed for other advanced ceramic systems with heterogeneous microstructures. In pure dense alumina, quasi-ductility is controlled by twin fault formation where a transition from a fine grained to a coarse grained microstructure corresponds to a change from classical cone-crack behavior to a purely quasi-ductile indentation response. The quasi-ductility in the commercial alumina was unexpected because the average grain size was very small – well below the size where one should expect any contribution from a twin faulting mechanism.

Subsequent work focused on reproducing the commercial microstructures and then altering the grain size, porosity, and presence of the glassy (liquid) phase. Macroscopic indentation revealed a quasi-ductile residual impression formed prior to the observation of ring crack formation in the porous liquid phase sintered materials. Furthermore, the glass containing samples produced a deeper residual impression for an equivalent load and porosity level. Fully dense samples with or without a glass phase remained completely brittle. Subsurface images corresponded to the macroscopic observations; porous liquid phase materials with a 5 μm grain size revealed greater microstructural damage with increasing loads over that of the pure material.

A 2D theoretical treatment of the problem used finite element modeling and periodic boundary conditions to understand the magnifying effect of multiple pores on the stress around a given pore in a biaxial compressive stress state linked to the Hertzian stress at yield. A periodic pore structure was assumed to simplify the modeling. Peak stress was a function of the pore network orientation. The results were in agreement with previously published analytical work at the same orientations. When the pore network was tilted at 45° to the applied stress directions an increase of the peak stress around a pore was observed with increasing porosity. An attempt to randomize the pore network revealed only small changes in the peak stress. Therefore, a linear stress magnification function determined from the FEM results was incorporated into a previously published stress intensity factor solution for an individual pore/flaw arrangement. The stress concentrating effect of the subsurface pores were related to the macroscopic indentation driving force of the Hertzian indenter. Predictions of the critical mean indentation load to initiate subsurface damage were in reasonable agreement with published results. We conclude that porosity acted as a stress concentrator and was the controlling mechanism for quasi-ductility under Hertzian contact in the liquid phase sintered alumina.

1. INTRODUCTION

Hertzian contact, also known as spherical contact, was named after Heinrech Hertz, who first determined the elastic stress distribution between two glass lenses pressed together. The field of study known as contact mechanics is said to have started with Hertz's work (Fischer-Cripps, 1998). The study of contact mechanics has always been part of an essential understanding of material behavior. Early work and thus the foundations of the theories in contact mechanics have focused largely on metallic systems (Tabor, 1951; Johnson, 1985). Most of the indentation techniques were developed in the years following the work of Hertz. As time went by and advanced ceramics started to find more engineering applications, an increase in interest and ultimately understanding of the deformation character of these materials was obtained (McColm, 1990).

In particular, the use of Hertzian contact has reappeared as an investigative tool for understanding the effects of microstructure on the response of advanced ceramic systems to wear and contact damage (Lawn, 1998(a)). A recent observation in advanced ceramics that contain long-crack toughening mechanisms is a pronounced quasi-ductile response under Hertzian contact (Cai, 1994(a)). This is measured as a fall-off from the elastic stress-strain response on an indentation stress-strain curve and manifests itself through homogeneously distributed sub-surface microfracture. The advantage of the Hertzian technique is its ability to administer loads beginning in an elastic regime with subsequent higher loading causing a transition from reversible elastic behavior to irreversible "quasi-plastic" damage. Microstructural observations reveal the controlling mechanisms.

Understanding the role of microstructure and its effect on the initiation and evolution of damage under applied external stresses is of paramount importance with regard to designing and optimizing ceramic components in engineering applications. As a material with significant commercial applications, liquid phase sintered (LPS) alumina will be the system under investigation. Particular interest will be paid to the microstructural effects on the yielding or initiation of damage within the material system. To address the complicated mechanical behavior of liquid phase sintered alumina under Hertzian contact some basic concepts in mechanics of materials should be engaged.

2. BACKGROUND

2.1 Liquid Phase Sintering of Alumina

The bulk of this research will focus on the theory and evolution of damage in alumina as a function of microstructure at room temperature. Specifically, this investigation will attempt to show the interrelation between deformation under a Hertzian indenter and a microstructure with liquid (glass) phase and remnant porosity. Because the processing of the materials affects the microstructure and the observed deformation, a basic understanding of liquid phase sintering is provided.

Liquid phase sintering (LPS) is often used as a cost-effective method to produce solid ceramic bodies. The liquid phase (or glass) acts to enhance diffusion of the solid phase at a lower temperature than could be used for the material in pure form (Rahaman, 1995). In fact, some covalently bonded polycrystalline materials such as Si_3N_4 are not easily formed into dense bodies without the use of a liquid phase sintering aid (Vetrano, 1993; Schmid, 1984). The presence of a liquid phase in a material can come about intentionally from additives in the powder processing (Rahaman, 1995) or it can be unintentional, a result of glass-forming impurities present in the starting materials (Susnitzky, 1990; Clarke, 1977).

Several requirements exist for LPS: (1) A liquid phase must coexist with a solid phase at the sintering temperature, (2) The solid phase must have an appreciable solubility in the liquid phase, and (3) The liquid must significantly wet the surface of surrounding particles during the sintering process (Alves, 1997). Under good wetting conditions, the glass phase can be expected at grain boundaries (Brada & Clarke, 1997;

Clarke, 1987) and, under most conditions, triple points within the sintered microstructure (Raj, 1981). One should note, however, that the advantage of decreased firing time and temperature by the liquid phase can be offset by a reduction in the strength of the polycrystalline solid at elevated temperatures (Clarke, 1987; Lange 1983) due to the presence of the liquid phase at the grain boundaries.

Another major microstructural concern during the sintering process is the formation of abnormal grains. In both solid state sintering and LPS, certain grains in the microstructure may grow preferentially large due to the difference in boundary mobility between grains (Harmer, 1985). The effect of abnormal grains within the microstructure on mechanical properties will be addressed in Sec. 5.3.1.

A method of controlling abnormal grain growth is to decrease the mobility of the grain boundary migration through chemical dopants. In alumina, MgO is a dopant that has been successful in controlling abnormal grain growth in both solid state (Bennison, 1983) and LPS processes (Kaysser, 1987). MgO segregates to the grain boundaries where it reduces the boundary mobility, allowing pores to remain on the boundaries and offsetting the enhanced growth of special grain boundaries (Harmer, 1985) that can lead to abnormal grain growth.

The LPS alumina with residual porosity, properly doped with MgO, will subsequently contain a distribution of pores at grain boundaries separated with a glassy phase. Porosity will be homogeneously distributed provided that steps are taken to reduce powder agglomerates during processing. The microstructure just described is particularly susceptible to deformation under localized compressive stresses as will be shown in this research.

2.2 Elasticity

The basic concepts of elasticity theory form the cornerstone to virtually any study of mechanical properties of materials and structures. Studies in elasticity are quite numerous and extensive literature has been produced on this subject since the days of Galeleo (Love, 1944). Abundant texts exist on the subject; however, several texts are worth mentioning for the depth and quality of their treatment of the material. The classic text in elasticity is by Love (1944), which is mathematically rigorous although some of the notation is no longer used in modern elastic theory. Sokolnikoff (1946) is a classic Russian text that complements Love (1944) and is also mathematically thorough. Timoshenko and Goodier (1970) is largely referred to in modern work on elasticity and Gere and Timoshenko (1984) provides the most fundamental approach in a strength of materials format which is accessible to a larger audience. All of these texts highlight concepts necessary for a thorough analysis of problems concerning the fundamental relationships of elasticity.

2.2.1 Macroscopic Elasticity

From a macroscopic perspective, the fundamental relations of elasticity and plasticity are easily observed. Hooke's law demonstrates the simplest form of elastic behavior in materials. For instance, consider a rectangular homogeneous and isotropic material (Fig. 2.1) undergoing uniaxial tension. The stress in the bar will be related to strain by the equation:

$$\sigma = E \cdot \varepsilon \; ; \tag{2.1}$$

it follows that a graph of this loading relationship will be a straight line where the slope is the elastic (Young's) modulus. As the load (or stress) is increased from zero, the relation shown in Eq. 2.1 holds until a critical point is obtained where the loading is no longer elastic but a permanent deformation occurs in the material. The nature of the deformation and the load at which it occurs is a material dependant property. A brittle material will fail catastrophically, abruptly terminating the stress-strain curve (Fig. 2.2(a)), and a ductile material will cause a deviation from linearity (Fig. 2.2(b)).

2.2.2 Microscopic Elasticity

On a microstructural level, elasticity develops the same characteristics as that observed macroscopically. To describe the events on a microstructural level requires an increase in complexity in the relations of stress and strain, but the same principles still apply.

By using a continuum approach to elasticity, and simple force balances, one may consider an infinitesimal element taken from within the previously mentioned rectangular bar and examine the stress in three dimensions. Fig. 2.3 shows an element labeled within an orthogonal coordinate system (x,y,z). Equations and notations to follow will be presented in this coordinate system. Note that sometimes it is more convenient to represent a problem in a different coordinate system. In subsequent sections, equations used in this investigation will appear in the most convenient or standardized coordinate system.

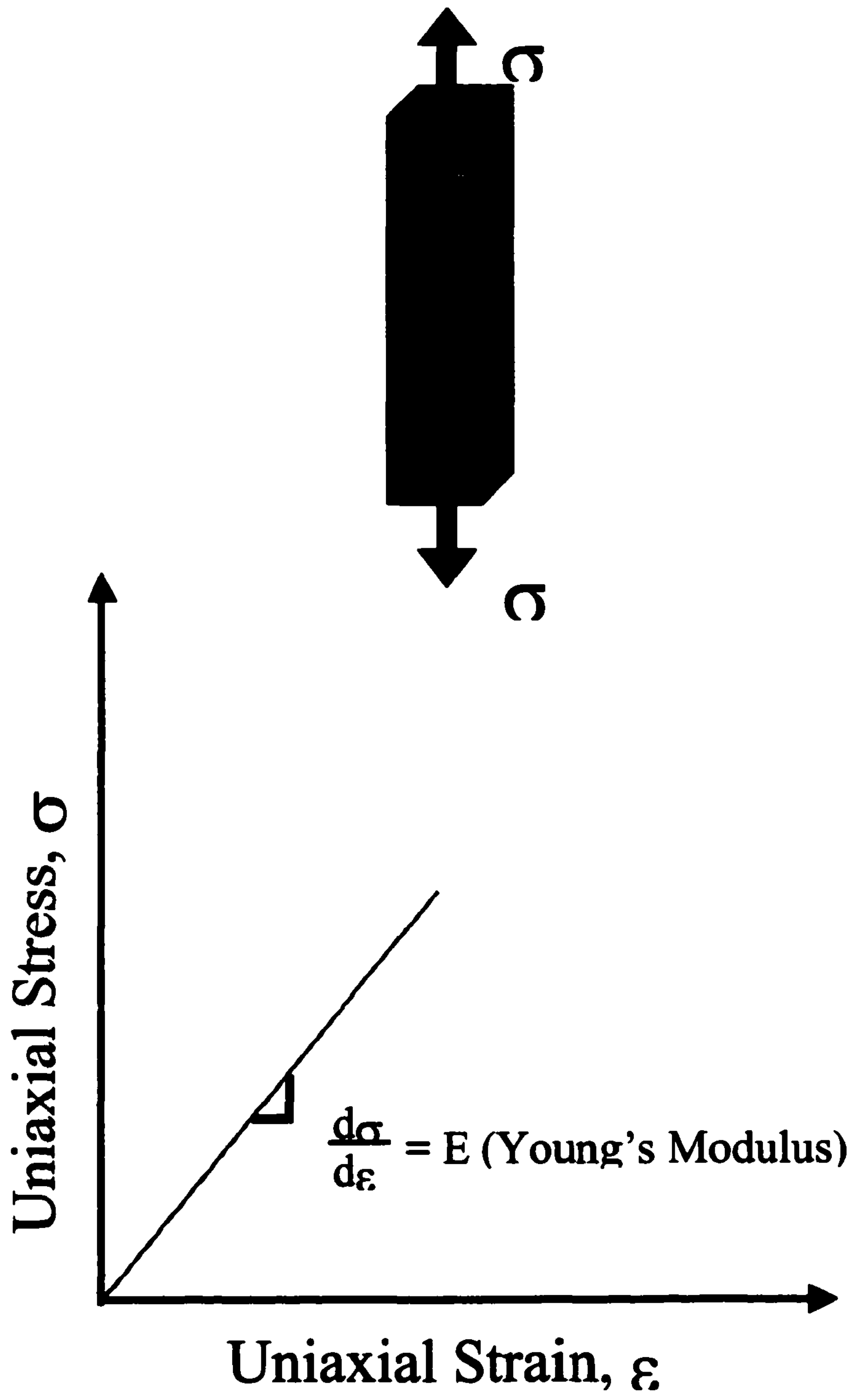

Figure 2. 1 A homogeneous isotropic material undergoing uniaxial tension. The plot follows the relation in Eq. 2.1 where the slope is equal to Young's modulus, E.

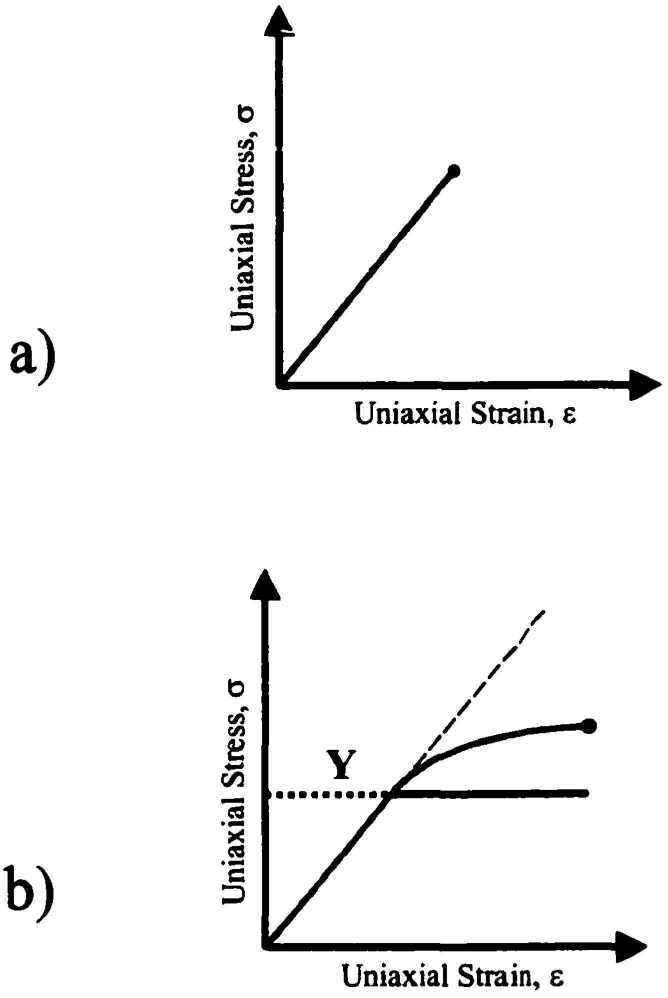

Figure 2. 2 (a) Linear elastic behavior ending in catastrophic failure of the sample (black dot). (b) Yielding, in the form of a ductile response, causes a deviation from linear elastic behavior at a stress Y. Loading past the yield point often follows a power-law relation and is considered strain-hardening. Perfectly plastic yielding, indicated by the solid black line, is characterized by an increase in strain without a further increase in load.

2.2.3 Strain Relations

The derivation of the relations between the stresses shown on the element of Fig. 2.3 can be found in any of the previously mentioned texts on elasticity. Relations between stress and strain that are pertinent to this investigation will be repeated here and are taken from Boresi (1993). Unless otherwise stated, all references to stresses will be principal stresses, where $\sigma_1 > \sigma_2 > \sigma_3$.

Simple engineering strain is defined as:

$$\varepsilon_i = \frac{ds_i}{s_i} \tag{2.2}$$

where *s* is the distance between two points, *ds* is the change in distance and the subscript, *i*, indicates the coordinate (*i* = x,y,z). The principal strains as a function of the principal stresses are given by:

$$\varepsilon_{xx} = \frac{1}{E}\left(\sigma_{xx} - \upsilon\sigma_{yy} - \upsilon\sigma_{zz}\right) \tag{2.3}$$

$$\varepsilon_{yy} = \frac{1}{E}\left(\sigma_{yy} - \upsilon\sigma_{xx} - \upsilon\sigma_{zz}\right) \tag{2.4}$$

$$\varepsilon_{zz} = \frac{1}{E}\left(\sigma_{zz} - \upsilon\sigma_{xx} - \upsilon\sigma_{yy}\right) \tag{2.5}$$

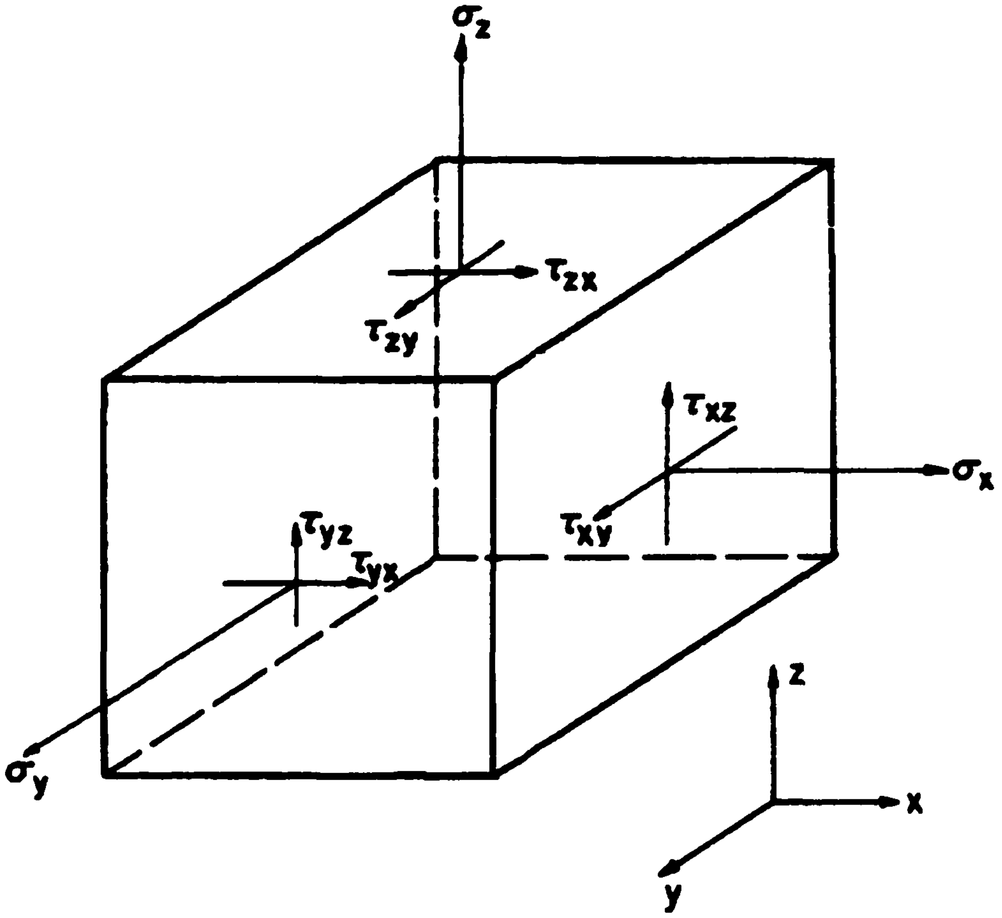

Figure 2. 3 Infinitesimal element labeling stresses and coordinates. Normal stress is indicated by σ and shear stress by τ. (Adapted from Chou and Pagano, 1967)

where ν is Poisson's ratio and E is the Young's modulus. Although experimentally, the systems under investigation experience an axisymmetric stress state, for simplicity, our modeling will be based on plane strain conditions. Under plain strain conditions, $\varepsilon_{zz} = 0$, and thus Eq. 2.5 yields:

$$\sigma_{zz} = \upsilon(\sigma_{xx} + \sigma_{yy}) \qquad (2.6)$$

from which we have:

$$\varepsilon_{yy} = \frac{1}{E}\left(\sigma_{yy} - \upsilon\sigma_{xx} - \upsilon^2\left(\sigma_{xx} + \sigma_{yy}\right)\right) \tag{2.7}$$

$$\varepsilon_{xx} = \frac{1}{E}\left(\sigma_{xx} - \upsilon\sigma_{yy} - \upsilon^2\left(\sigma_{xx} + \sigma_{yy}\right)\right) \tag{2.8}$$

The expressions (2.3-2.5) can alternatively be written for stresses.

2.2.4 Plasticity and Yielding

As the externally applied load is increased, the elastic limit of the material is approached. The elastic limit, usually referred to as the yield stress, Y (Fig. 2.2(b)), is a constant for a given material and function of its atomic structure. Once the elastic limit has been exceeded, permanent changes take place within the material associated with a disruption in the interatomic bonding. In metallic systems, the change results in generation of dislocations and their subsequent motion. By comparison, brittle materials will experience some form of fracture process.

2.2.4.1 Macroscopic Yielding

Macroscopic yielding has many forms that are material dependant and a typical response for a ductile metal was shown in Fig. 2.2(b). Once the yield stress has been exceeded, the stress-strain curve deviates from linearity and begins to strain harden. Strain hardening is characterized by a required increase in stress above the yield stress to produce an increment of strain. The general character of strain hardening results from specific microscopic mechanisms, such as dislocation motion in metals, that resist physical rearrangement under the applied stress.

As shown in Fig. 2.2(b), the relationship for ductile metals often follows a simple power law, $\sigma = A\varepsilon^m$ once the yield point has been exceeded. The exponent, m, in the power law relationship is referred to as the strain hardening coefficient and it is an indicator of the ductility in the system (Hertzberg, 1997). A coefficient of m = 1 signifies a purely elastic behavior, no ductility, which would reduce to Eq. 2.1, where A = E. The other extreme, m = 0, would represent a condition of full plasticity or perfectly plastic flow where further increases in stress produce proportional strain increments.

2.2.4.2 Microscopic Yielding

Under non-idealized loading conditions a body can experience multiaxial conditions of stress that simultaneously vary in magnitude at different places within the body. As the applied stress increases, the localized variations in stress can cause local yielding while the remainder of the material is only stressed elastically.

Subsequently, a yield criterion can be established at a given point within a material based on the local stress state. One of the simplest yield criteria was established by Tresca and is also known as the maximum shear-stress criterion (Boresi, 1993). Precise yield predictions use the von Mises yield criterion (Hill, 1950), but the difference between the Tresca and von Mises criteria is small enough to neglect for a simple first approximation (Boresi, 1993; Hill, 1950). The Tresca equation can be written as:

$$\tau_{max} = \tfrac{1}{2}\left(\sigma_{max} - \sigma_{min}\right). \tag{2.9}$$

where σ_{max} and σ_{min} are the elastic principal stresses, defined for any point within the body.

For a biaxial stress condition, the yield stress, Y, is related to the shear by:

$$\tau_Y = \tau_{\max} = \frac{Y}{2} \tag{2.10}$$

so that,

$$\sigma_{\max} - \sigma_{\min} = Y \tag{2.11}$$

which is suitable to evaluate yielding under Hertzian contact stresses (Tabor, 1951).

After yielding begins there is often a region in which strain hardening occurs, indicated in the previous section, as a material tends toward a condition of full plasticity and/or failure. The stress-strain region defined by the condition of first yield up to that of full plasticity or failure is known as the elastic-plastic region and will be briefly discussed in reference to this investigation in Sec. 2.9.4.

Unlike a simple uniaxial tensile test, a condition of ultimate or catastrophic failure does not apply to the indentation conditions studied here from a theoretical perspective. Analytically, a substrate is treated as an infinite half space and therefore any cracks that may develop during quasi-static indentation will eventually terminate at a finite length as the crack driving force eventually reaches zero (under a static load, P). Conversely, indenting a small sample creates a condition where catastrophic failure is not only possible, but also easily attained in a brittle material through the formation and extension of radial cracks around the indent.

2.3 Hertzian Stress and Indentation

In his seminal work, Heinrich Hertz (Hertz, 1881, 1896) calculated the solution to elastic stresses arising between two curved glass lenses in contact. Hertz used the geometric boundary conditions of this problem to obtain a solution of stress at the surface of the bodies and along the axis of symmetry. By noting the similarity in the elastic potential to that of the electrostatic one, Hertz obtained the solution to the governing integral equations with known solutions for elliptic integrals.

A vast amount of work has been performed on the elastic stresses involved in contact problems since Hertz's landmark discovery. Not long after Hertz made his discovery, the complete closed form expressions for the elastic stress state within the indented body appeared in the literature (Huber, 1904; Fuchs, 1913; Huber and Fuchs, 1914). Morton (1922) graphically displayed the principal stresses at selected angles from the loading axis and recent work by Hanson (1993) provides alternative closed form solutions for stresses and includes solutions for displacements and potentials.

Early solutions to Hertz's problem were also explored by well-known Russian researchers such as Dinnik and Belayev and are reviewed by Krolevets (1966). General solutions to elliptical contact (where Hertz's solution is a simplified case) are shown by Sackfield (1993, 1983a), Fabrikant (1985), Galin (1961), and recently by Hanson (1997) including shear loading. Sackfield (1983b) also considered shear effects on Hertzian contact.

Significant early applications for contact theory included rail and bearing work using two-dimensional solutions to the contact problems (Poritsky, 1949; Thomas and Hoersch, 1930). The current investigation only requires Hertz's solution for normal frictionless loading in 3D (axisymetric).

2.3.1 Macroscopic Relations of Indentation Stress and Strain

According to Hertz, the relationship for the area of contact between two curved bodies under a load, P, is:

$$a^3 = \frac{3}{4}\frac{P}{E^*}\frac{R_1 R_2}{R_1 + R_2} \tag{2.12}$$

and

$$\frac{1}{E^*} = \frac{\left(1-v_1^2\right)}{E_1} + \frac{\left(1-v_2^2\right)}{E_2} \tag{2.13}$$

where a is the radius of the resulting circle of contact between the two bodies, R is the radius of each body in contact, and the E* term is the composite modulus. For the specific case of a spherical indenter impinging upon a flat substrate (see Fig. 2.4), the radius of one of the bodies is considered infinite. Eq. 2.12 may then be rewritten as[a]:

$$a^3 = \frac{3}{4}\frac{PR}{E^*}. \tag{2.14}$$

Eq. 2.14 is the fundamental equation governing the elastic Hertzian indentation process.

Developing a macroscopic understanding of the indentation process requires knowledge of the stresses and strains that develop between the two bodies. The radial pressure distribution beneath the spherical indenter is shown in Fig. 2.5 and may be described by the equation (Johnson, 1985):

$$P = P_o\left(1 - \frac{r^2}{a^2}\right)^{1/2} \tag{2.15}$$

where r is the distance from the loading axis.

The peak pressure occurs directly on the loading axis, $r = 0$, with a value of P_o and falls off to zero at the edge of contact, $r = a$. The peak pressure, P_o, is equal to 3/2 P_m,

---

[a] Note some authors prefer the expression $a^3 = (4k/3E_1)$ PR; where $k = 9/16[(1-v_1^2) + (1-v_2^2)E_1/E_2]$ which is equivalent to Eq. (2.14).

the mean pressure between the two bodies, defined by the applied load, P, and area of contact as:

$$P_m = \frac{P}{\pi a^2}. \tag{2.16}$$

P_m may also be considered as the indentation stress.

The mean pressure or indentation stress, may be obtained from Eq. 2.14 by adding a π term to both sides:

$$\frac{P}{\pi a^2} = \frac{4E^*}{3\pi}\frac{a}{R} \tag{2.17}$$

and along with Eq. 2.16 gives:

$$P_m = \left[\frac{4E^*}{3\pi}\right]\frac{a}{R} \tag{2.18}$$

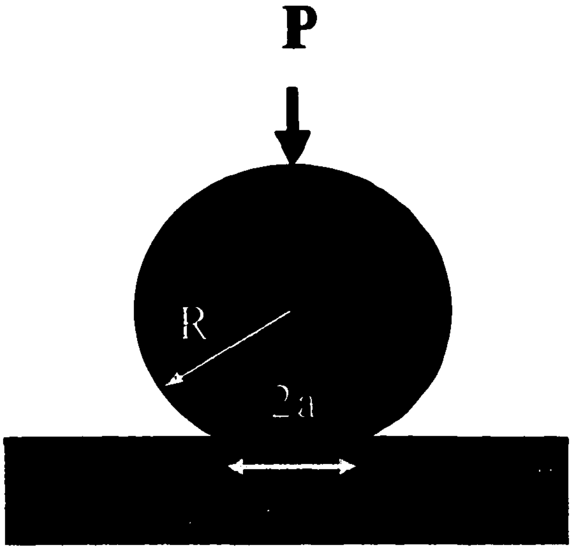

Figure 2. 4 Spherical indenter, radius R, impinging on a substrate. Diameter of the area of contact is defined as *2a*.

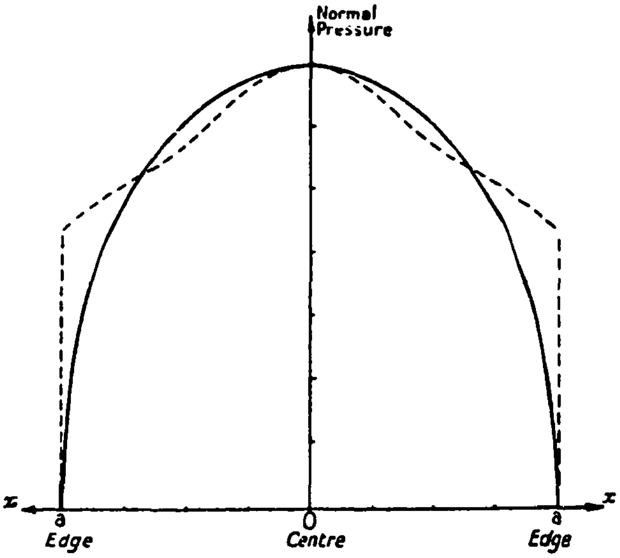

Figure 2. 5 Elastic pressure distribution beneath a Hertzian indenter given by Eq. 2.15 [solid line]. Radius of contact is defined by *a*. Dashed line indicates the change in pressure after full yielding of a ductile metal. After Tabor (1951).

such that P_m is the indentation stress, a/R, is the relative indentation strain and the constant in brackets is a function of the elastic constants of the two bodies. Macroscopically this parallels the stress-strain behavior shown in Fig. 2.1 with P_m and a/R as the stress-strain equivalent.

Elastic behavior under the indenter is observed until a yield point is obtained. At the yield point, the indentation stress-strain curve begins to deviate from the linear relation, Eq. 2.18, and exhibits a strain-hardening characteristic.

2.3.2 Microscopic Stress and Strain

Although Hertz was the first to solve the elasticity problem of curved bodies in contact with respect to their macroscopic relationship of stress, it was only at the contacting surfaces and along the loading axis. Hertz incorrectly estimated the stress trajectories beneath the indenter at other points in the body from his calculations. The correct solutions were published by Huber (1904) and then Huber and Fuchs (1914) who provided a closed form representation of the stresses in the body of the solid. In cylindrical coordinates, the Hertzian stresses within the body of the substrate are (Fischer-Cripps, 1997a):

$$\frac{\sigma_r}{P_m} = \frac{3}{2}\left\{\left(\frac{1-2\nu}{3}\right)\frac{a^2}{r^2}\left[1-\left(\frac{z}{\sqrt{u}}\right)^3\right]+\left(\frac{z}{\sqrt{u}}\right)^3\left(\frac{a^2u}{u^2+a^2z^2}\right)\right.$$

$$\left.+\frac{z}{\sqrt{u}}\left[(1-\nu)\frac{u}{a^2+u}+(1+\nu)\frac{\sqrt{u}}{a}\cdot\arctan\left(\frac{a}{\sqrt{u}}\right)-2\right]\right\} \tag{2.19}$$

$$\frac{\sigma_\theta}{P_m} = -\frac{3}{2}\left\{\left(\frac{1-2\nu}{3}\right)\frac{a^2}{r^2}\left[1-\left(\frac{z}{\sqrt{u}}\right)^3\right]\right.$$

$$\left.+\frac{z}{\sqrt{u}}\left[(2\nu)+(1+\nu)\frac{u}{a^2+u}-(1+\nu)\frac{\sqrt{u}}{a}\cdot\arctan\left(\frac{a}{\sqrt{u}}\right)\right]\right\} \tag{2.20}$$

$$\frac{\sigma_z}{P_m} = -\frac{3}{2}\left(\frac{z}{\sqrt{u}}\right)^3\left(\frac{a^2u}{u^2+a^2z^2}\right) \tag{2.21}$$

$$\frac{\tau_{rz}}{P_m} = -\frac{3}{2}\left(\frac{rz^2}{u^2+a^2z^2}\right)\left(\frac{a^2\sqrt{u}}{a^2+u}\right) \tag{2.22}$$

where

$$u = \frac{1}{2}\left\{\left(r^2+z^2-a^2\right)+\sqrt{\left(r^2+z^2-a^2\right)^2+4a^2z^2}\right\}. \tag{2.23}$$

and z is the distance along the loading axis direction. The Hertzian stresses are equal to the principal stresses at the surface of the substrate and along the loading axis. For all other points within the body of the substrate, the principal stresses can be determined using the following elementary relations:

$$\sigma_1 = \frac{\sigma_r + \sigma_z}{2} + \sqrt{\left(\frac{\sigma_r - \sigma_z}{2}\right)^2 + \tau_{rz}^2} \tag{2.24}$$

$$\sigma_2 = \sigma_\theta \tag{2.25}$$

$$\sigma_3 = \frac{\sigma_r + \sigma_z}{2} - \sqrt{\left(\frac{\sigma_r - \sigma_z}{2}\right)^2 + \tau_{rz}^2} \tag{2.26}$$

and contours of the three principal stresses beneath the Hertzian indenter are shown in Fig. 2.6(a-c) normalized to the mean indentation stress. In the figure, compressive stress regions are shaded gray and coordinates are normalized to the contact radius, *a*. The principal shear stress is shown in Fig. 2.6(d) with the maximum value attained beneath the surface (~0.5a) and is indicated with an 'X'.

2.3.2.1 Yielding Under Indentation

A general correlation between the compressive and tensile stress-strain behavior for annealed copper was established by Hill (1950) with a plot of stress against fractional reduction in area for tension and fractional reduction in height for compression (Fig. 2.7). Along the same lines, Tabor (1951) made a comparison for indented metals and their respective tensile behavior (Fig. 2.8) and determined that the respective stress-strain behavior differed only by a constant. Tabor's relation between

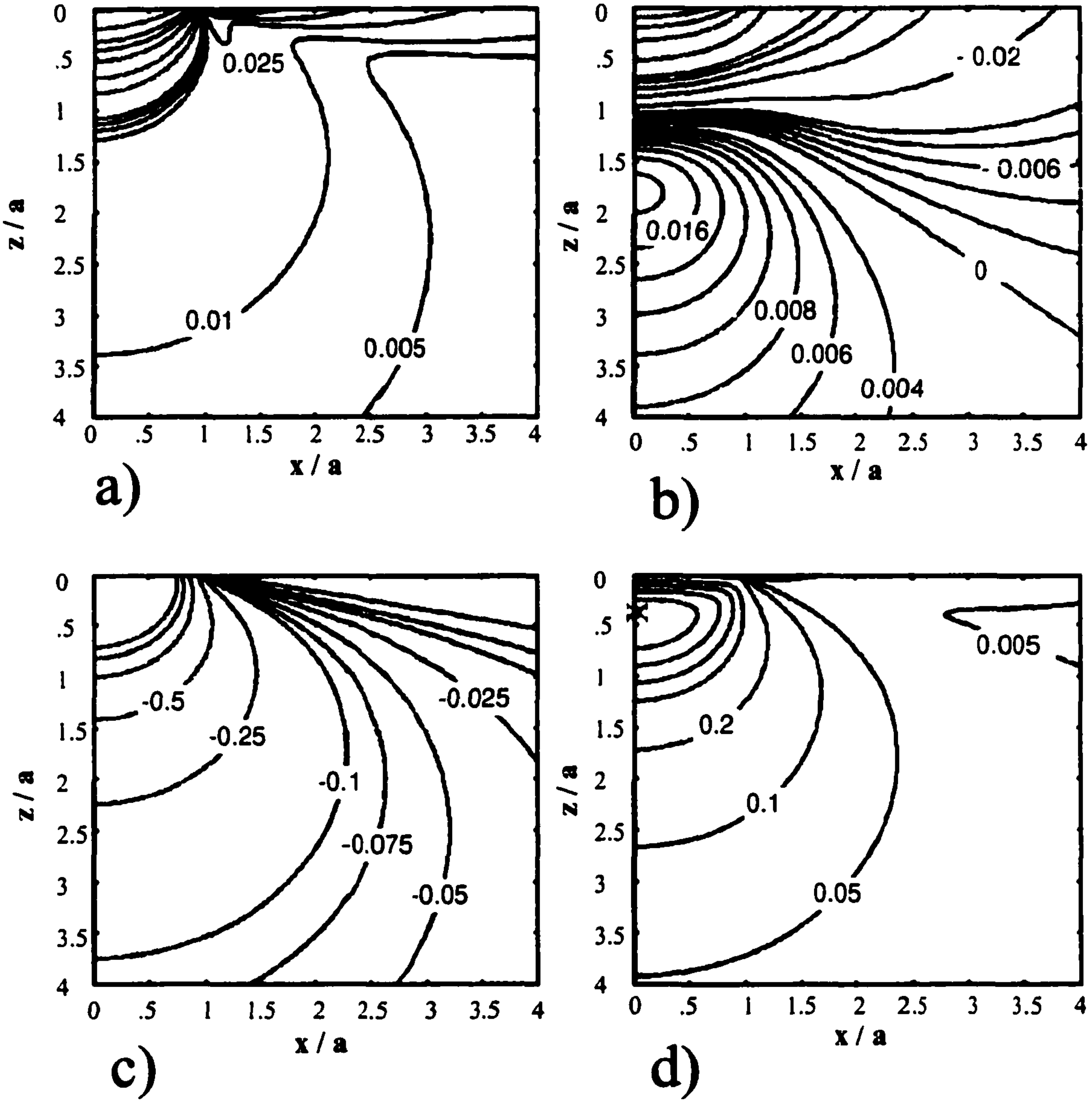

Figure 2. 6 Contours of principal stress beneath the Hertzian indenter. The contours represent stresses normalized to the mean stress, P_m at yield and for $\nu = 0.21$. Compressive regions are shaded. (a) σ_1, note the peak stress at the periphery of the contact area; contours -- -1, -.6, -.4, -.3, -.2, -.1, -.05, -.005, 0, .005, .01, .025, .05, .1; (b) σ_2, hoop stress; contours -- -.8, -.6, -.4, -.2, -.1, -.08, -.06, -.04, -.02, -.01, -.008, -.006, -.004, -.002, 0, .004, .006, .008, .01, .012, .014, .016, .018; (c) σ_3, contours -- -1, -.9, -.75, -.5, -.25, -.1, -.075, -.05, -.025, -.01, -.005, -.001; (d) τ_{13}, principal shear stress; maximum shear stress region is indicated by the X; contours -- .005, .05, .1, .2, .3, .35, .4, .45.

uniaxial strain and indentation strain is given by:

$$\varepsilon = 0.2\frac{a}{R} \qquad (2.27).$$

Tabor additionally noted that a plot of the indentation stress-strain curve for different indenter diameters (Fig. 2.9) was self-consistent: an advantage exploited by current practitioners of the Hertzian indentation technique to produce complete stress-strain curves.

To further understand the influence of the Hertzian stress field on deformation in our material, focus will be directed to the regions in which these stresses are maximum and likely to initiate irreversible damage.

Outside the circle of contact ($r > a$), the stresses at the surface ($z = 0$) are equal in magnitude and opposite in sign and take the form (Johnson, 1985):

$$\frac{\sigma_r}{P_m} = -\frac{\sigma_\theta}{P_m} = \frac{(1-2\upsilon)}{2}\frac{a^2}{r^2} \qquad (2.28)$$

It follows, therefore, from Eq. 2.28 that the maximum tensile stress at the surface of the substrate occurs when $r = a$ and has a value of (Johnson, 1985):

$$\frac{\sigma_r}{P_m} = \frac{(1-2\upsilon)}{2} \qquad (2.29)$$

at the edge of the contact area ($r = a$) between the indenter and the substrate.

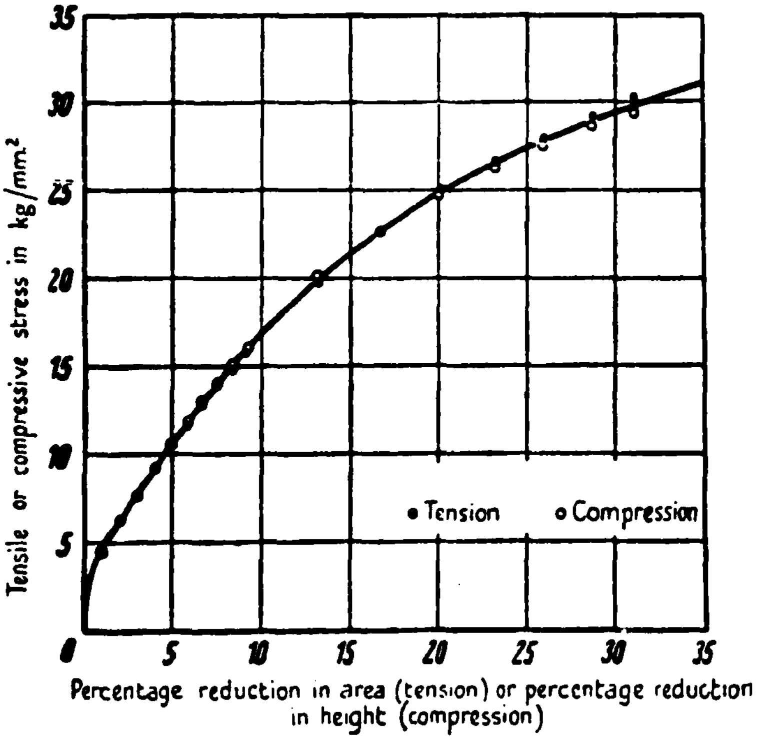

Figure 2. 7 A plot of the compressive and tensile stress-strain behavior for annealed copper. After Hill (1950)

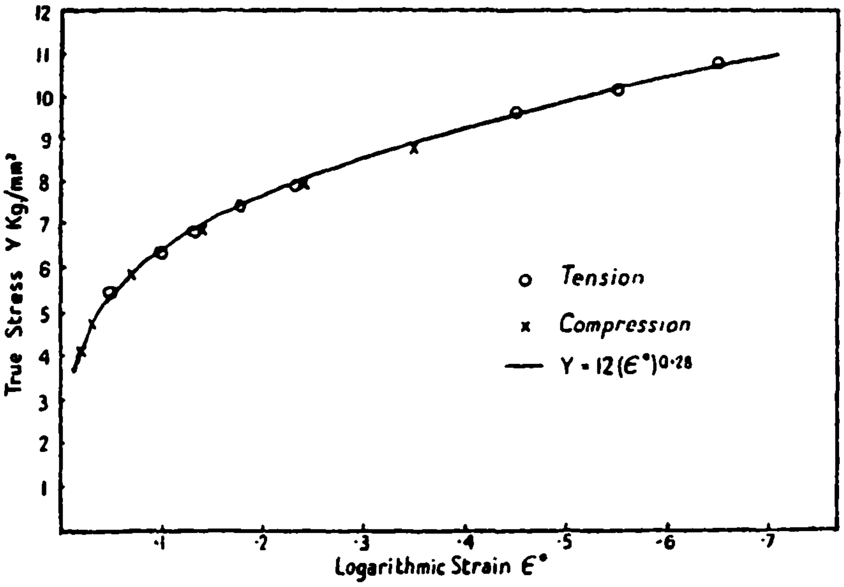

Figure 2. 8 Indentation stress as a function of strain compared to uniaxial tension stress-strain. Curves differ only by a constant. After Tabor (1951).

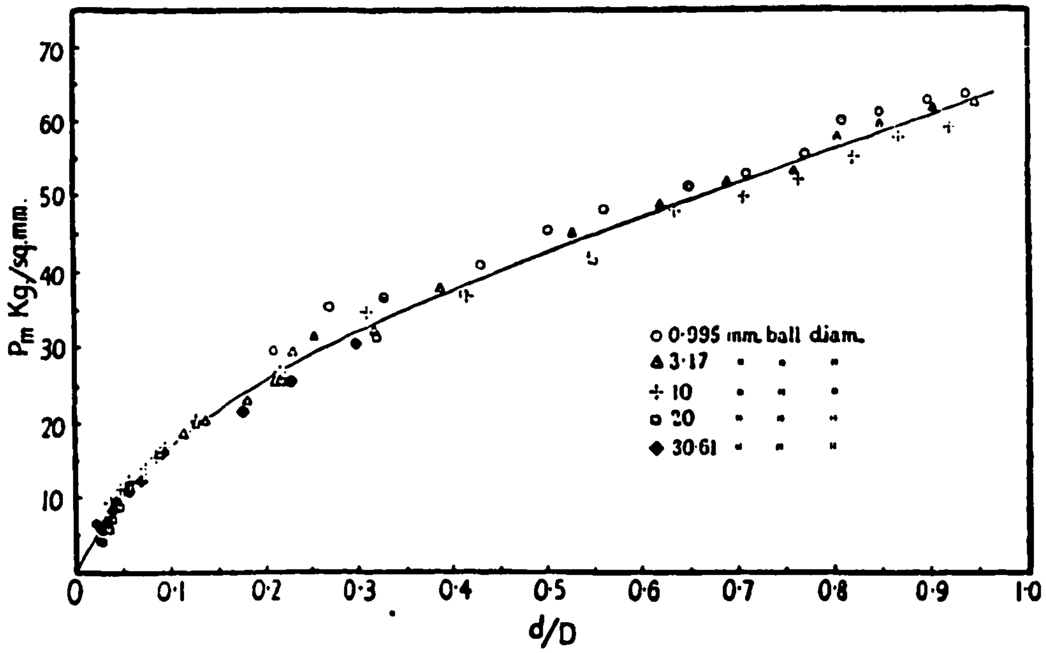

Figure 2. 9 Indentation stress-strain behavior for different diameter indenters. Self-consistent indentation behavior produces one curve for various load-diameter combinations. After Tabor (1951).

Although the theoretical maximum tensile stress is derived at the edge of contact, experimental observations of crack growth occur just outside of this boundary. The reason for the discrepancy arises from frictional effects between the indenter and substrate that act to modify the stresses slightly in the system (see Sec. 2.9.1). Frictional effects between the indenter and substrate will be assumed negligible in this investigation.

It is well established in ductile metals that the point of initial yielding occurs where the principal shear stress is a maximum (Tabor, 1951). The shear stress attains this maximum value along the loading axis at a point beneath the surface of the indenter as shown in Fig. 2.6(d). From Eqs. 2.19 to 2.21 we can obtain normalized expressions for the stresses at the loading axis (Johnson, 1985) as:

$$\frac{\sigma_r}{p_o} = \frac{\sigma_\theta}{p_o} = -(1+\upsilon)\left\{1 - \frac{z}{a}\arctan\left(\frac{a}{z}\right)\right\} + \frac{1}{2}\left(1 + \frac{z^2}{a^2}\right)^{-1} \tag{2.30}$$

$$\frac{\sigma_z}{p_o} = -\left(1 + \frac{z^2}{a^2}\right)^{-1} \tag{2.31}$$

The principal shear stress along the loading axis is then given by:

$$\tau_1 = \frac{1}{2}\left|\sigma_z - \sigma_\theta\right| \tag{2.32}$$

Plotting τ_1 along z normalized to a with $\nu = 0.21$ (Fig. 2.10) gives a maximum principal shear value of:

$$\tau_1 = 0.4968 \cdot P_m \tag{2.33}$$

at a depth of $z = 0.45\ a$. The point of initial yield, (Z) in Fig. 2.11(a), also corresponds to the point at which a residual impression first forms on the indented surface (Tabor, 1951). As the load is increased, the deformed region beneath the indenter expands until it reaches the indented surface and a condition of plastic flow is achieved (Fig. 2.11(b)). Upon full yielding the pressure profile changes from the parabolic distribution, Fig. 2.5 (straight line), to that shown by the dashed line with the largest change taking place at the extreme of the contact circle.

2.4 Linear Elastic Fracture Mechanics

Although macroscopic yielding of brittle materials under Hertzian indentation can resemble yielding in ductile metals, the mechanisms are completely different. Dislocation motion is chiefly responsible for metal plasticity. In contrast, many ceramic systems yield by distributed microfracture under compressive loading. The microfracture events

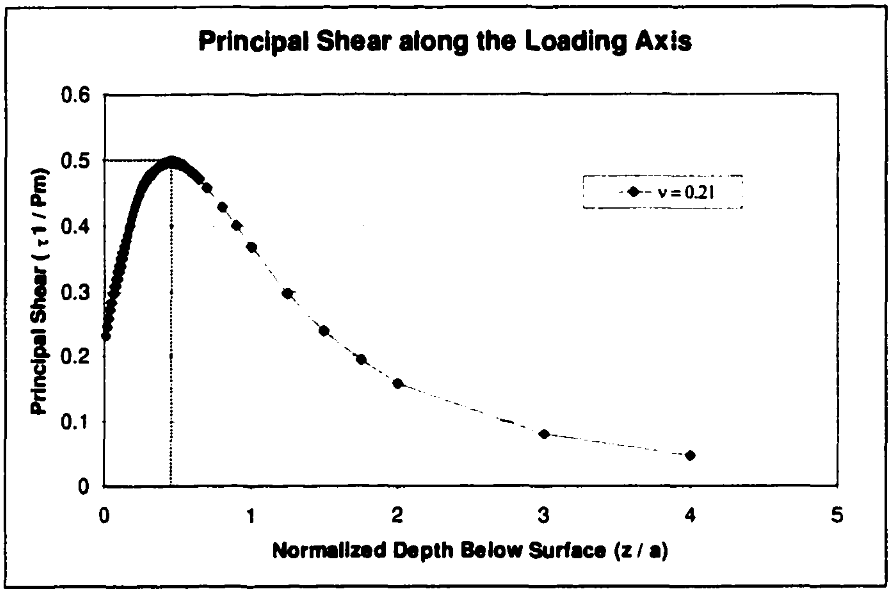

Figure 2. 10 Graph of Eq. 2.32, principal shear stress for Poisson's ratio = 0.21, beneath the loading axis of a Hertzian indenter. Dashed lines indicate the peak.

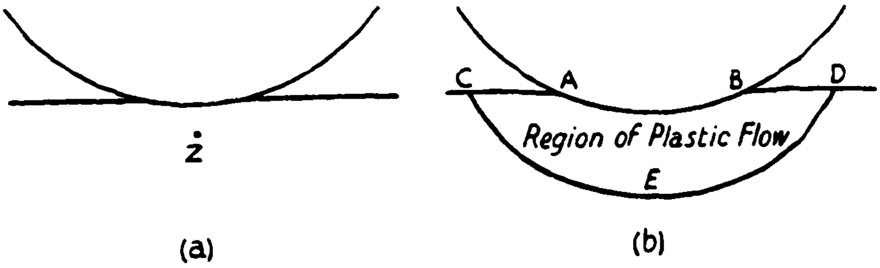

Figure 2. 11 (a) Diagram of sub-surface point (Z) for yielding in region of maximum shear stress calculated by Eq. 2.33. (b) Growth of plastic deformation results in flow of the material beneath the indenter at higher loading. After Tabor (1951).

are driven by localized tensile or shear forces within the microstructure that arise from stress concentrating features. These will be discussed in detail in subsequent sections. We proceed with the assumption that brittle linear elastic fracture is the dominant process at the microstructural level at the onset of yielding.

The foundation of linear elastic fracture mechanics is owed to an early and essential discovery by Griffith (1924) based on an energy balance of the fracture process. As a result of a balance between the decrease in potential energy and the increase in surface energy due to new crack surfaces, Griffith obtained the following relation:

$$\sigma = \sqrt{\frac{2E\gamma_S}{\pi\left(1-\nu^2\right)l}} \tag{2.34}$$

Equation 2.34 is based on a 2D infinite elastic body, Fig. 2.12, with a through-thickness crack of length $2l$ under a stress, σ, applied perpendicular to the crack plane. γ_S, is the surface energy of the crack per unit area and ν is Poisson's ratio. Note that the above equation is for a plane strain condition. The Poisson's ratio term would be removed for plane stress conditions. A derivation of Griffith's result may be found in any elementary fracture mechanics textbook (for example Hertzberg, 1997 or Broek, 1991).

Griffith's relation was an important step to understand the essence of fracture phenomena from a theoretical standpoint. However, the Griffith relation does not specify the magnitude of localized stresses for a given crack. Another fundamental relationship that helped to quantify the intensity of stress at the crack tip for a given loading condition was developed from elastic considerations of stress levels around the crack tip singularity. Stress magnification at a crack tip is finite and proportional to the remote applied stress. The measure of stress increase, or *stress intensity*, is also dependent on the crack size, l, and can be described by the following relation for the situation shown in Fig. 2.8:

$$K_I = f \cdot \sigma \sqrt{\pi l} \tag{2.35}$$

where K_I is known as the stress intensity factor and f represents a function that accounts for the specific loading geometry. In the simplest case, f is equal to one. The subscript on K indicates pure tensile mode "I" loading. The different crack loading modes are shown in Fig. 2.13. Modes II and III are shear based fracture modes and the corresponding shear stress would be used for σ in Eq. 2.35.

The stress intensity factor increases with the remote applied loading for a given crack geometry until a critical value is obtained and the crack begins to propagate. The fracture toughness of a material, K_{Ic} or T_o, is a fundamental material property and expressed in units of Pa·m$^{1/2}$. When the stress intensity factor, K, becomes infinitesimally greater than the toughness, the crack will propagate. Whether the crack propagates without limit or arrests depends strongly on how the material and sample changes with crack propagation.

Taking Griffith's concepts further, Irwin (1949) introduced a "critical energy release rate", G_c, into Griffith's relation as:

$$\sigma_c = \sqrt{\frac{EG_c}{\pi a}} \tag{2.36}$$

which allowed for a critical or failure stress, σ_c, to be determined based on the energy

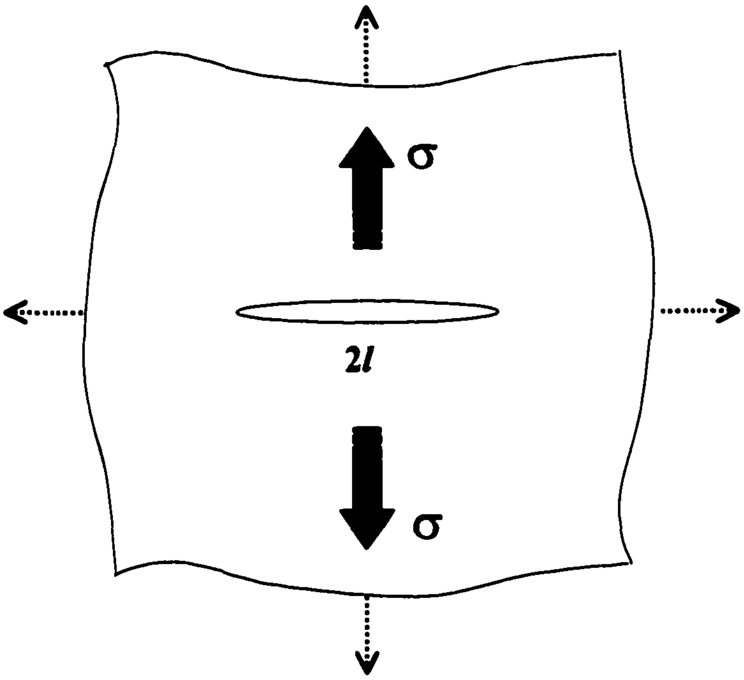

Figure 2. 12 An infinite elastic material with a through-thickness crack of length 2*l*. A uniform tensile stress, σ, is applied remotely across the sample. The stress intensity at the crack tip is given by Eq. 2.35.

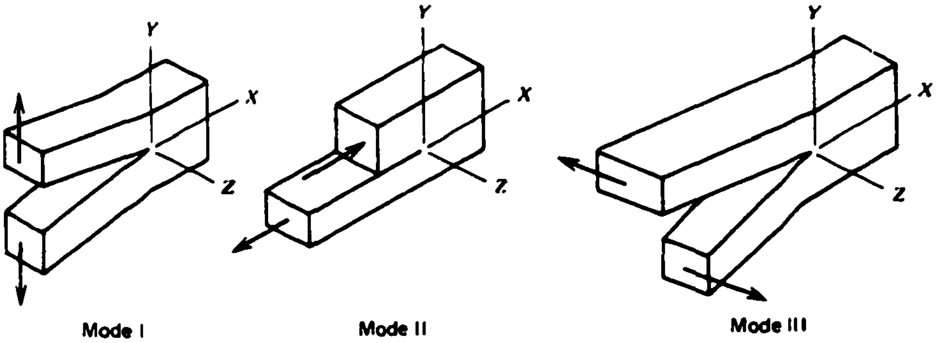

Figure 2. 13 Modes of crack loading. Mode I is pure tensile and modes II and III are shear driven. After Hertzberg (1997).

release rate of the fracture process. The critical energy release rate was later shown to be related to the already defined fracture toughness (Irwin, 1957):

$$G_C = \frac{K_C^2}{E'} \tag{2.37}$$

$$E' = E \qquad \text{(plane stress)} \tag{2.38}$$

$$E' = \frac{1-\nu^2}{E} \qquad \text{(plane strain)} \tag{2.39}$$

which tied the whole fracture process together from a fundamental understanding of crack geometry and energy balance.

2.5 Elastic Stress Distribution around a Hole

The effect of a spherical void on altering a uniform applied stress field has been reported as early as Kirsch (1898) for a hole in an infinite plate of uniform thickness. Since then, the elastic solutions to the distribution of stresses around a void have been established for two (Greenwood, 1989; Bickley, 1928) and three (Goodier, 1933; Southwell, 1926) dimensions for finite and infinite bodies. Goodier (1933) also described the equations for a solid particle of higher modulus in a lower modulus matrix.

2.5.1 Distribution under Tensile Stress

A spherical void will perturb a uniform stress field, σ, in the immediate vicinity of the defect with tensile stress levels of some regions and compressive stress levels of other regions, increasing. For example, when a remote tensile stress is applied to a sphere, a region of maximum tensile stress, 2σ, develops tangentially at the periphery of the defect parallel to the loading axis illustrated at point (B) in Fig. 2.14(a). The peak tensile stress **zz** falls off rapidly as the radial distance away from the sphere increases (Fig. 2.14(b)). Extending outward from point (B), the other principal stresses also fall off very quickly with increasing distance from the sphere surface. The radial stress, **rr**, reaches a peak a short distance from the free surface and then decreases. Plots of the surface tangential stresses, θθ & φφ, from point (B) to (A) are shown in Fig. 2.14(c). θθ decreases from 2σ at point (B) to a value of $-2/3\sigma$ along the loading axis. The stresses around the sphere at any point are increased by 3/2 for the 2D case from the 3D case shown in Fig. 2.14 (Greenwood, 1989).

Several important points should be noted with respect to the stress state around circular or spherical defects. First, one should note that stress levels at the surface of the hole are constant for a given σ, regardless of the hole radius, R. This holds true provided the remotely applied stress is uniform across the defect. As will be discussed later, the introduction of a stress-concentrating flaw, to the sphere surface *does* create a dependency of the stress intensity factor on the size of the hole or sphere radius.

Additionally, according to Goodier (1933), a spherical defect that is situated at around 4 or more diameters from any other discontinuity (i.e. – a free surface or another defect) may be considered isolated. For uniform pores on a FCC lattice, four diameters corresponds to around 1% porosity. Because the majority of the materials in this investigation have porosity in excess of 1%, elastic interaction between pores will be considered and is discussed in Sec 2.8.

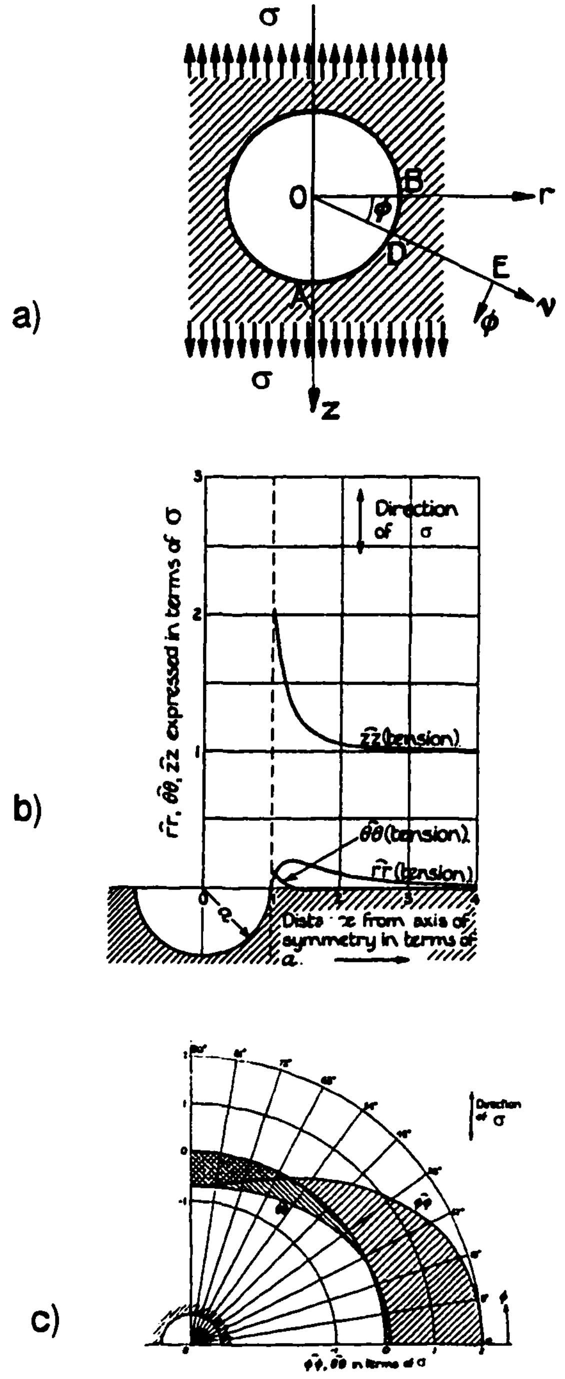

Figure 2. 14 Distribution of stress around a spherical void under a uniform tensile stress, σ. (a) Diagram of the void. Point B experiences the highest tensile stress and the largest compressive stress occurs at A. (b) A plot of the principal stress starting at B and extending radially outward. Note the rapid decay of the maximum tensile stress. (c) Distribution of stress on the surface of the void from point B to A. After Southwell (1926).

2.5.2 Distribution under Compressive Stress

If the applied stress field acting on a spherical void is compressive, the signs of tne distributed stress (Fig. 2.14) arc reversed but the magnitudes are the same. A uniaxial compressive load will create a tensile region as indicated in Fig. 2.15(a) [dashed line] and alter the stress trajectories as shown in Fig. 2.15(b) (Jaeger and Cook, 1969). Under Hertzian contact, however, a triaxially compressive stress state is produced beneath the indenter (see Fig. 2.6). Because of the axial symmetry in the stress field, a biaxial representation is often used. The biaxial representation will allow for simple approximations to be used with plane-strain loading conditions as will be shown in later sections.

For biaxially compressive stresses, p_2 and , p_1 where $p_1 > p_2$, the elastic solution to the stress that develops around a hole has been calculated by Jaeger and Cook (1969) and can be expressed as:

$$\sigma_r = \frac{1}{2}(p_1 + p_2)\left(1 - \frac{R^2}{r^2}\right) + \frac{1}{2}(p_1 - p_2)\left(1 - \frac{4R^2}{r^2} + \frac{3R^4}{r^4}\right)\cos(2\theta) \qquad (2.40)$$

$$\sigma_\theta = \frac{1}{2}(p_1 + p_2)\left(1 + \frac{R^2}{r^2}\right) - \frac{1}{2}(p_1 - p_2)\left(1 + \frac{3R^4}{r^4}\right)\cos(2\theta) \qquad (2.41)$$

$$\tau_{r\theta} = -\frac{1}{2}(p_1 - p_2)\left(1 + \frac{2R^2}{r^2} - \frac{3R^4}{r^4}\right)\sin(2\theta) \qquad (2.42)$$

where the σ_θ term is the stress tangential to the surface of the hole and σ_r extends radially outward from the hole surface. Note that in this solution, the applied compressive stresses are considered positive and tensile stresses are negative (the standard convention for rock mechanics). Therefore, the maximum tangential stresses on the surface of the hole are given by:

$$\sigma_\theta = 3p_2 - p_1 \text{ when } \theta = 0 \tag{2.43}$$

$$\sigma_\theta = 3p_1 - p_2 \text{ when } \theta = \pi / 2 \tag{2.44}$$

The Hertzian stresses calculated at the point of maximum shear stress will be substituted into Eq. 2.41 where $p_1 = \sigma_z$ and $p_2 = \sigma_r$ and is discussed in detail in Chapter 7.

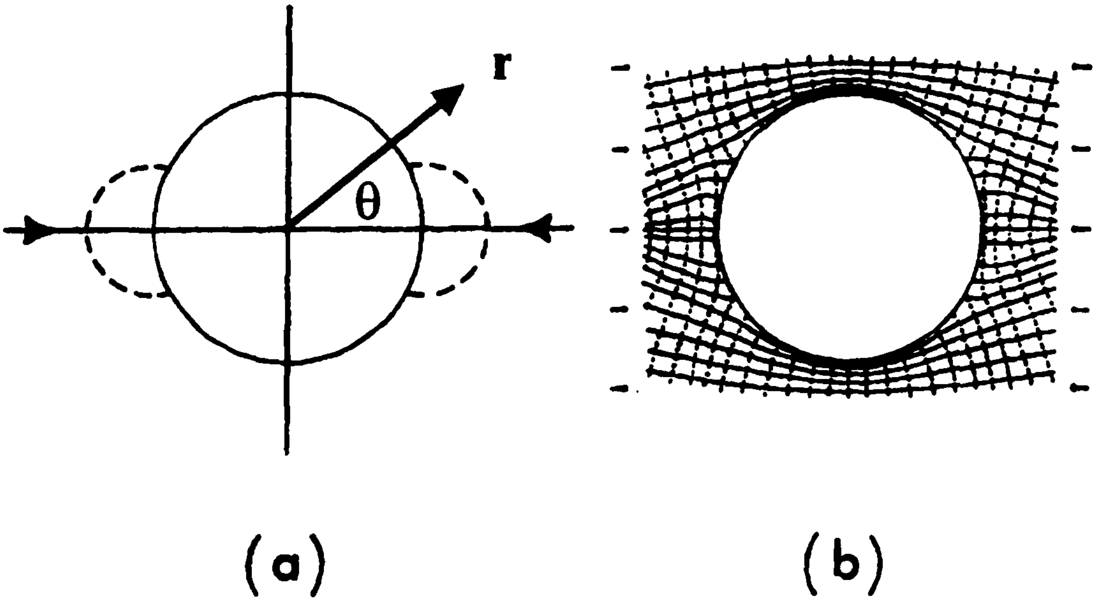

Figure 2. 15 Hole defect in a uniform uniaxial compressive field. (a) Inside the dashed lines is the tensile region; (b) Alterations in stress trajectories near hole. After Jaeger and Cook (1969).

2.6 Stress Intensity of a Flaw at a Circular Hole: Applied Tensile Stress

Knowledge of the stress distribution around a circular hole permits the determination of the stress intensity factor for a flaw located normal to the hole surface (Fig. 2.16). Bowie (1956) was the first to address this by considering two cracks at opposite ends of the hole and perpendicular to the applied tensile field. Instead of calculating the stress intensity factor, Bowie chose to evaluate a failure criterion similar to Griffith's (1920). Later, Tweed (1973) supplied a stress intensity factor calculation of the problem for a single crack in an infinite body. Stress intensity factor solutions for finite bodies followed and were summarized by Wu and Carlsson (1991),Wang (1990), and Schijve (1983). The calculations by Wu and Carlsson (1991) are shown in Fig. 2.17 for one- and two-crack systems. In Fig. 2.17, N is the number of cracks, $a = A/R$ and A is the flaw size, and the graph of *f* is the geometric factor used in calculating the stress intensity in the equation (see Eq. 2.35):

$$K_I = f \cdot \sigma \sqrt{\pi a R} \qquad (2.45).$$

The R dependence of the stress intensity factor is not seen explicitly in Eq. 2.48 but is accounted for in the *f* term. From the values of *f* and Eq. 2.45 one can see that for smaller flaw sizes, the geometric stress magnification factor, f, is increased or conversely for a fixed flaw size, the stress intensity will be increased by increasing the hole radius. Note that in pure tension, K_I increases with increasing flaw size, A, for a fixed radius hole. Under biaxial compression, the flaw is propagated from a tensile region into a compressive one with a corresponding decrease in K_I with crack growth, as shown in the next section.

2.7 Stress Intensity of a Flaw at a Circular Hole: Biaxial Compressive Stress

While numerous investigations have calculated the stress intensity factors of a flaw in a hole under tensile stress, little work has addressed the issue of biaxial compressive stress. A paper by Sammis and Ashby (1986) was one of the earliest to treat the biaxial compressive stresses and stress intensity factor calculations. Sammis and Ashby attempted to provide a simple closed form expression to the stress intensity under biaxial compressive stresses using approximations of the Green's functions for the load distributions around the crack (Fig. 2.18). The approximated equation of the stress intensity factor may be expressed in the form of Eq. 2.35 as:

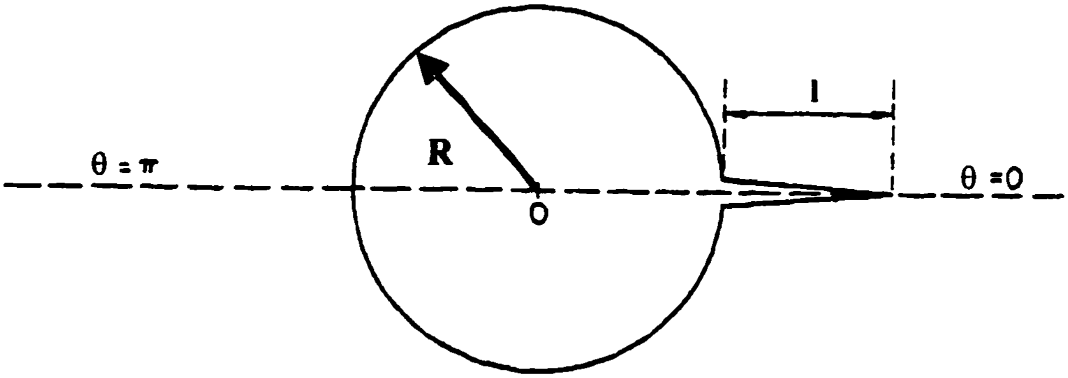

Figure 2. 16 Diagram of circular hole and flaw arrangement used to calculate stress intensity factors. After Tweed (1973).

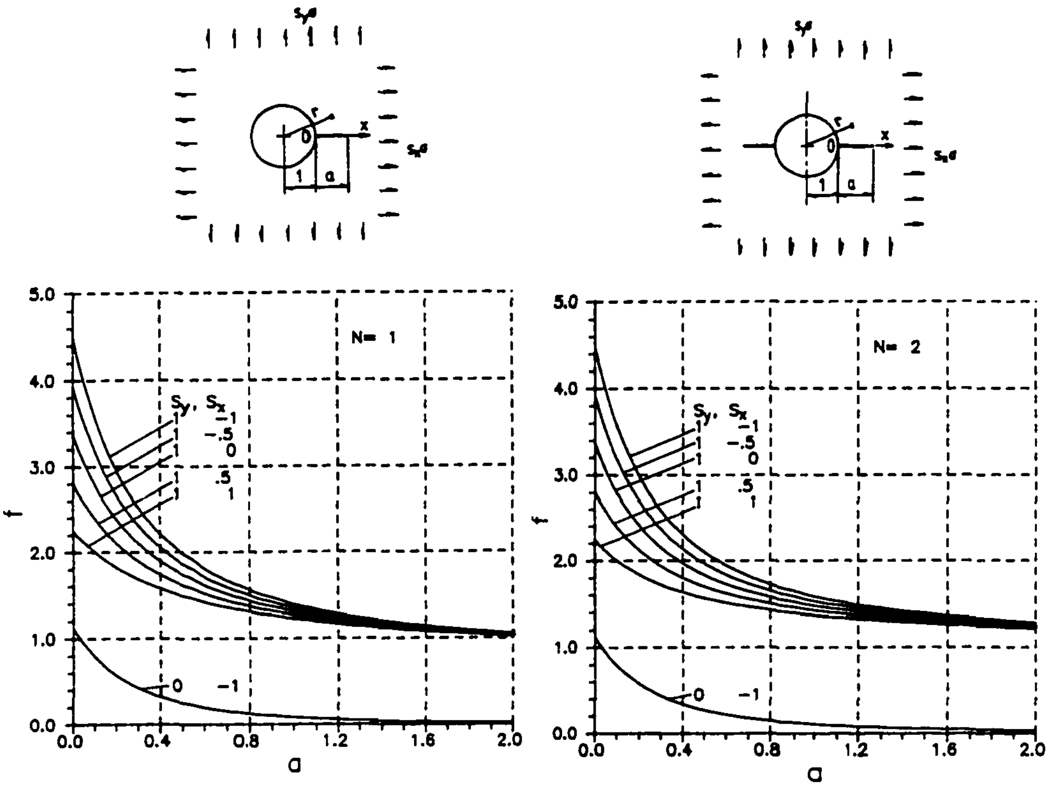

Figure 2. 17 Geometric stress concentration factors, *f*, for several loading conditions. Biaxial loads normalized to σ. Number of cracks = N and flaw size is A where a = A when R = 1 (as shown above). Increases in R for a fixed flaw size are expressed as a decrease in *a*. After Wu and Carlsson (1991).

$$K_I = -F(\lambda, L)\cdot\sigma_1\sqrt{\pi l} \tag{2.46}$$

where

$$F(\lambda, L) \cong \frac{1.1(1-2.1\lambda)}{(1+L)^{3.3}} - \lambda \tag{2.47}$$

so that the stress intensity factor can be expressed in closed form as:

$$K_I = -L^{1/2}\left\{\frac{1.1(1-2.1\lambda)}{(1+L)^{3.3}} - \lambda\right\}\cdot\sigma\sqrt{\pi R} \tag{2.48}$$

where l is the crack length, R is the hole radius, $L = l/R$, and λ is the ratio of the remotely applied stresses σ_3/σ_1. Values of $F(\lambda, L)$ are shown in Fig. 2.19 and it is easily observed that for large values of R (small L), F is increasing in agreement with the predictions of Wu and Carlsson (1991) from the previous section.

One should note further that for values of $\lambda > 0$, there exists a finite value of L at which the crack will terminate. Also, if λ, the ratio of the smallest principal compressive stress to the largest is greater than or equal to 1/3, cracks cannot initiate at all (Sammis and Ashby, 1986). This fact is also shown in Eq. 2.43 when $p_2 = 1/3\ p_1$, the maximum tangential stress at the hole surface becomes zero. As will be shown in Sec. 6.3.3, this is an essential factor for controlling distributed damage and ultimately for producing a quasi-ductile response under Hertzian contact or other compressive loading conditions.

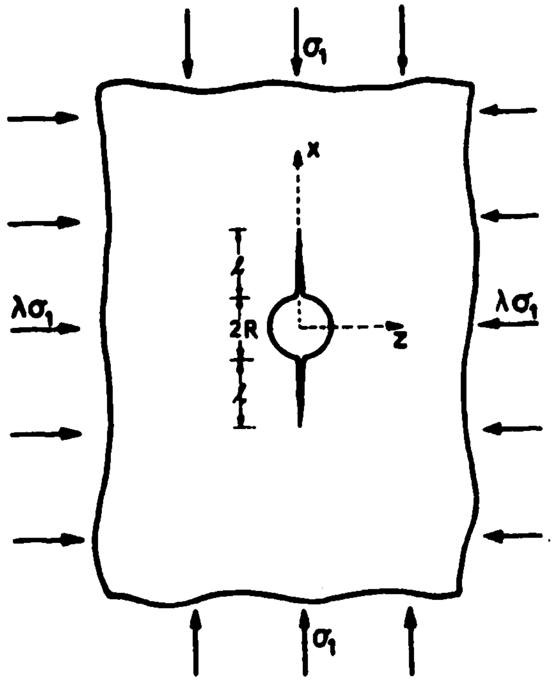

Figure 2. 18 Orientation of stress and cracks for stress intensity factor calculation by Sammis and Ashby (1986). The hole radius is R, the flaw size l, and λ is the ratio of stresses σ_3/σ_1.

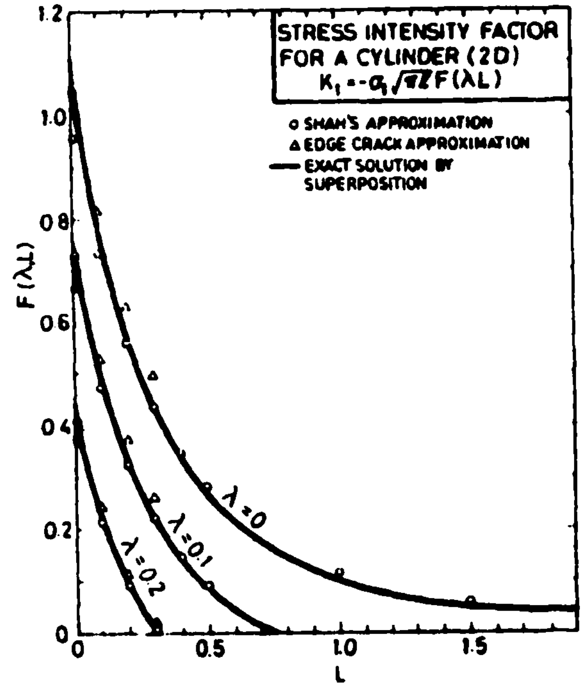

Figure 2. 19 Plot of the stress concentration factor under biaxial compression for different values of the stress ratio, λ.

2.8 Interaction Effect of Pores and Holes

The solutions provided in the literature for tensile and compressive stresses applied to a single hole or spherical void are instructive. However, situations involving porous structures involve a multitude of voids. Understanding volumetric interaction effects between voids on the elastic stress distributions around them is essential to making accurate microstructural damage predictions.

One of the first studies involving the interaction of holes under a uniform stress was by Howland (1935) who considered an infinite linear periodic array of holes under the action of a uniform tensile stress. Howland arranged the holes perpendicular and parallel within the remote uniform applied stress field. Fig. 2.20 shows the plots of the stresses for the two different orientations and compares two extremes of separation distance: 4R center-to-center spacing and infinite spacing (isolated hole). In Fig. 2.20(a) the tensile stress is applied perpendicular to the line of holes. In the middle of the graph is a plot of the tensile stress for an isolated hole, IIb (dashed line). This stress increases in the presence of the other holes, IIa (solid line) to a value around 8% above the isolated value at the center-to-center distance of 4R. The surface stress is also shown to increase uniformly over the same change in spacing, Ib to Ia. Notice that a remotely applied compressive stress would cause the peak tensile stress (90°) to *decrease* with increasing proximity. Fig. 2.20(b) illustrates the behavior of the pores aligned parallel in the stress field. Notice the large decrease (~30%) of the peak tensile stress, Ib to Ia at 90° at the surface and into the bulk, IIb to IIa. Furthermore, the behavior of the surface tangential stress is not uniformly affected as it was in Fig. 2.20(a). The Ia, Ib curves overlap at 30 and reverse the trend shown in (a). The difference may partially explain an orientation dependence of multiple pores calculated later using finite element modeling. These values will be compared to those calculations in Chapter 7.

Localized stress calculations in a two-dimensional periodic array of holes has not been explicitly addressed in the literature. However, Isida and Nemat-Nasser (1987) provided detailed work on cracked bodies under biaxial compression. Isida's results followed directly from Sammis and Ashby (1986), mentioned previously. Neither Sammis nor Isida intended to provide an answer to the interaction effect of hole spacing on stress, but it can be inferred from their findings.

Fig. 2.21 is a series of graphs from Isida and Nemat-Nasser (1987) showing the geometric stress concentrating factor, f (see Eq. 2.35), as it varies with normalized crack length. Isida considered three different periodic arrangements of holes, which were defined by their x-y center-to-center spacing. Fig. 2.21(b) has a square matrix of holes indicated by the term, b/c = 1. An equilateral triangular arrangement is indicated in Fig. 2.21(a) and Fig. 2.21(c) shows the results for an asymmetric arrangement of holes. Clearly, the geometric periodicity of the holes influences the stress intensity behavior, as does the crack length. Each graph (a-c) contains curves for different c/a values that represent hole spacing (or porosity), where a is the hole radius. Lower values of c/a represent closer spacing or higher porosity. Fig. 2.21(b)&(c) show a clear trend of

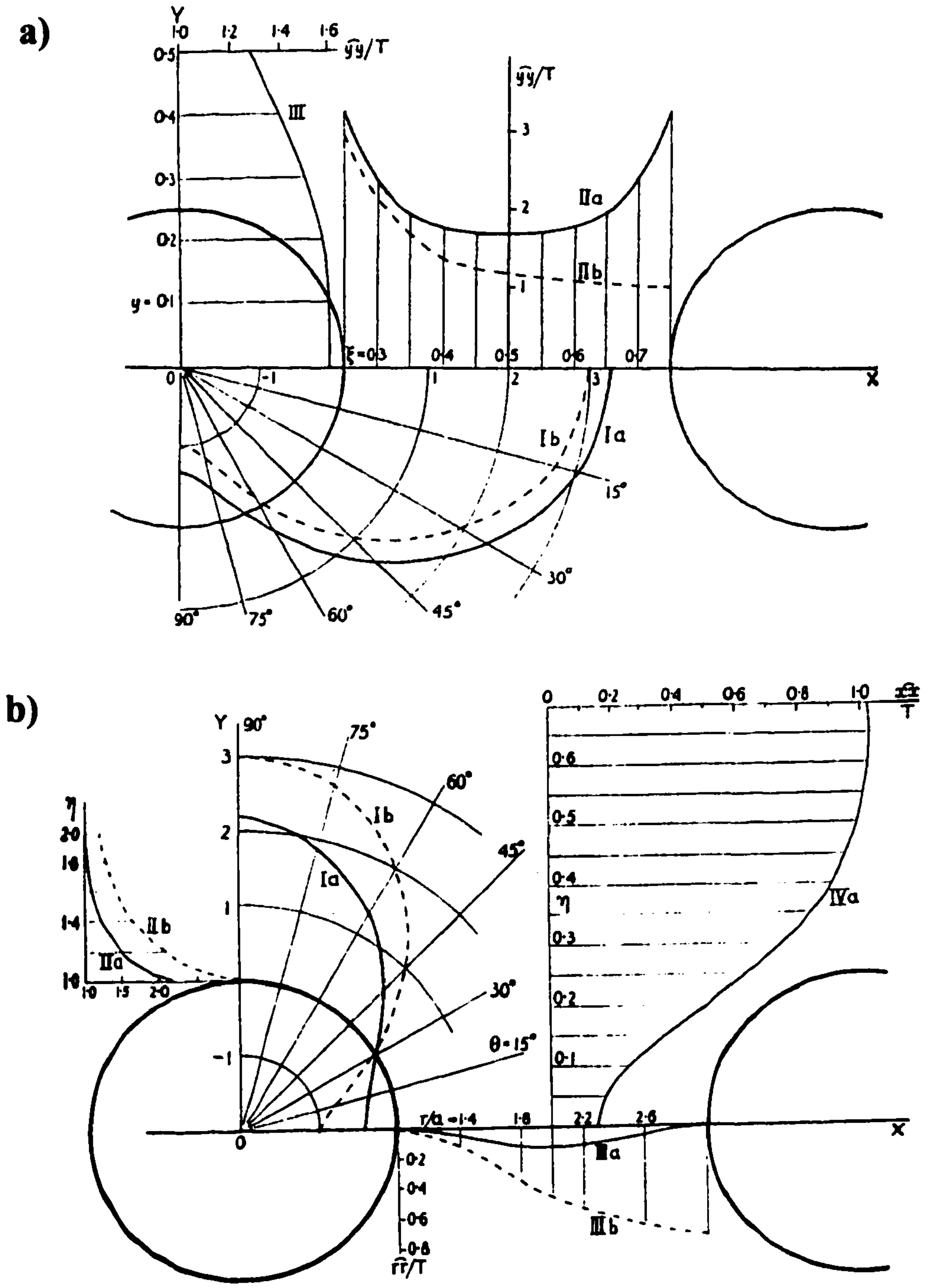

Figure 2. 20 Solutions to the stress change for an infinite row of holes under the action of a uniform remote tensile field, solution 'b' is for an isolated hole, solution 'a' is for a center-to-center distance of 4R: (a) Tensile stress applied perpendicular to the line of holes (b) Tensile stress applied parallel to the line of holes. After Howland (1935).

increasing *f* at a given crack length for changes in c/a. In contrast, Fig. 2.21(a) remained constant for most crack lengths. The results in Fig. 2.21 infer a stress magnification effect that is dependent upon the hole spacing and therefore the porosity of a structure. This issue will be addressed further in Chapter 7.

Lastly, Sammis and Ashby proved evidence of a pore interaction effect albeit less direct than Isida and Nemat-Nasser (1987). Fig. 2.21 is a graph from Sammis showing the normalized stress dependence on the crack length for a uniform array of holes under uniaxial compression. Cracks are located parallel to the axis of the applied load and Sammis and Ashby estimate damage accumulation and changes in elastic modulus with crack growth by modeling the uncracked solid ligaments in the structures as deflecting beams. The top half of the figure shows a series of curves at different porosity; the higher the porosity, the lower the normalized stress needed to cause crack growth. Because the fracture toughness is constant (and normalized out) the lower stress at a constant crack length indicates an enhancement to the stress concentration effect by the porosity. The lower half of the figure shows a decline in the elastic modulus with crack growth as one would expect.

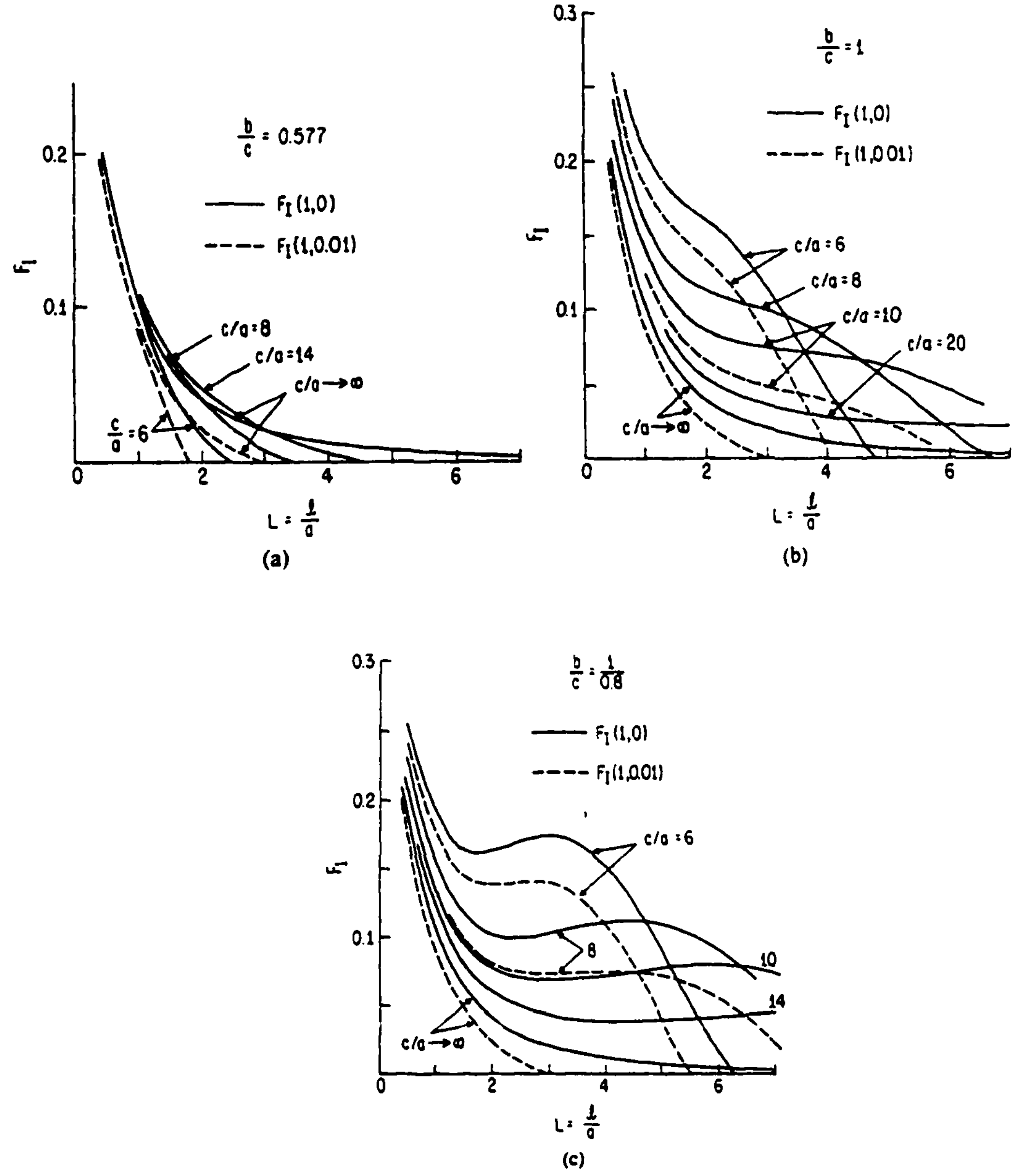

Figure 2. 21 Graphs of the stress magnification factor, *f*, for three different hole spacing, b/c, and for several hole spacing, c/*a*. The hole radius is defined by *a*. Graph results imply an increasing functional dependence on porosity (c/a) for the hole arrangements in (b) and (c). **(a)** An equilateral triangular spacing, b/c = 0.577 shows little change with variations in c/a. **(b)** A square matrix of holes, b/c = 1, indicates an increasing effect on *f* with an increase in hole spacing, c/a. **(c)** An asymmetric array of holes, b/c = 1.25, shows an even larger increase at intermediate crack lengths with a region of stable growth for L ~2. After Isida and Nemat-Nasser (1987).

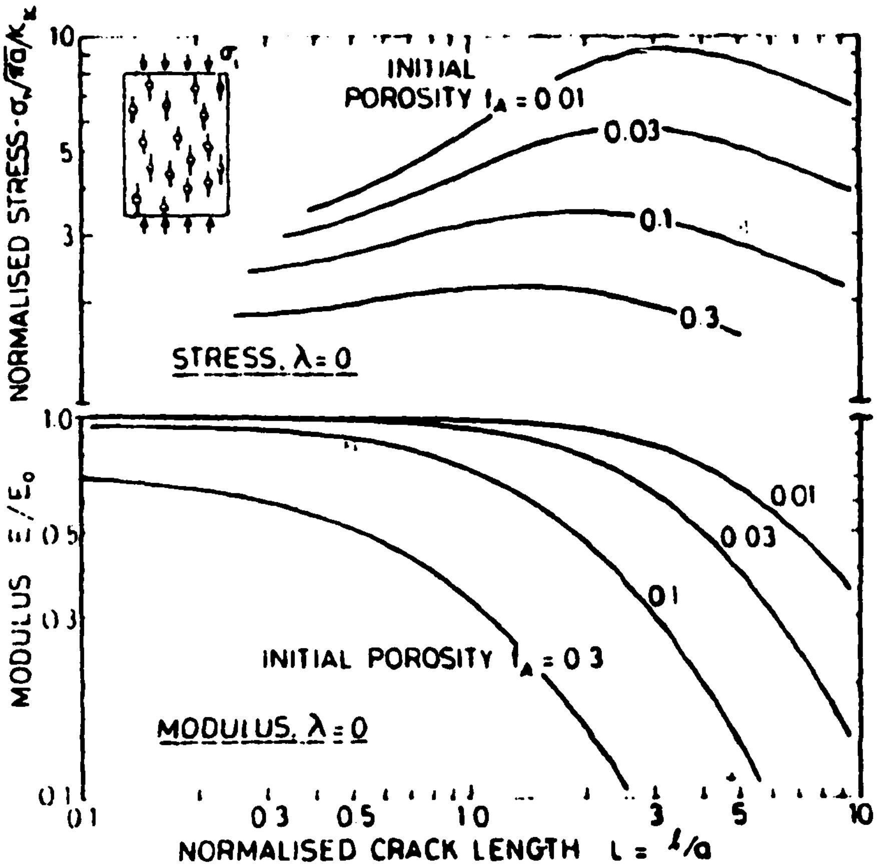

Figure 2. 22 A plot of the normalized stress to cause crack propagation as a function of crack length (top). Under an applied uniaxial stress, $\lambda = 0$, the normalized stress decreases with increased porosity for a given crack length, implying a pore interaction effect. Correspondingly, the elastic modulus decreases as cracks grow and increasingly so for higher porosity (bottom). After Sammis and Ashby (1986).

2.9 Hertzian Indentation Damage

Very recently, Lawn (1998(a)) reviewed the past 100 years of research into Hertzian contact. As discussed previously, the attractive feature of blunt indentation is the transition from reversible elastic deformation to irreversible damage. This section will address the types of irreversible damage that can occur beneath a Hertzian indentation. As stress is increased around the indentation as described in Sec. 2.3.3.1, some combination of brittle fracture and/or plastic damage will occur. In modern ceramic systems, brittle fracture is often the only way a material can respond to loading past its yield point[‡]; fracture occurring macroscopically in the form of a cone-crack, at the microstructural level as distributed damage or sometimes both. Observations of macroscopic yield behavior can resemble that of a ductile metal under Hertzian contact.

2.9.1 The Classic Brittle Response

The investigation of Hertzian induced brittle fracture began almost immediately following Hertz's elastic contact experiments. Auerbach (1891) first established a relationship between the size of an indenter radius, R, and the critical load for cone cracking, P_c, such that $P_c \sim R^2$. The fact that the critical load for failure depended on the indenter radius and not the inherent toughness (K_{Ic}) of the material remained an unexplained paradox for more than 70 years. Frank and Lawn (1967) were the first to prove Auerbach's relation by integrating the maximum principal stress along the minimum principal stress trajectory and calculating fracture toughness for a normalized crack size. Fig. 2.23 illustrates how the fracture behavior depends on the applied load and the growth of the flaw during indentation (Lawn, 1993).

As a load P' is applied, surface flaws in the region $c_0 < c_i < c_c$ spontaneously form a ring around the contact area. The ring crack experiences short but stable downward growth upon increasing the load to P'', where cracks will grow to the length c_c (region 1 to 2). Cone cracks pop in to their final length, c_f (region 3 to 4), once the instability criterion is met at load P'''. It is important to note that the surface ring-crack will always

---

[‡] Yield, in this case refers to any form of irreversible damage

form first (Dai, 1995; Frank and Lawn, 1967) and can exist to a size c_c before developing into a cone-crack. Therefore, one cannot always assume that the presence of a ring crack on the surface is indicative of a sub-surface cone-crack unless it is first confirmed by some other method for a given indenter radius. A number of studies have confirmed this (Fischer-Cripps & Lawn, 1996(a); Guiberteau, 1994)

Experimentally, ring cracking is seldom encountered at the exact contact boundary but is usually found at a slightly larger radius then that of indenter contact (Lawn, 1993). The discrepancy exists because of the frictional traction, Poisson ratio effects, and a difference in elastic modulus between the indenter and the indented body (Andersson, 1996; Warren, 1994(a)). A higher modulus in one of the two contacting bodies will increase tensile forces in the second as well as to extend the location of the peak tensile force on its surface away from the periphery of contact (Andersson, 1996).

Despite the agreement of Frank and Lawn (1967) with Auerbach's law, many researchers support a statistical failure criterion (Fischer-Cripps, 1997a; Fischer-Cripps & Collins, 1994; Warren, 1994(b); Zeng, 1992(a)(b); Hamilton & Rawson, 1970). However, some research does suggest that Auerbach's law is valid in alumina (Bouras, 1996; Laugier, 1984). Furthermore, newer and more detailed solutions to the governing fracture equations continue to appear in the literature (Dai, 1995; Chen, 1995; Zeng, 1992(a); Yingzhi, 1991). The complete description of brittle cone-crack behavior is by no means a simple matter. Even current research (Kocer and Collins, 1998) is proving some of the original assumptions about cone-cracking to be incomplete: previous researchers predicted cone-crack trajectory based on the minimum principal stress trajectory *before* cracking began and found a discrepancy between the theoretical and observed angle of the cone cracks. Kocer and Collins used an iterative finite element technique to calculate stress intensity and crack trajectory that ultimately had excellent agreement with experimental findings and published results.

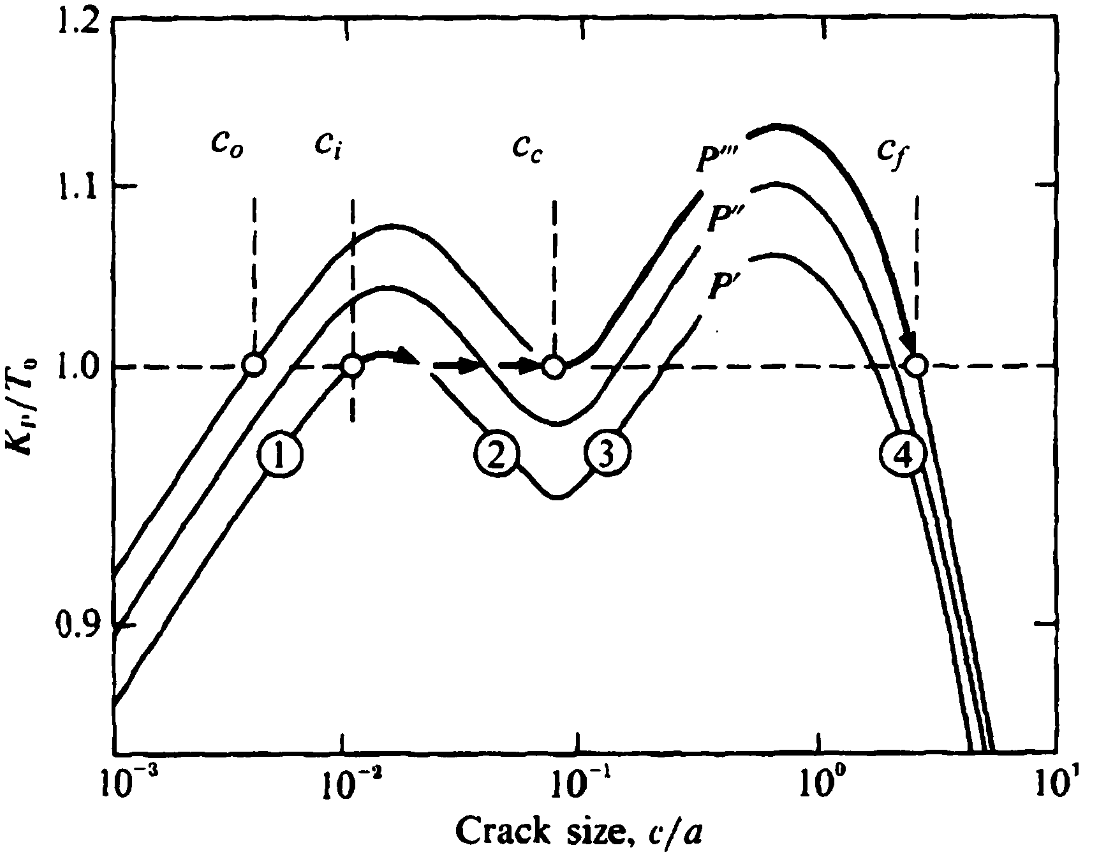

Figure 2. 23 An evaluation of the stresses that cause cone-cracking. Ring cracks form from flaws $c_0 < c_i < c_c$ at P'. Growth of ring cracks into substrate is stable (region 1 to 2) with load P''. Instability is reached at c_c with load P''' and cone crack pops in to final length c_f (region 3 to 4). After Lawn (1993).

2.9.2 Quasi-Ductile Response

The term "quasi-ductility" is used to describe macroscopic behavior of an inherently brittle material that resembles behavior normally found in a material like a ductile metal. Conventional ductility arises from dislocation motion at the atomic level. Quasi-ductility occurs at the grain scale and largely relies on brittle fracture, albeit homogeneously distributed throughout the bulk of the deformation region.

As will be described in detail below, some brittle materials exhibit macroscopic ductility when subjected to the multiaxial compression found beneath a Hertzian indenter (Lawn, 1998(a); Pajares, 1995(a); Lawn, 1994(a); Cai, 1994(a); Makino, 1991). Advanced ceramics exhibiting long-crack toughening mechanisms were found to be particularly susceptible to indentation induced damage in the form of distributed microcracking (Lawn, 1998(a); Padture, 1995(a); Lawn, 1994(b)). Often, altering the microstructure for long-crack toughness compromised short-crack toughening (Padture & Lawn, 1995(a); Lawn, 1994(b)). The short-crack toughness is important with regard to wear and machinability (Lawn, 1998(a); Padture, 1995(a)). Subsequently, advanced ceramics with long-crack toughening mechanisms were tested under Hertzian contact to simulate damage accumulation in service wear conditions (Padture, 1995(a); Lawn, 1994(b)). Moreover, the effects of repeated contact to imitate wear (Pajares, 1995(b); Padture, 1995(a)(b); Guiberteau, 1993) are associated with reductions in bulk strength for a wide variety of materials and microstructures (Lawn, 1998(a); Lee, 1998; Wuttiphan, 1996; Cai, 1994(b))

In addition to monolithic ceramics, layered ceramics have similarly shown macroscopic quasi-ductile behavior when at least one of the layered materials experiences distributed damage (Liu, 1996; Wuttiphan, 1996; An, 1996).

2.9.3 Shear Faulting

Shear faulting has long been known as a mechanism for producing distributed damage in geological (Ashby & Hallam, 1986; Nemat-Nasser & Horii, 1982; Brace, 1966) and advanced ceramic materials (Lawn, 1998(a); Padture, 1995(a); Pajares, 1995(a); Lawn, 1994(b)). The specific occurrences of indentation induced shear faulting are discussed below.

2.9.3.1 Twin Formation

In dense materials with a large enough grain size, a twin will form across the grain diameter often aligned in the direction of maximum shear stress (Lawn, 1994(a)). As an initiation site for distributed damage under Hertzian contact, twin-faulting has most commonly been found in alumina (Lawn, 1994(a); Guiberteau 1994 & 1993), but can also occur in Mg-partially stabilized zirconia (Pajares, 1995(a)).

Guiberteau (1994) has shown that the critical grain size for twin formation and subsequent shear faulting in alumina is around 20 μm. For microstructures with grains above this critical grain size, the distributed damage scales with increasing load. Below the critical load for fault formation, only a minimal amount of damage is observed in the sub-surface region (Guiberteau 1994 & 1993).

After twin fault formation occurs, subsequent loading can produce wing cracks at grain interfaces that ultimately propagate under increased loads. The basic concept of wing crack formation has been modeled extensively in the geomechanics literature (Ashby and Hallam, 1986; Nemat-Nasser and Horii, 1982; Brace, 1966). Lawn (1994(a)) has used that basic model to account for damage accumulation beneath Hertzian indenters.

Fig. 2.24 shows the basic shear fault model with the twin fault designated by (F). Under the compressive stresses shown ($\sigma_3 > \sigma_1$), wing cracks form at the grain boundary (F-C). The driving force for crack propagation originates from the shearing forces that develop along the crack face as shown in the diagram. By accounting for

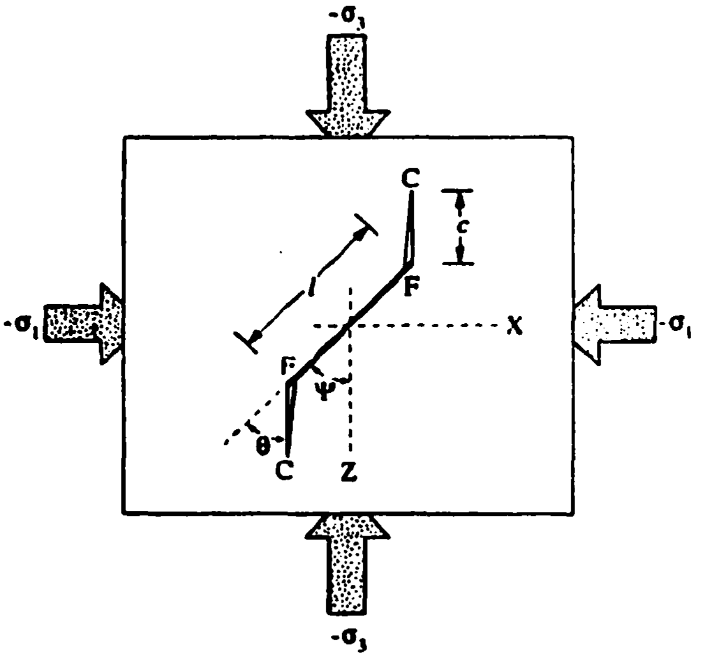

Figure 2. 24 Shear fault model. Faulting occurs along the line defined by F along the plane of maximum shear. Wing cracks develop at fault ends usually at grain boundaries. After Lawn (1994(a)).

the stresses on the crack face and assuming a value, μ, for the frictional sliding across the interface, the net shear stress, S, across the interface can be written as (Cai, 1994(a); Lawn, 1994(a)):

$$S = |\tau_F| - \mu|\sigma_F| \tag{2.49}$$

where τ_F and σ_F are the local shear and compressive stresses along F-F. Using the equation outlined above, Cai (1994(a)) was able to show how different frictional coefficients would prevent shear fault formation in the regions directly beneath the indenter (Fig. 2.25). His predictions agreed with experimental observations of reduced microfracture in the same area (Fig. 2.26) on Si_3N_4 samples (Xu, 1995).

2.9.3.2 Weak or Pre-Existing Interfaces

Weak interfaces, often between second phases or elongated grains and the surrounding microstructure, exhibit an intergrain failure like that outlined above for twinning (Lawn, 1998(a); Padture, 1995(a)(b); Xu, 1995; Cai, 1994(a)(b); Lawn, 1994(a)(b); Makino, 1991). This mechanism is the most common occurring in advanced ceramic materials under Hertzian contact and is also responsible for their long-crack toughness (Padture, 1995(b); Cai, 1994(a)). The weak interfaces of these materials act as fault nucleation sites for intergrain twinning/slip mechanisms, which ultimately lead to intergranular microfracture under the indentation stress.

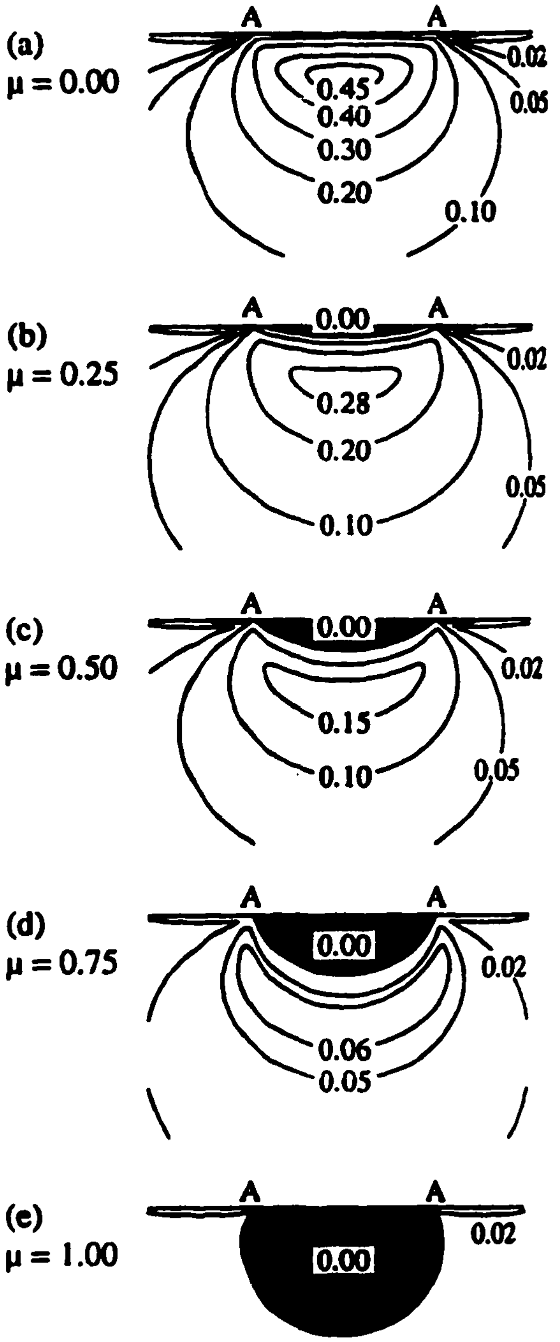

Figure 2. 25 Growth of the region of frictionally prohibited shear faulting as a function of sliding friction coefficient (Eq. 2.49). Regions shown in (c) to (d) correlate with experimental findings (see Fig. 2.26). After Cai (1994(a)).

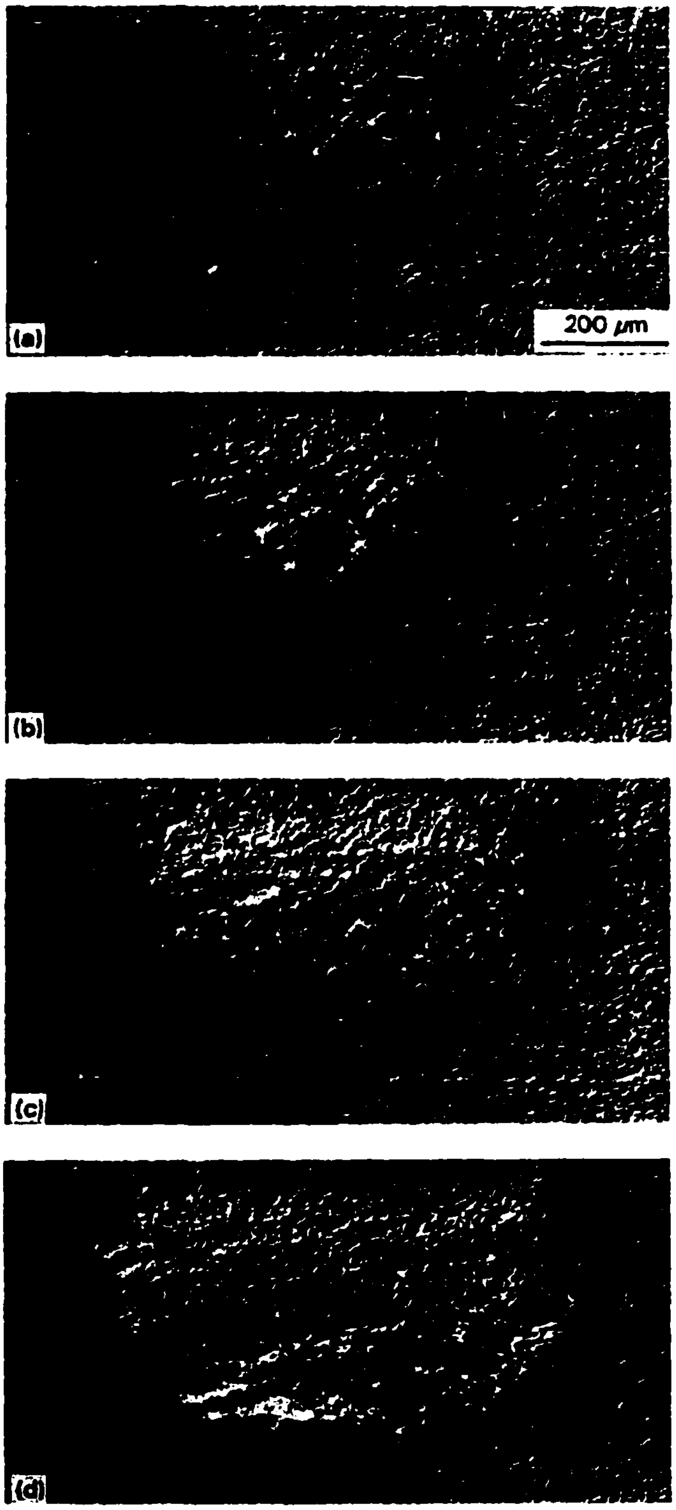

Figure 2. 26 Progressive damage in Si_3N_4 and the friction reducing area beneath the indenter. Compare with the friction predictions of Fig. 2.25 (c) & (d). After Xu (1995).

2.9.4 Elastic-Plastic Behavior

There exists a region of mechanical behavior between the realm of elasticity and plasticity. It may be defined by the transition from purely elastic to purely plastic response and is where the strain hardening characteristics described in Sec. 2.2.4.1 – 2.2.4.2, are activated. Micromechanical modeling of the elastic-plastic response beneath an indenter is difficult for brittle materials. However, several continuum based analytical solutions exist for brittle systems (Adler, 1994; Tanaka, 1987; Yoffe, 1982) based on Hill's (1950) expanding cavity model. A recent attempt by Fischer-Cripps (1997(b)) uses finite element modeling, an experimentally calibrated constant, and the cavity model to fit the Hertzian indentation stress-strain curves. Fischer-Cripps and Lawn (1996(b)) put forth an analytical model to describe the indentation curves with a linear approximation in the elastic-plastic region based on a Mohr-Coulomb approximation. The Fischer-Cripps (1997(b)) model has a more universal fit but relies on experimental calibration while the Fischer-Cripps and Lawn (1996(b)) work is completely analytical. Lawn and Marshall (1998) have recently extended the earlier shear faulting models to provide a more comprehensive explanation of the brittle elastic-plastic behavior from a mechanistic standpoint.

While the successful identification of a deformation mechanism in porous liquid phase sintered alumina (PLPS) alumina would enable the development of an analytic description of the Hertzian stress-strain behavior, it is beyond the scope of this investigation. Moreover, while literature on brittle spherical indentation is limited, it should be noted that there exists extensive literature on the spherical indentation of metals with theory related to elastic-plastic behavior (Huber, 1998; Storåkers, 1997;

Chaudhri, 1993; Milman, 1993; Montmitonnet, 1993; Field, 1993; Johnson, 1985; Follansbee, 1984; Yoffe, 1984; Rickerby, 1979; Studman, 1976; Richmond, 1974; Hardy, 1971; Tabor, 1951) and elastic-plastic behavior with porosity (Koval'chenko, 1993; Fleck, 1992).

2.10 Geological Testing (Triaxial Compaction)

Researchers in the rock mechanics community have been investigating the deformation behavior of naturally occurring brittle materials for many years. The impetus for their work derives from a need to understand how various layers of rock shift and change under the large pressures beneath the surface of the earth. Much like the region beneath a Hertzian indenter, rock materials experience large compressive stresses. To simulate these stresses in the laboratory, a special triaxial compression test had been developed (Kármán, 1911) of which there are several variations (Patterson, 1978), the most common being a variation of Griggs (1936).

The basic experimental setup is shown in Fig. 2.27(a) and several load cells are shown in Fig. 2.27(b). A right cylindrical sample is obtained from a coring process and placed in a deformable metal sheath. The metal most often used is lead because of its low modulus and hardness. The jacketed sample is then placed between two pressing rams of a mechanical testing frame. A pressurizing fluid then surrounds the jacketed sample and a hydrostatic pressure is applied and maintained constant during testing. Compression forces are applied at each end of the cylinder above that of the hydrostatic force, and the sample is tested to failure. A plot is made from the experimental data of the differential

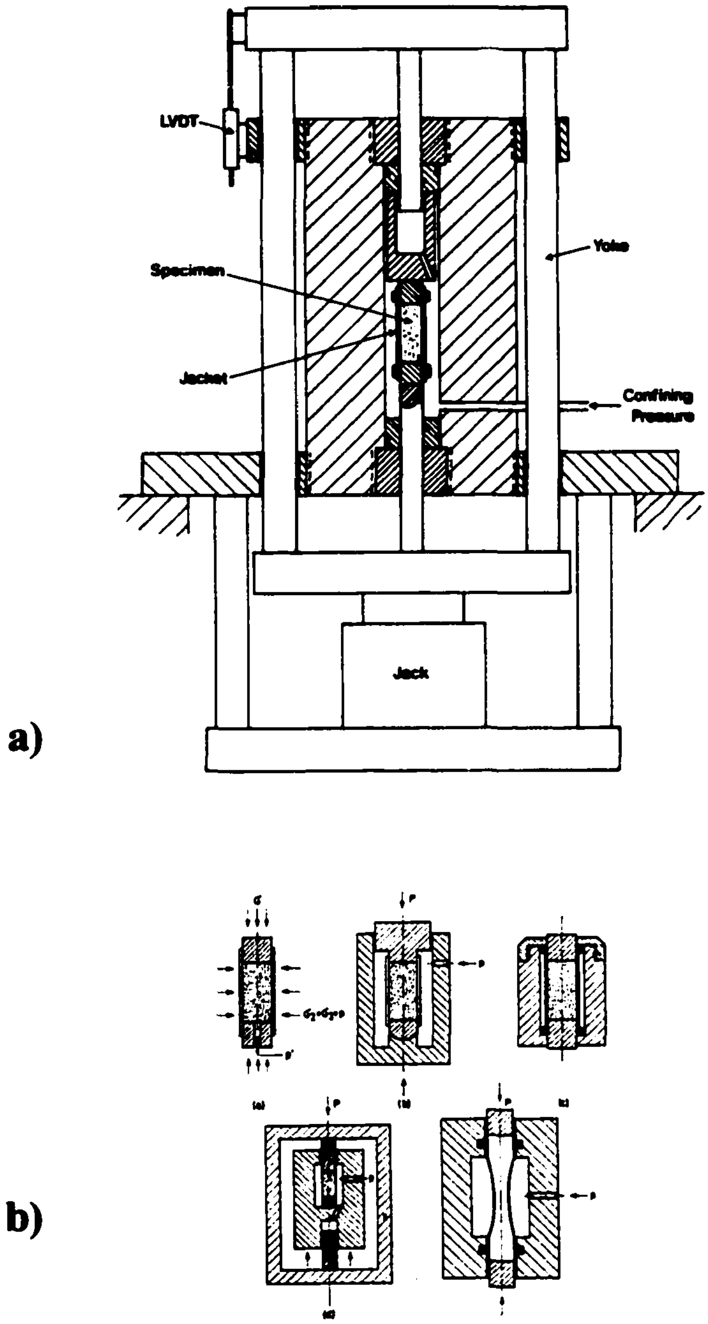

Figure 2. 27 (a) Triaxial testing experimental setup for geological materials, based on design by Griggs (1936). Fluid enters chamber to provide a hydrostatic confining pressure while rams apply a uniaxial compressive force. Brittle specimen is encased in a metal sheath to exclude pressurizing fluid. After Patterson (1978). (b) Several specimen chamber designs used in test apparatus (a). After Jaeger and Cook (1969).

stress (*axial* (σ_1) – *hydrostatic* (σ_3)) against the axial shortening or strain.

Three main failure modes exist for right cylindrical test specimens under the triaxial loading conditions. The type of macroscopic response to loading is dependent upon the microstructural makeup of the geological material. A schematic of the general failure characteristics are shown in Fig. 2.28 along with their corresponding stress-strain response (Sammis and Ashby, 1986). Note that the example in the figure is based on a porous material but may be applied equally to materials with shear-faulting mechanisms.

Under low confining pressure or uniaxial compressive stress, Fig. 2.28(a), vertical fracture (slabbing) will occur. The differential stress-strain curve is linear until fracture occurs causing immediate and catastrophic failure of the sample. As the confining pressure (σ_3) is increased, Fig. 2.28(b), a transition region is obtained where macro-shear-faults cut across the sample corners. The microstructure within the shear-fault zone will show signs of distributed damage and microfracture while the regions away from the macro-fault remain undamaged. The differential stress-strain curve will exhibit a strain-softening characteristic prior to failure and after a yielding stress is exceeded. The faulting region is sometimes termed the brittle-ductile transition region as the material behaves in a ductile-like manner at higher confining pressures as will be discussed next.

Some geological materials will yield a ductile response after the confining pressure exceeds a critical value. Ductility is observed in the differential stress-strain

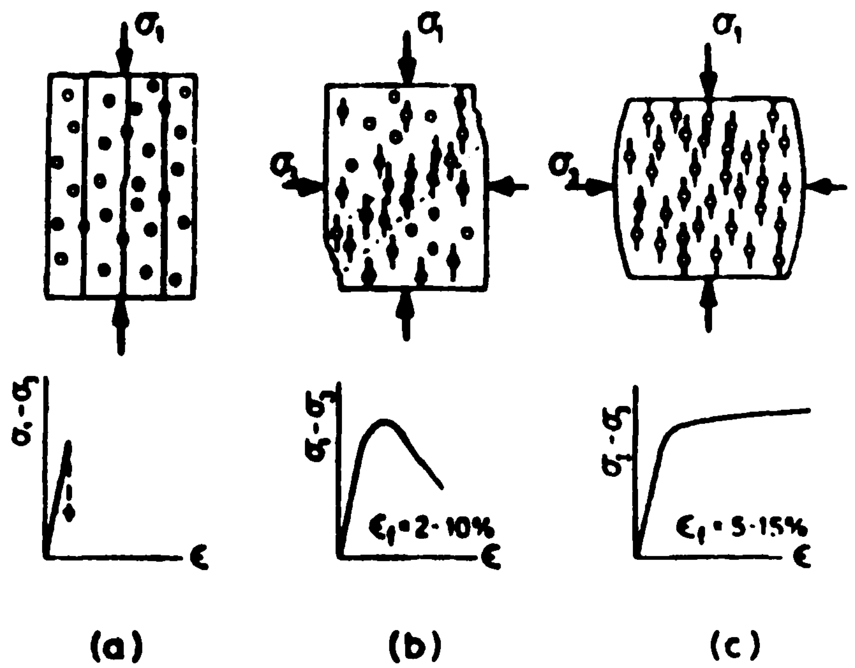

Figure 2. 28 Deformation modes under triaxial compaction and their corresponding differential stress-strain plot. (a) Brittle deformation characterized by macrofractures in the compression direction. Stress-strain curve terminates abruptly. (b) Brittle-ductile transition; shear fault contains distributed damage while material away from shear fault is largely undamaged. Stress-strain curve shows strain softening. (c) Ductile behavior occurs by homogeneously distributed microfracture. Stress-strain curve shows prominent strain hardening characteristics. After Sammis and Ashby (1986).

curve with a resemblance to the typical strain-hardening characteristics described in Sec. 2.2.4.1. This condition of ductility is referred to as *cataclastic flow* (Hirth and Tullis, 1989; Jaeger and Cook, 1971; Mogi, 1966) and results from homogeneously distributed microfracture in the sample. As a result of the ductile behavior, the sample will barrel in shape and the stress-strain curve will resemble that of a ductile metal with a yield and subsequent strain-hardening character (Patterson, 1978).

A graph of the three deformation regions (brittle, brittle-ductile, ductile) is shown in Fig 2.29(a) for Mizuho trachyte (Mogi, 1966) and for Wombegan marble in Fig.

2.29(b) (Patterson, 1978). Fig. 2.29 shows how the strain hardening can increase with increasing confining pressure. Selected samples of the Wombegan marble are shown in Fig. 2.30 from the different regions of deformation characterized in Fig. 2.28. The progressive change in failure modes with increasing confining pressure is apparent as the macro-faults Fig. 2.30(a-c) disappear and the sample experiences more uniformly distributed deformation (d).

On the microscopic level, ductile damage is characterized by distributed microfracture stemming from preexisting cracks (Ashby & Hallam, 1986; Nemat-Nasser & Horii, 1982; Brace, 1966) and/or pore collapse (Rutter and Hadizadeh, 1991; Wong, 1990; Evans, 1990; Hirth and Tullis, 1989; Hadizadeh & Rutter, 1983; Patterson, 1978; Jaeger and Cook, 1969; Byerlee, 1968; Mogi, 1966). In addition, some minerals, such as granite and marble, experience a degree of dislocation motion and creation of defects during deformation (Fredrich, 1989; Tullis and Yund, 1977). As will be shown, one of the main components necessary for cataclastic flow in geomaterials is porosity (Rutter and Hadizadeh, 1991).

The type of microfracture that occurs during deformation depends highly on the nature of the material being deformed and spatial arrangement of the various phases within the microstructure. The amount, location, and size of porosity has been attributed

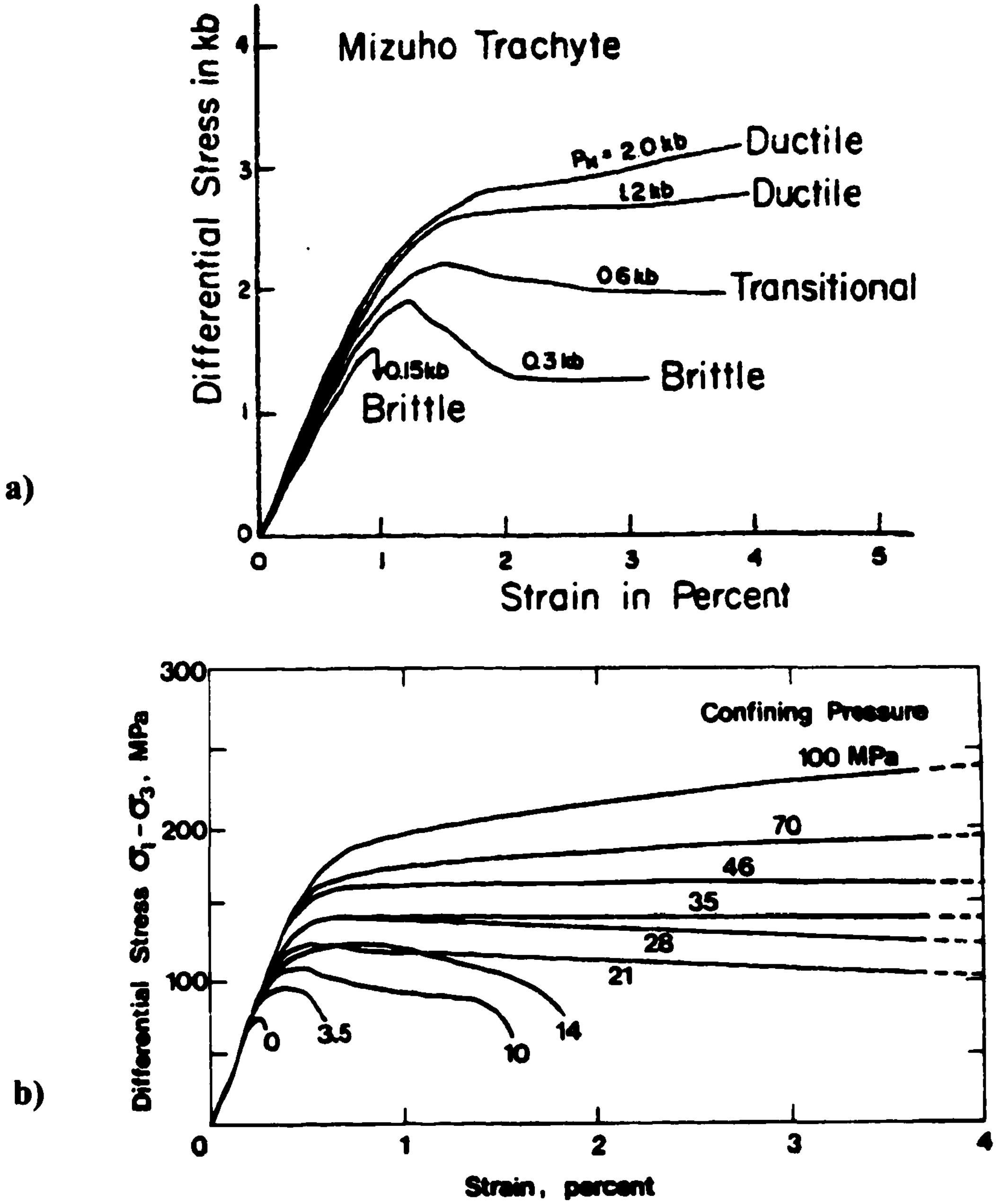

Figure 2. 29 Experimental triaxial compaction results for Mizuho Trachyte and Wombegan marble. The three main deformation responses are labeled in (a) for the Trachyte. (b) Marble displays similar characteristics as (a) and shows a progressively increasing strain hardening behavior with increased confining pressure. (a) After Mogi (1966); (b) After Patterson (1978).

Figure 2. 30 Progressive damage in Wombegan marble. Confining pressure is increased from zero (a) to 100 MPa (b). Brittle failure (a), single shear fault (b), conjugate shear faulting (c), and ductile behavior (d). After Patterson (1978).

to causing ductility or compressive damage in geomaterials (Menendez, 1996; Renner and Rummel, 1996; Rutter and Hadizedah, 1991; Wong, 1990; Hirth and Tullis, 1989; Mogi, 1966). The specific details about the mechanisms of fracture, especially in regard to porosity, will be discussed below.

2.11 Porosity

The evaluation of the effects of porosity on bulk properties in ceramics has recently been considered extensively by Rice (1998). According to Rice, the majority of mechanical behavior literature shows the effects on Young's modulus and tensile fracture in material systems. Although Rice devotes a chapter of his book to compressive failure, he admits that very little theoretical data exists on the effects of porosity on hardness, compressive strength and wear. Because porosity can affect a multitude of physical parameters, this section will try to illustrate some basic trends observed in the literature for mechanical testing.

2.11.1 Porosity's Effect on Hardness

McColm (1990) describes an empirically derived formulation for the dependence of Vickers hardness measurements on porosity in brittle materials. The relationship is:

$$H_V = H_O(1-P)^2 \exp(-BP) \tag{2.50}$$

where H_V is the Vickers hardness, p is the porosity, and H_O is the hardness for the dense material (p = 0). The B term is a material dependent constant and usually less than one. For example, B_4C has a value of B = 0.35. Notably, McColm states that this relation is in contrast to empirical strength relations such as:

$$\sigma = \sigma_O \exp(-bP) \tag{2.51}$$

which has been successfully used to predict hydraulic cement strength for years. A clear explanation of these differences has not been found in the literature.

2.11.2 Bulk Effect on Elastic Constants

One may assume that the elastic modulus of a body will decrease as a function of increasing porosity; derived at a basic level from a simple rule-of-mixture analysis. Experimental evidence suggests that the rule-of-mixture relation is inadequate to describe measured properties. In alumina, several equations have been put forth over the years; some are purely empirical (Spriggs, 1962; Knudsen; 1962) and some are semi-empirical relations (Wagh, 1991; Hassleman, 1962) to relate bulk porosity to Young's modulus.

Many of these studies provide elastic modulus calculations in addition to or to support other more critical investigations of fracture behavior or flow behavior.

In addition to affecting the elastic modulus, changes in porosity will also affect the Poisson's ratio. However, measurements of the effect of porosity on Poisson's ratio are often difficult. Boccaccini (1994) surveyed the literature, Fig. 2.31, and calculated the normalized change in Poisson's ratio with increasing porosity for materials with an initial Poisson's ratio greater than 0.25 (A) and less than 0.25 (B). Clearly, there is little evidence to suggest any qualitative or quantitative trend to the data.

2.11.3 Porosity Effect in Geomechanics

Previously, the influence of a singular pore on stress distributions and stress intensities in a uniform stress field was discussed. This section will now examine the influence of distributed porosity on microscopic and macroscopic observations. Few theoretical studies based on fundamental mechanics exist that relate porosity and compressive failure; however, several researchers have developed some simple mechanistic solutions to this problem.

2.11.3.1 Macroscopic Behavior

Following from the geological data, many researchers have attempted to account for the behavior of porosity and how it affects distributed microfracture. In Sec. 2.7, a model by Sammis and Ashby (1986) used basic fracture mechanics to estimate crack

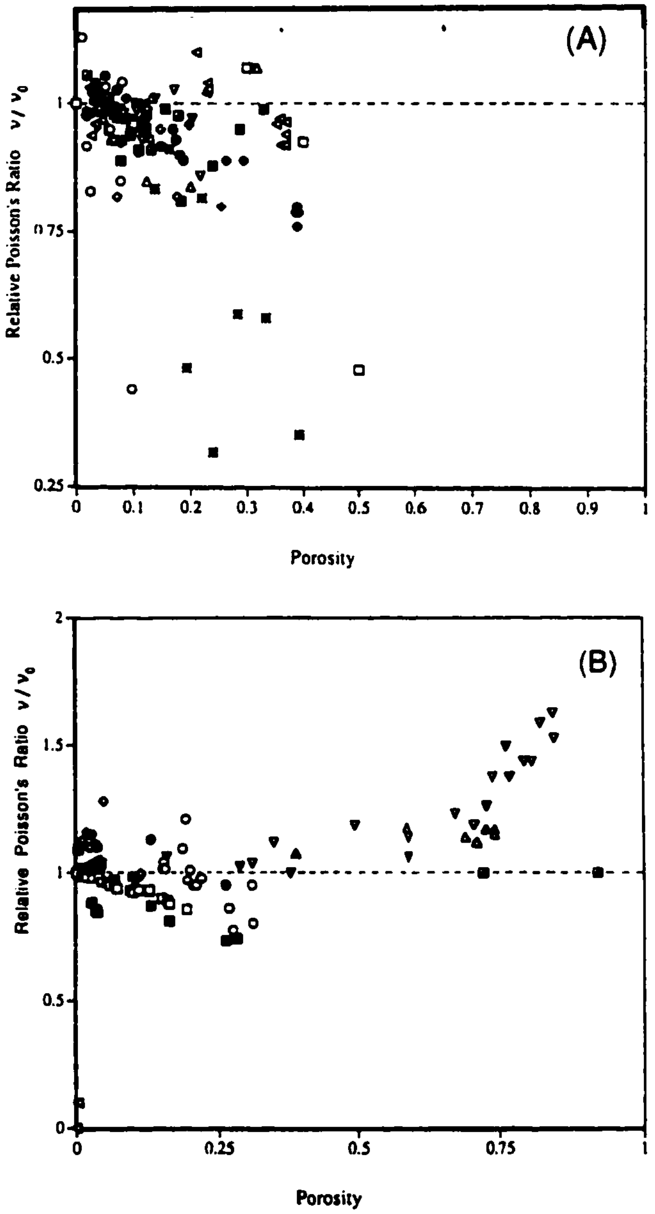

Figure 2. 31 Published results of Poisson's ratio measurements normalized to initial value for materials with n > 0.25 (a) and n < 0.25 (b). After Boccaccini (1994).

interaction and calculate macroscopic properties such as stress-strain behavior. They considered porosity in two and three dimensions and made comparisons with two-dimensional experiments on PMMA. However, according to results by Isida (1987), Sammis and Ashby overestimated the influence of porosity on the crack interaction emanating from pores and their model should be used only as an upper-bound estimate (Wong, 1990).

Another excellent investigation from a geological perspective is that of Hirth and Tullis (1989) who studied the stresses around a pore and its effects on cataclastic flow of sandstones with varying porosity. The Hirth (1989) paper uses Goodier's (1933) solution for stress around a pore to calculate the change in compressive and tensile forces as a function of macroscopically applied confining pressure (described previously, Sec.2.5). Hirth and Tullis realized that the compressive stress is many times higher than the tensile stress and that in some quartzite and plaster of Paris models (Vekinis, 1993; Lajtai and Lajtai, 1975) failure can first occur from the highly compressive region rather than the tensile region as expected from elasticity theory.

They also reported that cataclastic flow was transitional in the quartzite as the samples displayed a shear-faulting behavior at higher confining pressures.

Volume changes affect the macroscopic deformation behavior and porosity is an essential contributing factor. Volume reduction is most often associated with pore collapse (Menendez, 1996; Rutter and Hadizedah, 1991; Hirth and Tullis, 1989) and may be accomplished with hydrostatic pressure (Menendez, 1996). However, deviatoric shear forces have been shown to enhance volume reduction more significantly than hydrostatic ones (Menendez, 1996). At low confining pressures, some geological materials display an increase in sample volume prior to densification at higher loading (Menendez, 1996). Dilatational effects are fundamentally important and can contribute to the localization failures in rock materials. Theoretically this has been addressed by Rudnicki and Rice (1975), B. Evans (1990), and Fredrich (1989). The dilatational effects – if any – on indentation processes of porous brittle materials are unknown.

2.11.3.2 Microscopic Behavior

Several microscopic mechanisms have been identified in relation to distributed damage and microfracture during cataclastic flow or ductile behavior in geomaterials (Nemat-Nasser and Horii, 1982; Ashby and Hallam, 1986). As mentioned several times, the preexisting fault or crack is a mechanism that is activated when the fault plane becomes favorably aligned with a plane of maximum shear stress. Frictional effects are a large factor in determining the activation of this type of damage as well as the inherent presence of microcracks within the body.

Porosity has been shown to be responsible for compressive strengths (Mogi, 1966; Brace, 1966) and has been attributed to the observation of cataclastic behavior for in conjunction with an increasing confining pressure (Menendez, 1996; Renner and Rummel, 1996; Wong, 1990; Hirth and Tullis, 1989; Patterson, 1978). A number of researchers identify intergranular microcracks stemming from pore spaces at the early stages of deformation in materials that exhibit ductility prior to pore collapse and axial microfracture of surrounding grains (Hirth and Tullis, 1989; Hadizadeh and Rutter, 1983, 1982).

A third mechanism that can be found resembles Hertzian contact but at the grain-scale. It is most common under conditions where particles have been loosened and are impinging on one another (Wong, 1990). It is the only mechanism that can be activated under hydrostatic stress and is usually restricted to materials with higher levels of porosity (Wong and Wu, 1995).

2.12 Finite Element Analysis

Finite element modeling (FEM) or finite element analysis (FEA) has existed long enough to become commonplace in the field of fracture and solid mechanics. The advent of inexpensive and powerful computers and many commercially available finite element codes has allowed its utility to extend out of the realm of the mechanical engineer and into general scientific use. Zienkiewicz and Taylor (1991) wrote an excellent text that covers the essentials of the technique.

The technique uses mathematical approximation routines to solve the Cauchy-Reimann tensors for stress and strain. Each "element" is a matrix equation with the Lamé constants derived from material considerations. Each successive element is linked together with its boundary providing the input boundary conditions for its neighboring elements. Each element is comprised of a series of nodes, the number and arrangement determining the accuracy of the approximation. Loads and fixed points of reference are all that are needed to obtain a convergent solution to the problem which will be represented by calculated displacements and/or principal values of stress at each node within the model.

Finding the optimal number of elements in a model is a balance between accuracy and ease of calculation. Meshes with finer and more numerous elements produce more accurate solutions but at the cost of increased calculation time. Conversely, the coarser the mesh, the quicker a solution may be obtained, but the likelihood of larger errors is present.

Most models used in this investigation have between 200 – 600 elements in a combination of squares and triangles. The finite element code[§] uses an automatic mesh generator to fill in the geometric outline of the system under consideration. After establishing the mesh, the model is run with the appropriate boundary conditions and solution data is directed to an output file for later use.

[§] A modified form of FRAC2D, a code developed internally at G.E. Corporate Research Labs, Schenectady, NY. (Courtesy H.F.N., dissertation committee member)

3. STATEMENT OF PURPOSE

This investigation began as an attempt to impart a residual compressive stress into the surface of a commercial porous liquid phase sintered alumina substrate using a patented chemical ion-exchange process. Damage was occurring in a hybrid microelectronic circuit fabrication process using the substrates with damage sites linked to contact with cylindrical locator pins of tungsten carbide (WC). It was hypothesized that a residual compressive surface stress would enhance the resistance to contact damage accumulation.

The unique microstructural characteristics of this material – the combination of glass phase with a small amount of porosity – provided an unexpected development of quasi-ductility. The commercial alumina, having a small average grain size (4 um), was expected to behave in a brittle fashion as previous studies in fine-grained alumina have shown. The development of quasi-ductility in this system was therefore unique, and it suggested that a new mechanism was responsible for its manifestation.

Partial motivation for conducting this study derived from the need to understand the deformation characteristics of commercial alumina in a service environment that is susceptible to repeated contact or loading. Because damage can accumulate due to wear or contact fatigue, the engineer must be aware of the necessary design criteria to optimize a material and ultimately a product's performance for a given manufacturing or service environment.

Inferring a damage mechanics solution to this system based on previous studies was prohibitive in light of the experimental evidence. It became apparent that detailed knowledge of the deformation character of the alumina with respect to microstructural variables was needed. Furthermore, little scientific evidence had been presented in the literature to suggest how microstructural variables would effect contact-type deformation in an alumina system with significant porosity or second phase.

The objective of this investigation, therefore, is to understand the deformation of porous liquid phase sintered alumina microstructures under the highly compressive contact stress under a Hertzian indenter. By tailoring sintered microstructures to systematically study grain size, porosity, and second phase, it is expected that the precise mechanism controlling deformation will be identified and ultimately that that information will enable the design engineer to manipulate physical end-properties through controlled processing.

4. EXPERIMENTAL PROCEDURE

As a rule, all sample preparation and testing was performed under ambient conditions unless otherwise specified.

4.1 Sample Preparation

4.1.1 Commercial Material

Commercial polycrystalline alumina substrate was obtained from Coors Ceramics Company (designated AD96R) with 96% alumina by weight and the remaining 4% being a glass phase. The alumina substrates were 7.62 cm by 15.24 cm on a side and had a thickness of 3 mm. Squares were cut from the substrates on a low speed diamond saw (Beuhler, Isomet, WI) into pieces approximately 2.54 cm per side. The cut squares were mounted on cylindrical aluminum polishing disks, 3.175 cm in diameter and 12.7 mm thick, using a low temperature bonding wax. The alumina was subsequently polished for testing in a planar configuration or assembling into bonded interface specimens, respectively (Sec. 4.1.3).

4.1.2 Lab Produced Material

4.1.2.1 Pressureless Sintered Material

A series of liquid phase sintered alumina materials were produced to simulate the commercial material AD96R. Laboratory produced samples were prepared by first dissolving reagent grade magnesium nitrate (Johnson Matthey, Part no. 10799) in 200 mL of methanol (99.9%) in a 500ml Pyrex beaker with a magnetic stir-bar (Fischer

Scientific) and stirring hot plate (Corning PC-351) to produce a MgO dopant level of 1000 ppm. High purity alumina (Sumitomo USA, Edison, NJ) powders listed in Table 4.1 were slowly added once the magnesium nitrate had dissolved. After mixing, the methanol was evaporated and the dried powder was calcined in a box furnace (Lindberg Model 54434, Watertown, WI) at 1000 °C for 24 hours to drive off the nitrates and other organics. The calcined powder was crushed and ball milled for 10 hours with partially stabilized zirconia balls (Tosoh Corporation, Tokyo; 9mm) after which the powder was dried, crushed and passed through a 180 μm sieve. All ball milling was performed in 250 mL Nalgene containers (VWR Scientific, 16126-130). The sieved powder was mixed with anorthite glass powder (18.2 CaO, 41.8 Al2O3, and 40.0 SiO2 wt%; Alcoa Technical Center) to a level of 10 volume percent and milled with small diameter zirconia balls (3 mm) for 1 hour. The mixture was strained to separate the milling media from the slurry and the slurry was returned to the rolling mill for 24 hours. After milling, the slurry was dried while stirring over low heat in the Pyrex beaker. The dried powder was scraped from the beaker with a Teflon policeman (Fischer Scientific), ground with mortar and pestle, combined by hand with a liquid polyvinyl alcohol (PVA) binder and passed through the 180 μm sieve again. After sieving, the powder was loaded into a high-purity precision machined graphite die (Poco Graphite, Decatur, TX) and pressed (Carver Model M, Menomenee Falls, WI) at 35 MPa into disks 25.4 mm diameter and roughly 3-4 mm thick. The disks were then cold isostatically pressed (Model CP3-12-69, Fluitron Inc.) at ~350 MPa. The pressed disks were calcined in air to remove the binder phase by heating to 800 °C at 5 °C / min., holding for 48 hours, and then further heating to 1600

°C. The furnace was held at that temperature for 2, 1, 0.5 and 0 hours and then cooled to room temperature at 10 °C / min.

Table 4. 1 High-purity alumina powders used to produce microstructurally controlled samples for comparison to AD96R.

Powder	MEAN Particle Size (μm)	Material
Sumitomo AA5	5	α-alumina
Sumitomo AA2	2.3	α-alumina
Sumitomo AKP-50	0.2	α-alumina

4.1.2.2 Hot Pressed Material

4.1.2.2.1 Pure Alumina

All pure alumina hot pressed samples were fabricated using strict impurity controlled processes as described below. Some of the AA5 and AA2 alumina were taken in its as-received condition from the manufacturer (double plastic bag) and brought into a class 1000 clean room environment. The powder, containers, and all equipment used in the processing of samples in the clean room were always handled wearing polyethylene gloves. The outer plastic bag was removed and discarded and the inner plastic bag was opened and its contents poured into an acid washed polypropylene container following the procedure outlined by Stearns (1995). The powder was stored in the clean room at all times.

In preparation to begin hot pressing, a new graphite die was cleaned with acetone. The inside of the die, its spacers, and loading rams were coated with a boron nitride (BN) acetone slurry applied with a standard air-brush tool. The BN coating was used as a die lubricant to facilitate separation of the die parts after firing. The die was partially assembled immediately following the application of the BN coating and taken to the clean room on a tray covered with aluminum foil. The open die was filled completely with the as-received alumina and assembled in a sub-class 100 hood enclosure contained within the clean room. The die was compressed and proof tested in a manually activated hydraulic press (Carver, Model M) to a load of 3000 kg. After proof testing, the die was taken to a vacuum hot press (Astro Model 1000-2560, Astro Industries Inc., Santa Barbara, CA) reserved exclusively for clean room processed pure alumina. The load-temperature schedule varied according to the desired final density and initial particle starting size (Table 4.2). The temperature schedule was applied through manual adjustments of a potentiometer regulating current to the heating coils in a two-step increment; the first to 800°C and the second to the desired sintering temperature once the vacuum had stabilized to less than 200 millitorr. The sample was removed from the die in the clean room and the BN-alumina reaction layer was removed using a high speed saw (Buehler Accutom-5). Approximately 500 microns of the outer surface (Fig. 4.1) was cut in a hexagonal pattern. The sharp edges of the hexagon were manually ground down using a 200 grit fixed diamond polishing wheel (Leco PSA backed diamond disks) in water at 100 RPM.

Table 4. 2 High purity alumina powders, clean room processed and hot pressed to varying densities.

Powder	Temperature (°C)	Time (min.)	Pressure (MPa)	Density (%)
AA2	1450	60	30	97.2
AA5	1600	60	50	96.3
AA5	1650	60	50	96.1
AA5	1500	180	50	95.2
AA2	1450	40	30	94.4
AA5	1550	60	30	90.0
AA2	1350	60	30	86.1
AA2	1350	15	30	78.9

4.1.2.2.2 Liquid Phase Sintered Alumina

A commercially available glass[‡], common to electronics applications, was combined with high purity alumina as described in Sec. 4.1.2.1. A graphite die was coated with BN and loaded with a 10 g mixture of alumina and glass. The die was assembled and inserted into a hot press designated for unclean systems (Astro Model HP20-4560-FP20; Astro Industries Inc., Santa Barbara, CA). The sample was hot pressed at 1250°C at 50 MPa for 30 minutes. Heating was accomplished by setting a calibrated current level whereby the furnace ramped up to the target temperature at an uncontrolled rate. Similarly, the power was slowly ramped down and the furnace was water cooled in an unregulated fashion. After cooling, the sample was removed for characterization.

[‡] Ferro EG2770, Powders Division, Ferro Inc.

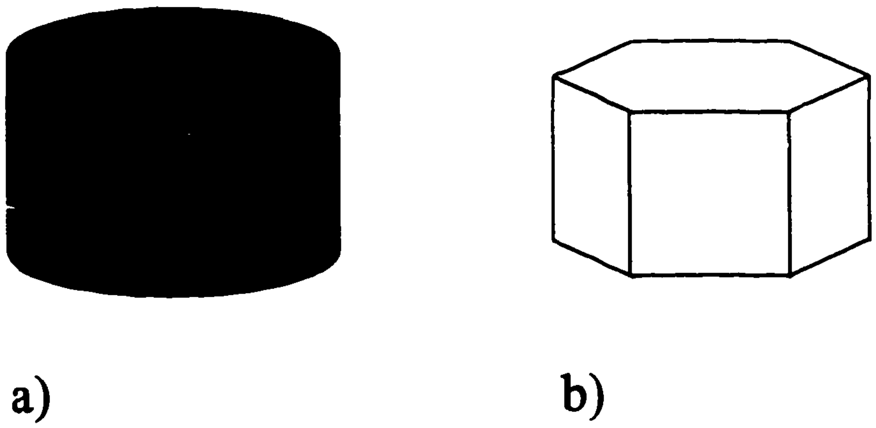

Figure 4. 1 (a) Hot pressed alumina sample after being removed from graphite die. (b) The BN reacted layer is removed by cutting with a high-speed diamond saw into a hexagonal shape.

4.1.3 Grinding and Polishing

Grinding was utilized to obtain a general flat surface across the specimen and was accomplished with either of two automated grinding/polishing units (Leco and Abropol) as described below. Prior to grinding, the sample surface was marked with a standard #2 pencil to help monitor the progress of grinding. Initial grinding was performed with a 200 or 400 grit wheel until the pencil marks had been removed. After the 400 grit, a 600 grit wheel was utilized along with the pencil technique. Grinding was halted after examining the surface under a microscope to ensure very large scratches had been removed. Polishing was performed in a series of gradations from 15 to 1 μm. Finer polishing was accomplished with a series of diamond paste (Hyprez, Engis, Wheeling, IL) on nap cloth (Struers; NAP or DAC) starting with 15 μm and getting progressively smaller to 9 and 6 microns. A final 1 μm polish was achieved by placing the samples in special fixtures and using an automated vibratory polisher (Vibromet 2, Beuhler) for 12-24 hours.

4.1.3.1 Non-Parallel Configuration

Sintered samples were attached to an aluminum stud 1 1/4" diameter with low temperature mounting wax. After attaching the samples to the stud, the exposed metal face and outer surface of the cylinder were coated with mold release. A standard metallographic mounting mold minus the bottom piece was also coated with mold release and placed over the metal stud and sample (Fig. 4.2(a)). The epoxy resin and hardener were mixed appropriately and poured into the mold until it just covered the top of the sample. The epoxy was allowed to cure overnight. After removal from the mold, the

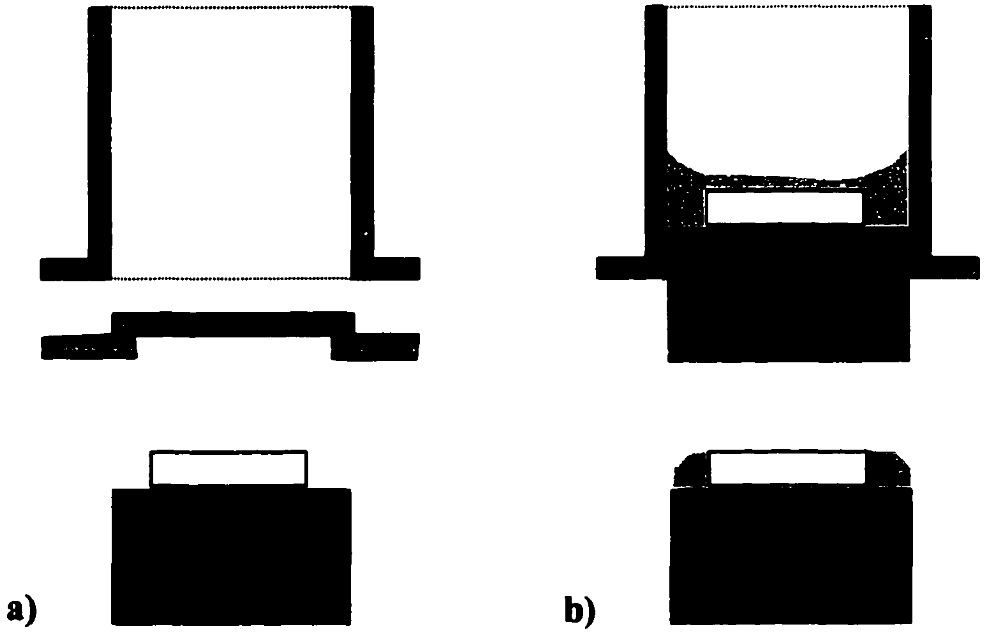

Figure 4. 2 Modified sample mounting technique. (a) A conventional epoxy mounting mold was separated and combined with metal disk mounted samples. (b) The metal disk, coated with mold release, was inserted into the mold and filled with epoxy. After curing, the epoxy was beveled on SiC paper and then ground and polished according to Sec. 4.1.3.

epoxy layer was beveled (Fig. 4.2(b)) to facilitate polishing with the automated equipment. Polishing proceeded as described in Sec. 4.1.3 using a Leco polisher (Model 150 Vari/Pol). Some glass-containing samples used for sub-surface investigations received an additional hand polishing with 0.03 μm colloidal silica (Syton HT50, Remet Corporation, Chadwick, NY) to preferentially polish down the glassy phase.

Upon completion of the polishing steps, the sample was removed by boiling in water until the epoxy became soft. The sample was removed from the water and placed on the lab top where the epoxy was separated from the sample with a knife. After removal, the sample was cleaned in acetone to remove any excess wax and immediately cleaned in ethanol.

4.1.3.2 Parallel Configuration

Preparation of bonded interface specimens required the use of the Abropol automated polishing system (Struers, Westlake, OH) to maintain parallelism between the faces of the sample surfaces. Preparation and polishing of the samples proceeded in the same way as described in Sec. 4.1.3. However, grinding was performed with a 30 μm fixed diamond wheel. Coarse polishing began at 15 microns and went directly to 6 microns. After this, the samples were placed on the vibratory polisher as mentioned before.

4.1.3.3 Bonded Interface Configuration

A bonded interface technique was used to facilitate the observation of sub-surface damage from indentation testing (Mulhearn, 1959; Lawn, 1994(a)). The technique relies on a strong bond between similar halves of material that are first polished at the interface to be bonded. For the alumina, preparation of bonded interface specimens used two identically sized samples polished in the parallel configuration described above. A cyanoacrylate-based adhesive was used to affix the polished interfaces to each other under an externally applied pressure. The composite sample was cured overnight under pressure applied by a vise. The cured sample was cut into three pieces as shown in Fig. 4.3(a). Each individual piece was mounted to an aluminum disk and ground flat on the Abropol, as described in Sec. 4.1.3.1. The samples were flipped over, epoxy mounted, and polished as in Sec. 4.1.3.2. After the samples were polished, they were removed from the epoxy as in Sec. 4.1.3.1. It should be noted that extra care was taken to remove the glued samples from the epoxy as the boiling water significantly weakened the cyanoacrylate adhesive. Polished sections are tested at the bonded interface as shown in Fig. 4.3(b) and as described in Sec. 4.2.2.3 below. The specimen halves were separated after soaking in acetone overnight. Specimen halves were then cleaned with acetone, and followed immediately rinsed with ethanol.

4.2 Sample Characterization

4.2.1 Density Measurements

Density measurements were made on the fired disks using the Archimedes method and deionized water as the immersion medium (Pennings, 1989). Samples were weighed on a high precision balance (+/- 10 μg; Mettler H51, Mettler Instrument Corp., Princeton, NJ) and used to calculate porosity, which ranged from 0-10% for the samples used in this investigation.

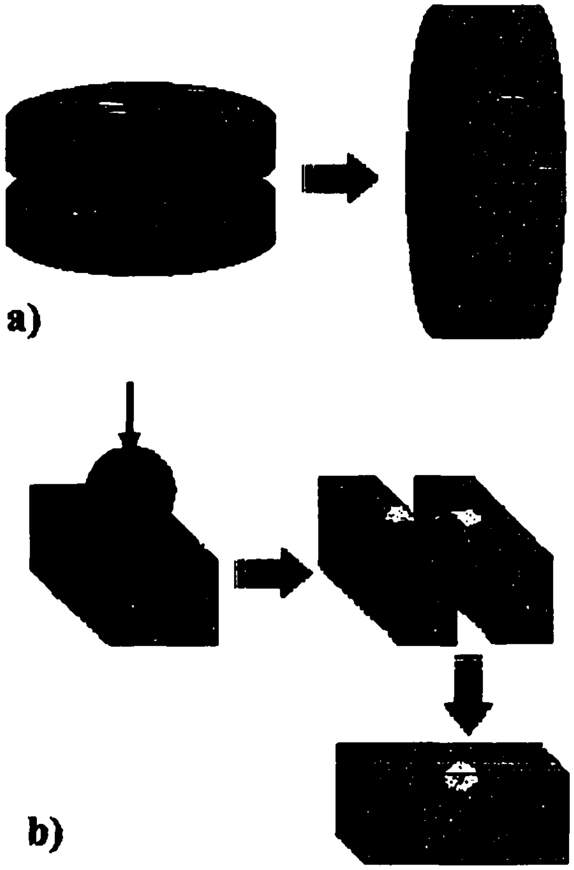

Figure 4. 3 Bonded interface preparation technique. (a) Polished disks were glued together and cut into three pieces as shown. (b) The cut sections were ground, polished and tested at the interface as shown. After testing, the halves were separated revealing sub-surface damage.

4.2.2 Indentation Testing

4.2.2.1 Hertzian Indentation

The indentation apparatus used for these experiments consisted of a precision x-y stage, mounted in a hydraulic test frame (Fig. 4.4) on an adjustable tripod support system to allow leveling. Leveling was accomplished with a circular bubble-type leveler (Edmond Scientific). The polished disks were sputter-coated (Polaron, Model E5100, U.K.) with a gold-palladium (Au-Pd) film to identify the area of contact between the indenter and substrate. For planar testing, samples were placed on a tungsten carbide (WC) platen 32 mm diameter x 6.4 mm thick (Carbide Probes, Dayton, OH). For bonded interface testing, samples were placed on the WC platen and secured in a small vise with steel shims (Fig. 4.5). WC spheres were chosen in accordance with calculations of the elastic stress-strain curve and the desired region of that curve wanting to be produced. A custom designed threaded shaft, made of casehardened steel (Carbide Probes) and a half-inch WC insert with a shallow conical face was used to hold each sphere (Fig. 4.6). High vacuum grease (Dow Corning, Midland, MI) was used to secure spheres as large as 12.7 mm in radius. Sphere sizes used in this investigation were made of WC and varied from 1.191 to 12.700 ± 0.0013 mm in radius (Carbide Probes).

Indentation stress-strain curves were produced using polished planar samples as described in Sec. 4.1.3 and 4.1.3.1. These samples were sputter-coated with a Au- Pd film to easily distinguish the region of contact between the indenter and sample. A WC sphere was chosen in accordance with calculations of the elastic stress-strain response, Eq. 2.14, and the corresponding load was applied to the specimen.

After leveling the x-y stage, an aluminum dummy sample was placed at the indexing corner of the test stage. The sphere was attached to the holder and a test run was made on an aluminum disk at a load of 400 N to ensure proper seating of the sphere and to remove excess "slack" from the load frame. The dummy sample was replaced with the test specimen and the indenter was aligned by eye on a region near the upper left edge of the sample. Single-cycle (0.1 Hz) indentation was performed by a servo-hydraulic test

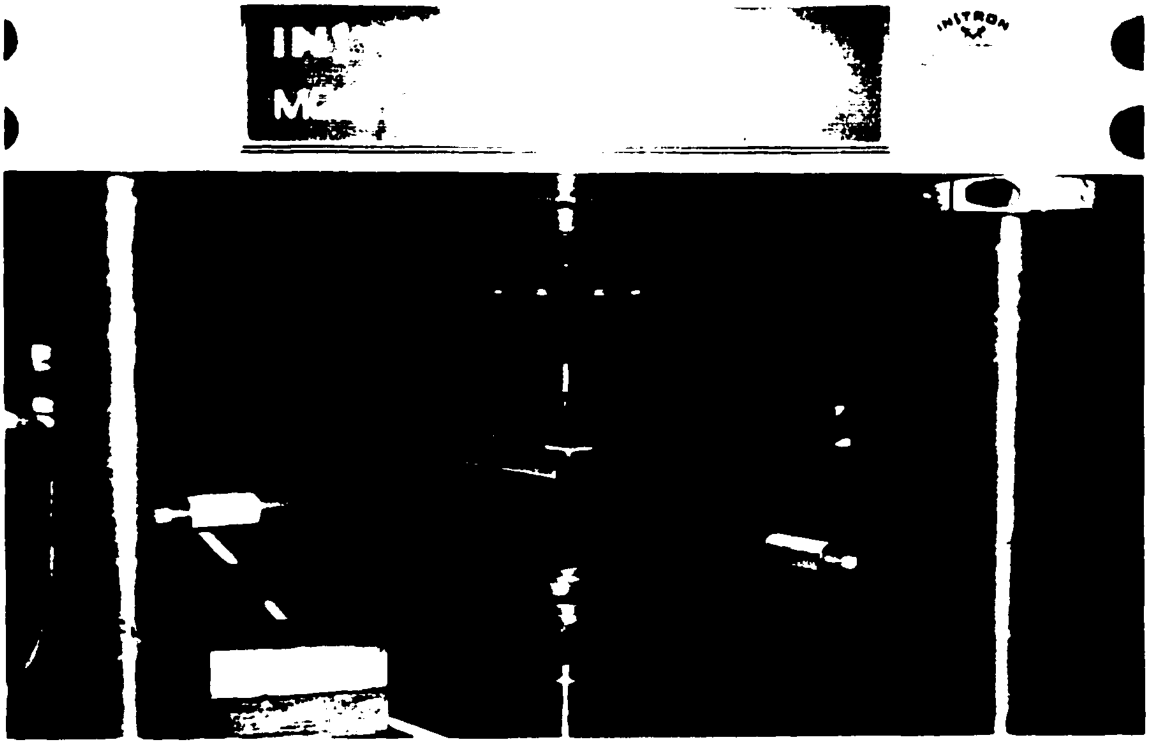

Figure 4. 4 Experimental indentation setup. Instron fixture with precision x-y stage. Sample is shown in the middle just below spherical indenter.

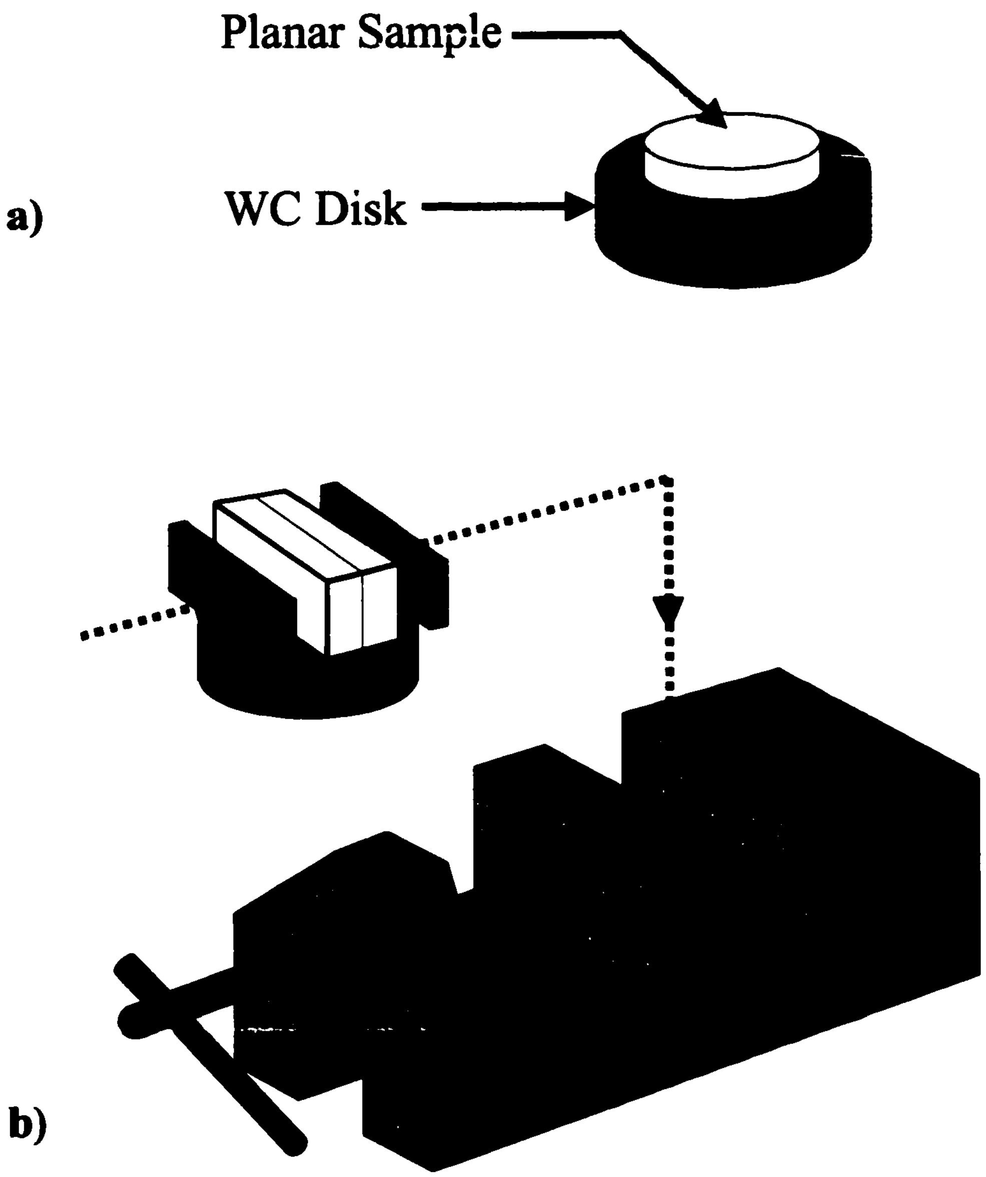

Figure 4. 5 Testing configurations. (a) Planar testing: sample rests on WC disk. (b) Bonded interface testing: sample is wedged into vise with steel shims.

frame (Instron, Model 1350, Canton, MA; Fig. 4.4) using loads from 45 to 4000 N. An oscilloscope (Nicolet 310, Nicolet Instrument Corporation, Madison, WI) recorded the output from the load cell in millivolts which was later converted into load.

Indenting proceeded along the sample surface and indents were placed such that 1.5 to 2.0 mm separated each indent to eliminate interaction between the sub-surface damage. Loading proceeded in a linear manner until the sample edge was reached and then another row of indents was placed to the right. The pattern was repeated until the sample surface was covered or no further testing was required. The indented sample was removed from the load frame and taken to the optical microscopes for recording of the contact areas as described in Section 4.2.4.2.1.

4.2.2.2 Vickers Indentation

Several samples were indented with a Vickers microhardness indenter (Leco, M-400 FT) to obtain limiting values to the deformation plotted in the stress-strain curves. Indents were made in groups of five or ten, often in the middle of the sample to minimize edge effects. Occasionally, a singular indent was made as a probe to examine crack propagation.

4.2.2.3 Bonded Interface Testing

Polished interface specimens were sputter-coated as described in Sec. 4.2.2.1, and placed into a small hand vise on a WC platen and held in place by a combination of steel shims or rods (Fig. 4.6). After the sample was placed in the vise, it was visually inspected from the side for light leaks at the interface between the WC platen and the sample

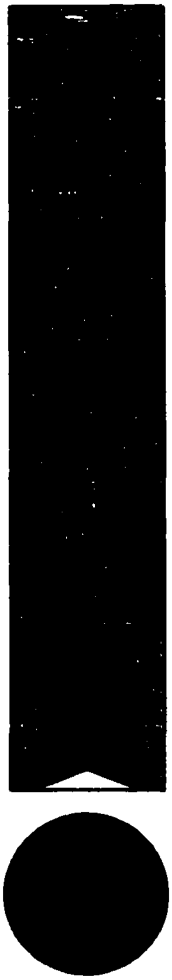

Figure 4. 6 Cross sectional view of Hertzian indentation fixture. Casehardened steel shaft is threaded 5/8 – 18 and supports a removable WC insert with a conical face. Vacuum grease adheres the indenter as shown. Sphere sizes ranged from 1.91 to 12.70 mm in radius.

bottom. Light leaks occur because of the extreme difficulty in producing perfectly parallel and orthogonal polished sample faces. The slightest errors in fabrication can cause large uneven stress distributions that ultimately can break apart the bonded interface (Fig. 4.7(a)). In order to account for the slight unevenness of the samples, rods were used in place of rectangular shims (Fig. 4.7(b)). Mild clamping pressure was applied through the use of a vertical rod placed between the vise wall and the other rod.

Once the sample was properly seated and clamped, the load frame was setup as described in Sec. 4.2.2.1. The vise was seated in an indexing fixture on the x-y stage and the indenter was aligned at one end of the specimen as close to the interface as could be determined by eye. A preload (45-67 N) was applied to deform the coating and to establish the precise location of the loading axis with respect to the interface. After the preload, the sample was removed and inspected in a light optical microscope (Nikon, Optiphot 312066, Japan) at 100x to verify the alignment of the indent over the interface. The micrometer on the x-y stage was adjusted to place the loading axis at the interface of the specimen. The appropriate load was applied, the sample was moved, and the process repeated until the other end of the specimen was reached. After loading was completed, the interface specimen was removed from the vise and taken to the optical microscope to record the surface indentation marks as described below in Sec. 4.2.4.2.1.

4.2.2.4 Pre-Indentation and Post-Indentation Testing (PPI)

To eliminate uncertainty in the evaluation of sub-surface damage patterns and to acquire definitive information regarding the nature of deformation in the subsurface microstructure of the alumina, the bonded interface technique described previously was modified as follows: interfacial areas in the high shear region were imaged prior to and after the Hertzian indent was applied by separating and reassembling the bonded interface specimen. Given that the new technique for sub-surface investigation is merely an extension of the previous technique of preparing bonded interface specimens, the procedure begins in similar fashion.

Two sintered and polished disks were joined with a cyanoacrylate-based adhesive and then cut into three parts. The bonded sections were then ground perpendicular to the interface and polished to 1 μm as described in Sec. 4.1.3.3. To test in a pre- and post-indentation (PPI) configuration, the bonded and polished interface specimen was placed into a furnace at 800 °C for 5 hours to remove the adhesive. Upon removal from the furnace, the sample was cleaned in ethanol and reassembled with the two polished halves fixed in place with a small piece of carbon tape (SPI Supplies, West Chester, PA) placed at each end.

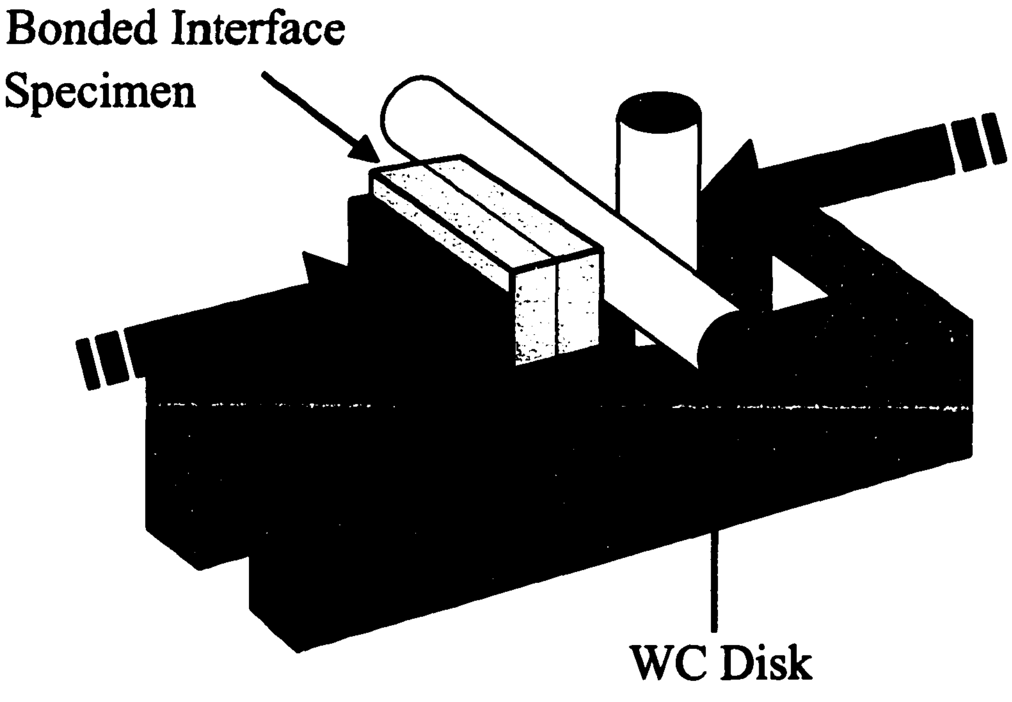

Figure 4. 7 Non-orthogonal sample testing. Steel rods are used to maintain even pressure across the sample faces during loading. Rods and/or spacers are used according to degree of misalignment and detailed in Fig. 4.8. Arrows indicate applied clamping pressure by vise. (Drawing not to scale)

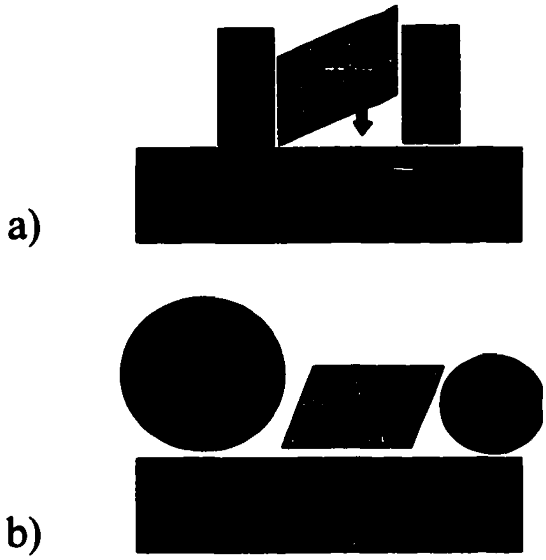

Figure 4. 8 Bonded interface shim configurations. (a) Non-orthogonal samples sheared apart under indentation when supported by rectangular shims. (b) Rods were used to compensate for non-orthogonal faces.

After ensuring the sample was taped together, a series of Vickers indents (10 N) were placed in a rectangular fashion symmetrically about the interface of the sample (long direction of rectangle parallel to interface), large enough to contain a single Hertzian indent (Fig. 4.9). A fifth Vickers indent was placed directly at the interface in the centroid of the rectangular region defined by the Vickers indents. The purpose of the central indent was to facilitate the locating of the area of interest on the interface surface in the SEM. After placing the indents, the sample halves were mounted on SEM stubs and imaged uncoated in the microscope (Jeol, Model 6300, Peabody, MA).

Imaging started at the Vickers indent site and extended outward in a tiling pattern large enough to sufficiently map out the deformation zone. With knowledge of the contact area for a given load from stress-strain measurements, the region of maximum shear stress could be estimated prior to testing. A series of high magnification images (~3000 – 9000x) were collected from this region prior to testing.

After the sample was imaged, it was placed on top of the WC disk in a small hand-operated vise and wedged in place by steel shims. Prior to tightening the vise, the entire sample setup including the vise was placed under an optical microscope to allow precision alignment of the two halves. Once aligned, the sample was taped together as before and a Au-Pd film was sputter-coated on to the surface. The Au-Pd film was used to identify the area of contact between sample and indenter and to allow precision alignment prior to high-load testing. Once the indenter was positioned properly, the desired load was applied and the sample was separated again and immediately reimaged in the same areas acquired before application of the load.

4.2.3 Profilometry

Select indented samples were analyzed in a profilometer (Tencor P2, Santa Clara,CA) with 2 Å resolution to measure the geometry of the residual impression. A sample was placed on the WC platen used for indentation support and an identifying mark was placed near the indent to be measured simplifying the positioning of the indent in the low power optical imaging system of the profilometer. The instrument was calibrated and a three-dimensional scan was obtained by making a series of line scans over a fixed distance using the profilometer's automated software. Once the 3D scan was completed, the information was saved to a file and printed out in color.

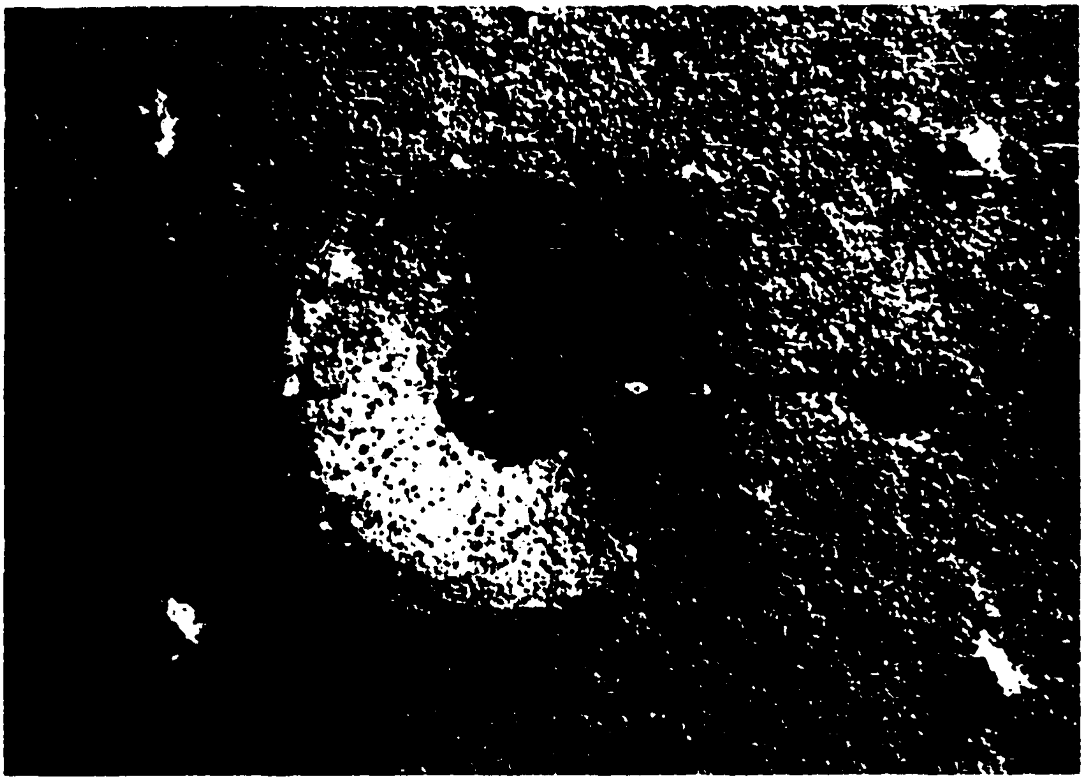

Figure 4. 9 Pre- and post-indentation bonded interface specimen testing. Four 10 N Vickers indents form a rectangle around the area to be indented. A fifth indent is placed at the interface for locating in the SEM. After imaging, the Hertzian indent is applied at the interface on top of the Vickers indent. The halves are separated and reimaged. Bar = 500 μm.

4.2.4 Microstructural Analysis

4.2.4.1 Thermal Etching

In order to facilitate grain boundary measurement, the samples were thermally etched to reveal the grain structure. Thermal etching was performed in either a tube furnace (Lindberg Model 54434) or an elevator box furnace (Lindberg Model 56724), depending on availability. Etching was performed in air and ranged in temperatures from 1300°C to 1500°C for 18 to 60 minutes depending on the sample.

4.2.4.2 Microscopy

4.2.4.2.1 Light Optical Microscopy

Samples were examined in a light optical microscope equipped with a Nomarski, interference contrast illumination (Olympus Vanox, Japan). The Nomarski microscope was used to photograph indentations and subsurface damage from bonded interface experiments. The contact area, measured from calibrated photographs, was used to determine the value *a* in Eq. 2.16 and Eq. 2.18. A black and white Polaroid image (Polaroid T52) was taken initially to establish the correct focus and lighting conditions for the microscope, after which the image recording was performed by a 35 mm camera attachment using the microscope's internal metering system. A picture of a stage micrometer was taken at every microscope session for every change in objective magnification. Images were recorded at magnifications from 40x to 1000x.

4.2.4.2.2 Scanning Electron Microscopy

The scanning electron microscope (SEM) was a major research tool used in this investigation. Samples were analyzed in two different SEMs depending on the objective of the analysis: (1) grain size morphology determination with Au-Pd coated samples (< 10,000x; ETEC Autoscan) in a tungsten filament machine at 20 kV and (2) fractography measurements uncoated in a high-resolution field emission microscope at 3.1 kV (> 1,500x; Jeol 6300, Jeol USA, Peabody, MA). Samples used for grain size evaluation were cleaned thoroughly and a Au-Pd film was sputter-coated on the surface for 1 minute. The sample was removed from the chamber, mounted on an aluminum stub, and the 1 minute sputtering run was repeated. Recording of the images was performed digitally using commercially available software (Digital Micrograph, 2.5.4, Gatan, Pleasanton, CA). The digital files were later imported into a word processor and printed out on a high-resolution laser printer (1200 dpi, Lexmark: Optra R+).

4.2.4.2.3 Grain Size Measurements

The method of determining grain size followed that of Underwood (1970) and used the random line point intercept from the microstructures printed out in the previous section. Measurements were taken from 5 – 10 micrographs with several hundred grains per micrograph.

4.2.4.2.4 Pore Morphology

Pore morphology was determined by a computerized image analysis system (Leco 2001) consisting of a digital camera interfaced to a Nikon 12x objective. Although the system is capable of importing and manipulating digital images, the best results were found using laser printed images with an optical interface. The laser-printed image was placed beneath a vertically mounted lens and aligned on the viewing monitor. After calibration, the threshold of the observed image was altered such that the system recognized the pore structure of the image. Once this had been accomplished, the software was configured to calculate mean pore size, interpore spacing, and the distribution of both.

4.3 Finite Element Modeling

Finite element modeling (FEM) was used to calculate the interaction between pores on the effect of increasing maximum tensile stresses around the inner surface of a given pore. All solutions are elastic and the models utilized the isotropic or polycrystalline values for the AD96R alumina ($E = 3.03$ GPa, $\nu = 0.21$).

To determine the stress concentration around an individual pore, a model network of five pores was established on a simple cubic lattice and oriented 45 degrees with respect to the loading axis. Pore radius was fixed at 1 micron and the spacing of the pores in the model was adjusted to control the effective volume fraction of porosity. Stresses at orthogonal positions on the pores (corresponding to regions of maximum tensile and compressive stress) were plotted as a function of the porosity.

5. COMMERCIAL LPS ALUMINA

5.1 Introduction

As discussed in Chapter 2, previous Hertzian indentation studies of dense alumina have shown that a sub-surface quasi-ductile response is controlled by the grain size of the alumina. Significant twin-faulting was detected in acoustic emissions above a 20 micron grain size and sub-surface images revealed the corresponding damage. Initially, it was assumed that the behavior of the commercial alumina material should parallel that of the dense alumina considering that the mean grain size was very small and the porosity level was low (~3%). Normal characterization of the response to a ceramic material under Hertzian contact proceeds by both macroscopic and then microscopic means. Macroscopically, one can measure the fall-off from linear elastic behavior calculated by Hertz. It has been established that an increase in the elastic fall-off is attributed to an increase in sub-surface damage in systems such as mica-containing glass, silicon carbide and silicon nitride. The increased sub-surface damage also correlated with a larger and deeper residual impression of the indentation. In metallic systems, the characteristic of the residual impression was the primary way to determine material properties such as hardness, or strain hardening behavior. However, the same cannot always be said for ceramics since the deformation mechanisms are very different.

Planar indentation was performed near the limit of detectable contact, and up to stress levels that began to deform the indenter (~12 GPa). The large stress levels had to be administered with a very small indenter of 1.19 mm radius because the commercial substrates were limited to 3 mm in thickness: larger indenters causing radial cracking and catastrophic failure of the sample. As the radius of an indenter becomes smaller, it samples a corresponding smaller volume of material (fewer grains), and is more susceptible to microstructural variations (McColm, 1990) producing variations in the indentation response. Although there is not an explicit relation to determine the radius at which an indentation size effect becomes prevalent, an indenter with a 1 mm radius is a useful limit in medium grained alumina (~10-20 μm).

Very recent work by Latella (1997) showed the general characteristics of porous liquid phase sintered alumina for porosity ranging from 2.5 to 17.8%. The commercial alumina in this investigation (3% porosity) will compare favorably with their findings. The purpose of this chapter is to illustrate the quasi-ductile nature of the AD96R alumina.

5.2 Observations

Indentation response was characterized through macroscopic and microscopic observations alike. Microscopic observations consisted of a qualitative assessment of the microstructure by optical and SEM techniques. This was done for both deformed and undeformed materials. Macroscopic deformation was recorded from stress-strain behavior as well as the physical observations of deformed surfaces. The extent of deformation to the sample surface was characterized with a surface profilometry technique. These observations will be compared to similar ones for the laboratory produced materials in Chapter 6.

5.2.1 Microstructure

Polished cross sections of the AD96R were thermally etched at 1500°C for 20 minutes to reveal the character of the grain morphology. Fig. 5.1 shows a representative sample of the microstructure. Grain size was reported by the manufacturer to have a mean value of nominally four microns. The figure shows several grains that were much larger than the average and other images suggested that the grain size distribution was large; several grains have been observed above 20 microns in diameter. The thermal etch has removed the glassy phase, however it was evident that glass was residing at the grain boundaries and triple points in the microstructure. Occasional small pores (<1 micron) were found inside of grains but the majority of porosity existed at the boundary. This was attributed to the presence of MgO as a sintering aid.

5.2.2 Stress-Strain Behavior

Indentation processes can reveal a general understanding of the deformation characteristics of a material. Specifically, an indentation stress-strain curve characterizes a material's ability to accommodate increasing concentrated loads. The stress-strain response of the AD96R material was compared with known responses of alumina materials and furthermore, was needed to compare with the laboratory produced alumina of Chapter 6 to fully understand the effects of microstructure.

Stress-strain curves of AD96R were obtained from polished samples according to Sec. 4.2 using the loads described in Table 5.1. Each data point on the stress-strain curve was an average of three indentations on the sample surface. Two diameter measurements were taken from each indent on the color images recorded from the microscope. The diameters were measured with a dial caliper (+/- 0.1 mm) in orthogonal directions and averaged. The applied load, used to calculate the indentation stress, was determined from the difference of maximum and minimum outputs from the oscilloscope. The applied

Figure 5. 1 AD96R commercial alumina: 4wt% glass phase, 3% porosity, 4 micron average grain size; polished to 1 micron and thermally etched 1500°C/20 min. Grain size distribution was found to be large with some of the largest grains approaching 20 microns. Bar = 10 microns.

load divided by the indentation area was the indentation stress and the indentation strain was determined from the radius of contact divided by the indenter radius. The resulting stress-strain curve is shown in Fig. 5.2.

Using Eq. 2.18, the straight-line elastic indentation stress-strain relation was plotted for the manufacturer's quoted values of elastic modulus and Poisson's ratio. The elastic modulus determined from the linear portion of the experimental stress-strain curve was 303 GPa – the same as that specified by the manufacturer.

Deviation from linear elasticity is marked by fall-off from the stress-strain curve that occurred about 5.5 GPa. Using a simple power-law for the data past the yield stress, the strain-hardening coefficient for the AD96R alumina was 0.5. The strain hardening coefficient was quoted as a qualitative measure since a theoretical meaning has yet to be established in relation to the damage mechanics of brittle materials. The indentation stress-strain curve plateaus at the Vickers hardness value of 12.4 GPa.

Table 5. 1 A list of the most common indenter radius and load combination used in Hertzian contact testing to produce the stress-strain curve.

Radius (mm)	Load (N)
4.76	67
4.76, 1.59	133
4.76, 1.59	267
4.76, 1.59	400
1.59	534
1.59	667
1.59	800
1.59	980

5.2.3 Indented Surface

Observations of the planar specimens were performed with a light optical microscope using Nomarski interference contrast. Characteristic damage was in the form of residual impressions and surface ring cracks. A typical indent is shown in Fig. 5.3 where slight evidence of ring-cracking was observed at the periphery of the contact impression at lower magnification. Higher magnification revealed full ring- cracking . The size of the residual impression increased with increasing load and radial cracks started to form at loads in excess of 1100 N using a 1.59 mm radius indenter. The visibly detectable limit of a residual impression corresponded to the point of initial fall-off from the linear region on the stress-strain curve and is the point of initial plastic yielding in metallic systems (Tabor, 1951).

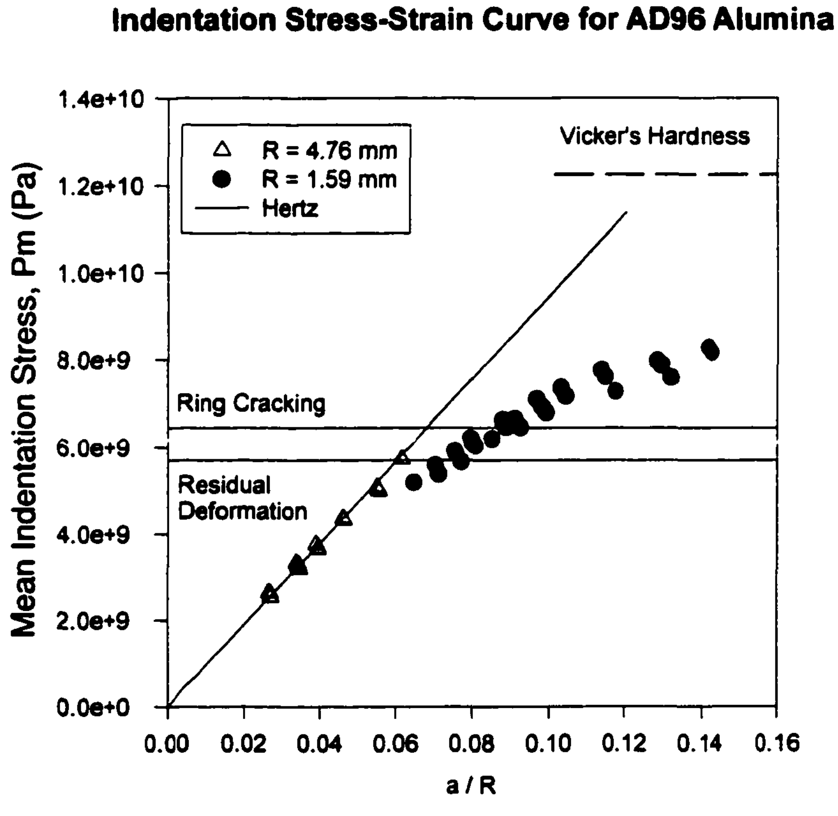
Indentation Stress-Strain Curve for AD96 Alumina

Figure 5. 2 Indentation stress-strain curve for AD96R alumina. Deviation from Hertzian behavior is correlated with the observation of residual surface deformation under Nomarski LOM. Ring cracking occurs at higher loading with increased fall-off in the stress-strain curve. Stress-strain curve plateaus at the Vickers hardness.

5.2.3.1 Residual Impression

The most notable and surprising experimental result on AD96R alumina was the significant fall-off from the elastic behavior, accompanied by an obvious residual impression after indentation. Optically, one can only confirm the existence of a residual impression; quantitative measurements have to be obtained from other means. Therefore, three-dimensional surface profiling was used to characterize the extent of the residual depth and curvature of the indent (Fig. 5.4). All indents measured by the surface profilometer technique were applied with a 1.59 mm radius indenter using an 800 N applied load. The load/indenter combination was equivalent to about 8 GPa on the stress-strain curve. A single trace through the center of the impression is shown in Fig. 5.4(bottom). The depth was just over 1 micron. The average depth for three scans was 1.5 microns.

5.2.3.2 Cracking

Besides the apparent residual impression left in the substrate surface, ring cracks were often observed at the periphery of contact. As mentioned earlier, the presence of a ring crack does not imply that a cone-crack exists beneath the visible surface. However, the propensity for a surface to display damage can ultimately be correlated with failure as often is demonstrated in bend or break tests. A comparison of the percent ring cracking between AD96R and fully dense fine-grained alumina is shown in Fig. 5.5 for increasing indentation load. The observable limit for the formation of ring-cracks on the sample surface occurred at a stress level of 6.3 GPa. This correlated to a load of 400 N in Fig. 5.5.

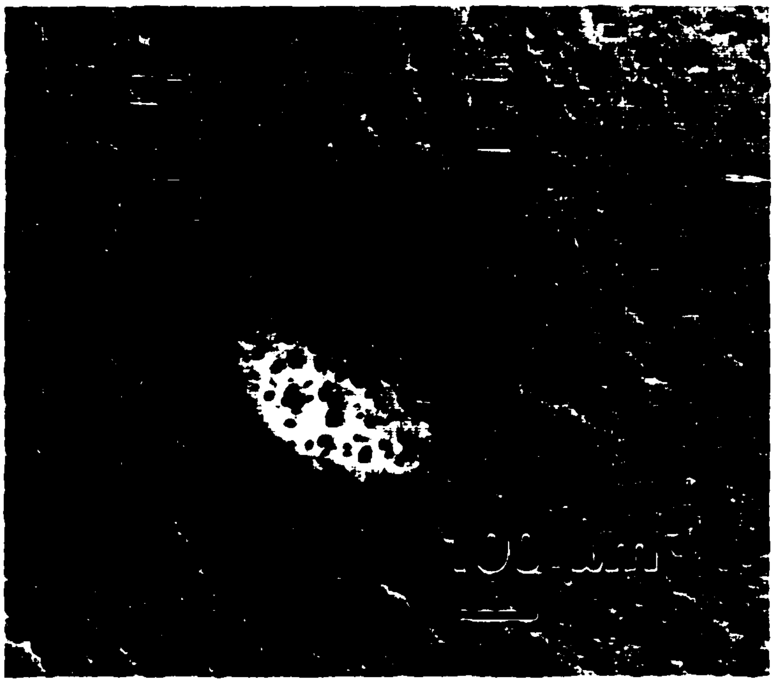

Figure 5. 3 Nomarski optical micrograph of the indented surface of AD96R. The residual impression was clearly observed. P = 800 N, R = 1.59 mm. Slight ring-cracking is visible at the perimeter of contact on the upper-right of the impression. Higher magnification reveals a fine ring-crack surrounding the entire indent.

5.2.4 Sub-Surface

The nature of quasi-ductile damage in AD96R was apparent from a macroscopic level. The obvious question was then, what microstructural mechanisms were responsible for the macroscopically observed quasi-ductility? Microstructural observations were obtained from bonded interface specimens using the technique described previously in Chapter 4 in the hopes of elucidating the underlying cause for quasi-ductility. Damage was first characterized with light optical microscopy (LOM) and then with scanning electron microscopy (SEM). The results are discussed below.

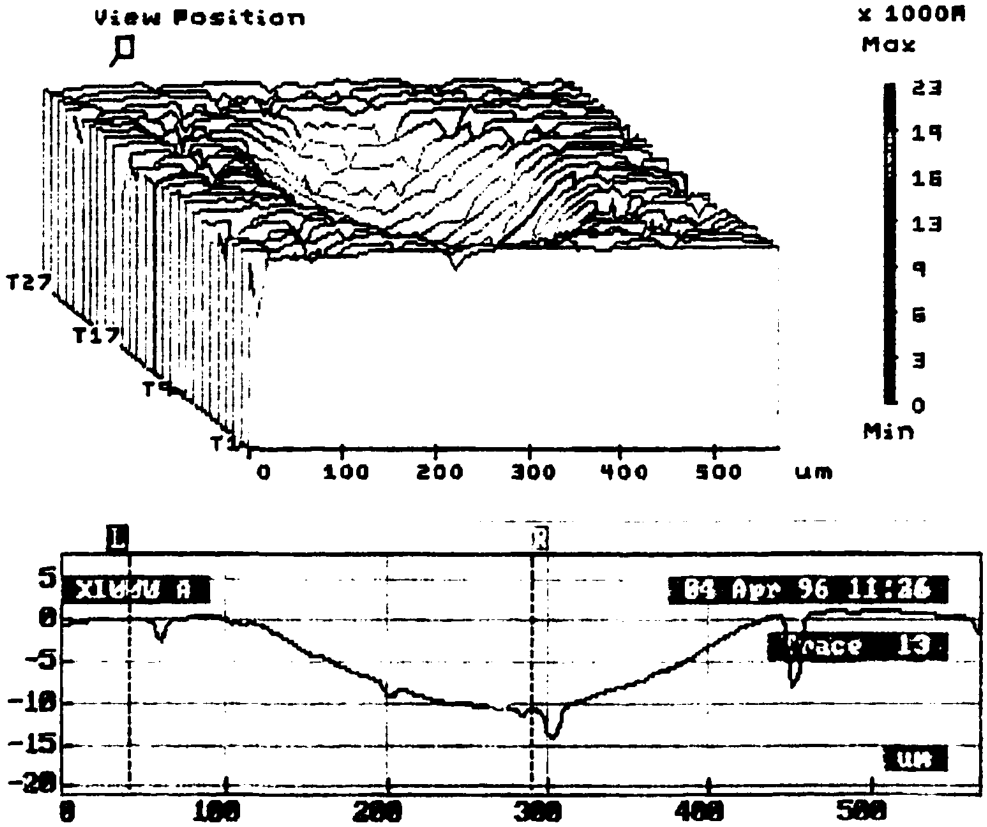

Figure 5. 4 Three-dimensional surface profile of the AD96R sample in Fig. 5.3 (top). A single trace reveals a residual depth around 1 micron (bottom). The average residual depth for 4 indents was 1.5 microns.

5.2.4.1 Light Optical Microscopy

At low magnification, the commercial AD96R alumina displays both the characteristic cone-cracking behavior and the diffuse damage region associated with most quasi-ductile ceramics (Fig. 5.6). Using the Nomarski illumination at higher magnification, images revealed a small amount of twinning in the largest grains. Looking in the sub-surface damage zone around 1000x, it appeared that micro cracking was associated with the porous regions of the microstructure (Fig. 5.7). Pores seem to be linked by a network of cracks (arrows) but it was not always easy to distinguish polishing scratches from actual cracks.

5.2.4.2 Scanning Electron Microscopy

Bonded interface specimens were indented with a 1.59 mm Hertzian indenter at a load of 500 N. Evaluation of the sub-surface regions with the electron microscope revealed uniformly distributed microcracking. An example of the images recorded (Fig. 5.8) suggested that cracking took place near the pores and possibly through the glassy areas of the material along the grain boundary (arrows). The grains themselves did not appear to be damaged. Evidence of twinning was not seen nor was there evidence to suggest grain fracture or rearrangement.

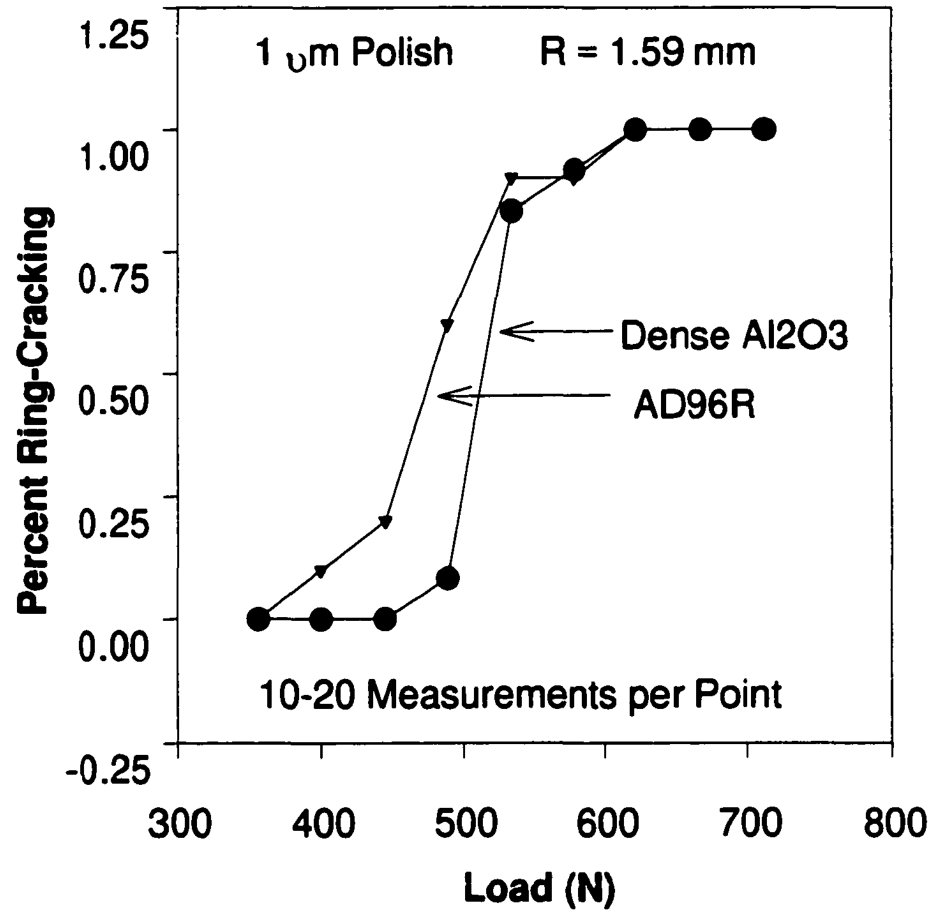

Figure 5. 5 Ring-crack statistics as a function of increasing load. The load for first observations of ring-cracks in AD96R corresponds to a stress of 6.3 GPa.

5.3 Discussion

It is apparent from the previous results that the response of the AD96R material under Hertzian contact was one characterized by significant quasi-ductility. The response was observed most notably in the macroscopic observations of indented surface profiles and subsequent fall-off from the linear behavior on the indentation stress-strain curve. Microstructurally, the material appeared to deform by cracking through the grain boundary regions containing the glass phase. High magnification optical images indicate cracks joining porous regions. The nature of these results is discussed below with reference to previous work in alumina.

5.3.1 Unexpected Quasi-Ductility

The quasi-ductile response under the Hertzian indenter was unexpected from the standpoint of the grain size of 4 microns reported by the manufacturer. As discussed in Chapter 2, dense alumina displayed a quasi-ductile response for large grained material: defined for grain sizes above 20 microns (Guiberteau, 1994). The sub-surface damage in dense alumina determined by Guiberteau (1994) is shown in Fig. 5.9. Alumina with a 3 micron grain size was found to exhibit a purely brittle cone-cracking behavior (Fig. 5.9(a)). The nature of the large-scale twin-faults was easily observed in Fig. 5.9(b). By comparison, the damaged regions shown in Fig. 5.7 and Fig. 5.8 did not show similar characteristics. It is reasonable to assume that although there are some abnormally large grains in the AD96R material, they did not contribute significantly to the observed quasi-ductility.

Figure 5. 6 Sub-surface view of AD96R showing the simultaneous cone-cracking and distributed quasi-ductile damage. Bar = 100 microns.

Figure 5. 7 High magnification optical image of the sub-surface damage region in AD96R. Cracking was observed between porous regions (arrows). Bar = 10 microns.

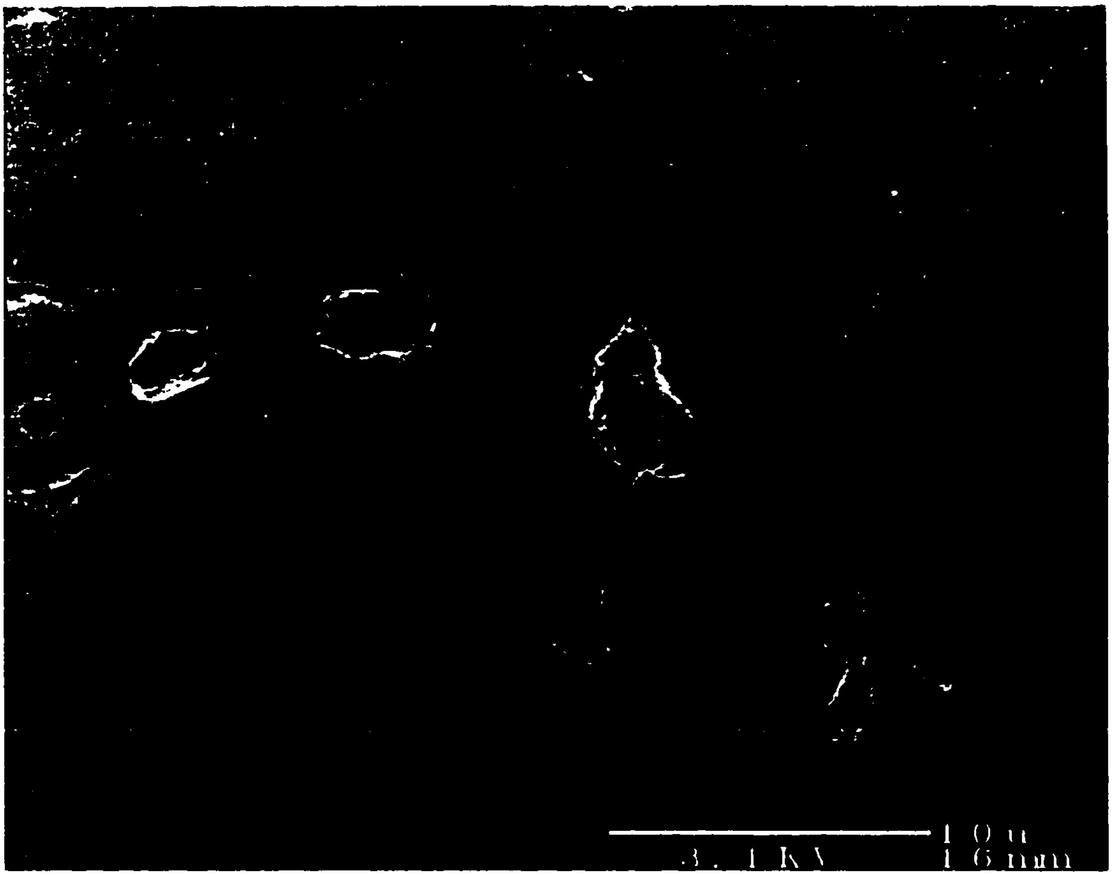

Figure 5. 8 High magnification SEM image of the sub-surface damage region in AD96R. Microcracking (arrows) appeared to travel through grain boundary areas where the liquid phase was present. Pores appear to intersect most crack paths.

The recent work by Latella (1997) confirmed the presence of quasi-ductility for several porosity levels in LPS alumina. They also confirmed the coexistence of cone cracking and diffuse damage for their intermediate porosity sample (6.8%). Correspondingly, their stress-strain curves showed lower yield values and more fall-off as porosity increased; the 17.5% porosity sample displaying almost perfect plasticity. The 2.5% porosity material displayed a typical brittle response with cone-cracks, no residual impression, and no distributed sub-surface damage zone (Latella, 1997). The progressive increase in the size of the residual impression was also notable in Fig. 5.10. While no quantitative measurement of the depth was available, the correlation between increased sub-surface damage is obvious.

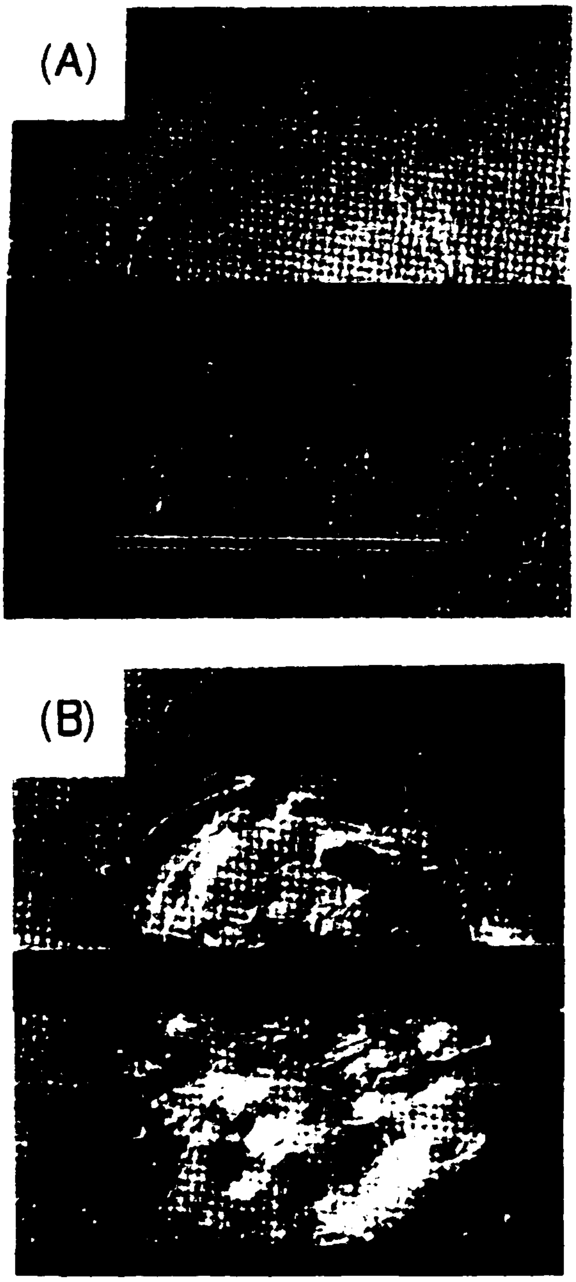

Figure 5. 9 Hertzian contact damage in pure dense polycrystalline alumina. (a) Fine-grained alumina (2 micron) exhibits classic cone-cracking behavior with the sub-surface region remaining intact. (b) Increasing the grain size above 20 microns causes a transition to sub-surface shear faulting and the elimination of cone-cracking behavior. After Guiberteau (1994).

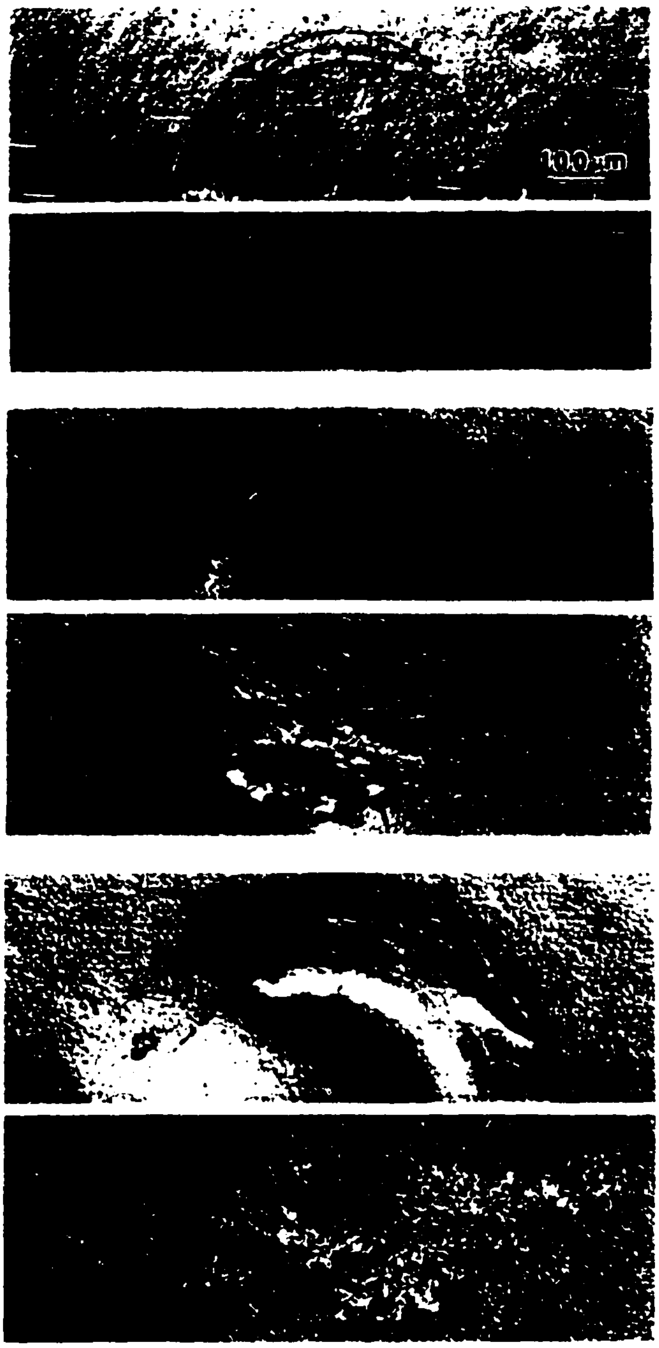

Figure 5. 10 Hertzian contact damage in porous liquid phase sintered alumina. 2.5% porosity (top), 6.8% (middle), 17.8% (bottom). Increasing porosity reveals an increase in the sub-surface damage and residual surface impression. P = 1500 N and R = 3.18 mm. After Latella (1997).

5.3.2 Controlling Factors

Latella (1997) did not determine a mechanism responsible for the quasi-ductile nature of his materials, however he conjectured that it was dependent upon the presence of porosity. Furthermore, Latella did not present any high magnification information from the damage region. From his work and the results on AD96R (Fig. 5.8), the mechanism responsible for quasi-ductile damage in these systems is likely to involve porosity and even the glass phase at the grain boundary. Confirmation of such a hypothesis required the production of specimens within the laboratory to control microstructural variables independently. Discussion of damage mechanisms occurs in later sections in more detail as attention now turns to laboratory produced alumina.

5.4 CONCLUSIONS

- The commercial AD96R revealed substantial macroscopic quasi-ductility under Hertizian contact with an indentation yield point of 5.5 GPa.
- Subsurface images using LOM and SEM indicated that damage may have originated from porosity and proceeded through grain boundary areas.
- The quasi-ductility was unexpected because the small grain size prevented the well known twin-faulting behavior

6. LABORATORY PRODUCED LPS ALUMINA

6.1 Introduction

Indentation tests on AD96R suggest that a different mechanism is responsible for controlling the quasi-ductility observed under Hertzian contact in PLPS alumina. In this chapter we will attempt to show experimentally the relationship between grain size, porosity, and presence of liquid phase in controlling quasi-ductility in the sub-surface region beneath the Hertzian indenter. Moreover, by producing microstructures with controlled porosity and glassy phase content, it was possible to isolate and identify the microstructural variables giving rise to quasi-ductility under Hertzian contact.

6.2 Experimental Observations

Very high-purity alumina powders were the starting point for all sintered microstructures because some impurities in the starting materials can greatly effect the sintering behavior, often causing abnormal grain growth. The first objective in making laboratory samples was to re-create a liquid phase sintered alumina that displayed similar indentation behavior as the AD96R material. The first attempts at re-creating a commercial microstructure used AKP-50 alumina powder with sub-micron starting particle size (0.2 – 0.3 μm). This powder had a high surface area and easily densified at low sintering temperatures (~1350°C). The first LPS alumina sample (A50-5G) combined a commercial microelectronic glass (EG-2770), having a similar composition to that of the AD96R glass, with the AKP-50 alumina. This sample, and the others used in this investigation are listed in Table 6.1. When the A50-5G sample, with 5wt% of glass, was sintered to a final density of 95% and tested under Hertzian indentation, the response was completely brittle! A quasi-ductile response was anticipated, as the sample composition appeared similar to the AD96R: fine grained, 5% porosity, and similar amount of liquid phase. The reason for the lack of quasi-ductility was not clear until a detailed micromechanical analysis was performed and is discussed later in Chapter 7. Changing to a powder with a particle size around 3.5 microns[§] (AA5) and different glass phase successfully produced a quasi-ductile response similar to AD96R. Anorthite glass was used in place of the EG-2770 after the processing route was changed to an established procedure (Dong, 1997). The only other sample to use EG-2770 glass was the hot pressed A50-0G, all other samples were processed with anorthite. Having reproduced the quasi-ductile response, systematically altering the alumina microstructure determined when the quasi-ductility would disappear. As shown in Table 6.1, the porosity level of the LPS alumina varied from 0% – 6.5% and the pure alumina varied from 0% – 8%. Porosity in the laboratory produced materials was kept at about 8% or less in order to most closely approximate a condition of uniform isolated pores. The porosity was found to be closed in all samples except one of the 8% which had open porosity. The determination of open/closed porosity was made by wet submersion density measurements discussed in Chapter 4.

[§] Average size was initially 4 μm but was reduced during ball milling.

Table 6. 1 Laboratory produced alumina used in this investigation. Commercial AD96R is shown for comparison.

Name	Material	Method	Temp. (°C)	Time (h)	Glass (wt%)	Porosity (%)	Av. Gr. (μm)
A50-1	AKP-50	AS	1325	5	-	1	2
AA2-5	AA2	HP, 30 MPa	1450	0.67	-	5	7
AA5-5	AA5	HP, 50 MPa	1500	3	-	5	5
A50-8	AKP-50	AS, Etch	1300, 1300	0, 0.5	-	14, 8	<1
A50-0G	AKP-50	HP, 50 MPa	1250	0.5	5	~0	3
AA2-6.5G	AA2	AS	1600	2	4.5	6.5	4
AA5-5G	AA5	AS	1600	10	4.5	5	5
	AD96R	**AS**	*	*	**4**	**3**	**4**

Sintering of the alumina samples was either by vacuum hot-pressing or in a furnace under ambient conditions and is also indicated in the table. The sintered alumina samples were all produced as 1 inch disks of various thickness. Most samples were thermally etched at a temperature slightly below their sintering temperature for 20-40 minutes. Densification during thermal etching was negligible except where noted. Usually, grain size measurements were made from images (Fig. 6.1 to 6.9) obtained from a small section of a disk, cut and polished specifically for that purpose. Occasionally, however, microstructural analysis was performed from the polished disk surface subjected to Hertzian contact. Macroscopic measurements, stress-strain behavior, depth profiles, and surface cracking were obtained from the polished disk surface (Fig. 6.13 – 6.14). Limited ring-crack statistics were also gathered from polished disk surfaces. General observations were made of cone-cracking behavior, but not studied in detail (Fig.

6.11 – 6.12). Microscopic observations (Fig. 6.17 – 6.25) were taken from sub-surface regions of bonded interface specimens. Detailed study of the sub-surface damage regions is presented and a novel technique to elucidate the damage is also discussed.

6.2.1 Microstructural Characterization

Polished and etched microstructures revealed homogeneous grains in all the sintered materials. There was no evidence of abnormal grain growth in any of the samples; this was attributed the additions of MgO (Kaysser, 1997; Harmer, 1985). Grain sizes were small (1-7 microns) and porosity was found to be homogeneously distributed at grain boundaries and triple points, except where noted. This fact was also attributed to the use of the MgO (Zhao & Harmer, 1988). The distributions of porosity and grain size in most cases were estimated qualitatively from micrographs by comparing the largest observable feature compared to the calculated average.

The A50-5G alumina shown in Fig. 6.1 was air-sintered at 1400°C for 1.5 h to produce a density 95% of theoretical ($\rho_{th} = 3.986$ g / cc). This sample had porosity divided between large agglomerated pores, on the order of several microns, and finely distributed sub-micron pores at the grain interstices similar to that observed in Fig 6.6 for A50-8. The large pores comprised less than 1% of the total porosity in this sample. Sample A50-0G, shown in Fig. 6.2, was compositionally the same as the A50-5G samples. However, A50-0G was hot pressed to an undetectable amount of porosity. After thermal etching, Fig. 6.2 revealed slightly faceted and elongated grains with a 3 micron grain size. The distribution of grain size appears to be somewhat larger than the other lab samples of liquid phase sintered alumina, but that did not have any effect on the indentation behavior as will be shown later. Notably, Bennison & Harmer (1985) have shown that the vacuum hot-pressing of LPS alumina caused a significant amount of carbon to dissolve into the sample. When the sample was thermally etched, the carbon

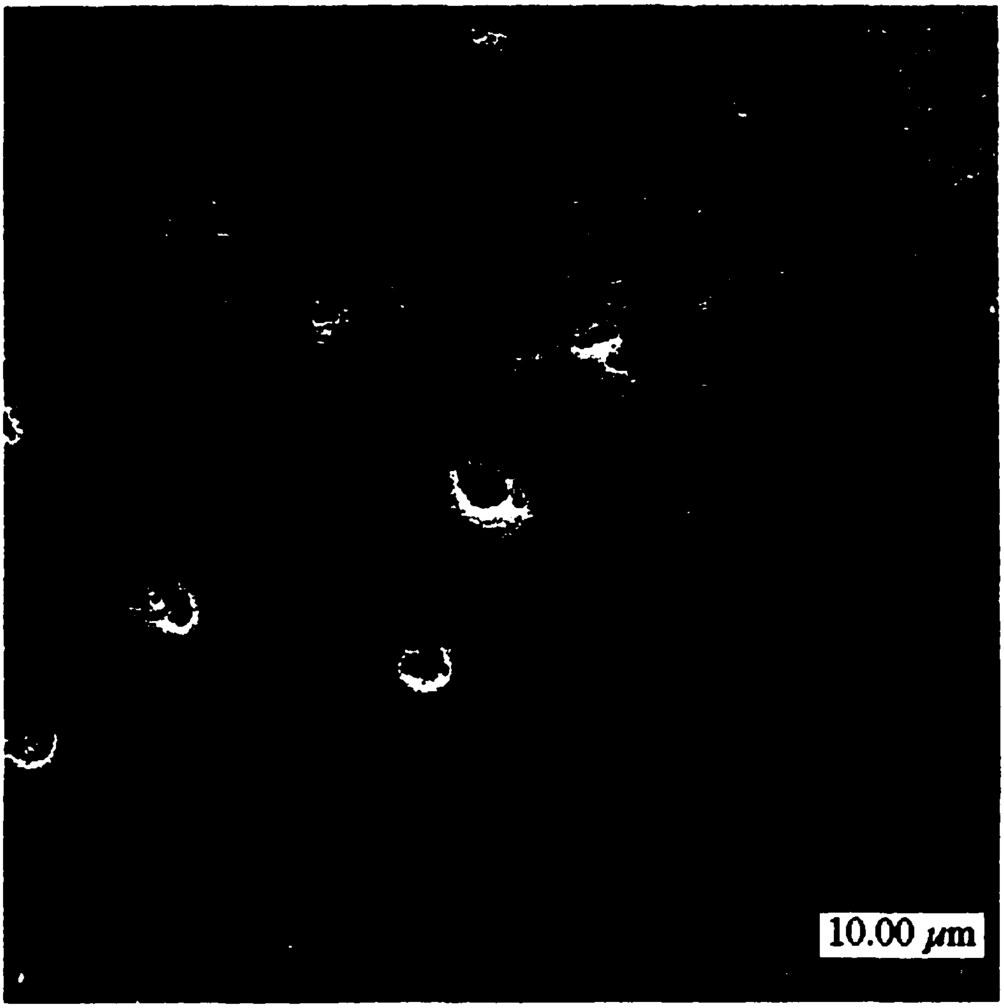

Figure 6. 1 Sub-micron grained alumina with 5wt% glass phase (EG2770). 5% porosity is distributed between sub-micron pores at grain interstices and larger pores resulting from unbroken agglomerates during processing.

Figure 6. 2 Hot pressed liquid phase sintered alumina (A50-0G). Thermal etch revealed elongated grains with approximately a 3 micron average grain size.

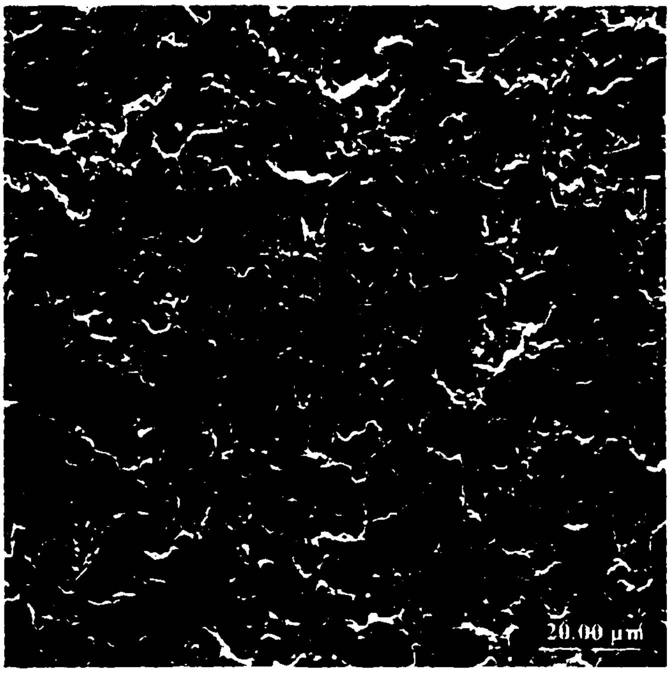

Figure 6. 3 After thermally etching, the A50-0G microstructure exploded due to dissolved carbon acquired during the vacuum hot pressing (Bennison and Harmer, 1985).

out-gassed, causing significant porosity to form as shown in Fig. 6.3. The sample was indented prior to thermally etching. The AA5-5G alumina is shown in Fig. 6.4. The 5 micron average grain size was very uniform and produced a similar indentation response as the AD96R as will be shown below. The AA2-6.5G alumina (Fig. 6.5) was produced to gauge the effect of even higher levels of porosity in the LPS alumina. The microstructure is shown without a thermal etch as an indicator of porous character of the material.

Pure alumina samples were made to understand the effect the glass phase would have on the quasi-ductile damage for similar porosity. A50-8 was the most porous pure alumina sample and was first sintered to 14% porosity but subsequently densified after a thermal etch. Most of the porosity in this sample was uniformly distributed and sub-micron (Fig. 6.6). Similar to A50-5G (Fig. 6.1), this sample had occasional pockets of larger porosity (Fig. 6.7). The large pore clusters appeared less often in the pure alumina than the LPS alumina. An intermediate level or porosity was obtained in the AA2-5 sample shown in Fig. 6.8. The sample was pressureless sintered to a 5 micron average grain size and had evenly distributed porosity. A low porosity sample, A50-1 shown in Fig. 6.9, had small pores occasionally found within grains themselves. Pores were also found in small clusters at certain parts of the microstructure. The movement of pores off the grain boundary and into the grain normally would be of concern. However, because of the low porosity level, it was unlikely that this had a noticeable effect on the indentation response shown later.

Figure 6. 4 AA5-5G sintered microstructure. Average grain size was 5 microns with a narrow distribution and contained 10 vol% glass. Glass phase is absent from image due to thermal etch.

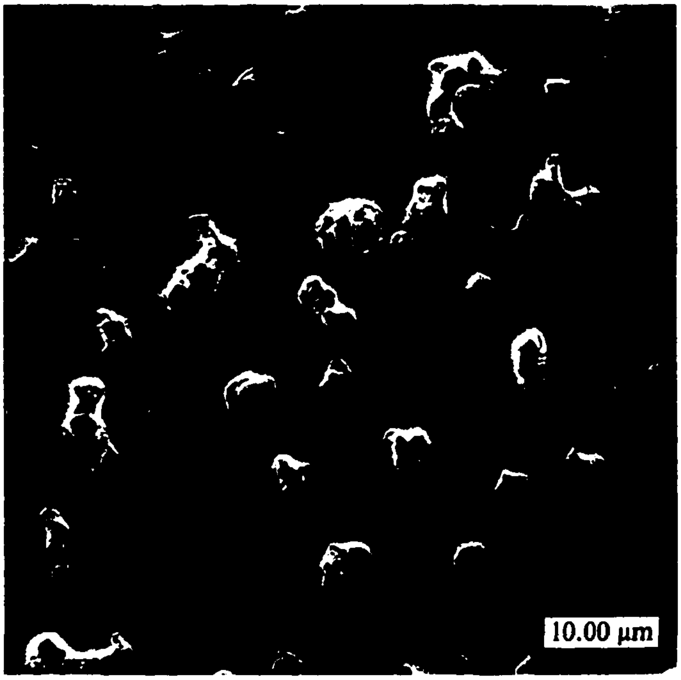

Figure 6. 5 AA5-6.5G sintered microstructure. A smaller starting particle size (AA2) was used and sintered longer. Grain size averaged 4 microns and was also narrow. Image shown unetched.

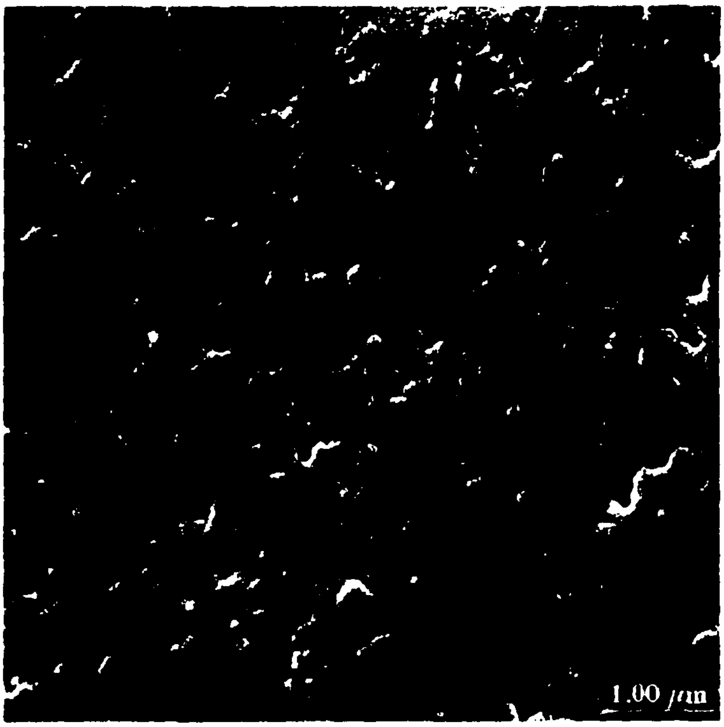

Figure 6. 6 A50-8 sintered microstructure. Very fine starting particle size (0.2-0.3 microns) and short sintering time lead to a fine grained microstructure. Pore size is clearly sub-micron.

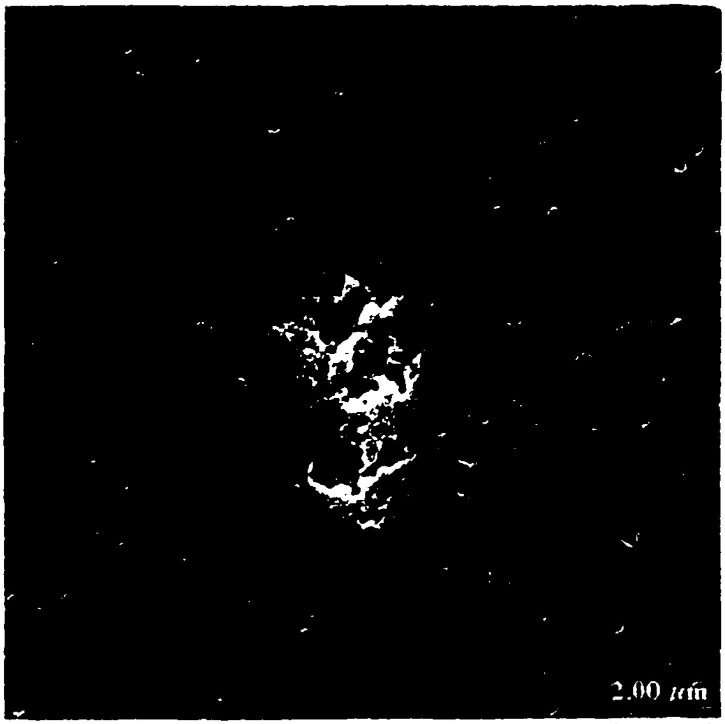

Figure 6. 7 A50-8 microstructure showing the pore clusters similar to Fig. 6.1

Figure 6. 8 The AA2-5 microstructure. 5% porosity with a 5 micron grain size.

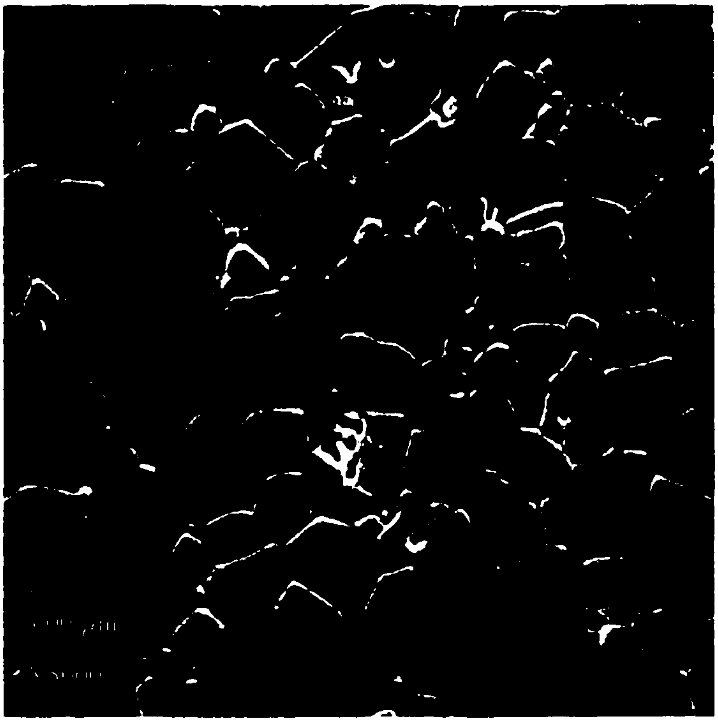

Figure 6. 9 Dense pure alumina with 1% porosity (A50-1). Grain size averaged 2 microns and some pores had moved off the boundaries into the grains.

6.2.2 Stress-Strain Behavior

An easy way to characterize deformation characteristics in a material is with a stress-strain plot. Both elastic and plastic response may be quantified which allows for the determination of useful design limits. Similarly, an *indentation* stress-strain curve is useful to understand the mechanical response of a material during the indentation process. The indentation stress-strain curve in brittle material systems is useful for providing a qualitative comparison between different materials and can provide a general idea of yield characteristics. However, care should be taken when attempting to use the stress-strain results for computational analysis as the technique is not overly sensitive in the inelastic regime and analytical expressions are still being developed (Lawn and Marshall, 1998; Fischer-Cripps, 1997(b); Fischer-Cripps and Lawn, 1996(b)). Furthermore, the stress-strain curve is influenced by the behavior of the indenter and substrate simultaneously: yielding in the indenter is an integral part of the curve. For example, data past the 7.5 GPa yield stress of WC will contain a multiple material yield effect. Fortunately, Hertzian contact has been shown to be effective in the elastic regime (Zeng, 1992) which was confirmed in Chapter 5 for the stress-strain behavior of AD96R. This section will illustrate the general behavior between the AD96R material and laboratory produced samples of similar porosity level with and without a glass phase present. The differences in macroscopic indentation behavior correlated with changes in microstructure.

Firstly, one notes that the fall-off from the elastic behavior for AA5-5G coincided with that of the commercial AD96R, seen in Fig. 6.10. The fall off appeared slightly less than that of the AD96R material for AA5-5G, indicating a lower quasi-ductile response.

Despite the lack of sensitivity in the stress-strain measurements, one might suggest the reason for the difference was the occurrence of large grains in the AD96R. Observations in the commercial material revealed grains as large as four or five times the mean. As was shown by Guiberteau (1994), the larger grains were more susceptible to twin-faulting and therefore would contribute to an increased ductility. The pure alumina sample experienced even less fall-off from the linear elastic behavior compared to AA5-5G and AD96R, for similar porosity. All the samples displayed a similar elastic response beneath the Hertzian indenter. This indentation behavior implicated the grain boundary glass phase as contributing to the increase of quasi-ductility under Hertzian contact.

6.2.3 Indented Surface

Several important aspects of sample response to indentation can be observed from the area where the indentation was applied. As shown in Eq. 2.15 – 2.18, the size of the contact area can be used in conjunction with the applied load to determine stress- strain behavior. Qualitatively, the easiest and quickest observation to make on an indentation surface is to look for a residual impression. The absence of a residual impression indicates minimal sub-surface microstructural damage; the presence of an impression mandates a mechanism to accommodate the physical rearrangement of material. Furthermore, cracking is often visible at the surface near the periphery of the contact area. The presence of cracking in conjunction with other observations provides information about which inelastic mechanisms activate as stress increased around the indenter.

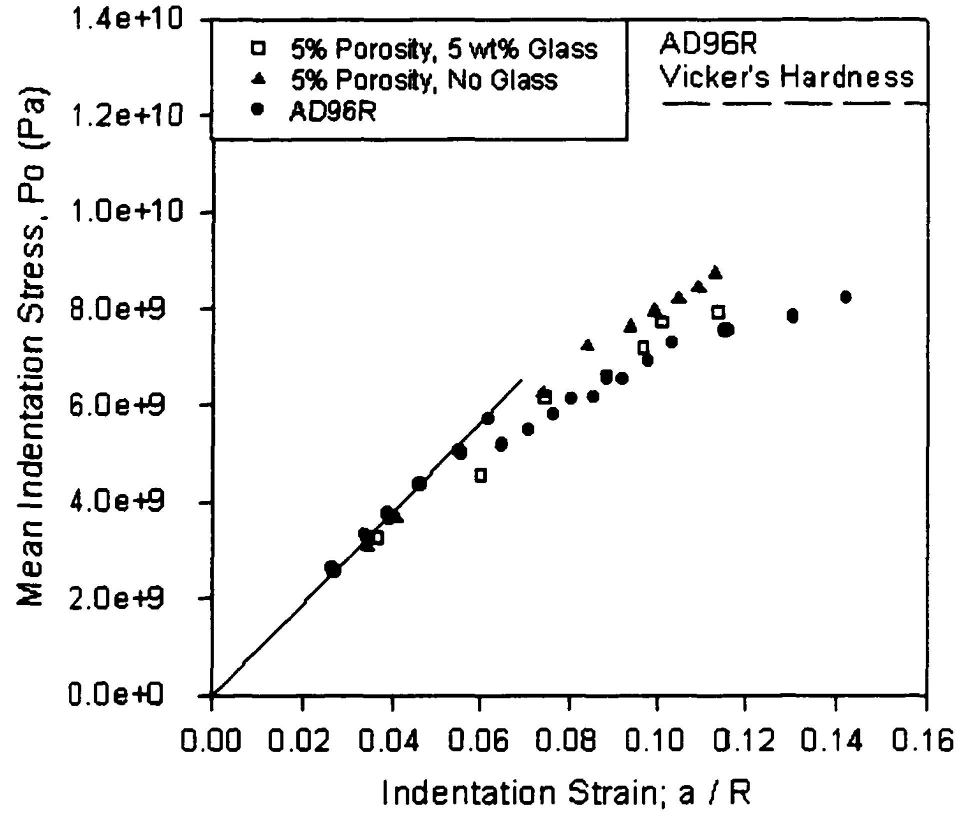

Figure 6. 10 Indentation stress-strain curve of alumina with 5% porosity containing 5wt% glass phase and no glass. Previous results of AD96R shown as black circles.

6.2.3.1 Cracking

Optical microscopy was very useful in determining the presence of ring-cracks at the indented surface. Most observations were performed on the same specimens used to produce stress-strain curves. However, some samples were tested specifically to identify the nature of the surface cracking. Cracks eventually developed in all samples tested somewhere above the yield stress. All the pure alumina samples began cracking near the yield stress. AD96R, AA5-5G, and AA2-6.5G samples yielded quasi-ductility and then developed ring cracks after the stress increased.

The ring-cracks that formed in the A50-8 and A50-5G alumina prior to the formation of a residual impression are shown in Fig. 6.11 and 6.12 respectively. The region of contact between the indenter and substrate deformed the thin metallic film and showed as a bright circular mark in the image. Notice that the full ring-crack exists outside the area of contact. As the load was increased, ring cracks can form incrementally for loads higher than the yield stress. Quasi-ductility did not develop in A50-8 until the stress was increased near 7 GPa. In A50-5G applied loads generating an equivalent stress in excess of 8 GPa produced only a marginally detectable residual impression. The obvious difference between theses two samples and the others is their very fine (sub-micron) pore size distribution. The suppression of quasi-ductility was traced to the stress concentrating effect of the pores and will be addressed further in Chapter 7. Fully dense alumina showed prominent ring cracking and no quasi-ductility.

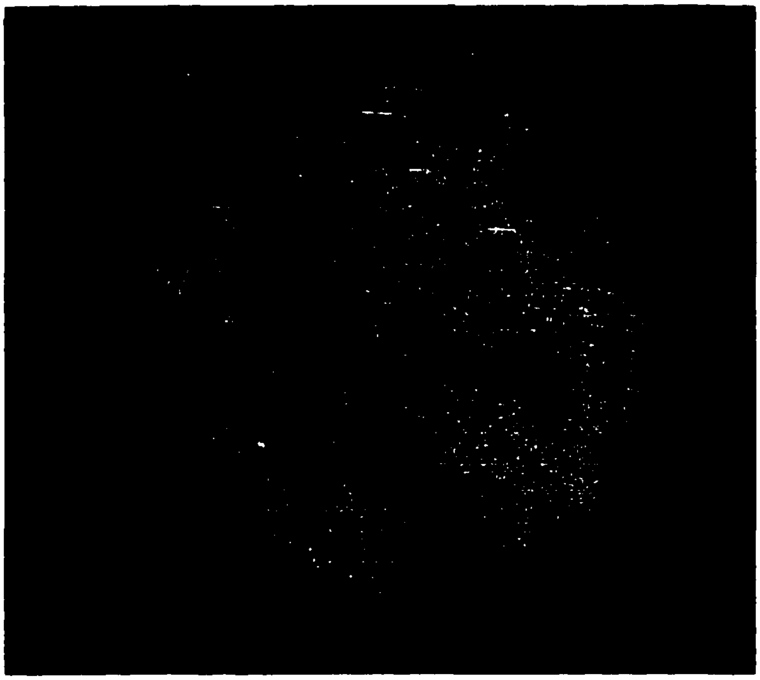

Figure 6. 11 Optical microscope view of indented surface of A50-8. No quasi-ductility was observed for indentation stresses near the yield stress. Higher indentation loads produced a residual impression depth of 1.1 micron.

Figure 6. 12 Surface indentation of A50-5G showing pure brittle cone-cracking behavior. Very little quasi-ductility was generated even at loads well past the yield stress.

6.2.3.2 Profilometry

In this section, we analyzed the behavior of our samples from the surface response to indentation. It was assumed that the presence of a residual impression under the action of the indenter is associated with homogeneously distributed microdamage mechanisms that will be called quasi-ductility. Proof of this will be presented in the discussion. Although the existence of a residual impression was confirmed using Nomarski optical microscopy, quantitative information was not obtained by this technique. Therefore, an accurate method of obtaining quantitative information regarding the nature of the residual impression was by surface scanning profilometry. Three-dimensional scans of indents tested at fixed load of 800 N with an indenter radius of 1.59 mm were performed on selected samples. This load/indenter combination results in a 7 GPa applied stress that varies several percent with the different elastic moduli for each sample. Three indents were measured for each sample with only two measurements made on the dense A50-1 and A50-5G samples. A comparison of the residual impression made by the Hertzian indentations in the alumina samples is shown in Table 6.2. A typical 3D profilometer scan of the AA5-5G material can be seen in Fig. 6.14(a). The depth of the impression shown in the single scan, Fig. 6.14(b) was 1.0 micron.

Table 6. 2 Summary of residual depth measurements from the profilometer in the alumina samples.

Sample	Porosity (%)	Residual Depth (μm)
A50-1	1	0.1
AA2-5	5	0.5
A50-8	8	1.1
A50-0G	~0	~0
AA5-5G	5	1.0
AA2-6.5G	6.5	1.5
AD96R	3	1.5

A Nomarski polarized microscope facilitated the observation of the surface impression by displaying a color grading across the surface of the material where it was deformed. A typical residual impression left in the AA5-5G sample is shown in Fig. 6.2. This quasi-ductile response can be compared A50-5G in Fig. 6.12, which displayed a purely brittle response. The AA5-5G material was found to produce the same effect under the action of the Hertzian indenter as that of the AD96R material.

In comparison to AA5-5G, the other LPS samples AA2-6.5G, A50-5G, and A50-0G provide further insight into the combined role of porosity and glass. At loads near the yield stress, A50-5G and A50-0G displayed no trace of a residual impression in the sample surface. The A50-0G sample was uniaxially hot-pressed and had no porosity. In the absence of porosity, quasi-ductility was not observed in A50-0G at loads as high as 1100 N with a 1.59 mm indenter (~10 GPa). Increased stress in A50-5G showed only a slight residual impression. AA2-6.5G displayed an increased residual depth of 1.5 microns to correspond to the increase in porosity over the AA5-5G specimen.

Absence of the glass phase alone was not enough to remove the quasi-ductile response. For instance, the A50-1 sample had a residual impression depth of around 0.1 microns; the AA2-5 sample had a depth of 0.5 microns and the A50-8 a depth of 1.0 microns. Fig. 6.14 contains a graph of the depth for the pure alumina samples as a function of porosity as well as the liquid phase sintered sample. Although the indentation load indentation depth relation is actually non-linear (Johnson, 1985), a line was used as a visual aid because of the limited data and is sufficient for a qualitative comparison. The residual depth for the glass containing materials is clearly greater at equivalent values of

Figure 6. 13 Nomarski optical image of the residual impression in AA5-5G. Barely visible at this magnification, ring cracking was observed at higher magnification.

porosity in the laboratory produced material. All indents were performed with a 1.59 mm radius indenter under the action of an 800 N load.

6.2.4 Sub-Surface

To this point, the measurements and observations of Hertzian contact damage have all been macroscopic in nature. We now turn to the critical part of the experimental work that focused on correlating microstructural observations with macroscopic observations. Of paramount importance was learning the sub-surface relationship among the porosity, glass, and grain size of the material. This part of the research relied on samples made by the bonded interface technique of sample preparation.

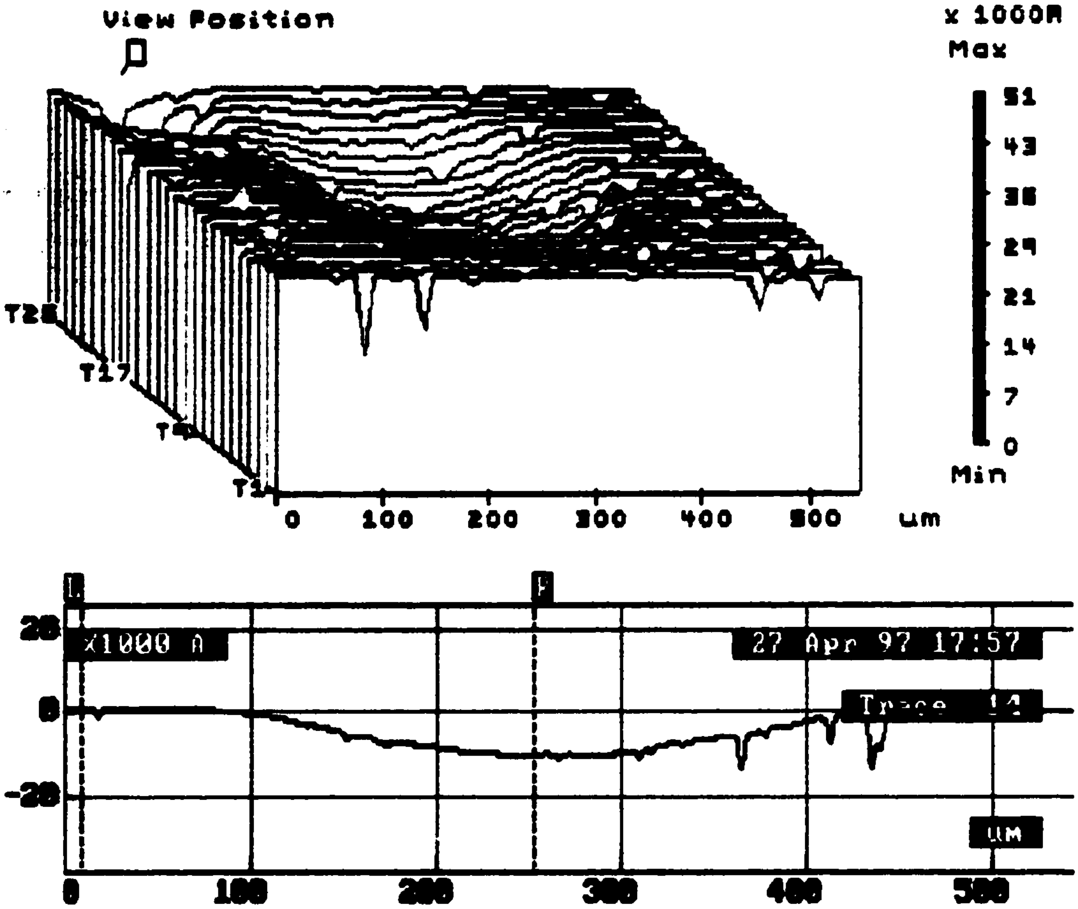

Figure 6. 14 Profilometer measurements of the indent shown in Fig. 6.13. Three-dimensional surface impression (top) and single scan from the center of the impression (bottom). Average depth for three indents = 1.0 microns.

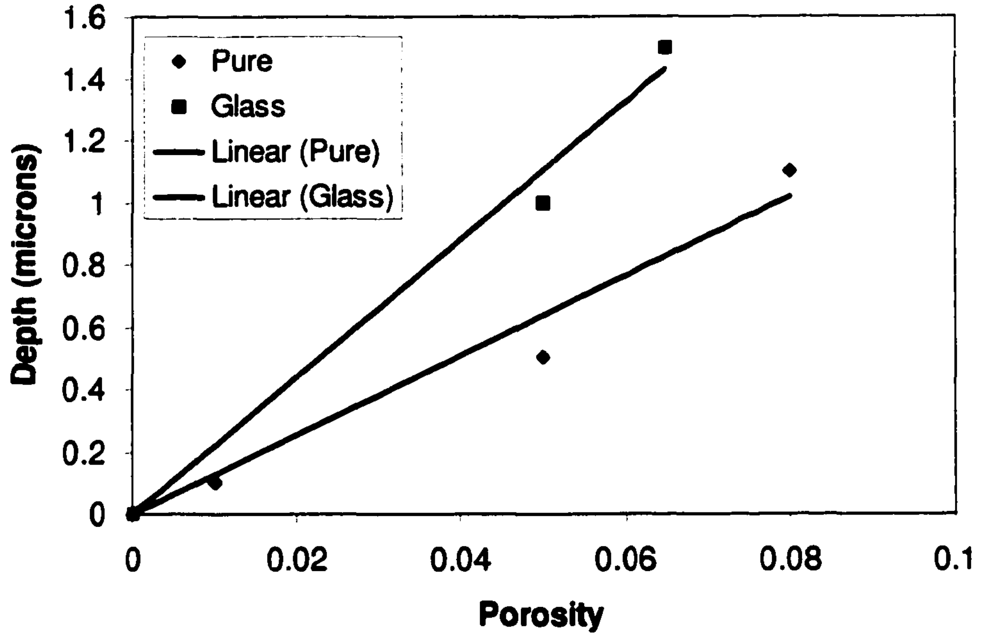

Figure 6. 15 Plot of the residual depths of indentation test results in laboratory produced alumina. Linear fits through the origin are provided as a guide to the eye.

Samples were prepared according to the procedure outlined in Chapter 4. A series of 6 to 12 indents were made, spaced 1.5 – 2 mm apart, on each bonded interface specimen depending on the loads applied. Damage was characterized with Nomarski light optical microscopy (LOM) and scanning electron microscopy (SEM). Magnifications of 50-1000x were used in LOM and 500-20,000x in the SEM. High magnification images in LOM were taken with a Au-Pd coating and SEM images were obtained on uncoated specimens.

6.2.4.1 Light Optical Microscopy

The light optical microscope with the Nomarski objective was used primarily to view the low magnification characteristics of the indentations. Occasionally, higher magnification was used to view the damaged region, however, because of the limited resolution of optical microscopy, provided only limited information. At low magnification, the cone-cracks in many of the LPS alumina were not visible. Just above the yield stress in AA5-5G, cone-cracking had only partially developed and was barely detectable. Furthermore, the sub-surface region was devoid of any evidence of quasi-ductility. However, as the next section will show, microcracking had indeed been initiated.

Twinning was the easiest to identify using the LOM equipment and existed in a small amount in the AD96R samples. None of the laboratory produced specimens showed any evidence of twinning within the damaged region. This result was consistent with recorded grain sizes and previous studies in alumina (Guiberteau, 1994). However, heavily damaged regions contained cracks between pores in the microstructure, as seen in Fig. 5.2. Comparison of optical and SEM images of the same region verified the damage character and will be discussed next.

Fig. 6.16 contains an optical sub-surface region of A50-8 which clearly shows the brittle cone-cracking behavior. Note further that a quasi-ductile damage zone is absent from the high shear region. This corresponded to the absence of a residual impression at low loads shown in Fig. 6.11.

Figure 6. 16 Sub-surface optical micrograph of A50-8 sample at a load near the yield stress. Only cone-cracking was observed, no evidence of quasi-ductile damage was present. Dark regions at top of image are a result of edge chipping.

6.2.4.2 Scanning Electron Microscopy

The scanning electron microscope images of the damage region provided the most valuable data to understand the factors that control the quasi-ductile deformation. As the grains of the alumina have been kept small enough to exclude twin-faulting as a primary mechanism for ductile damage formation, the information from these experiments provided a quasi-ductile mechanism not addressed in the current Hertzian contact literature.

Information in this section is provided for the AA5-5G and AA5-5 samples indented with a 3.18 mm radius indenter at 1100 N (~6 GPa) and again with an increase in load to 4000 N[‡]. The high magnification images were recorded from the maximum shear region beneath the surface of the substrate.

[‡] Due to the severe damage, stress could not be calculated.

Near the yield stress, the microstructure of AA5-5 showed virtually no visible sign of damage in the maximum-shear region (Fig. 6.17). Careful searching of similar indents failed to reveal any damage. Note the AA5-5 samples were thermally etched prior to Hertzian indentation. Conversely, AA5-5G displayed readily visible signs of microfracture seen in Fig. 6.18 after an applied load slightly above the yield stress. Fracture in AA5-5G was predominantly through grain boundary areas but an occasional fracture through a grain was observed. In Fig. 6.19, the porosity of AA5-5 remained intact after loading to 4000 N with some cracking observed within the grains (A). Possible cracks through grains were observed in other areas (B). The 4000 N loading produced severe damage in the AA5-5G alumina with pore collapse and grain rearrangement evident (Fig. 6.20). Furthermore, cracking within grains started to become evident (arrow A) and some grains looked as if they might have been sheared or microtwinned (arrow B). The damage observations in Fig. 6.17 – 6.20 were consistent with the fall-off from the stress-strain curve observed in Fig. 6.15 and the plot of the residual depth from the profilometer measurements (Fig. 6.2).

The uncertainty and ambiguity in the interpretation of microstructural damage seen in a variety of images led to the modification of the standard bonded interface technique to obtain a pre- and post-indentation view of the damage region (DiGiovanni, 1999). The next section will address these results.

Figure 6. 17 Sub-surface region of AA5-5 at low indentation stress. No visible damage could be observed in the high shear region beneath the indenter.

Figure 6. 18 Indentation of the AA5-5G sample at low indentation stress produced visible cracking within the microstructure in the high-shear region beneath the indenter.

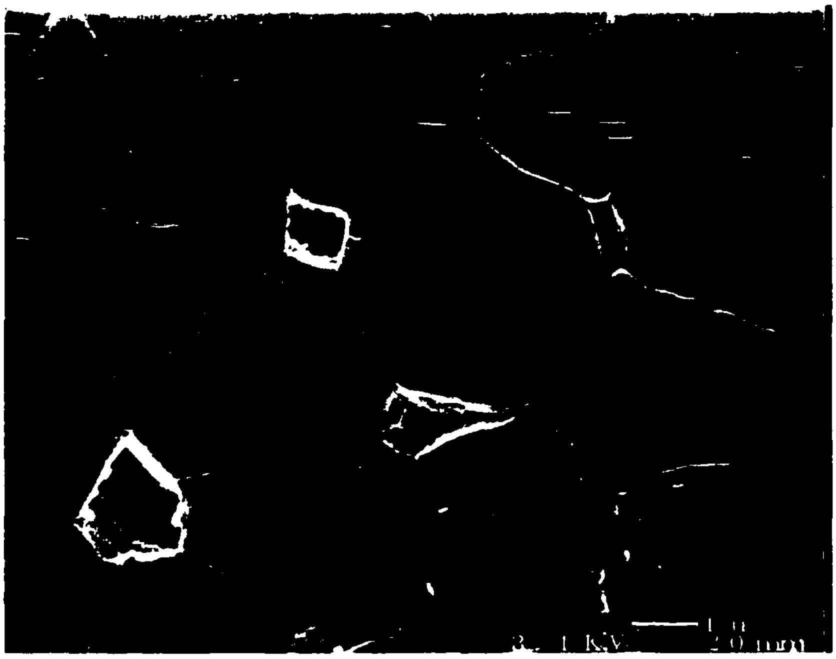

Figure 6. 19 4000 N loading produced only marginal amounts of damage within the high shear sub-surface region of AA5-5. Cracking could be observed within grains (arrow, A) and some cracking was suspected elsewhere (arrows, B).

Figure 6. 20 AA5-5G sample after extreme loading. Grain rearrangement and pore collapse were evident. Grain fracture was also seen (A). Microtwinning may have occurred in some of the grains (B).

6.2.4.3 Pre-Indentation and Post-Indentation (PPI)

This section will illustrate the effect of a pre- and post-indentation investigation into the sub-surface contact damage in the porous alumina systems. The details of the sample preparation were outlined in Chapter 4. One of the AA5-5G specimens was carefully cleaned and imaged in the SEM to sufficiently map out the area of anticipated damage. After imaging, the sample was reassembled and an 1100 N load was applied with a 3.18 mm radius indenter (~6 GPa). As Fig. 4.9 showed, the indent was perfectly placed at the interface and a ring crack is observed outside the area of contact.

The maximum shear region beneath the indenter was estimated before testing, based on prior indentation results. Using a FEG SEM[‡] the estimated region of maximum shear stress was mapped out in a tiling pattern with captured digital images from the microscope. The tiling began in a centralized location near the Vicker's indenter locator mark and proceeded outward to cover an area slightly larger than the estimated diameter of the contact dimension between the indenter and substrate for a load just above the yield conditions for the material (Fig 6.21(a)). A series of higher magnification images was also captured of microstructural features such as pores or regions of glassy pockets (Fig 6.21(a): box). Since the porosity was believed to be the controlling factor in deformation, these images provided the necessary insights to deformation.

The identical region shown in Fig. 6.21(a) is shown in Fig. 6.21(b) after the application of the Hertzian indent. The Vickers locating indent is clearly seen at the top of the image. The damage resulting from this indent was negligible because the applied load was an order of magnitude smaller than the Hertzian indent and the observed damage patters were consistent with other samples lacking a Vickers indent. Using the elastic stress equations described in Chapter 2, stress contours (normalized to P_0) for an indent under an applied load equal to the LPS alumina yield stress, were overlaid onto the mapped microstructure (Fig. 6.21(b)). Accordingly, it was shown that the high magnification images came from the region of maximum shear stress.

The high magnification image of Fig. 6.22(a) shows a cluster of large glassy pockets taken from within the maximum shear stress region before loading. After the application of the Hertzian indent, the same area revealed no observable damage (Fig. 6.22(b)). In the same region, another porous area, with several large glassy pockets nearby, was examined (Fig. 6.23(a)). In this case, intergranular cracking (arrows) was observed and proceeded, in particular, through the large glassy pocket in the upper-right hand portion of the image after the loading. Note that the majority of the surrounding grains were undamaged.

[‡] JEOL 6300F, field emmission gun operated at 3.1 kV with uncoated specimens.

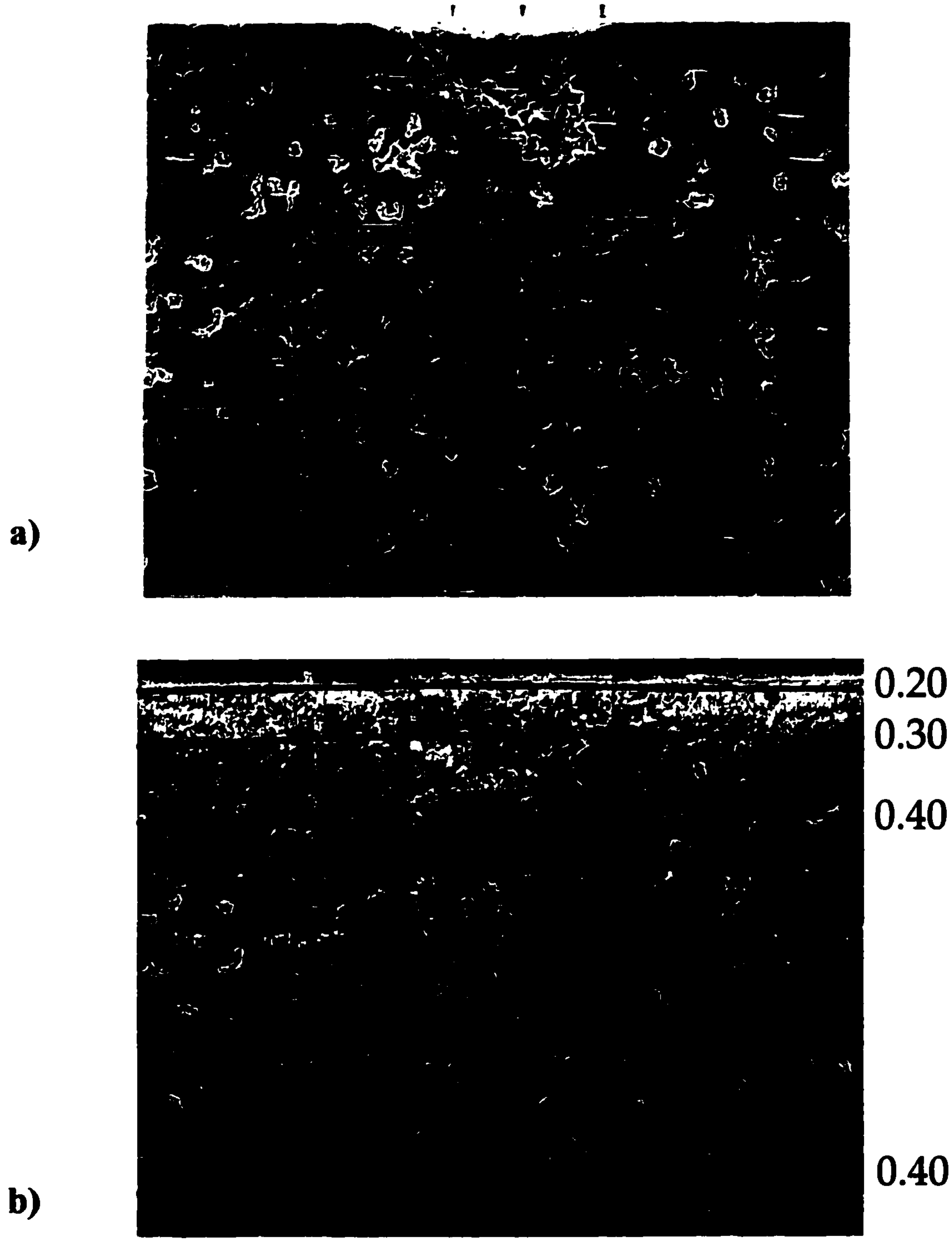

Figure 6. 21 Pre- and post-indentation results of AA5-5G. Multiple SEM images mapped out the indentation region around the Vickers indent (top of picture). After loading, shear stress contours, normalized to P_o, showed that the subsequent high magnification images were taken from within the region of maximum shear.

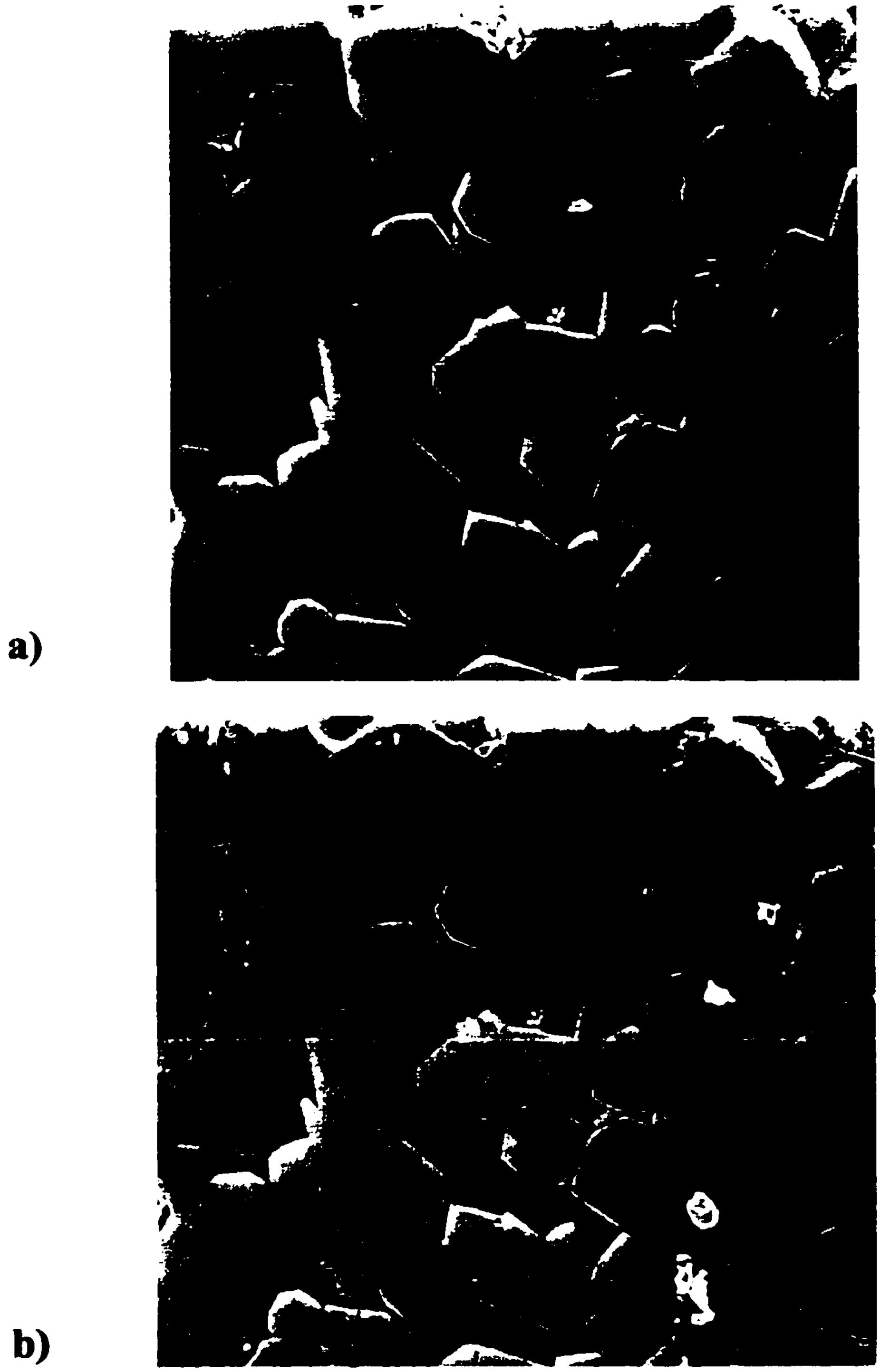

Figure 6. 22 High magnification region from the maximum shear zone beneath the indenter (AA5-5G). Several large glassy pockets are shown before indentation (a) and after indentation (b) undamaged from the applied load.

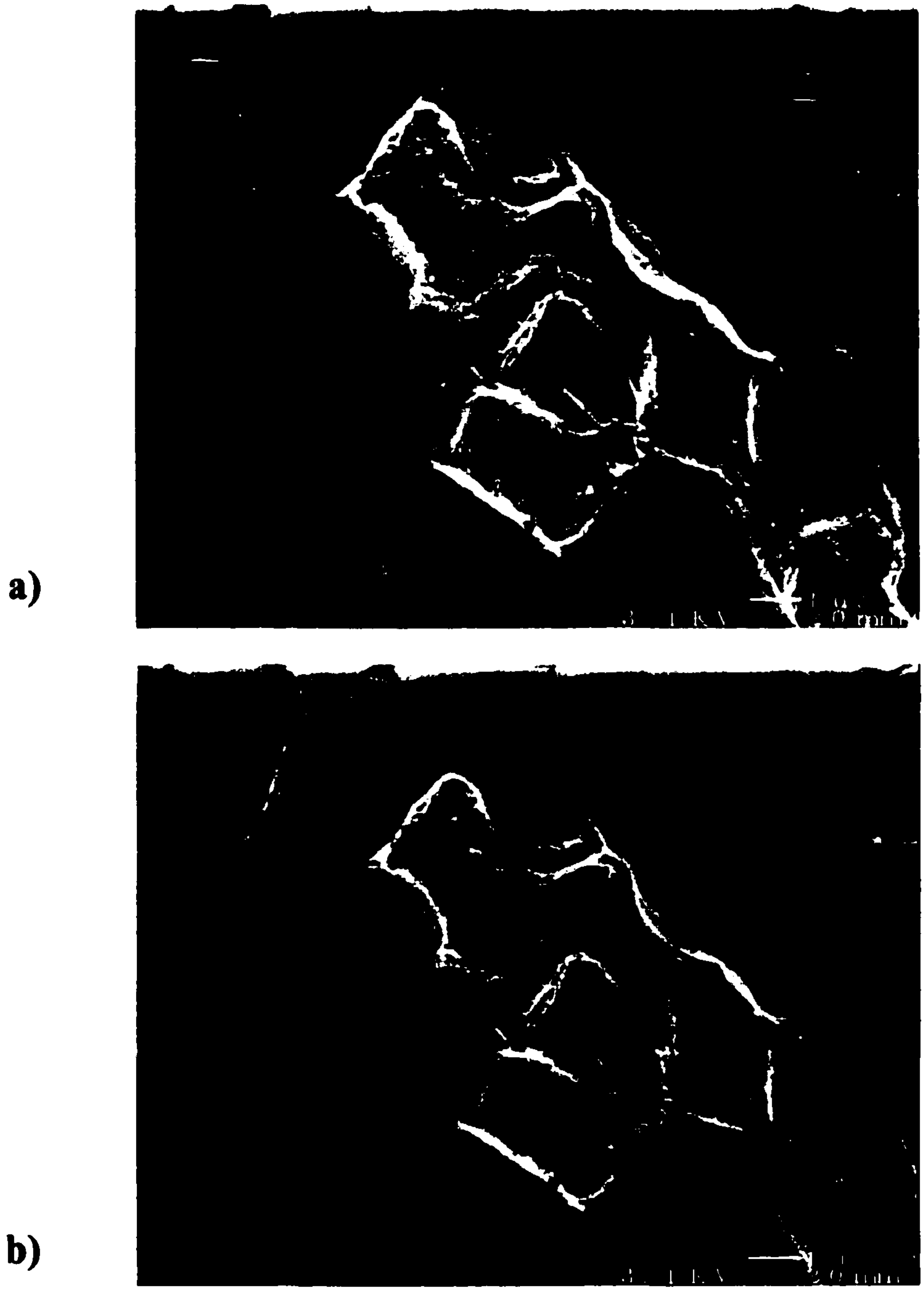

Figure 6. 23 A pore cluster, located in a region indicated with a box in Fig. 6.21(a), revealed the intergranular cracking (arrows) and the fracture proceeding through large glassy pockets (upper right). (a) before loading and (b) after loading.

Figure 6. 24 Several pores with glassy pockets nearby, before loading (AA5-5G). Acquired from the high shear region on the opposite sample face shown in Fig. 6.21.

Figure 6. 25 After loading slightly above the yield stress, fracture proceeded along grain boundaries (arrows) and through the glass pocket near the large pore. Fracture at top of image may be linked to the large pore in the center of the picture or may be associated with a pore beneath the image plane.

Examining another porous area within the high-shear zone (Fig. 6.24) revealed isolated pores surrounded by several glassy pockets. After loading, Fig. 6.25, intergranular fracture was unmistakable. Moreover, intergranular fracture was observed almost exclusively in the vicinity of the pores: surrounding dense regions remained undamaged. Similarly, the grains themselves revealed little evidence of damage. The top of the image shows what appears to be an isolated crack. This crack may be connected to the large pore found lower in the image or it may be associated with a pore beneath the plane of the image. The implications of this fracture behavior will be discussed below.

6.2.5 Geological Testing

The results of the tests performed at Brown University on AA5-5G material are shown in Fig. 6.26 – 6.28. A right circular cylinder approximately 5 mm x 11 mm was cored from a larger block of material. The sample was sheathed in silver and surrounded in a thick lead jacket. Under triaxial compaction, the sample failed brittlely (Fig. 6.26). Although the SEM image of the microstructure (Fig. 6.27) revealed no damage, it should be noted that the sample was ground into its center and polished so that critical information concerning the fracture behavior could have been obscured. The graph of the differential stress-strain curve terminates at the point of brittle failure. Despite the fact that fine microstructural damage may have been obscured by polishing, the likelihood of widespread distributed damage is unlikely given the large macrofault observed in Fig. 6.26 and the abrupt termination of the differential stress-strain curve.

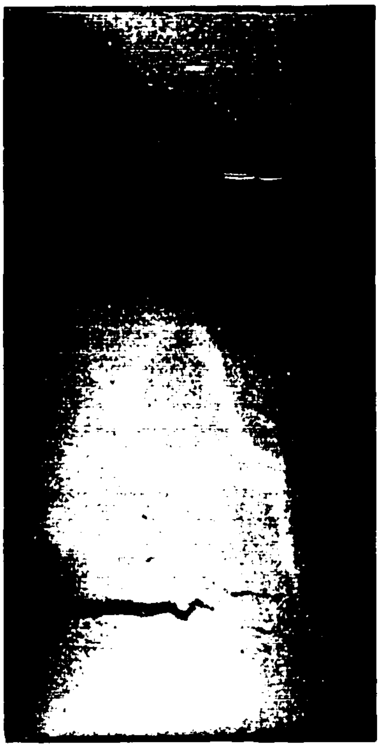

Figure 6. 26 Geological testing of AA5-5G sample. Sample failed brittlely and the large macrofault can be seen originating from the top left of the image. Compare with results outlined in Chapter 2.

Figure 6. 27 High magnification image of center region in the geological specimen. Little evidence suggests any microfracture occurred, however polishing may have obscured finer damage.

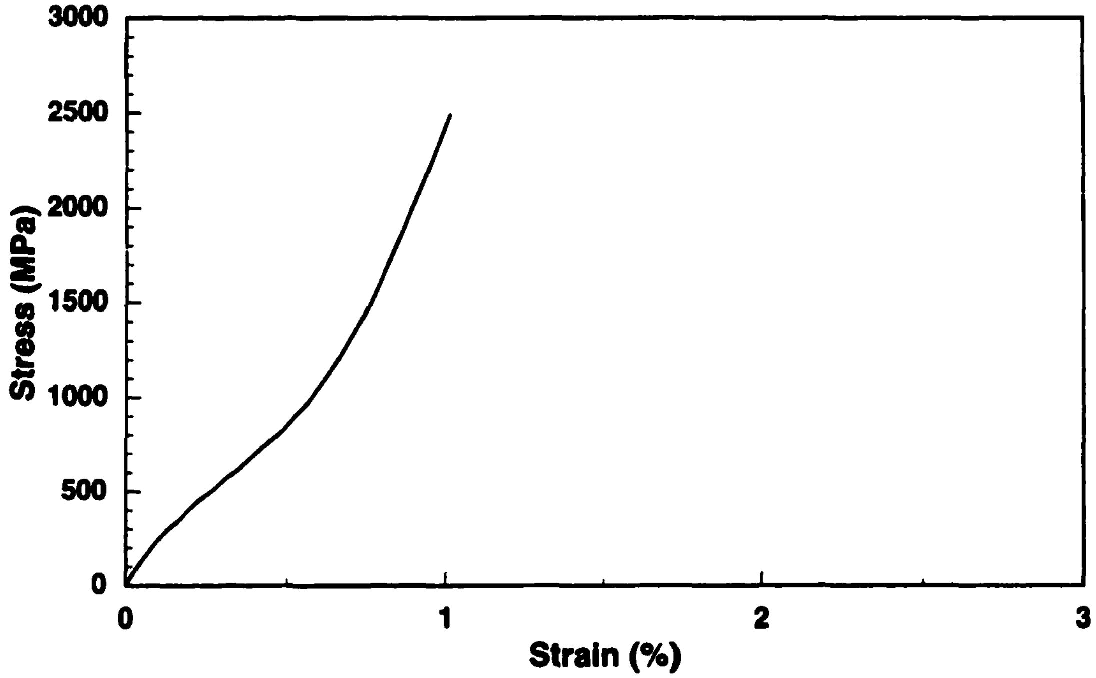

Figure 6. 28 Differential stress-strain curve of the test on specimen shown in Fig. 6.26. Although not perfectly linear, the curve represents elastic behavior that terminated abruptly due to brittle failure.

6.3 Discussion

6.3.1 Macroscopic Indentation Behavior

The results from Chapter 5 suggested that porosity, glass phase, and grain size contributed to the observed quasi-ductility in the AD96R material. Laboratory produced LPS and pure alumina had a fine (<10 μm) and much narrower grain size that eliminated the contributions from twin-faulting. The results in this chapter directly address the role of porosity and the glass phase at the grain boundary in the development of sub-surface deformation under Hertzian contact. In particular, direct measurements were made from the indented surface and observations of the resultant damage.

Johnson (1985) showed the residual indentation depth in metals to approach the penetration depth of the loaded indenter in the limit of full plasticity. Johnson's work was based on the expanding cavity model of Hill (1950) and compared favorably to the FEM investigation of Hardy (1971). In general, therefore, one may attribute an increased residual indentation depth with increased material plasticity or in this case, quasi-ductility.

Increasing indentation depth with porosity was observed for both the pure and LPS alumina in Fig. 6.15. As the porosity increased in the pure alumina samples, the ductile response likewise increased. A residual impression did not exist for fully dense fine-grained alumina[*]; a purely brittle response being observed instead. This result is in perfect agreement with the findings of Guiberteau (1994) mentioned previously. The observed increase in residual depth nearly doubled for the LPS alumina at similar porosity levels under a constant load (800 N) and indenter radius (1.59 mm). This suggests that porosity was essential in the development of quasi-ductility, but the glass phase enhanced the process. Removing the porosity in LPS alumina (A50-0G) also removed the quasi-ductile response at stress levels as high as 10 GPa.

Anomalous indentation behavior occurred in the 5wt% glass containing alumina with 5% porosity (A50-5G): no quasi-ductility occurred under a load of 800 N with a 1.59 mm indenter. The A50-5G alumina had a sub-micron starting particle size with correspondingly smaller pore size, an indication that pore size *and* porosity level controlled the initiation of quasi-ductility. Similarly, the A50-8 sample also had sub-

---

[*] This sample is not listed in Table 6.1 because it was made by another student. Microstructural analysis revealed a 2-3 micron grain size and the sample was fully dense.

micron particle and pore size and exhibited distinct brittle characteristics under Hertzian contact before developing quasi-ductile character. The surface indentation, Fig. 6.11 of A50-8 showed the classic ring-cracking at loads near the yield stress. Sub-surface views, Fig. 6.18, also confirmed the lack of quasi-ductility. Increasing the load on the sample created a significant residual impression (Table 6.2). In the A50-8 sample, it was very clear that cone-cracking occurred before the quasi-ductile response. The same was true for the A50-5G sample (Fig. 6.12), although the material was not loaded to a point where quasi-ductility became prominent. This behavior can be understood in terms of the stress concentrating effect of porosity and will be discussed further in Chapter 7.

Stress-strain curves, although not sensitive to small changes in material response to indentation, support the results observed from the profilometer. The commercial and lab produced LPS alumina (AA5-5G) had a slightly larger fall-off from the linear elastic Hertzian behavior than the pure alumina (AA5-5) with a similar porosity level. This trend, coupled with that of the residual depth measured by the profilometer, where the LPS alumina produced a deeper residual impression for equivalent porosity, again indicated that both glass and porosity combined to enhance quasi-ductility. At an extreme level, the results of Latella (Fig. 5.10) showed a visual change in the sample for an increase in quasi-ductility as porosity was increased: deeper residual impression and larger sub-surface quasi-ductile response (Johnson, 1985). The corresponding stress-strain behavior, shown in Fig. 6.2, revealed an increased fall-off from linear stress-strain behavior, consistent with our observations.

6.3.2 Microscopic Indentation Behavior

Macroscopic Hertzian contact damage in the laboratory-produced alumina confirmed the interrelationship of a glass phase and porosity for increasing the quasi-ductile response observed in AD96R. Microscopic observations directly addressed these variables and showed that the glass acted as a weak path for short crack propagation, initiated by stress concentrations around the pore.

6.3.2.1 Effect of Grain Size

The role of grain size was illustrated in Chapter 2 as controlling the critical twin-faulting behavior or by providing a weak interface for shear faulting. The occurrence of faulting was clearly associated with an increased fall-off from the linear elastic Hertzian stress behavior in alumina (Guiberteau, 1994). Based on sub-surface observations and acoustic emission measurements, a critical grain size for shear faulting was estimated at 20 microns. It should be noted, however, that the reduction of shear faulting below the 20 micron threshold was gradual and thus the transition point should not be considered abrupt. The AA5-5G closely resembled the character of the commercial material and had an average grain size of 5 microns, a porosity level of 5 percent and 10 volume percent liquid phase. The 5 micron grain size would therefore not be expected to contribute to quasi-ductility based on a twin fault mechanism during the loading cycle. There is also an estimated grain size dependency of wing crack growth on the unloading cycle (Lawn, 1994(b)). The tendency is for larger alumina grains to have a larger influence on crack growth during unloading from the peak indentation stress. Although the effect of porosity on subsequent crack growth during unloading has yet to be investigated, the grain size of

5 microns in AA5-5G was unlikely to have contributed to the observed crack lengths emanating from the pores in the sub-surface images.

Grain size did show an indirect effect on the quasi-ductile deformation of the alumina samples investigated. In particular, with A50-0G and A50-8, the initiation of quasi-ductility was shifted to a higher stress level. The reason for the shift was likely a result of the decrease in the average pore size within the matrix, where the sub-micron starting particle size produced sub-micron pores between grains. The role of pore size will be considered analytically in Chapter 7. Experimentally, one concludes that the grain size did not contribute directly to the quasi-ductile damage observed in this investigation through known mechanisms.

6.3.2.2 Effect of Porosity

Figs. 6.17 to 6.20 depict the differences in general deformation character between glassy alumina and pure alumina with similar porosity. For comparable indentation stresses, the LPS alumina revealed significantly more damage to the microstructure in the form of cracks, grain rearrangement, and even grain fracture. The microstructure results correlated directly to the profilometer results (Fig. 6.14), and the indentation stress-strain behavior in this study and with the work of Latella (1997). The PPI results (Fig. 6.21 to 6.24) proved unambiguously the preferential fracture behavior of cracks proceeding through the grain boundary regions where the glass phase is present. Large glassy pockets were clearly fractured through (Fig. 6.22 and 6.24) and had originated from porosity. Furthermore, the dense regions of the microstructure remained unfractured. This corresponded exactly to the observation of fully dense LPS alumina (A50-0G) which revealed no quasi-ductile behavior.

Although little evidence in the literature links porosity to quasi-ductility under Hertzian contact, there have been many investigations in the geomechanics community linking porosity to macroscopically observed ductility under triaxial compression (Menendez, 1996; Renner & Rummel, 1996; Wong, 1990; Hirth & Tullis, 1989; Mogi, 1966). Mechanistically, work in sedimentary rocks, such as porous sandstone, have shown that intergranular fracture predominated during initial deformation (Scott & Nielson, 1991; Hirth & Tullis, 1989; Hadizadeh & Rutter, 1983, 1982) and that cracking initiated at grain boundaries from pore spaces in quartzite (Hadizadeh & Rutter, 1983, 1982) as shown in Fig. 6.30. These findings correlate with the observations of the PPI investigation of alumina where, just past the yield stress, cracks formed along grain boundary paths emanating from porous regions. Kubicki (1996) provided further support, showing cracks to initiate from pores in powder metallurgy samples under compressive fatigue. Additionally, Nash (1983) suggested silica impurities at grain boundaries in compressive tests of D997 alumina caused intergranular fracture but did not confirm it experimentally. The short, intergranular cracking observed under indentation and compressive tests in geomechanics can differ substantially from typical long crack behavior in brittle materials.

Long-crack and short-crack toughness behavior is noticeably different when one observes the fracture surface of samples broken under biaxial flexure conditions. An important distinction needs to be made concerning the failure of brittle samples under

Figure 6. 29 Grain boundary cracking initiating from pore spaces under compressive loading in quartzite prior to pore collapse. After Rutter and Hadizadeh (1983, 1982).

compression and tension. Many investigations have addressed the issue of porosity on mechanical properties, especially strength (Rice, 1998). The work for tensile fracture is voluminous and differs from the multiaxial compression discussed here in several important ways. The most significant relates to the issue of catastrophic failure. Brittle fracture is a highly stochastic process whereby ultimate failure occurs from a single strength-limiting flaw. Exceeding the material fracture toughness causes the crack to propagate without limit, barring some well-known instances of increasing toughness with crack length (Lawn, 1993; A. Evans, 1990; Evans & Cannon, 1986). By contrast, multiaxial compressive loading of brittle materials involves stable crack growth or growth of cracks that terminate at a finite length (Isida & Nemat-Nasser, 1987; Sammis

& Ashby, 1986). Pre-existing cracks, weak interfaces, or pores can act as origins of tensile stress fields under compression. The ensuing crack growth proceeds until it reaches a region of compressive stress. Although coalescence can lead to instabilities under geological testing conditions, the same cannot be said for the indentation test. The highly localized stress condition during testing of a sample of reasonably large size simulates a theoretically infinite sample. There does not exist a condition whereby a yield criterion can be exceeded causing the indenter to propagate without limit into the sample. Therefore, indentation tests, and in particular the blunt indentation test, force a condition of distributed damage to develop within the material. In reality, this is challenged by the ability to acquire a sufficiently hard indenter material to resist deformation itself.

The difference between long crack and short crack toughness under compressive and tensile loading was revealed in Fig. 6.30 and 6.31. A LPS alumina fracture surface, showing prevailing intragranular fracture with only occasional intergranular fracture (arrows) was in direct contrast with the observations of sub-surface microfracture that proceeded almost exclusively through grain boundary regions (Fig. 6.23 to 6.25). However, the hot-pressed pure alumina indicated the reverse behavior: fracture was intergranular with occasional transgranular behavior (arrows). In the high-shear damage zone beneath the Hertzian indenter (Fig. 6.19), the cracking occurred through the grains and through some grain boundary regions. The nature of sub-surface brittle fracture and that of conventional brittle fracture phenomena is discussed in Chapter 7.

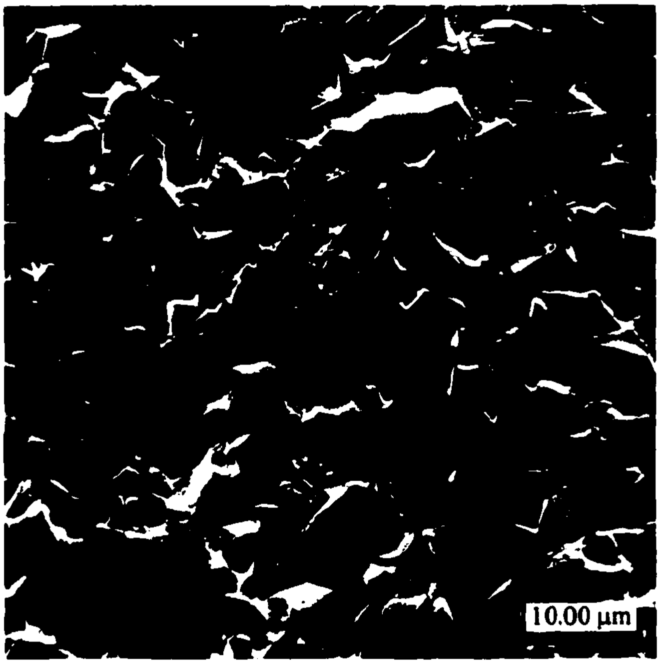

Figure 6. 30 Fracture surface of LPS alumina showing predominately intragranular fracture. Small regions of intergranular fracture were seen (arrows). Porosity (~3%) was also observed (circles). This far-field tensile driven long-crack behavior was in contrast to the far-field compressive-driven short-crack fracture paths that were predominately *intergranular*.

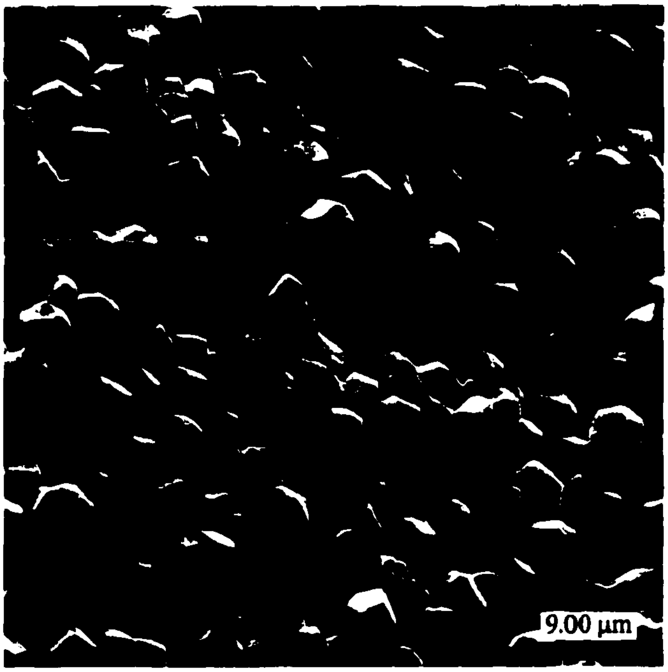

Figure 6. 31 Fracture surface of hot-pressed pure alumina with 5% porosity. Far-field tensile driven fracture is predominately intergranular. Some regions of intragranular fracture were found (arrows). Compare with Fig. 6.30.

6.3.2.3 Role of Second Phase

Up to now, the results of this investigation have established the presence of porosity as a necessity for producing quasi-ductility. Furthermore, the glass phase has been shown to enhance the deformation process by providing a weak path for crack propagation in the vicinity of stress concentrating pores. Notably, the influence of a second phase at the grain boundary on the compressive damage behavior is not unique to LPS alumina. For instance, the cementation phase in porous sandstone was shown to crack preferentially near pore spaces in the investigation of Rutter and Hadizadeh (1991). Similarly, intergranular phases in other quartzites showed a tendency to cause intergranular cracking from porosity (Wong, 1997; Menendez, 1996) under multiaxial compressive stress. Furthermore, Bruno & Nelson (1991) found that in sedimentary rock the mechanical properties of the intergranular phase were more important than the actual strength of the grains themselves to determine the macroscopic mechanical behavior. Interestingly, Bruno & Nelson (1991) also found that an increase in the second phase content increased the aggregate strength. Presumably, this is because of the cushioning effect simulated recently by Wong and Wu (1995) where the tensile stress at the grain contacts was reduced as the thickness of the cementing phase between grains increased. An increase of glass content in LPS alumina would, as a consequence of thermodynamic equilibrium, cause more glassy pockets at triple points (Raj, 1981) and maintain a reasonably constant intergranular thickness (Brada & Clarke, 1997; Clarke, 1987). Therefore, an increase in mechanical strength with glass content would be less predominant. In fact, the opposite may be true depending on the crystallinity of the glass phase as will be discussed next.

Glass is susceptible to large residual stresses owing to thermal expansion anisotropy between crystalline and glassy phases. Therefore, it is important to consider the effect that the grain boundary glass phase could have on the microstructural deformation. For instance, Zang (1993) found the presence of grain boundary stresses, determined by FEM analysis in feldspar-quartz systems, led to an increase in the microcracking of the system. Twigg (1996) also investigated the effect of MgO and CaO glass compositions on grain boundary stresses in LPS alumina, revealing tensile and compressive influences, respectively. The glass phase considered by Twigg (1996), which increased the tensile forces on the grain boundary, was a $MgO\text{-}Al_2O_3\text{-}SiO_2$ (MAS) glass. The clamping forces were caused by glass at the triple points rather than within the grain boundaries themselves. $CaO\text{-}Al_2O_3\text{-}SiO_2$ (CAS) glass caused a compressive stress by comparison. The LPS alumina in this investigation used MgO at around 1wt% compared with the 8wt% used by Twigg (1996) and furthermore, it was added to CAS glass. Therefore, the MgO addition is not likely to have caused significant changes in the mechanical properties or observed cracking behavior.

Powel-Dogan and Heuer (1990(b)(c)) found little change in room temperature mechanical properties resulting from the degree of crystallinity in the glassy phase of AD96 materials. Powel-Dogan and Heuer (1990(c)) observed that high calcia boundaries fractured intergranularly and high magnesia boundaries were primarily transgranular. Padture and Chan (1991) found little change in fracture properties in laboratory produced LPS alumina with a 28 vol% of anorthite after devitrification of the boundary glass. Padture postulated that the large amount of liquid phase allowed for stress relaxation by glass flow during recrystallization and therefore the residual stress in the glass phase was low. Padture and Chan (1992), however, did find a rising toughness response for a fully recrystallized anorthite (1 vol%) resulting from clamping forces on elongated grains.

Although it was not confirmed through transmission electron microscopy (TEM), the LPS alumina in this study was not highly recrystallized because the sample was subjected to rapid cooling (10°/min) and did not get annealed: Padture and Chan (1992) annealed their samples for 25h at 1200C. Moreover, at 10vol% glass, there exists a likelihood of a stress relaxation as mentioned above (Padture & Chan, 1991). Finally, what little compressive stress might occur by slight recrystallization during cooling could be offset by the small contribution from the 1wt% MgO addition for reasons discussed earlier.

6.3.3 Quasi-Ductile Mechanism

The mechanisms for quasi-ductility in fully dense advanced ceramics as well as numerous geological materials were discussed earlier. In this investigation, reference to the initiation of quasi-ductility in alumina refers to homogeneously distributed microfracture by twin faulting, which very little was observed or – as discussed below – from porosity in the microstructure. Recall that in geomaterials, increasing the porosity changed the deformation character from brittle to ductile with the application of increasing confining pressures. Mechanistically, pores collapsed, grains fractured and grain fragments underwent rearrangement and consolidation under hydrostatic and deviatoric stresses: the majority of consolidation occurring under the deviatoric stresses (Wong, 1997; Menendez, 1996; Wong, 1990). However, the action of the hydrostatic stresses had a greater effect at higher porosity (Menendez, 1996).

Rutter and Hadizedah (1991) indicated that the availability of collapsible pore volume was ultimately responsible for cataclastic flow up to the point where net dilatation was dominant. This result compares favorably with our indentation study wherc the available pore volume was reduced by ~10% (AA5-5G) to ~25% (AD96R).[†] Though dilatancy is an important issue in brittle consolidation, especially with regard to instability phenomena (Rudnicki and Rice, 1975), its effects – if any – under Hertzian contact have yet to be reported.

With regard to compressive stresses, Hirth and Tullis (1989) showed how the transition from tensile dominated fracture at pore spaces changed to compressive dominated fracture as the differential stress was increased. This correlated with the macroscopically observed change from brittle to ductile behavior in the quartzite. Hirth and Tullis (1989) also found that at low strain, many grain boundary cracks were observed, while pores remained largely in tact. Higher strain resulted in pore collapse and more importantly, intragranular fracture or communition of grains. By comparison, the LPS alumina (AA5-5G) displayed similar behavior initially: grain boundary cracks ensued at low pressure. Higher pressures did produce some pore collapse and grain rearrangement, but there was not widespread axial splitting of the grains, although some grains fractured. The discrepancy may lie in the overall difference in applied strain. The Hertzian samples, on average, deformed by a linear equivalent 3% strain (using Eq. 2.27). Geological tests often deform samples up to 30% axial strain, far beyond that imposed by a Hertzian indenter and past the limit of a Vickers indenter, 8%. Furthermore, the confining pressure to axial pressure ratio remained constant under the Hertzian indenter,

---

[†] Based on a hemispherical volume defined by the contact radius, a.

as opposed to the geological tests that start with a hydrostatic load and then increase the axial load. This ratio is key in understanding the deformation character of brittle materials and will be addressed further in the next chapter.

Besides the differential stress, the locations and sizes of pores in geomaterials were significant with respect to the fracture mechanisms. For instance, in quartzite, the presence of a cementing phase at the grain boundary increased the likelihood of fracture through the grain boundary (Wong, 1997; Menendez, 1996; Rutter and Hadizedah, 1991; Hadizedah & Rutter, 1983, 1982). By comparison, the pores in the LPS alumina were located at the grain boundaries and triple points due to the MgO additions. The results of this chapter clearly show intergranular fracture from pore origins, suggesting that the pore and grain boundary phase play a similar role in the development of macroscopic quasi-ductility as in the quartzite.

The effect of the size of a pore under compression was demonstrated by Kubicki (1996) to decrease the strength in brittle metals under fatigue. Menendez (1996) also found that large pores collapse first in Berea sandstone. The pore size distributions were not measured directly on the LPS alumina samples in this investigation, however, careful measurements on identically processed samples revealed an average pore size of around 4 microns (Dong, 1997). Measurements of the hot pressed pure alumina used in this study revealed a pore size between 1-2 microns. The pore size of the A50 sample series was not measured, but judging from micrographs the average pore size is clearly sub-micron (excluding the large pores resulting from agglomeration). Specific issues dealing with pore size, shape, and interaction will be dealt with in detail in the next chapter.

Another concern, with respect to quasi-ductility, was that of crystalline plasticity. Ductility in dense alumina under ambient conditions can occur by prismatic slip under the action of a Vickers indenter (Chan and Lawn, 1988). The stresses under the Vickers indenter, nevertheless, were far in excess of those encountered under the Hertzian indentation of this investigation. Still, a blunt indenter with a sufficiently large load could eventually achieve a similar stress level. Adler (1994) showed this under extreme loading of dense alumina[‡] with a blunt diamond indenter, causing the residual impression shown in Fig. 6.32. Furthermore, Bridgeman (1952) tested sapphire under a high compressive stress and found that with a 2.5 GPa confining pressure the sapphire failed (by twinning and slip) under a 5 GPa axial load for a crystal orientation of 90° to the highest compressive axis and 9 GPa when the angle was 0°. Bridgeman's work was performed under ambient conditions, while Castaing (1981) found that the stress was lowered to around 2.5 GPa axial stress (1.5 GPa confining) at 800°C for an orientation of 0°.

Examining the SEM images of Fig. 6.22 to 6.25, there was little evidence suggesting deformation occurred to the grains themselves near the yield stress, microcracking notwithstanding. Extreme loading (Fig. 6.20) did reveal some grains that may have plastically deformed. However, the fact that the hot pressed LPS material exhibited no observable quasi-ductile response at stress levels as high as 10 GPa indicates that even if crystalline plasticity occurred, it was not significant enough to effect the macroscopic indentation behavior. The initiation of quasi-ductility, therefore, was not attributed to crystalline plasticity under Hertzian contact, based on these observations of sub-surface deformation. However, based on the work of Bridgeman (1952),

---

[‡] Bimodal grain size: <1 and 8 microns. 6400 N with 2 mm radius diamond. Exact density unknown.

microtwinning is a possible mechanism for deformation and ultimately a TEM investigation should be performed before one can definitively state the extent of crystalline plasticity within the grains themselves.

One final note concerns the geological testing of alumina using a standard triaxial configuration. The specimen is shown in cross-section in Fig. 6.26. A brittle shear fault is seen traversing the specimen diagonally. Based on the information given in Chapter 2, that indicates a largely brittle response. The microstructural evidence in Fig. 6.27 did not reveal cracking like that observed under Hertzian contact. Furthermore, the stress-strain curve terminated abruptly at 2.5 GPa, also an indication of brittle behavior. The differential stress that matches the shear stress in beneath the Hertzian indenter is 6.25 –

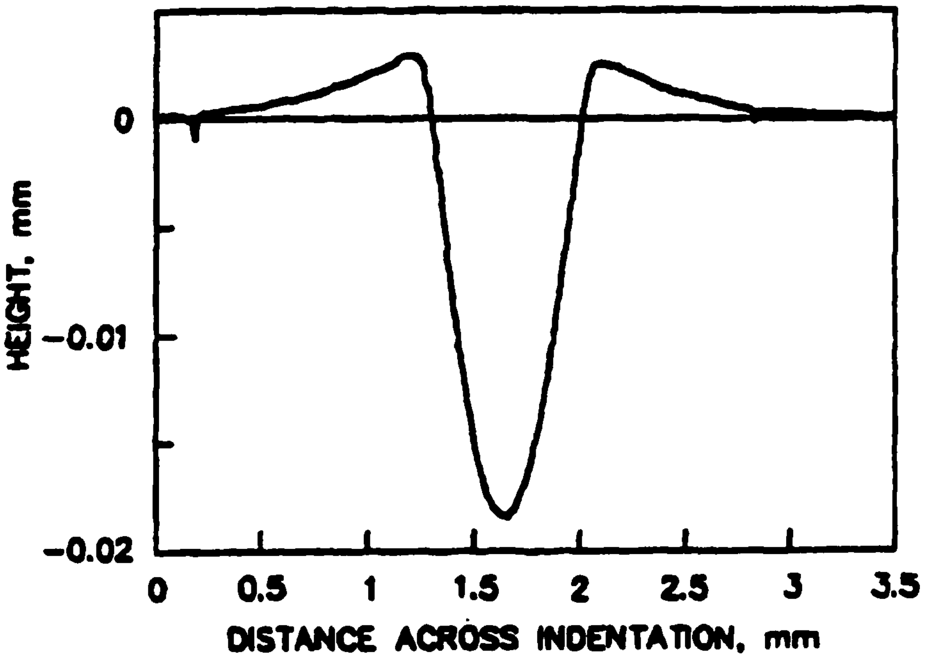

Figure 6. 32 Blunt indentation in alumina under a 6400 N load with a 2 mm radius indenter. Alumina had a bimodal grain size distribution with one mode less that 1 micron and the other at 8 microns. Indentation stress is equal to Vickers hardness value of just under 15 GPa. After Adler (1994).

1.25 GPa or approximately 5 GPa. The reasons for premature failure are varied (Patterson, 1978) and little can be concluded from a single experiment except that under the conditions of the test, no visible evidence of quasi-ductility existed.

6.4 CONCLUSIONS

- The experimental evidence on sub-surface damage in pure and porous LPS alumina revealed that the mechanism for quasi-ductility was directly associated with porosity.
- Fully dense materials, regardless of composition, displayed no quasi-ductile tendency in the absence of granular plasticity indicating it was not the glass phase alone causing quasi-ductility in LPS alumina.
- The presence of a weak grain boundary second phase greatly facilitated intergranular fracture; damage in LPS material was higher and for equivalent porosity.
- Pore size appeared to control the onset of quasi-ductility as observed in sub-micron grained alumina.
- Geomechanical literature showed similar deformation characteristics under multiaxial compressive loading conditions for materials with a weak intergranular phase.
- Considering a pore as a stress concentrator permitted the use of linear elastic fracture mechanics (LEFM) in determining a failure criterion. This is addressed in the next chapter.

7. MICROMECHANICAL MODELING

7.1 Introduction

An analytical understanding of the underlying microscopic mechanisms controlling deformation facilitates predictions of macroscopic indentation behavior. In contrast, quasi-ductile behavior in brittle systems, induced by indentation or similar triaxial compression, relies on distributed microfracture to accommodate increasing stresses. Differentiating between mechanisms of quasi-ductility, therefore, results from the manner in which the fracture process initiates and how the fracture propagates under these stresses. This research, like many prior mechanistic descriptions, focused more on the initiation aspects of damage. Interaction and accumulation of damage, decidedly more complex phenomena, was not suited to a first-approximation understanding from a mechanistic viewpoint. Understanding damage in this system required several areas of consideration. Important issues were: (1) The application of external stress; (2) How the stress was altered by the microstructure; (3) Establishing a criterion for failure. This chapter is dedicated to understanding the pore as a stress concentrating mechanism and using it as a means of making predictions of macroscopic indentation behavior based on the assumption that it was the initiation point for sub-surface damage.

7.2 Finite Element Modeling (FEM) of Porosity

Experimentally, the role of porosity was implicated in controlling the deformation processes. From a mechanics perspective, a pore acts to alter a uniformly applied stress field in an isotropic solid. Furthermore, the effect of multiple pores on the stress concentrations was discussed in Section 2.8. The presence of multiple pores on the stress concentrations around a given pore became the fundamental concern to develop a porosity-based failure condition. The purpose of this chapter is to address the issue of porosity on stress concentrations around the inner surface of a two dimensional hole. A crack initiation criterion was established based on a combination of analytical results and FEM modeling. In particular, the FEM technique elucidated the underlying relationship of the geometric effect of porosity and pore arrangement on stress concentrations. It was discovered that the choice of pore arrangement strongly influenced the behavior of the peak stress around the surface of the hole or sphere. Although the problem was three dimensional, only two dimensions were considered for modeling simplicity. Furthermore, the results of the interaction effect were used to produce a deterministic failure criterion at the microscopic level, linked to the macroscopic indentation stress, thereby allowing simple first-order approximations of damage initiation from microstructural parameters.

As with all modeling, the first step was to establish the assumptions and boundary conditions. The model incorporated orthogonal biaxial compressive stress states where the primary compressive stress was p_1 and the secondary compressive stress was p_2, where $p_1 > p_2$. The solution of the stress distribution around an isolated pore of radius R, was described in Chapter 2. Recall there were no tensile stresses anywhere on the surface of the hole when $p_2 = p_1 / 3$. The stresses p_1 and p_2 were considered remote uniform applied stresses where $p_1 = \sigma_z$ and $p_2 = \sigma_r$ from the Hertz solutions for stress along the loading axis (Eqs. 2.30 and 2.31). At the yield point, the ratio of these stresses was about 5:1 giving a value of $\lambda = 0.2$. A distinct advantage of the Hertzian stress state for this application was that the value of λ remained constant within the elastic regime. As was clearly shown in Fig. 2.6, the Hertzian stress is highly spatially variant. However, for a large indent, on the order of 300 microns, the sub-surface stresses in a 30 micron region containing porosity of 1 micron radius were approximately uniform. The issue of a uniform stress field and its relation to the limits of porosity will be discussed later in this chapter. The material constants used for the solid phase reflected that of the commercial material: E = 303 GPa and $\nu = 0.21$. It should be noted that these values actually reflect a material with 3% porosity but the material constants can be normalized out of the fundamental relationships.

7.2.1 Geometrical Considerations of Porosity

Although an important parameter, the shape of the pores was assumed spherical in the FEM process (again for simplification). Changing the shape of the pore can affect the peak stress value and its distribution (Savin, 1962), but the general character remains. The fluctuations of randomly oriented stress concentrators will have an average value that is represented by a hole in character albeit not necessarily in magnitude. The modeling focused on the spacing and orientation of the pores within the stress field. The stresses were defined in a cylindrical coordinate system with respect to the geometry shown in Fig. 7.1. The applied stresses are labeled (p_1 and p_2 are *not* coordinate directions) and the resulting stress around the hole is given by $\sigma_{\theta\theta}$, σ_{rr}, $\sigma_{r\theta}$ (Eq. 2.40-2.42). In the figure, the peak tensile stress occurred at a θ equal to $\pi / 2$ and $r = R$ with a value of 2.5 GPa for the applied load. A peak compressive stress is found at θ equal to zero and $r = R$ with a value of -17.5 GPa.

In real systems, porosity is positioned randomly and with a distribution of sizes. Holes were assumed monosized and arranged in a simple cubic geometry to facilitate modeling. The issue of aperiodicity will be discussed later. In two dimensions, a simple cubic geometry translated to a square lattice that was infinitely periodic under the applied stresses. To vary porosity, the area fraction of holes per unit area was changed.

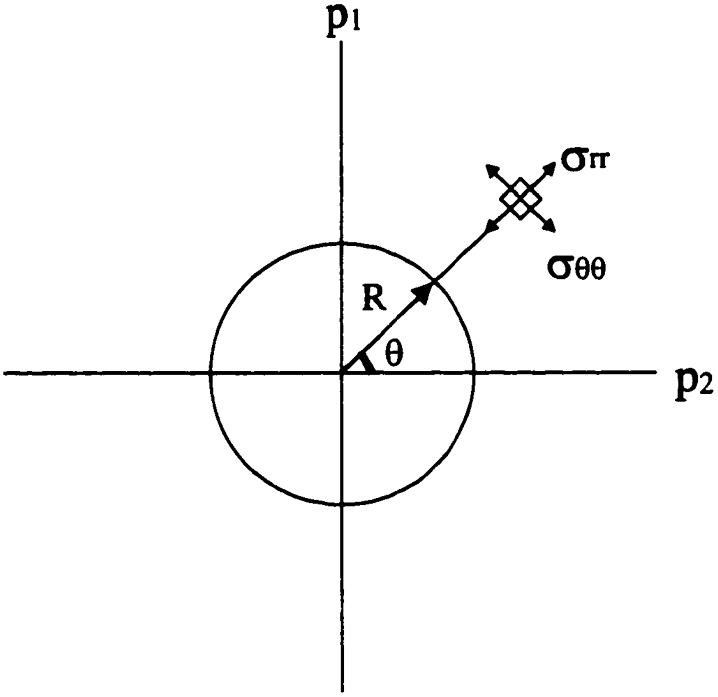

Figure 7. 1 Geometric indication of stress in cylindrical coordinates, with origin at the center of the circle, under a biaxially compressive stress field. Note p_1 and p_2 indicate applied stress directions and are not coordinate axes. When $r = R$ (at the hole surface) the value of the tangential stress, $\sigma_{\theta\theta} = 3p_2 - p_1$ at $\theta = \pi / 2$, is 2.5 GPa and $\sigma_{\theta\theta} = 3p_1 - p_2$ at $\theta = 0$ is -17.5 GPa.

The characteristic length in the system was the center-to-center hole spacing defined by the nearest neighbor distance, 2*N*. The area fraction of the hole per unit area represented the porosity, *P*, so that:

$$A\% = P = \frac{\pi/_4 R^2}{N^2} \tag{7.1}$$

where R was the radius of the hole. After normalizing the nearest neighbor distance to the hole radius, Eq. 7.1 was rewritten as:

$$P = \frac{\pi R^2}{4(nR)^2} = \frac{\pi}{4n^2} \tag{7.2}$$

or rearranged to:

$$n = \sqrt{\frac{\pi}{4P}} \tag{7.3}$$

where *n* represents the normalized interpore spacing. The porosity range of interest in this investigation existed in the dilute concentrations from one to ten percent and the values of *n* for the porosity levels tested are given in Table 7.1. The radius of the hole used in the models was 1 micron and therefore, the numbers listed in Table 7.1 are representative of the actual spacing in microns.

Table 7. 1 Values of the normalized nearest neighbor distance for different porosity.

P	*n*
0.01	8.86
0.05	3.96
0.10	2.80

Two different lattice orientations were chosen for modeling and were indexed according to the direction of the pore nearest neighbor distance (2*N*) as shown in Fig. 7.2.

The nearest neighbor direction (NND) was either aligned parallel (Fig. 7.2(a)) or at 45° to the applied stresses (Fig. 7.2(b)). In each case, four of the lattice mirror planes coincided with the four orthogonal boundaries that defined the model.

Intermediate lattice rotations could not be represented because no orthogonal mirror planes coincided with the model boundaries for other orientations. Larger models could approximate the effect of other rotations but this was not a feasible solution given the large number of models needed to provide an understanding of bulk behavior.

The remaining geometric issue addressed was that of non-periodicity of the pore spacing. Though not truly randomized, shifting the central pore with respect to the surrounding pores in the model created an aperiodicity to reflect the influence of disorder. The center pore was moved along a path coincident with the nearest neighbor direction and a path 45° to that direction. These results and those corresponding to the models just described are displayed in Sec. 7.2. Although important and not directly modeled, the issue of pore size distribution will be discussed briefly at the end of the chapter.

7.2.2 Defining the Model Boundaries

Modeling an infinite array of pores was accomplished with the use of periodic boundary conditions (PBC). A common modeling technique, PBC permitted the determination of bulk behavior using only a small representation of the bulk. As described above, pores were constrained to a simple cubic lattice. One benefit of

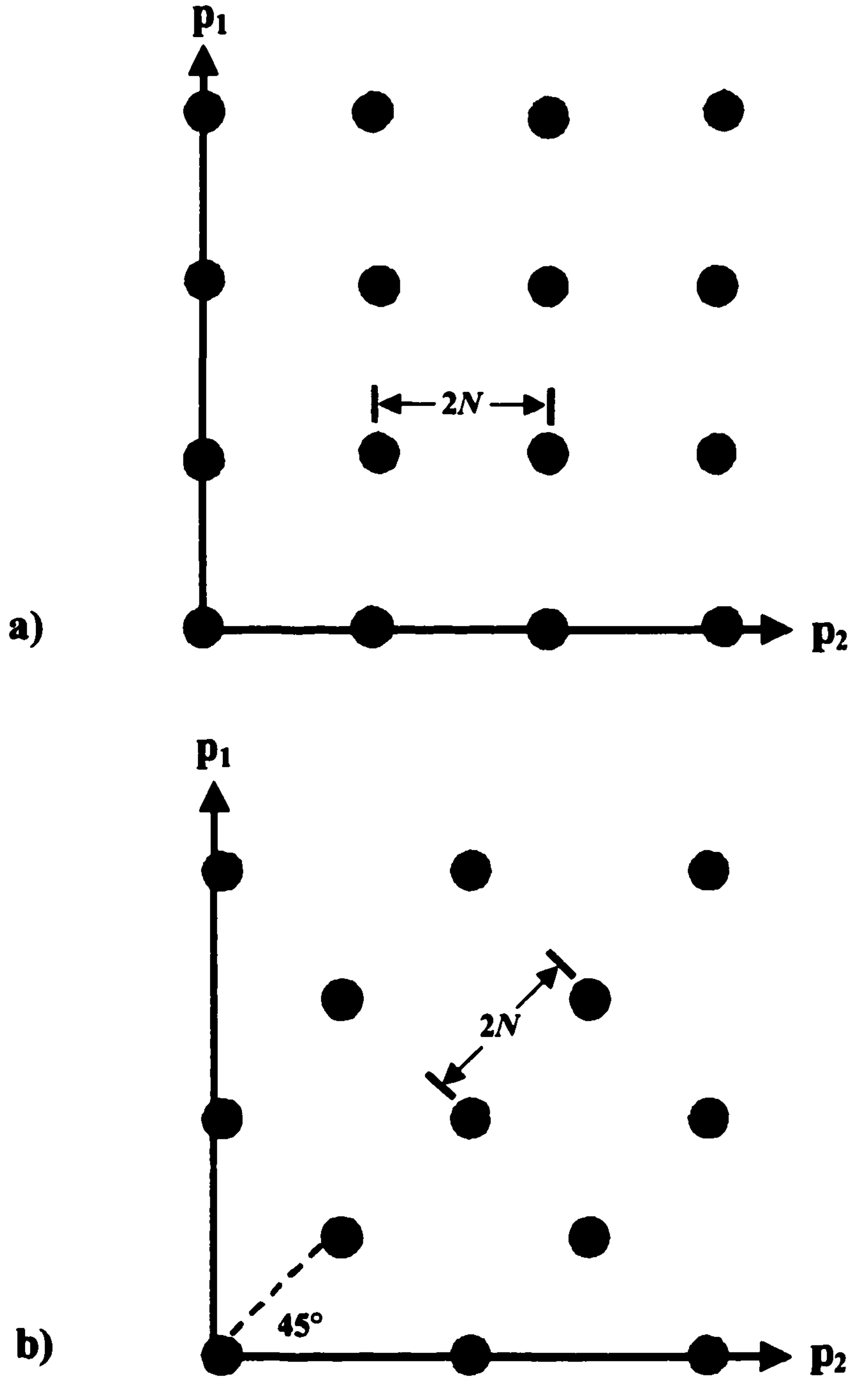

Figure 7. 2 (a) Orthogonal pore lattice indexed with the nearest neighbor distance (NND) parallel to the applied stress directions. (b) Tilted pore lattice showing the 45° tilting of the lattice with respect to the applied stress directions. Notice the coincidence of mirror planes with the stress axes in both cases.

using a simple cubic lattice was the large amount of symmetry in that system. For example, in two dimensions there exist four mirror planes – two along the NNDs and two at 45° to the NNDs – which were used to outline the geometric boundaries of the models. The mirror planes occurred in two orthogonal sets displaced by a $\pi / 4$ rotation. The physical boundaries of the model were arranged to coincide with the mirror planes of symmetry. With this scheme, the smallest repeatable unit cell would consist of an isosceles triangle with the center of a one-eighth pore coincident with a vertex on either side of the symmetry plane (Fig. 7.3(a)). Although a triangular quarter-pore model could define a unit cell, the FEM software placed restrictions on how to implement PBCs. A square quarter-pore model (SQP) was the smallest possible model and was further restricted to representing the orthogonal orientation, Fig. 7.3(a). The reason a triangular model could not be used nor could the square quarter pore model represent the tilted lattice is shown in Fig 7.4. The PBC require all points of a selected boundary to move in unison an unspecified amount with respect to the normal to the boundary (for the square models considered here). Fig. 7.4(a) shows a square model with a selected unit volume before and after deformation. The diagonal of the unit volume clearly violates the displacement requirements of the PBC. Fig. 7.4(b) shows the necessary rotation to represent the tilted lattice with a square model. Note that the external loading, using Mohr's circle, could be adjusted to represent the appropriate loading conditions. However, subsequent boundary motion would violate the PBCs as in 7.4(a). The smallest model to represent the tilted pore arrangement is shown in Fig. 7.3(b). Because the size of the model slightly affected the calculated stresses, the geometry

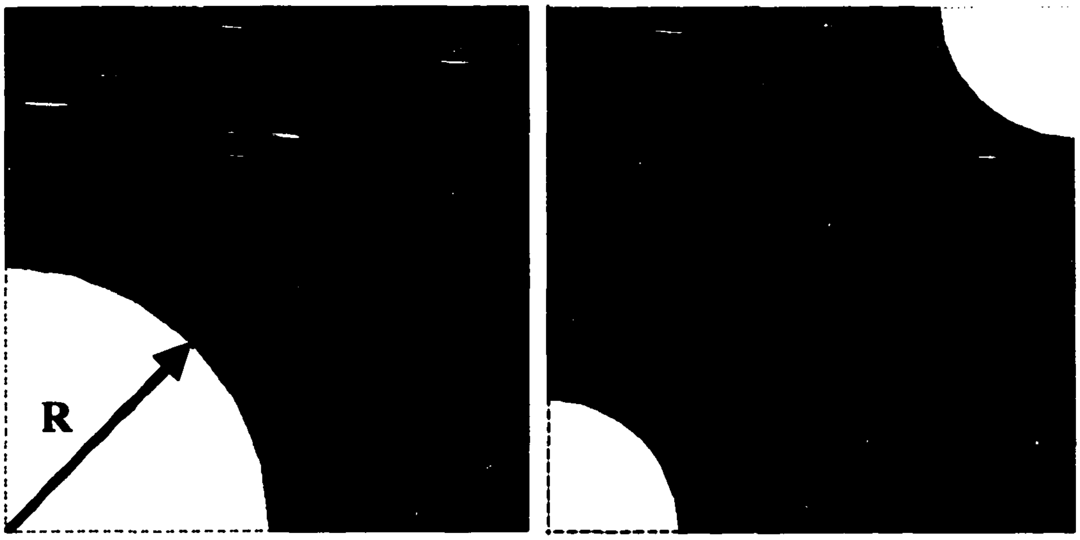

Figure 7. 3 (a) Square quarter-pore model geometry. Dashed line outlines the triangular eighth-pore model, the theoretically smallest unit cell. Because of the software limitations, the quarter-pore was the smallest available model. (b) The smallest unit cell to represent the tilted pore model.

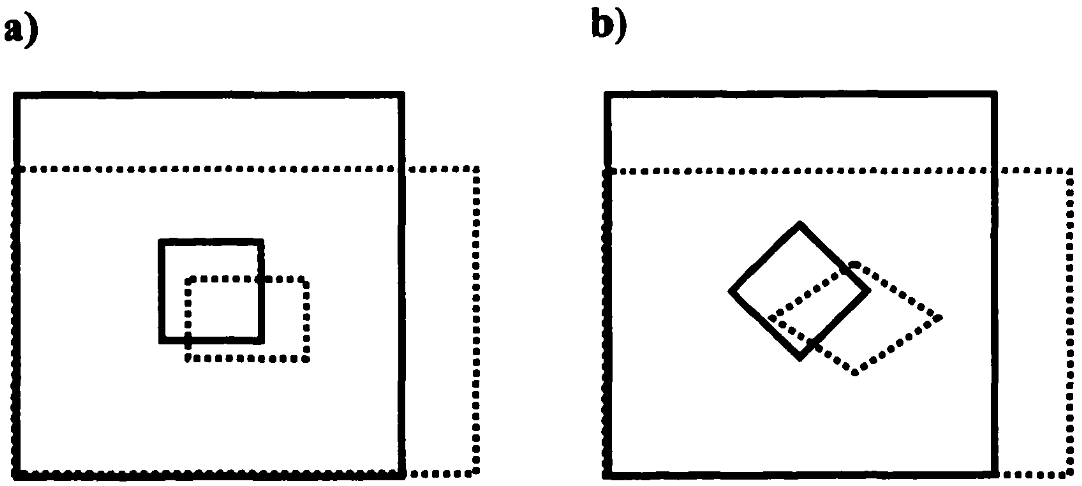

Figure 7. 4 (a) Deformation of a square model shows the necessary orthogonal boundary displacements. The triangular model boundary motion (a diagonal of the square) was not allowed within the software. (b) A square model could represent the tilted pore lattice but the PBCs do not allow for the tilting at the boundary, the same as the triangular model.

of Fig. 7.3(b) was not used. A larger model containing several whole pores was used for reasons discussed later.

7.2.3 Boundary Conditions

7.2.3.1 Nodal Constraints

Regardless of the phase arrangement within the model, the specific boundary conditions used are shown in Fig. 7.5. Two adjacent boundaries had their displacements fixed with respect to the direction normal to the boundary (Fig. 7.5, A). The remaining two boundaries had distributed loads applied in accordance with the Hertz stresses, σ_z and σ_r, (Fig. 7.5, B). PBCs were established by "tying" the nodes along the boundary where the requisite distributed load was applied which restricted the boundary points to move in unison but arbitrarily so. The use of tied nodes would clearly necessitate only the application of a concentrated load at the boundary, because the effect of tying the nodes would be to distribute the force over the tied region. However, from a practical standpoint, the redundancy of using a distributed load eliminated the need to recalculate the appropriate concentrated force each time the model dimensions were changed because the software did it automatically. Note recalculation of the pressure was necessary for the tilted geometry because the porosity intersected the boundaries.

7.2.3.2 Creating the Mesh

After establishing the boundary conditions and choosing the appropriate phase geometry, a mesh was applied with the fineness of the mesh reduced in the regions of interest. Each mesh contained between 250 and 1000 elements. The model geometry

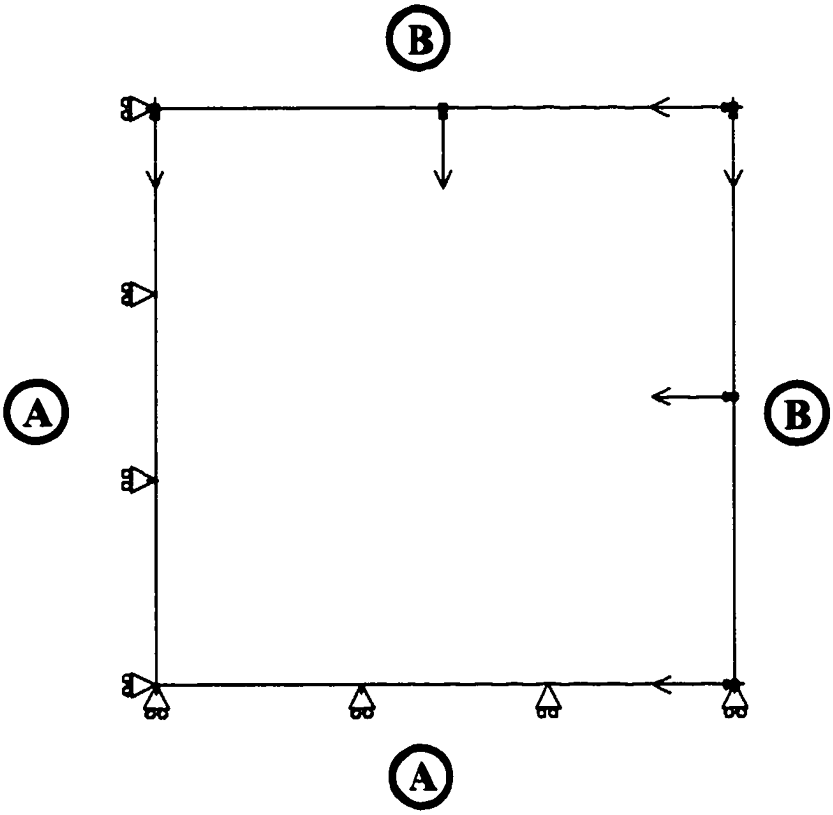

Figure 7. 5 The boundary conditions used for each model. Displacements were fixed normal to the boundaries marked, A. The uniform distributed loads, σ_{zz} and σ_{rr} were applied at B. The nodes along B were also tied, such that all boundary points were restricted to move in arbitrary unison.

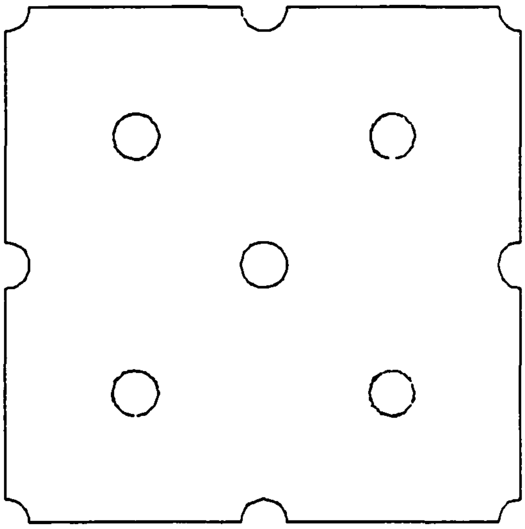

Figure 7. 6 The representation of the tilted pore geometry. Five whole pores are located within the boundary of the model. Notice that the geometry is infinitely repeatable along each edge using successive mirror operations.

chosen to represent the tilted pore structure is shown in Fig. 7.6. Five complete holes are contained within the boundaries of the model. Partial holes exist on all four boundaries and it is clear from the figure that successive mirror operations at the boundary will repeat the structure ad infinitum. Fig. 7.7 shows all three models used in the tilted axis investigation drawn to relative scale. For convenience, subsequent models will not be displayed to scale; however, the pore radius in each model will remain one micron. The square quarter-pore model (Fig. 7.3(a)) adequately represented the orthogonal pore structure for the porosity considered. This was confirmed by making two larger models, shown in Fig. 7.8, at the 5% porosity level for each orientation to compare with the smaller representations. The stress determined in the square quarter-pore model at 5% compared favorably to that of the larger model. Because of the large number of pores that would lie on the boundary of the larger tilted pore model, the boundary was placed halfway between two rows of pores. Strictly speaking, the model lacked infinite periodicity but the stresses were comparable in the interior to the other tilted pore models. The main difference was that the pores near the boundary were consistently more compressive.

Slight variations in computed stress were also observed and attributed to the fineness of mesh, mesh spacing, and location of points of interest with respect to boundaries regardless of model geometry. Because the FEM technique relies on interpolation of stresses, the finer the interpolation, the more accurate the solution. The computed stresses at a given node resulted from an averaging of the surrounding nodes. Therefore, an uneven number of elements along a stress path (a path leading from the edge of a hole for example) produced stress variations within the same model under the same boundary conditions: larger for unevenly spaced elements, and smaller for the reverse. On average, finer meshes produced an increasingly higher tensile stress for a given set of boundary conditions in the models studied.

7.2.4 Incorporating a Second Phase

Another important consideration was that of the glassy grain boundary phase. The square quarter-pore was chosen to evaluate the effects of a lower modulus phase placed in the plane of maximum shear stress (45° orientation). The advantage of using the square quarter-pore model to evaluate second phase effects, derives from its simplicity in implementation and that it represented a lower bound to the effects of pore interactions. It was assumed that the tilted pore arrangement would provide a similar, if not greater,

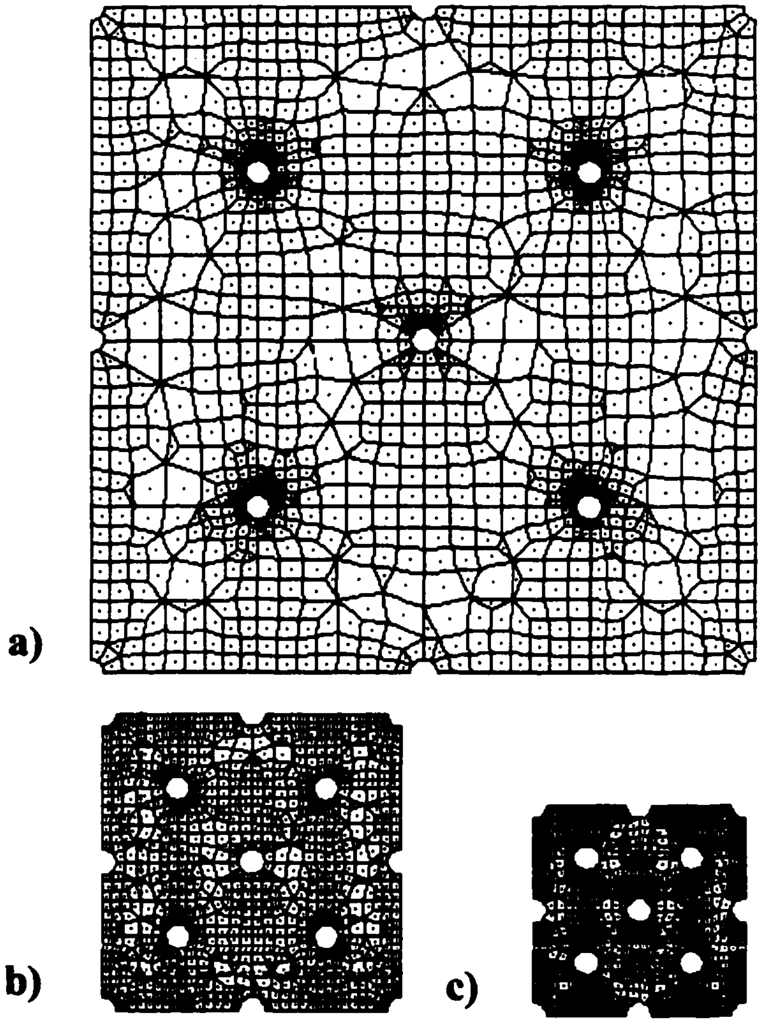

Figure 7. 7 The three tilted pore models drawn to relative scale, shown after the application of the mesh. Note the radius of the holes in each case is 1 micron. (a) 1% porosity; (b) 5% porosity; (c) 10% porosity

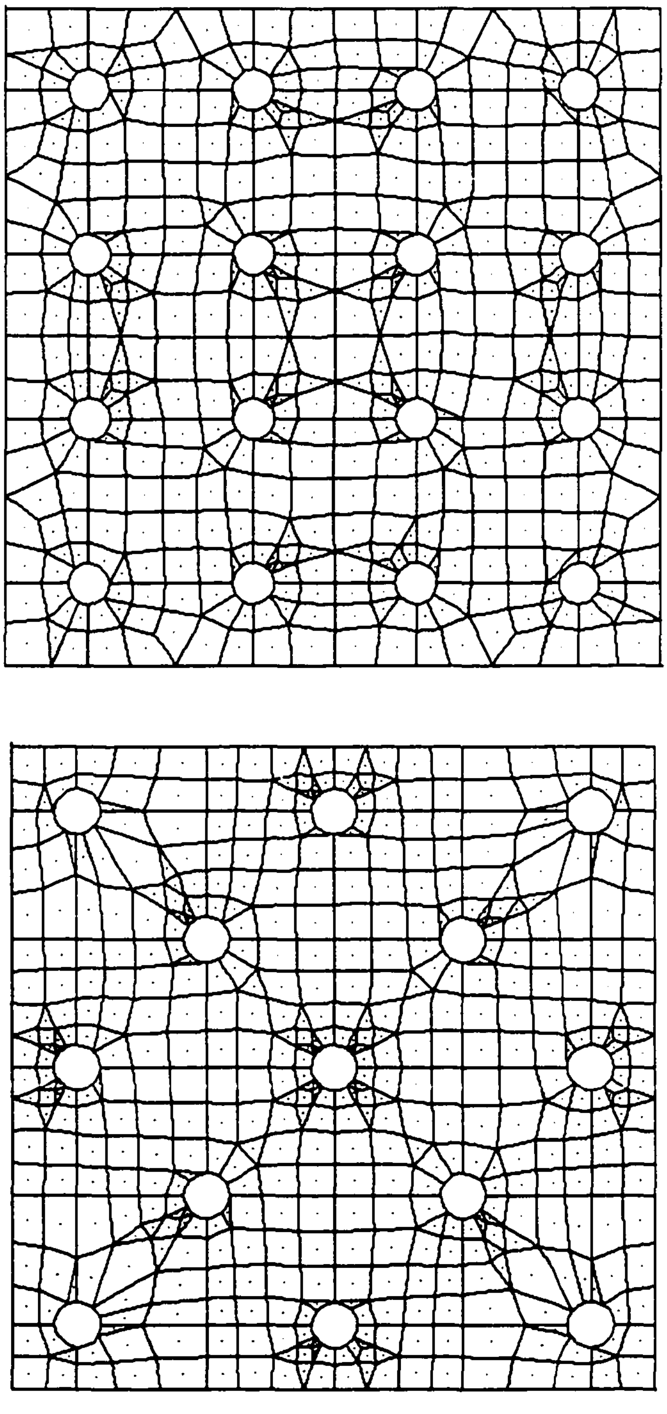

Figure 7. 8 Large models for the orthogonal orientation (a) and the tilted pore model (b). Note that the tilted pore model is not strictly periodic but the computed stresses were comparable to the smaller periodic model.

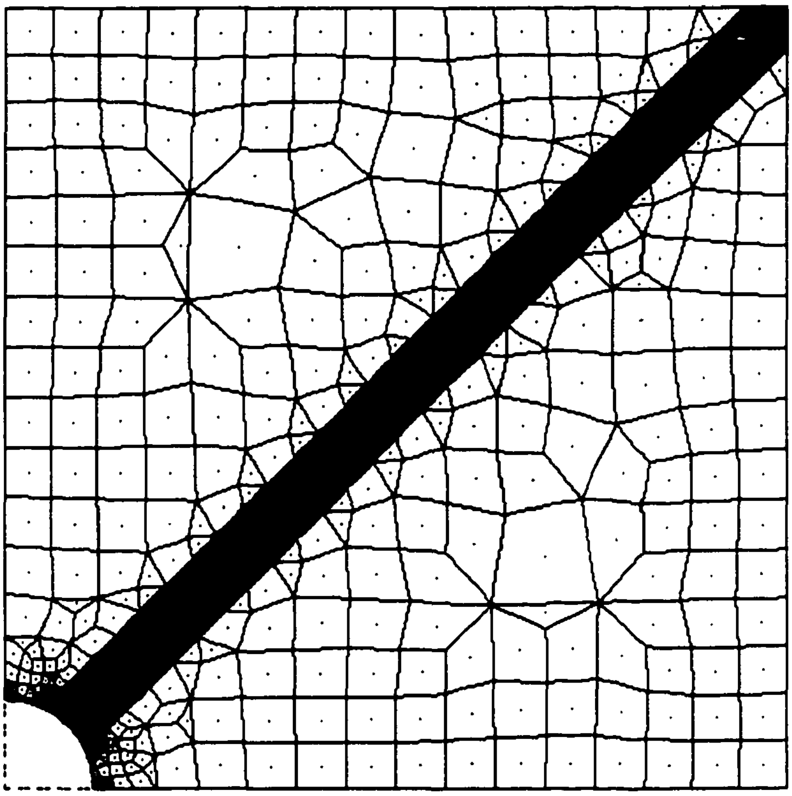

Figure 7. 9 Square quarter-pore model with 10 vol% glass phase at a simulated grain boundary oriented in the plane of maximum shear stress. The volume fraction of glass was kept constant as the porosity increased. The representation is not directly analogous to the real system because most glass is found in large pockets. Models with a thinner glass phase produced the same effect to a lesser extent.

response. A glass phase (E = 65 GPa, $\nu = 0.3$) was incorporated into the square quarter-pore model as shown in Fig. 7.9. The representation of Fig. 7.9 was believed to be adequate, although not an exact representation of the real system. Experimentally, the glass phase remained constant at 10 vol% in each sample. Likewise, the glass phase area (volume) fraction was kept constant in our models. However, the constant area fraction boundary condition forced the thickness of the glass layer to decrease slightly as the porosity of the model increased. Furthermore, because the glass phase was constrained to lie entirely at the grain boundary – instead of congregating at triple points within the microstructure – the thickness of the glass layer is much larger than would ever be encountered in reality. Nevertheless, the experimental results in Chapter 6 showed that the glass phase did exist primarily at the boundary between grains surrounding a pore, making the geometric representation of Fig. 7.9 a reasonable one.

7.3 FEM Results

Effect of Orientation on Stresses:

The tilted pore model porosity was varied from 1 to 10% and the peak tensile stress output is shown in Fig. 7.10 for the center pore. An increase in the peak stress was observed for increasing porosity with near perfect linearity. The value at zero porosity represented the peak stress value of a single pore in an infinite matrix, determined from Eq. 2.43 as 2.5 GPa, where $p_1 = \sigma_z = -6.25$ GPa and $p_2 = \sigma_r = -1.25$ GPa. Note the applied stress was rounded from the actual Hertzian values to facilitate modeling and differs by no more than 1% from actual values. For example, the applied Hertzian stress ratio, λ, was calculated as 0.202 and in the model, $\lambda = 0.2$.

The stresses plotted radially from the peak stress position along a line parallel to the primary axial load (normal to the hole surface) are shown in Fig. 7.11 – 7.13 for each of the five complete pores at each porosity. For a trajectory normal to the hole surface and coincident with the primary applied stress direction, p_1, the tangential stress, $\sigma_{\theta\theta}$, is equivalent to the principle stress, σ_1. Fig. 7.11 shows the stresses for the tilted pore lattice at 1% porosity. The pores were numbered to coincide with the graph legend and are the same in each successive figure. The stress is plotted along the path shown in Fig. 7.11 for each pore and the distance has been normalized to the pore radius with the origin at the pore surface (r = R). Fig. 7.13 and 7.14 are for 5% and 10% porosity respectively. The arrows in this and all subsequent stress plots indicate the isolated pore value, 2.5 GPa. A variation existed in the peak stress for the other holes in the model; however, the trend of increasing peak stress with increasing porosity prevailed. Despite the variation in the peak stress values from pore to pore, the stresses within the bulk were very consistent from pore to pore. There was an obvious trend in the tangential stresses, $\sigma_{\theta\theta}$, shown more clearly in Fig. 7.14 for the center pore of each model out to a distance of 3R from the hole surface. Several trends in the bulk stress were observed in this plot. First, one can see that the bulk stress near the hole surface increased with increasing porosity – not just the peak stress. Second, the bulk stress became more compressive further away from the hole as the porosity was increased. The increased compressive stress was attributed to stress field overlap as the pores moved closer; the highly compressive character of the adjacent pores in the radial direction encroached into the originally tensile $\sigma_{\theta\theta}$ region near the hole surface (Fig. 7.15). The radial component of compressive stress was shown in Fig. 2.14, **rr**, and was qualitatively superimposed at the holes in Fig. 7.15. Finally, the bulk stress along the radial path showed a convergence of the stress for all three models at approximately 1.9R (-1.7 GPa). After the convergence point, the derivative of each curve revealed three distinct behaviors. At 1% porosity, the derivative of the stress with position was slightly increasing in value. When the porosity was increased to 5%, the slope was approximately zero and the slope was significantly negative at 10% porosity.

By comparison, the stress became increasingly compressive along the identical path for the orthogonal orientation of pores as shown in Fig. 7.16. And more importantly, the peak stresses *decreased* with increasing porosity below the isolated pore value as shown in Fig. 7.17. The value of the peak stress at 1% porosity was slightly higher than the peak stress value for an isolated pore and was attributed to fluctuations described earlier. The increasing difference with porosity for each orientation was most notable in the series of graphs in Fig. 7.18 – 7.20. Fig. 7.18 shows the stresses at 1% porosity to be very close for the tilted pore and orthogonal pore orientations with the tilted orientation slightly higher. In the figure is the stress plot at a constant porosity for the tilted pore and orthogonal pore orientations. As the porosity was increased to 5%, the two curves in Fig. 7.19 separated from each other and more importantly, digressed from the isolated pore value in opposing directions. This trend was most noticeable at 10% porosity (Fig. 7.20).

Effect of Model Size:

As discussed previously, the appropriate size of the model was in question. In an effort to address this issue, large models were produced at 5% porosity as shown in Fig. 7.9. The orthogonal orientation contained 16 pores and the tilted orientation contained

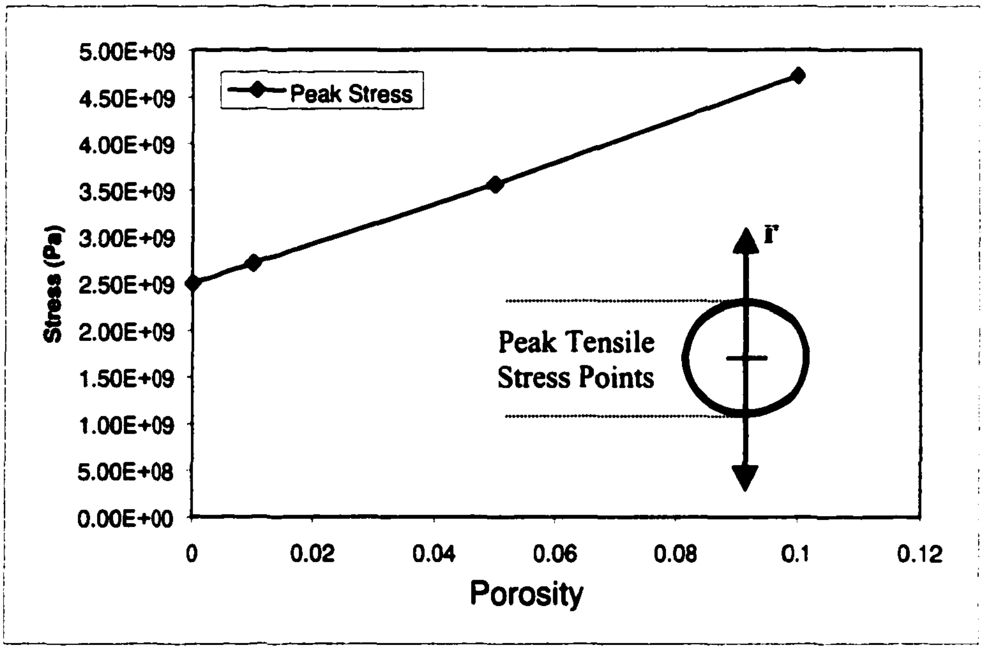

Figure 7. 10 Peak tensile stress, $\sigma_{\theta\theta}$ at $\theta = \pi / 2$, at the hole surface as a function of porosity was found to increase linearly for the tilted pore lattice. The isolated pore value was 2.5 GPa.

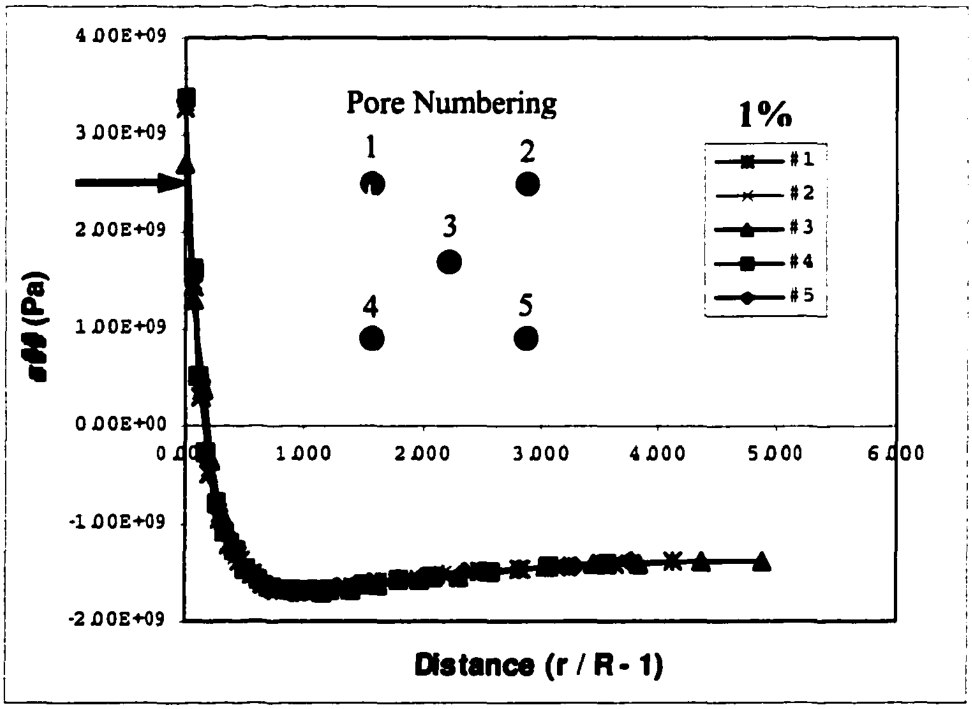

Figure 7. 11 A plot of the tangential stress from the peak stress point at 1% porosity. Curve legend corresponds to the numbered pores as shown. Arrow indicates isolated pore value 2.5 GPa. Note that peak stress exceeds this value.

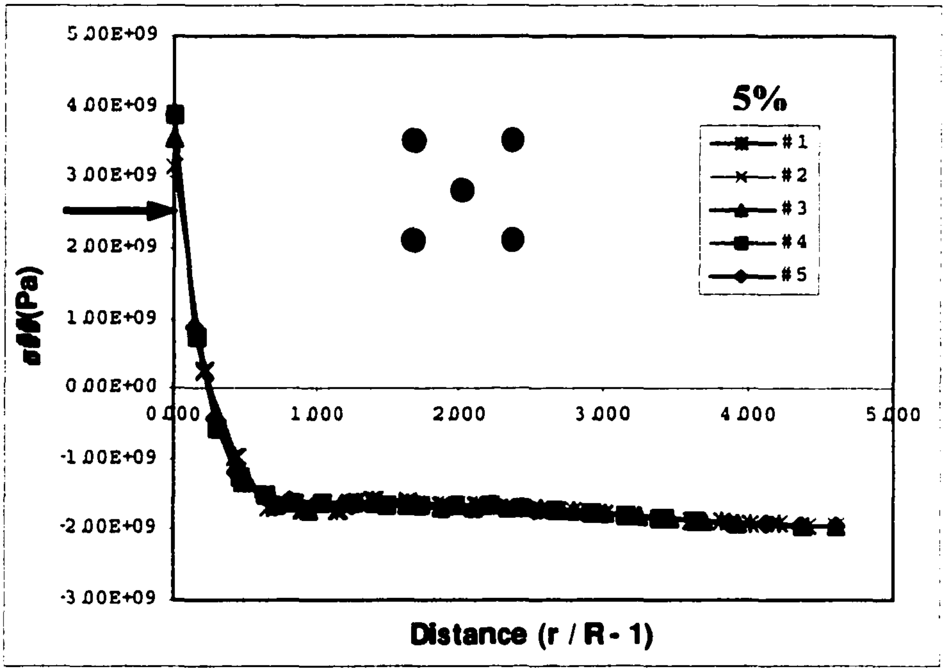

Figure 7. 12 A plot of $\sigma_{\theta\theta}$ from the peak stress point ($\theta = \pi / 2$) at 5% porosity. Pore numbering remains the same as in Fig. 7.11. Notice the increase in tensile stress near the hole surface.

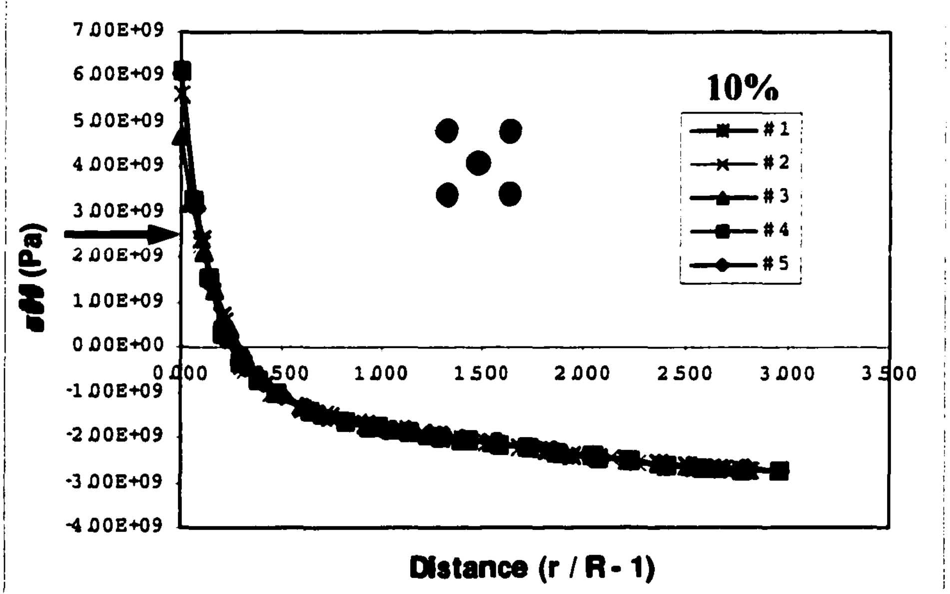

Figure 7. 13 A plot of $\sigma_{\theta\theta}$ from the peak stress point at 10% porosity. Pore numbering remains the same as in Fig. 7.11. The tensile stress near the hole surface has dramatically increased and likewise, the compressive stresses away from the hole surface have also increased.

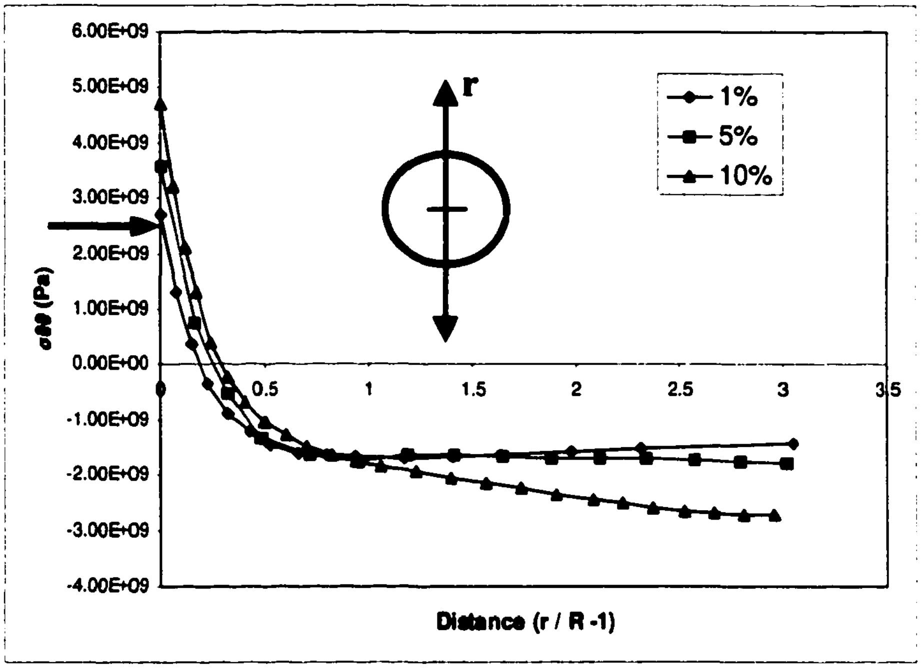

Figure 7. 14 A plot of $\sigma_{\theta\theta}$ along a radial direction starting at the peak tensile stress point for the tilted pore lattice. As porosity was increased, the bulk stresses near the hole surface (up to 1.9R) increased, not just the surface stress. Past the convergence point, the positional derivative of stress changed from slightly positive, to zero, to significantly negative as porosity was increased from 1%, 5%, and 10% respectively. Plots converged at 1.9R (-1.7 GPa).

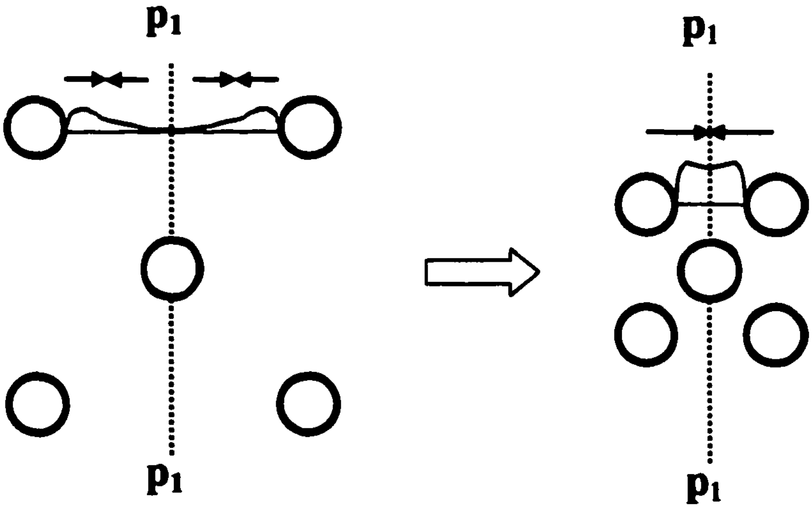

Figure 7. 15 The reason for the stress trend observed in Fig. 7.14 was likely due to the increasing proximity of the compressive stress fields of adjacent pores. As shown above for arbitrary pore spacing, the compressive stress fields, σ_{rr}, of the pores move into closer proximity to the tensile stress fields, resulting in the behavior of Fig. 7.14.

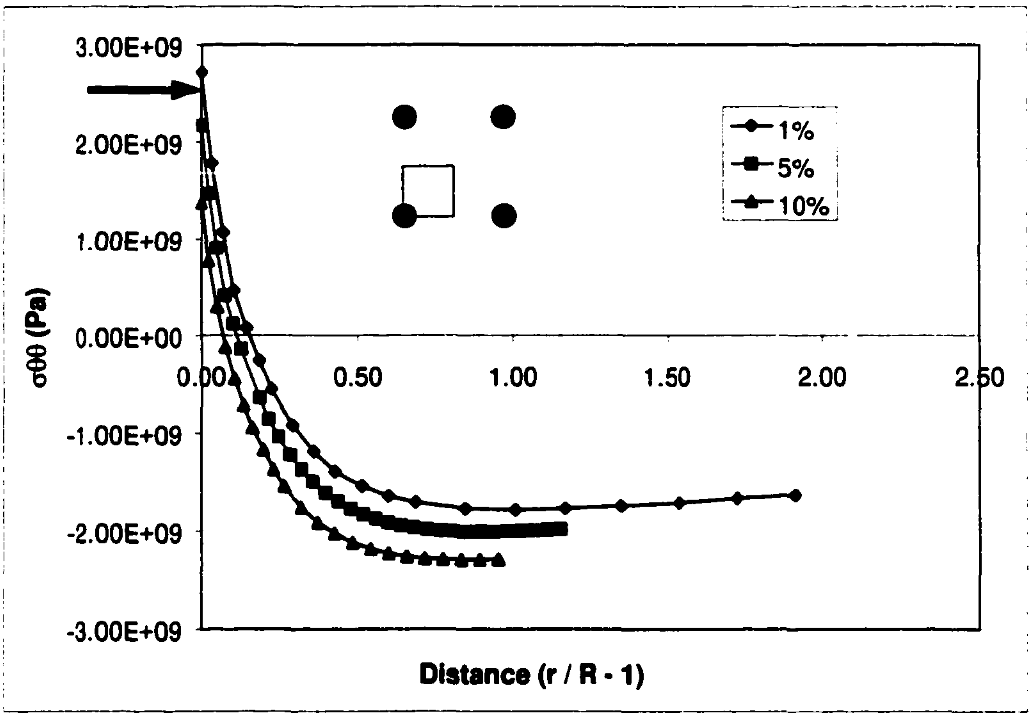

Figure 7. 16 A plot of the tangential stresses, $\sigma_{\theta\theta}$, for the orthogonal orientation as a function of porosity. Notice the stresses were increasingly compressive everywhere and were less than the isolated value (the small fluctuation in 1% notwithstanding)

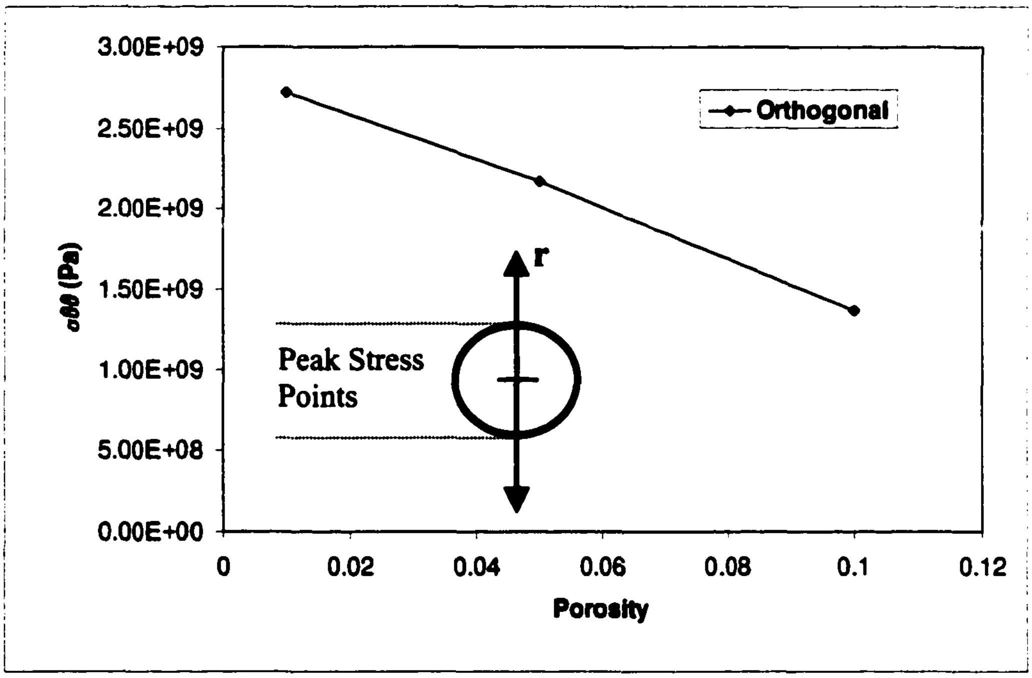

Figure 7. 17 Decrease in peak tensile stress, $\sigma_{\theta\theta}$, with porosity for the orthogonal orientation.

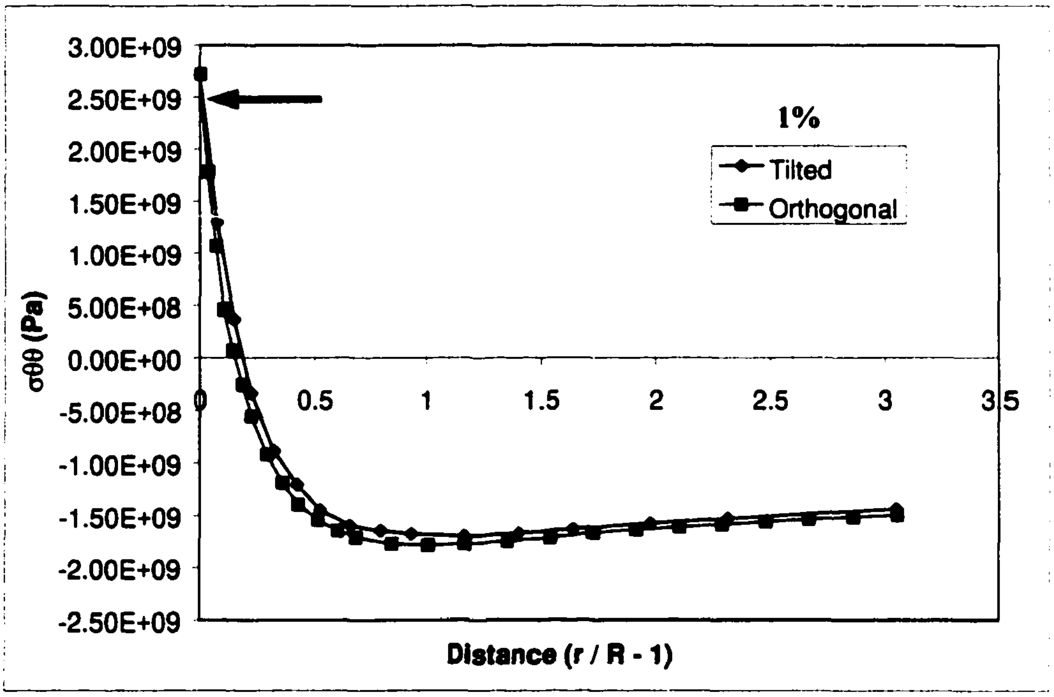

Figure 7. 18 A comparison of the tangential stresses at 1% porosity for the tilted and orthogonal pore lattice. The tilted orientation was slightly more tensile.

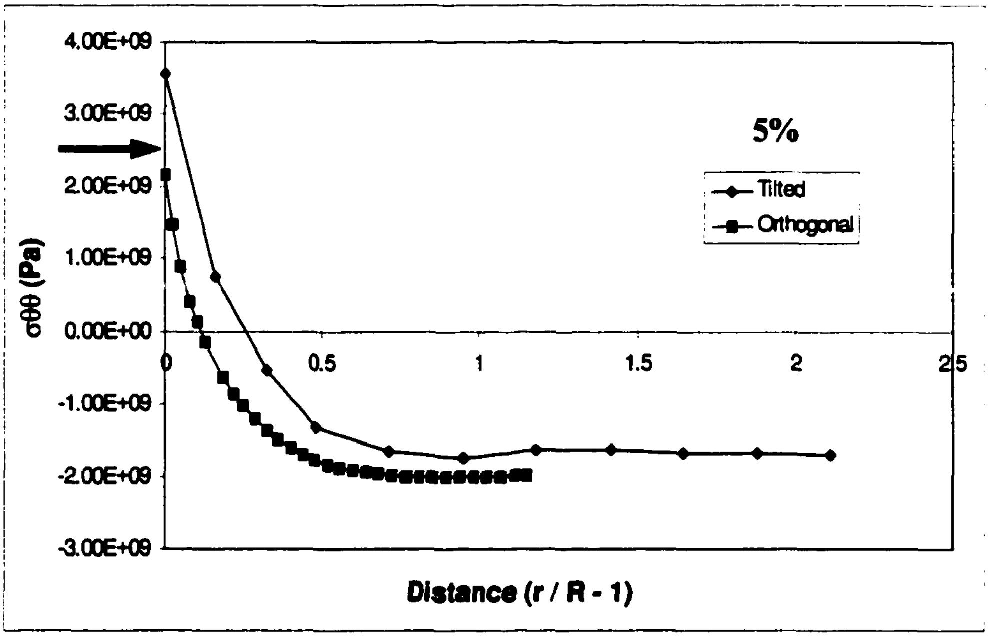

Figure 7. 19 At 5% porosity the difference between the two orientations was distinct. The tilted orientation increased its tensile character near the hole surface while the orthogonal lattice decreased. The peak stresses were above and below 2.5 GPa respectively.

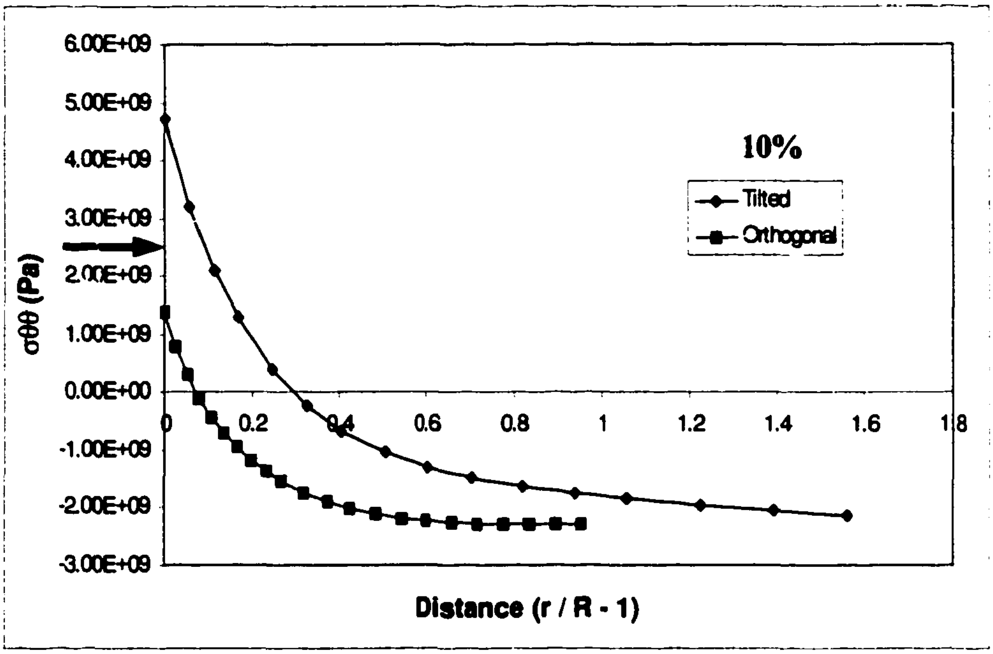

Figure 7. 20 At 10% porosity the difference between the two orientations was extremely obvious. In this and previous graphs, the stresses appeared to converge as the distance from the hole increased.

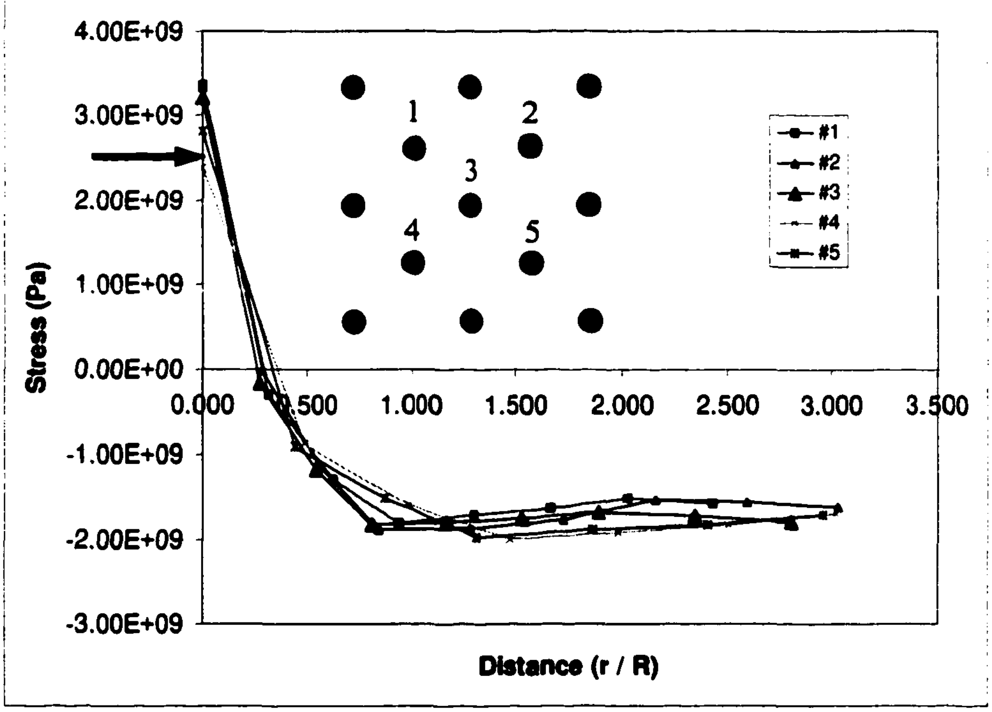

Figure 7. 21 Radial stress plots for large tilted pore model at 5% porosity. The results are in agreement with the smaller model shown in Fig. 7.12.

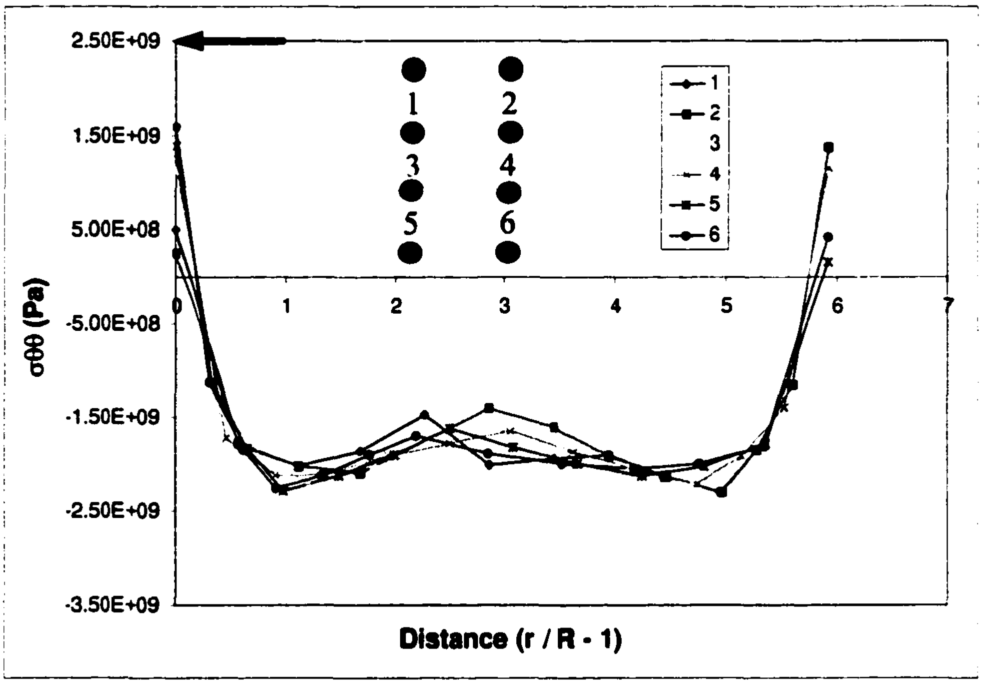

Figure 7. 22 The large orthogonal model at 5% porosity. Plots of stress are between pores as numbered. Calculated stresses in the bulk were comparable to the square quarter-pore model. Peak stress values were lower because of the coarser mesh.

13 internal pores. The tilted orientation was slightly modified to exclude pores from the boundary (Figs. 7.8 & 7.21), a model that was not strictly periodic but produced an equivalent stress behavior to that observed earlier as shown in Fig. 7.12. In the orthogonal orientation, the values of the bulk radial stress compared favorably and the peak stresses were slightly higher in the square quarter pore models. The difference in peak stress was attributed to the coarseness of the mesh in the larger models as discussed previously.

Randomizing the Network of Pores:

After identifying the trend of increasing porosity and influence of orientation for a periodic network of pores, the question of random pore arrangement remained. The effects of pore lattice asymmetry were addressed by moving the center pore of a model containing 5% porosity in two directions. The center pore was moved along a path in the NND and then at an angle of 45° with respect to the NND. In each case, the pore was moved to distances of 0.08R, 0.4R and 2.4R. Keeping external loads and boundary conditions constant, the peak stresses were plotted as before and are shown in Fig. 7.23 and Fig 7.24. The results showed a small degree of fluctuation with the movement in the NND (Fig. 7.23) and similarly with the 45° to NND movement (Fig. 7.24). However, notice that each plot still showed the characteristic increase of peak stress above the isolated pore value of 2.5 GPa found earlier in Fig. 7.10.

Modeling the Glassy Second Phase:

With the geometrical issues of porosity addressed, the attention shifted to the presence of the glass in the microstructure. The effect of the second phase was addressed by assuming that it was contained exclusively at the grain boundary in microstructure. The glass phase was held constant at 10 vol% while the porosity was varied as before producing the stress effects shown in Fig. 7.25. The trend in the stresses remained the same as the models without the glass phase, with the exception that $\sigma_{\theta\theta}$ at the peak and within the bulk experienced an increase toward greater tensile stress with increasing porosity. Fig. 7.26 shows the effect of the glass at 1% porosity to increase the tensile stress over that of the pure material. Similarly, in Fig. 7.27 and 7.28, the tensile stress increased for higher porosity. The increase in tensile stress at the peak stress location is a result of the compliant glass phase increasing the distortion of the pore as shown in Fig. 7.29. Notably, the overall stress became more compressive with increasing porosity but was higher than the isolated pore solution at 5% and 10% when the glass phase was present. Also apparent was a trend for the pure and glass solutions to converge with increasing porosity. The implications of these results are discussed and summarized below.

Effect of Compressive Stresses:

Although it was not directly applicable to the failure aspects of the alumina materials investigated – for reasons discussed at the end of this chapter – consideration was given to the peak compressive stresses located $\pi / 2$ from the peak tensile stresses. Fig. 7.30 shows the plot of the peak compressive stress with porosity for the tilted, orthogonal and orthogonal with glass models. The tilted pore model produced a less compressive stress response compared to that of the orthogonal models. The glass phase did succeed in increasing the tensile character of the peak stress over that of the single phase orthogonal model. However, one should note that the effects of porosity were to decrease the differences between the models as the values were converging with increased porosity. In the bulk stress plots for the orthogonal model (Fig. 7.31), the change in the stress character was almost imperceptible with increasing porosity. The compressive stress values tended toward the externally applied stress value of 6.25 GPa in all of the bulk stress plots. Fluctuations in the bulk stress of the tilted pore model are shown in Fig. 7.32 and were due largely to the coarser mesh compared to other models. However, like the other models, the stress values were very close with changing porosity. The largest differences as a function of porosity were observed in the glass containing models shown in Fig. 7.33. However, the differences between the 1% and 10% porosity curves, caused in the compressive stress by the glass phase, were approximately 1%. By comparison, the tensile stresses experienced roughly a 30% change in value from the glass phase presence.

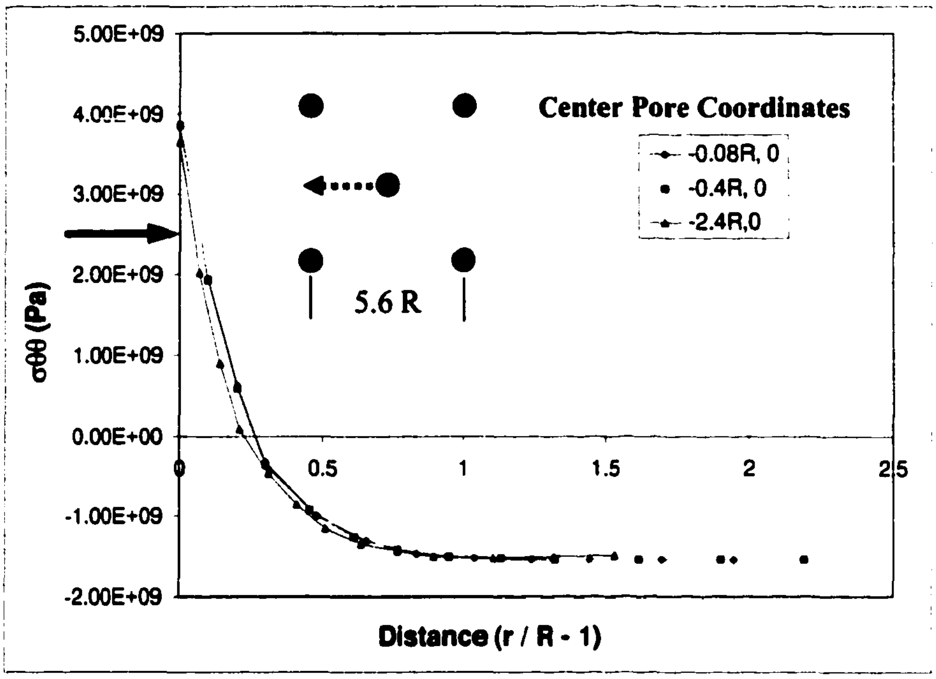

Figure 7. 23 To study the effect of asymmetry the center pore was moved from its location in the direction indicated up to 2.4R from center. Virtually no change in the stresses was observed as a function of position. Model represents 5% porosity.

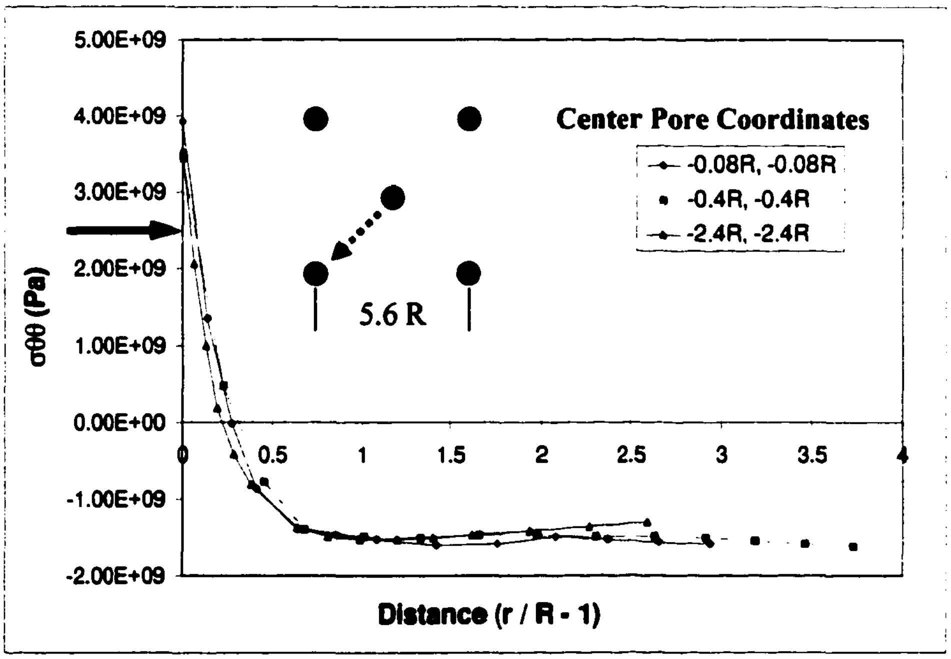

Figure 7. 24 The pore was also moved diagonally as shown. Similarly, there was little change in the stress response including the peak stress values.

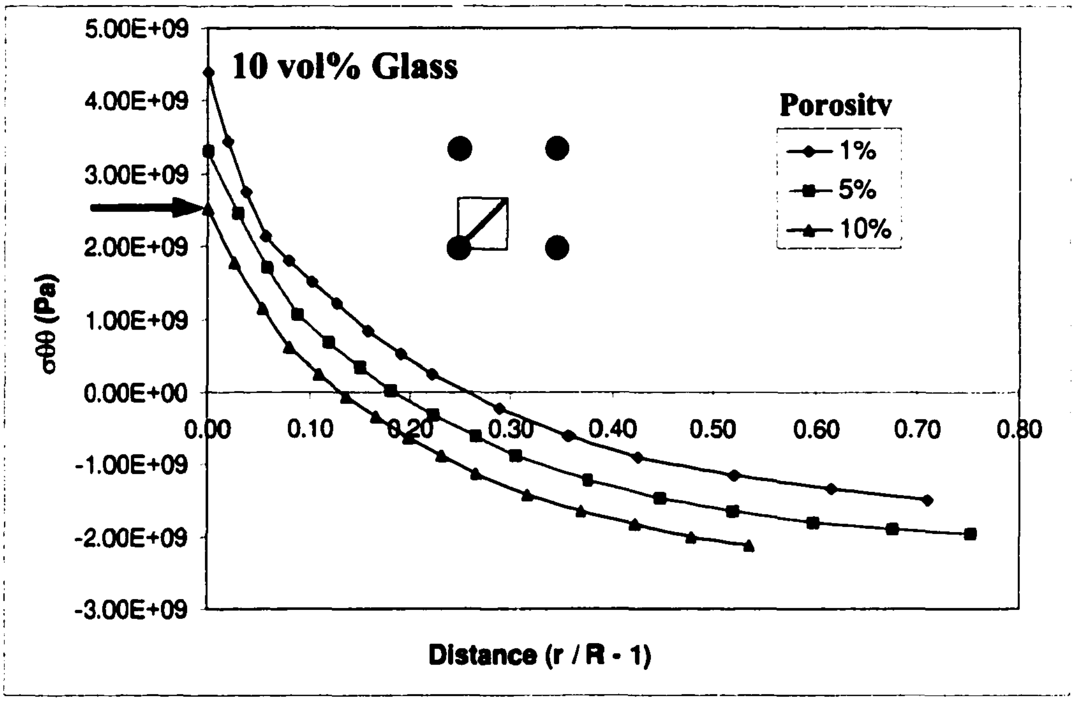

Figure 7. 25 10 vol% glass phase was introduced in the model at the grain boundary with 1%, 5%, and 10% porosity. As porosity increased, the stresses decreased, as before, however the overall stress level was higher.

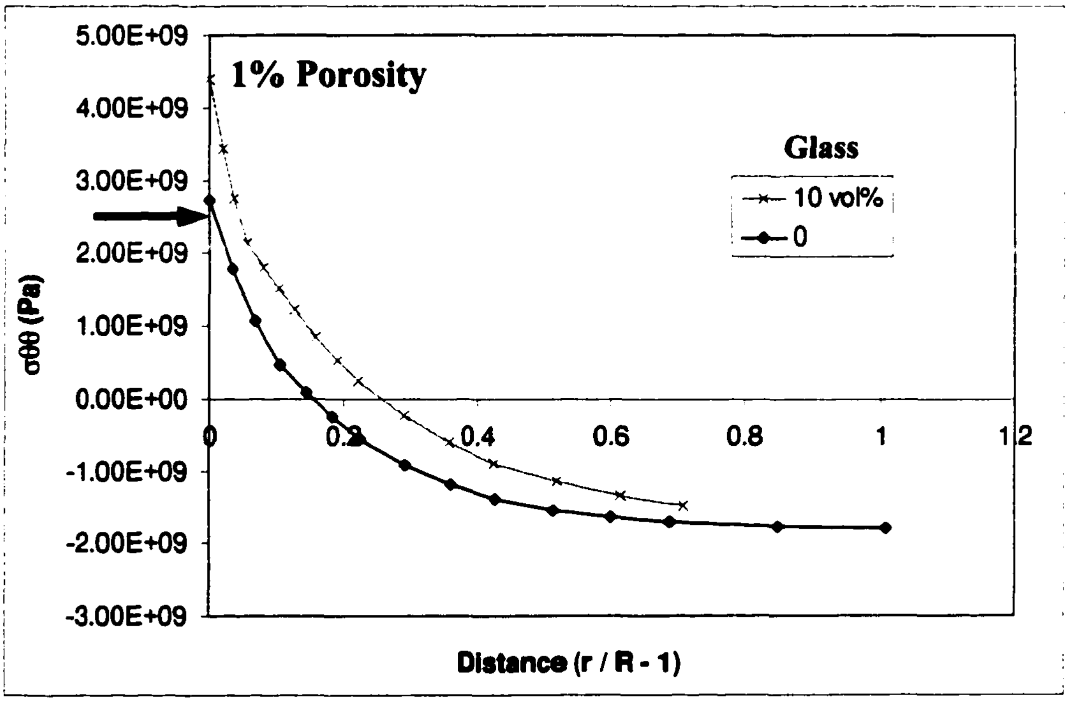

Figure 7. 26 Stresses for glassy sample and pure sample at 1% porosity.

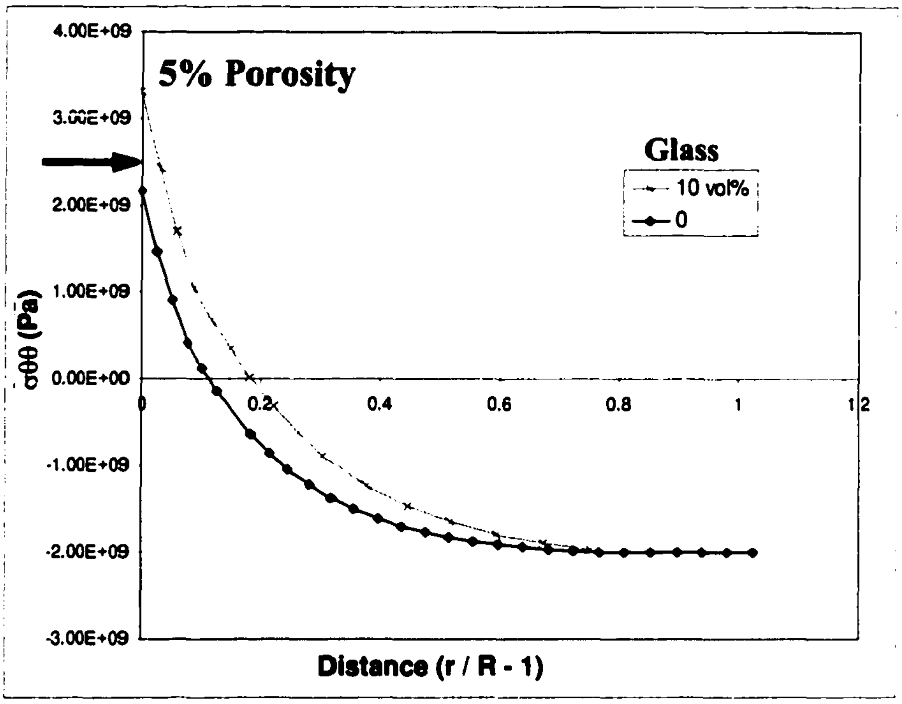

Figure 7. 27 Increasing the porosity to 5% caused an increase of the compressive stress with the glass containing model remaining higher.

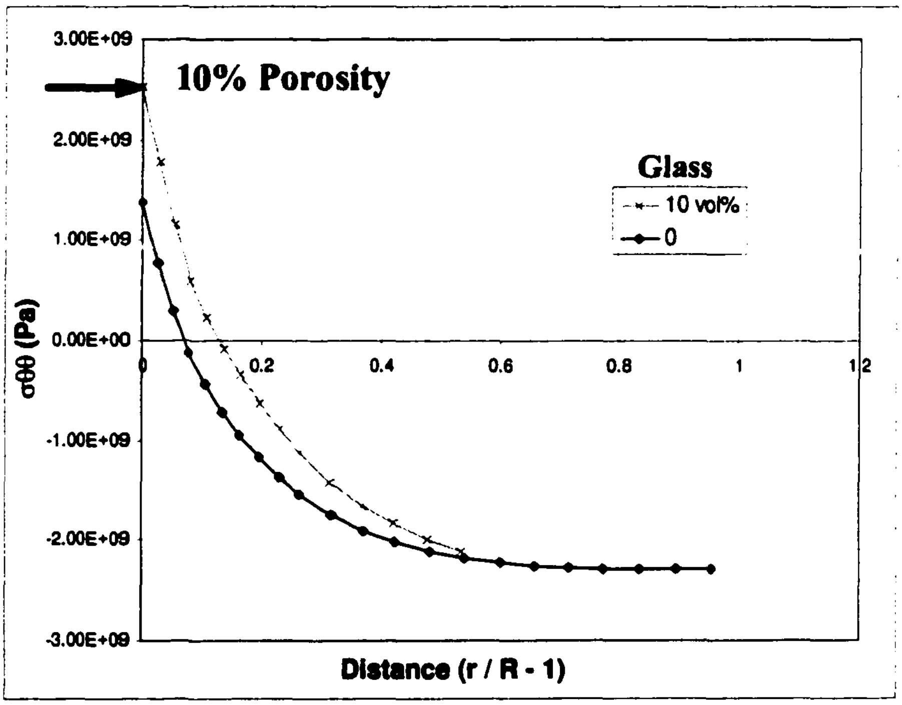

Figure 7. 28 Similar behavior was observed at 10% porosity with the glass phase model converging to the pure stress value at a smaller value from the pore surface.

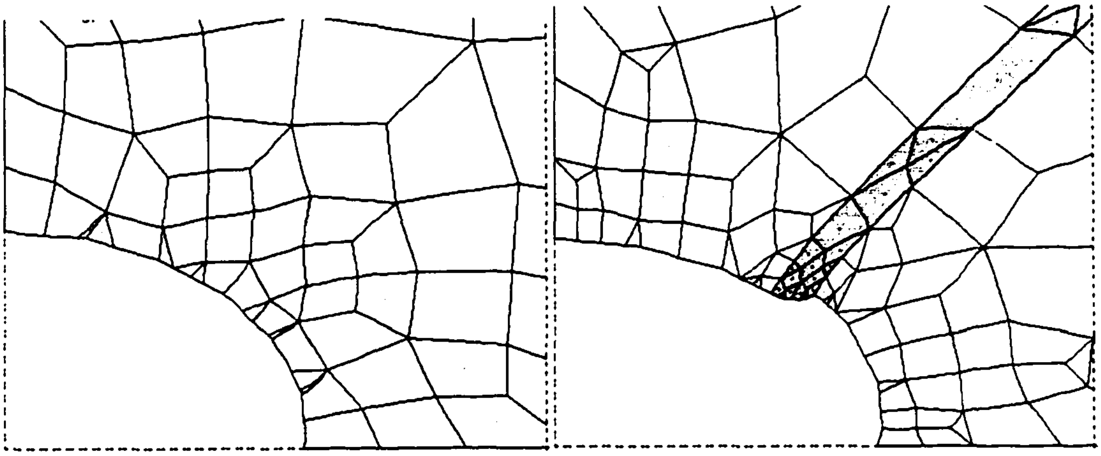

Figure 7. 29 Deformed models at the same porosity level with (a) and without a glass phase (b). Deformations magnified 5x105. Notice the distortion in the glass phase (gray). The model shown is for a smaller volume fraction of glass than the other models.

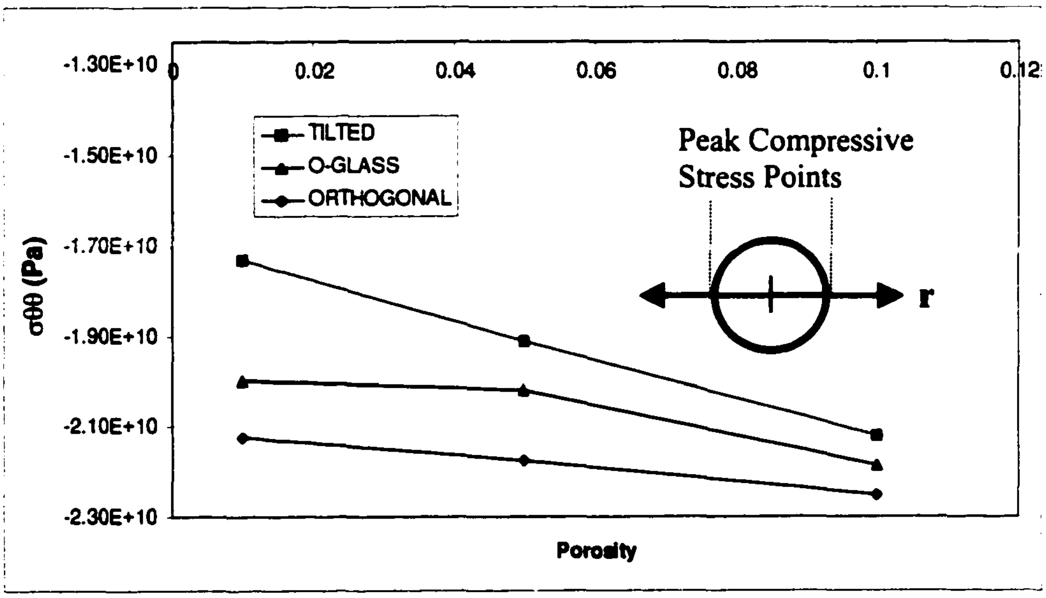

Figure 7. 30 Peak compressive stress at hole surface as a function of porosity for the tilted, orthogonal and orthogonal model with 10 vol% glass phase. Little change was seen for the orthogonal model. Glass created a less compressive stress than the single-phase material and the tilted pore lattice produced the least compressive stress. The change in peak stress was smaller at higher porosity than at lower porosity.

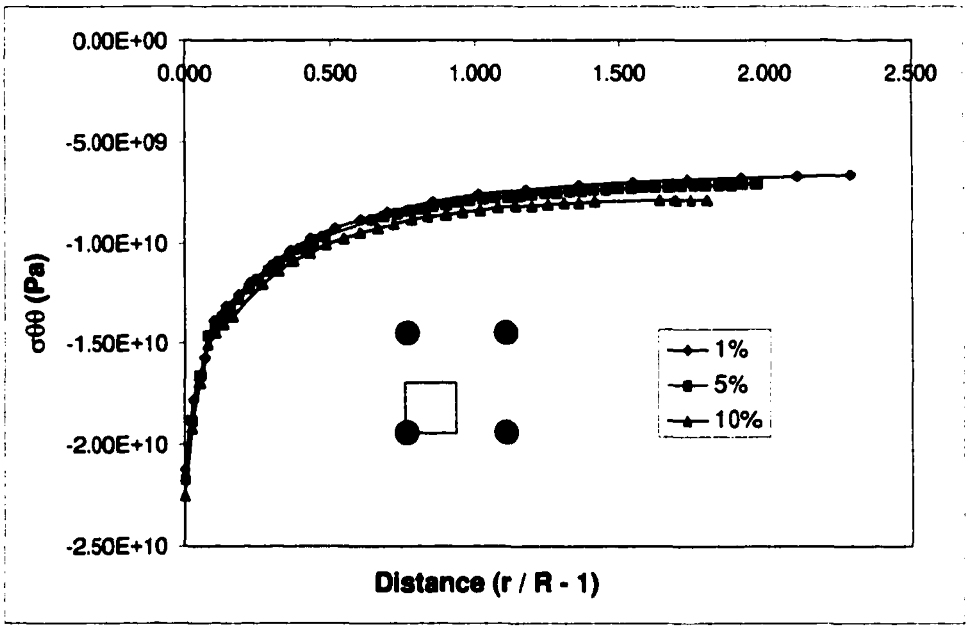

Figure 7. 31 The stresses in the bulk of the orthogonal model. Very little change was observed in the bulk as with the peak stress as a function of porosity. Bulk stress values approached the limit of applied stress, p_l = 6.25 GPa, away from the surface.

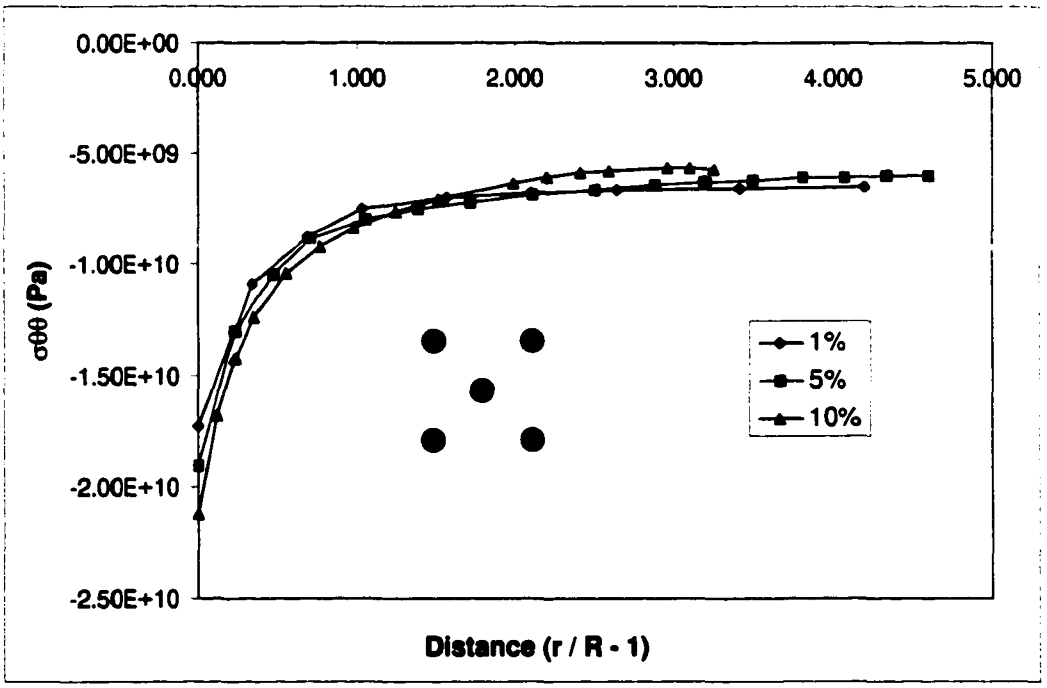

Figure 7. 32 Tilted pore stresses displayed a larger degree of fluctuation than the other models due to a coarser mesh. Stresses in the bulk were comparable to the orthogonal model and varied the most only at the hole surface.

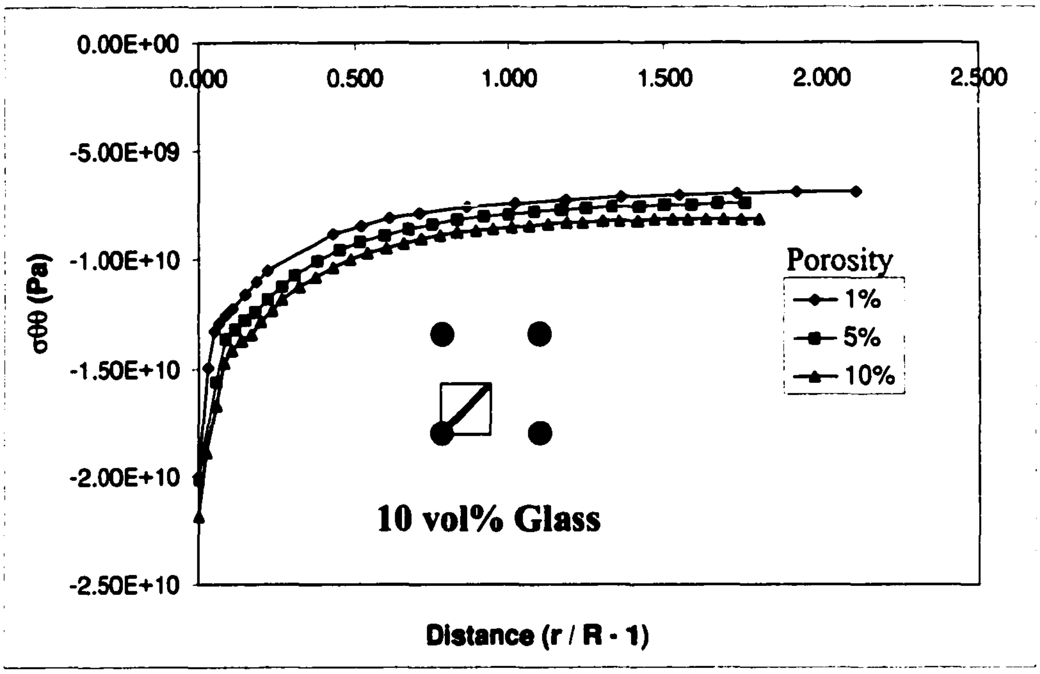

Figure 7. 33 Addition of the glass phase did produce the largest separation of compressive stress as a function of porosity but it was about half the effect as the tensile stresses (Fig. 7.25): 16% vs. 30% change.

7.4 Discussion of FEM Observations

7.4.1 Orientation and Geometry

Agarwal (1971) performed an early investigation into the effects of porosity on stress concentrations using the FEM technique. Using axisymmetric conditions, a remotely applied *tensile* stress, and a quarter-pore unit cell, Agarwal (1971) found an increase of the peak tensile stress (Fig. 7.30) with increasing porosity. Because PBCs were not used, the results reflect the stress response of a cylinder with a spherical cavity and were not directly comparable to the results in this investigation.

One of the first studies to investigate analytically the effect of multiple holes on stress concentrations was performed by Howland (1935), as discussed in Sec. 2.8. The

FEM results of Fig. 7.16 for the orthogonal lattice orientation were normalized and plotted in conjunction with the analytical work by Howland (1935) and are shown in Fig. 7.35. Signs were reversed from Howland's work to reflect a remotely applied compressive stress rather than a tensile one. The FEM results of the orthogonal pore orientation determined by the SQP model are shown for the equivalent normalized nearest neighbor distance, $2N$. The stress was normalized by the analytical value of an isolated pore, $3p_2 - p_1$. The FEM data for the orthogonal orientation did not exactly intercept the origin axis at the analytical value of 2.5 GPa as expected. The discrepancy was likely due to the size of the model and more importantly, the fineness of mesh. Optimizing the number of elements in critical areas would likely increase the accuracy. To compensate for the difference, the data was replotted and normalized by the linear regression intercept value of 2.88 GPa [FEM-SQP-LN]. In this way, the FEM results displayed the same trend as the analytical results of Howland (1935) and varied by less than 20% for the data shown. As was shown in Fig. 7.34 for the peak tensile stresses in the orthogonal model, a comparison can be made between Howland's (1935) calculations and the FEM results for the peak compressive stress. The raw data shown in Fig. 7.36 was normalized to the theoretical value of an isolated pore, $3p_1 - p_2$, and was shown to have the same slope as Howland's data. Normalizing the raw data to the linear intercept to the origin axis brought the data directly in line with that of Howland's.

Rice (1997) used the results of Savin (1961), who merely republished Howland's work, to infer that stress concentration effects at pores are not consistent with observed failure of brittle materials and not suitable for use as such. Rice's finding applies in tension at the surface of a sample, which for brittle fracture is valid because brittle fracture under remote tensile stress is largely a surface controlled phenomenon (Lawn, 1993). Rice (1998, 1997) indicated that brittle fracture under remotely applied compressive stresses was different, but that the stress reduction effect was applicable and mitigated only by the stability of crack growth under those circumstances. Brittle fracture under compressive stresses is significantly different and more importantly, the stress reduction effect of increased proximity of isolated pore space is false. This was demonstrated clearly in the results of Fig. 7.10 where the peak tensile stress was found to linearly increase with porosity for the tilted periodic array of pores. Hereby it has been established that under remotely applied compressive stresses there existed a stress magnification effect of both peak tensile stress and compressive stresses within the bulk (Fig. 7.11 – 7.15) along the radial trajectory from the peak stress point. The distinction was evident in the comparison of the orientation effects at each porosity (Fig. 7.17 – 7.20). One may suggest that each orientation represented a special case in which the alignment of the matrix within the stress field produced a maximum or minimum effect.

Examining the results of Fig. 7.23 and 7.24 showed that a disruption of the periodic structure did not appreciably change the peak or bulk stress characteristic compared to the tilted pore lattice for the equivalent porosity. The asymmetric pore structure is likely to be representative of a random real pore arrangement and therefore indicates that an increase in the stress concentration as a function of porosity under remotely applied compressive stresses should be expected. Du and Zok (1998) confirmed a periodic orientation dependence on computed yield surfaces for fibers of zero modulus in their investigation of metal matrix composites (MMCs) under biaxial tensile stress using FEM techniques.

The peak compressive stress was also effected by the orientation of the lattice as shown in Fig. 7.30. The tilted pore lattice again produced increased tensile behavior over that of the orthogonal lattice, although the magnitudes of the stresses remained compressive. The difference between the orthogonal model and tilted pore model was, oddly, more pronounced at low porosity (a 23% difference). This was in contrast to the bulk compressive stress behavior that varied around 15% for each model across the porosity spectrum. The reduction of the compressive stress for the orthogonal orientation becomes important for failure that actually initiates from within the compressive stress zone as opposed to the tensile region and will be discussed further at the end of this chapter. Small differences in the actual magnitude of bulk stresses existed for each of the three modeling conditions, but otherwise the behavior observed in Fig. 7.31 – 7.33 was similar.

We can conclude from the above FEM results that orientation dependence existed for two-dimensional arrays of periodic holes under biaxial compressive stresses. Specifically, the peak tensile stress at a given pore increased with increasing porosity for a simple cubic arrangement of pores when the NND was oriented 45° from the applied stress direction and the peak compressive stress decreased. Furthermore, the peak tensile and compressive stresses for the orthogonal model were found to be in agreement with previously published analytical results of Howland (1935). Because an asymmetric pore condition under the same loading conditions produced the same stress response as the tilted pore lattice, the increasing stress concentration effect under biaxial compression is valid when applied to bulk porosity. The only remaining issue was that of the second phase.

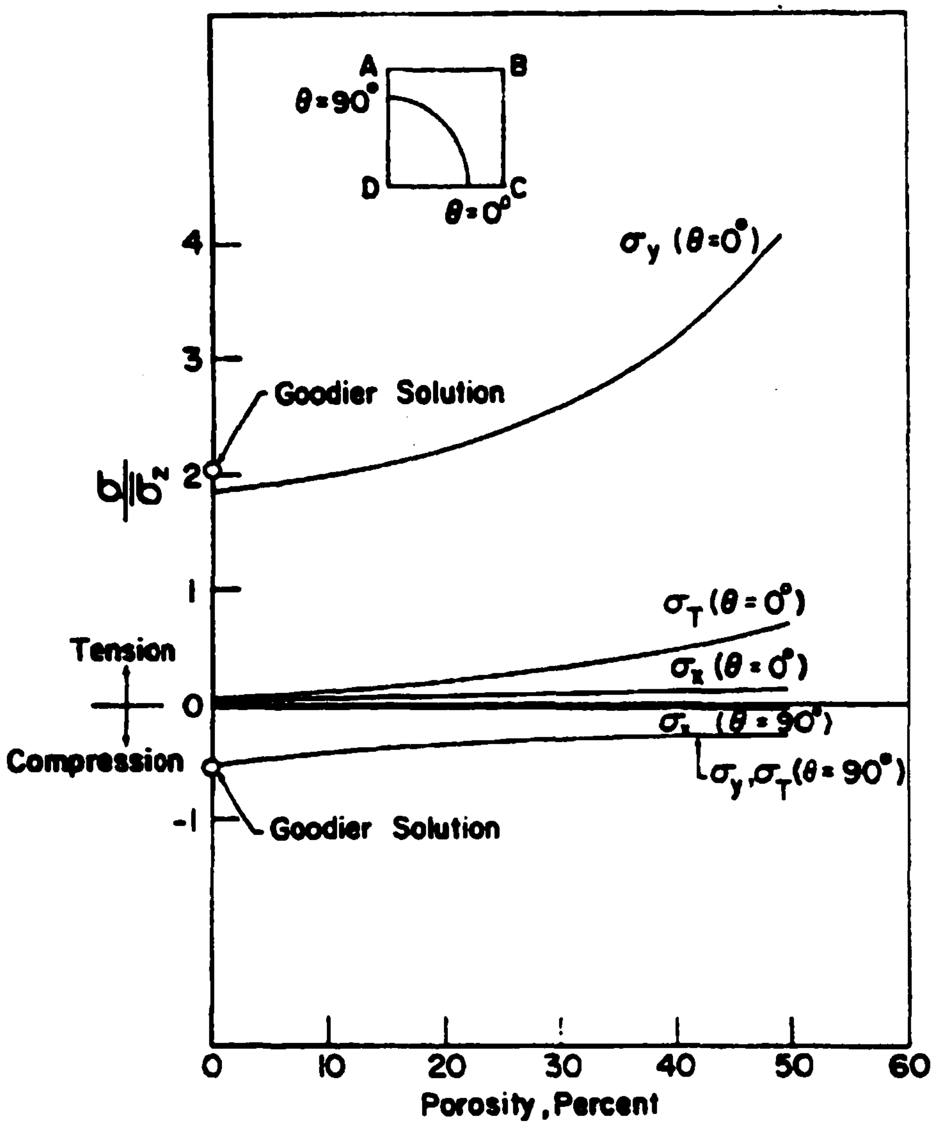

Figure 7. 34 FEM calculations of a cylindrical quarter-pore model in a uniform tensile stress field. The model shows an increase of the peak tensile stress with increasing porosity but did not use periodic boundary conditions and thus was not directly comparable to our results. After Agarwal (1971).

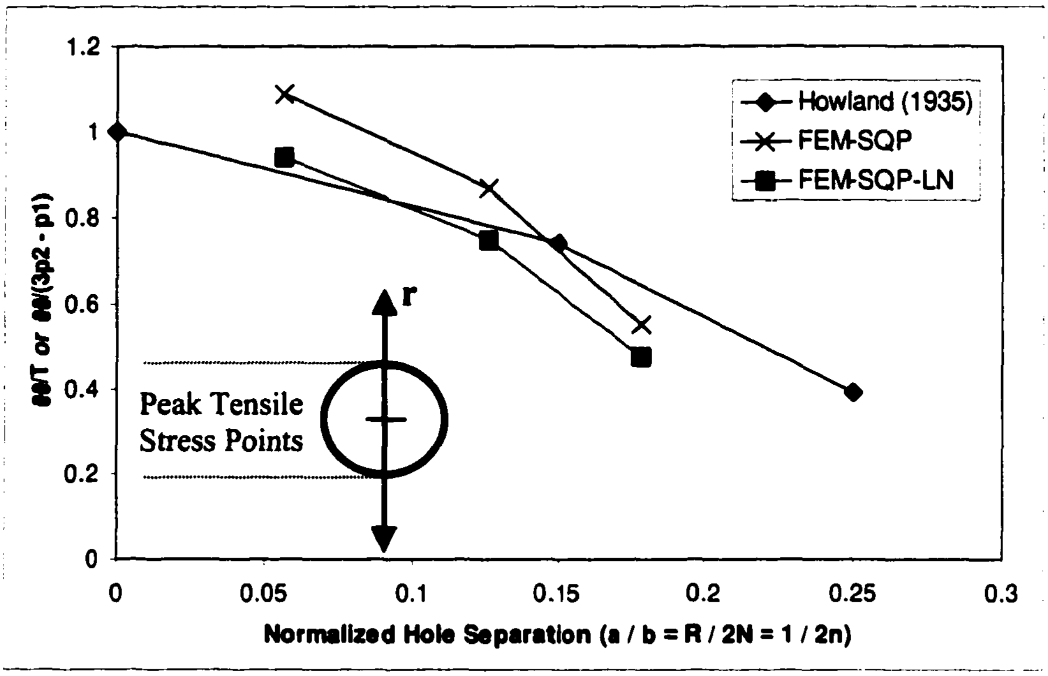

Figure 7. 35 A comparison of the analytical work by Howland (1935) on an infinite linear array of holes under a uniform applied tensile field. Signs were reversed from the original work to reflect a remote compressive stress rather than a tensile one. The FEM results of the orthogonal pore orientation determined by the square quarter-pore (SQP) model are shown for the normalized hole separation distance. The FEM-SQP results were normalized by the analytical value of an isolated pore, $3p_2 - p_1 = 2.5$ GPa. Normalizing the data with the linear regression intercept value of 2.88 GPa [FEM-SQP-LN] compensated for a discrepancy between the calculated value of peak stress for 0% porosity and the analytical value. Reasonable agreement with the analytical results of Howland (1935) was observed.

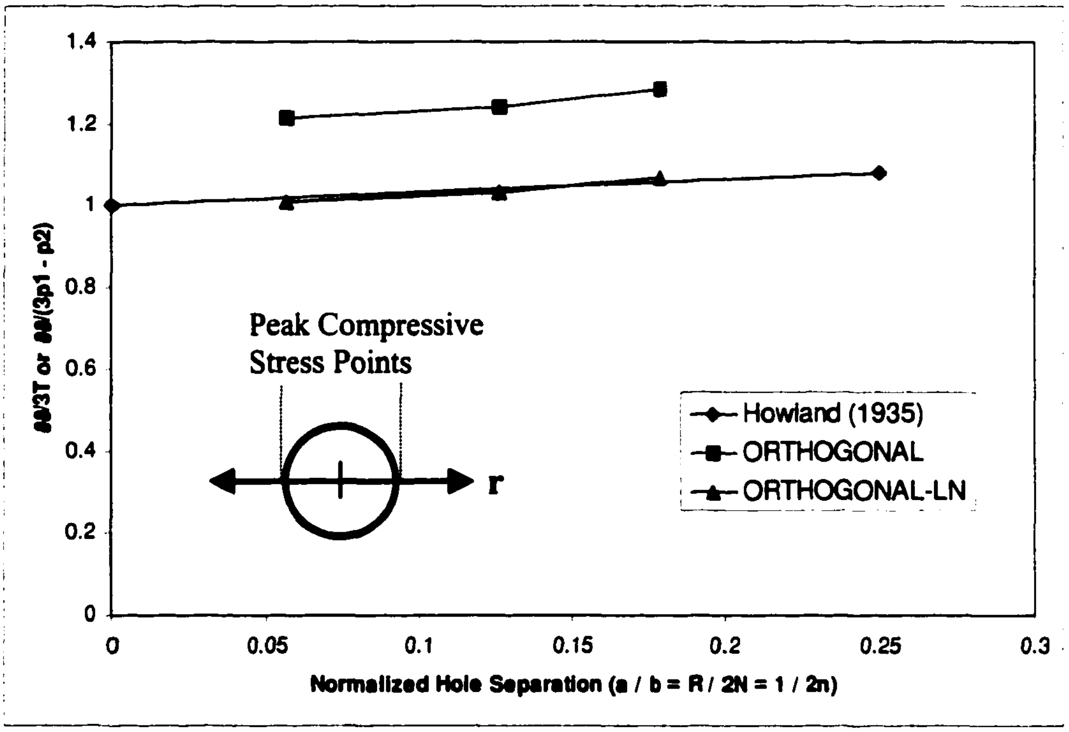

Figure 7. 36 The compressive stresses were also compared to the analytical work of Howland (1935) as in Fig. 7.35. Again, signs were reversed from the original work to reflect a remote compressive stress rather than a tensile one. The FEM results of the orthogonal pore orientation determined by the SQP model are shown for the normalized hole separation distance. The FEM-SQP results were normalized by the analytical value of an isolated pore, 3p1 – p2 (top curve). Because the data did not intercept the origin axis at the analytical value, the same data was replotted, normalized by the linear regression intercept value of 2.11 GPa [ORTHOGONAL-LN]. Clearly, the FEM results were in agreement with the analytical results of Howland (1935) after normalization.

7.4.2 Effect of a Second Phase

After determining the effect of porosity on stress concentrations around the surface of a hole, our attention turns to the role of the grain boundary glass phase. Many geometrical phase relationships occur between the porosity and the glass phase within the microstructures of LPS alumina. It was assumed that a glass film, aligned in the plane of maximum shear stress, would represent a critical and extreme effect on the mechanical properties; similar reasoning was applied to twin faulting (Lawn, 1994(b)). The model used in Fig. 7.9 reflects the presence of the glass phase at grain boundaries in the microstructure. At 10 vol% the peak stress and the stress within the bulk were similarly raised above the single phase material at all values of porosity. As noted before, 10 vol% glass was used in the models and was confined entirely at the grain boundary. In the real system, a majority of the glass was found in glassy pockets and in fact, the thickness at the grain boundary was limited by surface tension (Brada & Clarke, 1997; Clarke, 1987). A thinner glass film at the grain boundary caused the same behavior as the thick film and the distortional effects are shown in Fig. 7.29 for the model with the thinner film. The series of figures 7.25 – 7.27 revealed the bulk stresses of the model with the glass converged with the bulk stress value of the orthogonal model without glass. In fact, the point of convergence approached the surface of the hole as the porosity increased. At 1% porosity the convergence point was around r/R = 1. The crossover was equal to 0.8 for the 5% material and 0.6 in the 10% material. This result indicates that the glass phase was enhancing the compressive stress behavior of Fig. 7.16 and also modifying the tensile character of the stress at the hole surface. This fundamental result is clear evidence of the synergistic effect of the glass phase positioned at critical geometric points in the microstructure. For example, if the addition of a glass phase was simply a modulus effect, then the character of the stress would remain the same, only the magnitudes would be different. However, it was evident in the plots of both the compressive and tensile stresses that the fundamental distribution of stress within the microstructure was altered. This is in agreement with the recent FEM results of Wong and Wu (1995), although for a different geometric arrangement. It is important to note that Kulhawy (1975a,b,c,) studied the effect of an elastic and inelastic discontinuities using the FEM technique for a similar geometry but found little change in the stress conditions for several mismatches of elastic modulus. The discrepancy between the Kulhawy (1975(b)) results and the results presented herein can be explained by the choice of biaxial stress values. Kulhawy (1975(b)) used a biaxial stress ratio of $\lambda = 1/3$ or $3p_2 - p_1$ equaling zero: a condition where no tensile stresses are found on the interior of the hole. The lack of tensile stress by itself does not preclude the altering of the stress state within the body of the material. Ultimately, the controlling factor was the deviatoric stress which approaches zero as lambda approaches unity. Kulhawy also noted that the largest changes in the tensile and compressive stresses occurred when the discontinuity was aligned parallel to the direction of the primary compressive stress, p_1. Therefore, we conclude that at higher values of lambda, when the deviatoric or shear stresses tend to be reduced the influence of an elastic discontinuity on the plane of maximum shear stress is lessened. In this case, the inelastic discontinuity had a greater effect when aligned in the direction of the primary compressive load – presumably because the surface tangential stress on the hole would experience a reduced elastic modulus in the direction of its application. The glass phase within the microstructure significantly altered the local stress field around the surface of the pore such that a lowering of the critical failure stress would be expected from tensile regions.

7.5 Analytical Considerations of Fracture Mechanisms

7.5.1 Stress Intensity Factor for Biaxial Compression

Although the alumina samples under investigation were polycrystalline aggregates, they were strongly bonded enough to be considered isotropically solid materials. Continuum based solid mechanics and fracture principles were applied to develop an understanding of the damage initiation that would occur from a spherical defect under biaxial compressive stresses. The main assumption was that the 2D biaxial stress condition was similar to the axisymmetric stress condition beneath the Hertzian indenter. Remotely applied tensile failure has received the majority of attention in the literature with limited work focused on compressive failure of brittle materials by comparison. The notable exception has been from the geomechanics and geophysics research community. With respect to porosity, we now add the field of Hertzian contact to the areas of consideration for compressive failure. We will reiterate the limitations of continuum based mechanics to inherently discretized microstructures; the influence of crack growth, damage coalescence, and materials consolidation is better suited to computational methods (Bruno and Nelson, 1991) or analytical theories (Sammis and Ashby, 1986; Ashby and Hallam, 1986; Nemat-Nasser and Horii, 1982; Rudnicki and Rice, 1975; Biot, 1956, 1941). Our investigation was only concerned with the initiation of failure and did not address growth and subsequent accumulation of damage.

Accumulation of damage in this system from a mechanics perspective is a subject for future study.

Starting with the assumption of continuum mechanics and modeling the pore as circular, direct comparisons can be made to our experimental results shown in Chapter 6. In particular, we can directly compare the initiation of subsurface damage to surface initiated ring and cone cracking as a competition to reduce the overall system energy. As the strain energy density increases under the action of the indenter, many mechanisms exist to facilitate its release and are summarized at the end of this section. Here we will compare the macroscopic mechanism of ring/cone cracking to the microscopic mechanisms of quasi-ductile damage accumulation. We should note that the occurrence of one mechanism does not preclude the initiation of others at higher loading. Examining the surface, the stress intensity of a given flaw can be expressed as:

$$K_1 = \frac{1-2\nu}{2} \cdot P_m \cdot \sqrt{\pi c} \tag{7.4}$$

assuming a flaw size, c << δ, where $\delta = 0.02\,a = 2\ \mu\text{m}$ (compared to $c = 1\ \mu\text{m}$ this assumption is close but not exact: from Frank and Lawn, 1967). Because the indenter increases the stress on the surface as well as the bulk, Eq. 7.4 will be compared with Eq. 2.48 given for Sammis and Ashby's determination of K_I for a hole under biaxial compression. Eq. 2.48 may be rewritten in terms of the mean indentation load, P_m using Eq. 2.16 & 2.31:

$$K_I = -L^{1/2}\left\{\frac{1.1(1-2.1\lambda)}{(1+L)^{3.3}} - \lambda\right\} \cdot \left\{-\frac{3}{2}\left(1+\frac{z^2}{a^2}\right)^{-1} \cdot P_m\right\}\sqrt{\pi R} \tag{7.5}$$

where z = 0.45a such that Eq. 7.5 becomes:

$$K_I = -L^{1/2}\left\{\frac{1.1(1-2.1\lambda)}{(1+L)^{3.3}}-\lambda\right\}\cdot\{-1.25\cdot P_m\}\sqrt{\pi R} \qquad (7.6)$$

A plot of Eq. 7.4 and 7.6 is shown in Fig. 7.37 where Eq. 7.4 was normalized to K_{Ic} of the bulk alumina (3.25 MPa-$m^{1/2}$) and Eq. 7.5 was normalized to K_{Ic} of the glass phase (0.75 MPa-$m^{1/2}$). The bulk fracture toughness was used to normalize the surface stress intensity as the ring/cone crack path was largely transgranular. Conversely, cracking at the microstructural level proceeded through the glass containing grain boundaries and for that reason, a fracture toughness of glass was used to normalize Eq. 7.6. Moreover, Eq. 7.5 is shown for several values of L, which represented a range of flaw sizes for a fixed pore size or vice versa. Recalling the deformation character of the LPS alumina in Chapter 6, where quasi-ductility was observed before the presence of ring cracking, an explanation in light of the stress-concentrating behavior of the pore becomes evident. The flaw size for the surface was assumed similar to the subsurface flaw size of 1.1 micron ($L = 0.1$). A plot of the stress intensity for a given flaw size was shown in Fig. 7.37. From the graph, it becomes obvious that the critical stress intensity of the subsurface mechanism can be achieved first. We conclude that a stress intensity factor representation of porous failure was a plausible explanation for the experimental observations of quasi-ductility in the AA5-5G alumina.

Further examination the graph in Fig. 7.37 revealed that the surface stress intensity was lower for some flaw/pore size ratios than the stress intensity at the pore surfaces. The seemingly anomalous results observed for the fine grained A50-8 and A50-5G in Chapter 6 are now understood in terms of the stress intensity factors for the pore/flaw initiation. If the average flaw size remained constant when the pore radius was reduced, then the *L* value (*l* / *R*) would have increased. The short sintering time (~30 min) and low density may have left a larger radius of curvature on the grain faces resulting in a larger grain boundary groove depth and hence a larger effective flaw size – explaining why the flaw size may have effectively remained constant. Increasing the value of *L* for the A50-8 sample would explain its cone-cracking prior to quasi-ductile microfracture as the surface stress intensity factor exceeded the fracture toughness prior to exceeding the subsurface value of fracture toughness. Furthermore, the glass phase in A50-5G had a larger relative thickness of the grain boundary glass phase to the grain size which may have contributed to a tensile reduction in the grain contacts (Wong and Wu, 1995).

At this point we should reiterate a fundamental concept and assumption to understanding the damage in this system: brittle fracture under tension is inherently stochastic and hence probabilistic in nature. The distributed damage beneath the Hertzian indenter was tensile driven; however, the initiation of this damage will not be isolated to a single flaw, but distributed over the bulk. Therefore, damage was assumed to be controlled by the average pore/flaw statistics, rather than a single limiting value. In this way, one can immediately see the effect of size of the pore on the damage initiation behavior. Increasing the pore radius would increase the value of L and increase in the stress intensity factor for a fixed flaw size. The change in stress intensity factor is linked to the macroscopic indentation stress and would shift the curves in Fig. 7.37 as shown. From this analysis, we see how larger pores in the microstructure would be expected to collapse first.

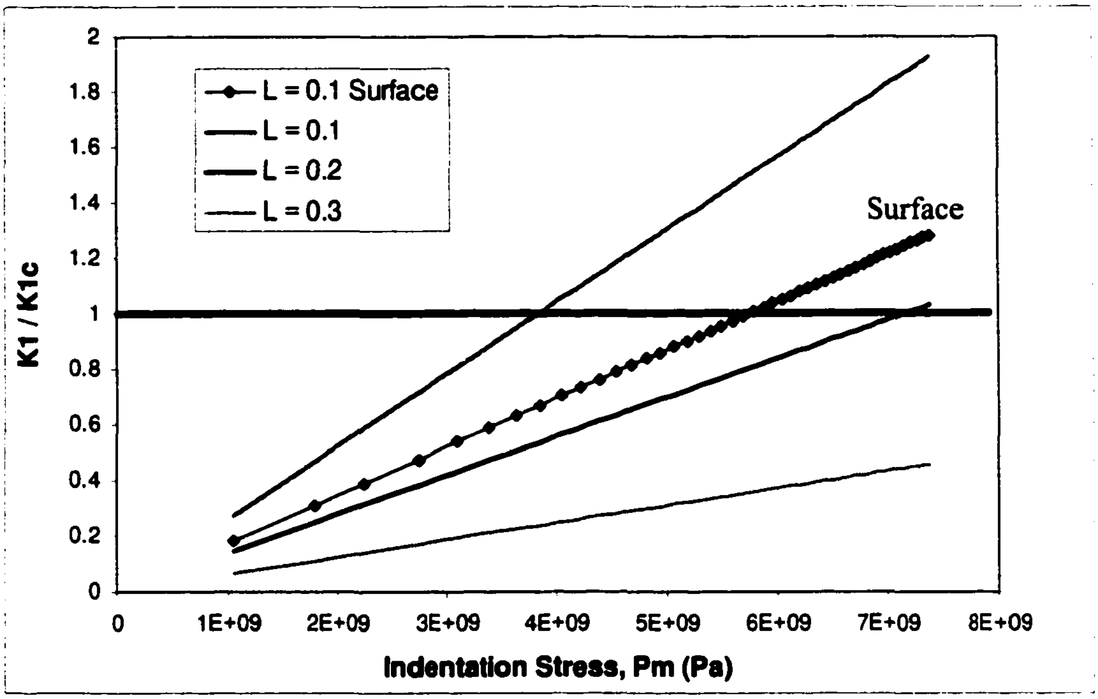

Figure 7. 37 Normalized stress intensity factor comparison between the indented surface and the subsurface porosity. For an assumed surface flaw size of 1.1 micron (*L* = 0.1), the surface stress intensity factor was lower than that of the subsurface porosity with a similar flaw size; fracture toughness being exceeded first beneath the indenter. This correlated with the observation of quasi-ductile damage initiation before ring-crack formation. Larger *L*, or smaller radius pores for a fixed flaw size would cause an decrease in the subsurface stress intensity factor leading to ring cracking being observed before the initiation of quasi-ductility. Experimental results confirmed this.

7.5.2 Predicting Critical Mean Indentation Stress

Having plotted the K_I values for the two independent failure initiation sites, it now becomes instructive to examine the microstructural variables in more detail to determine the influence of each. The FEM results indicated an increasing influence of porosity on the peak elastic stress concentrations around the pore. The results from Fig. 7.10, the plot of peak tensile stress, can be normalized with respect to the value of a peak tensile stress, $3p_2 - p_1 = 2.5$ GPa, for an isolated hole. The results are plotted in Fig. 7.38

and show a linearly increasing magnification of the peak tensile stress with porosity. This magnification effect can be incorporated into the Sammis and Ashby (1986) equation (Eq. 2.48) for stress intensity with a few assumptions. We must assume that the flaws within the pores are small such that they do not appreciably change the elastic modulus and ultimately the bulk stress distribution. Furthermore, to include the magnification factor into the Sammis and Ashby relation, it must be constant over the length of the crack for which the relation was determined. One can observe from Fig. 7.14 that the magnification of the stresses was constant to roughly a distance of 0.6 R (L = 0.6) from the surface of the hole. This defines the limitation of our assumption that magnification factor would be constant in the Green's function integral, integrated over the crack length, used by Sammis and Ashby (1986) to obtain Eq. 2.48. Being constant over the integration distance, the magnification relation modifies Sammis and Ashby's equation as follows:

$$K_I = -L^{1/2}\left\{\frac{1.1(1-2.1\lambda)}{(1+L)^{3.3}}-\lambda\right\}\cdot\{-1.25\cdot P_m\}\sqrt{\pi R}\cdot\{\xi P+1\} \qquad (7.7)$$

where P is the porosity and ξ is the slope of the normalized curve in Fig. 7.38. The magnification effect of porosity was indirectly supported by the analytical study of Isida and Nemat-Nasser (1987). From the graph in Fig. 2.22(b) Isida solved the stress intensity factors for a network of pores and cracks in various orientations. Isida conveniently used a tilted pore lattice (b/c = 1) and we can obtain the corresponding porosity from his values of interpore spacing. The pore magnification effect was extracted from data at short crack lengths as shown in Fig. 7.39. These results are plotted in Fig. 7.40 normalized to the isolated value (infinite pore spacing). A linear increase was observed with porosity paralleling the results obtained from FEM in our investigation. We acknowledge that the stress intensity factor will produce higher results than the pure elastic stress behavior but in the limit of very small flaw sizes they are nearly equal. The increased slope of Fig. 7.40 compared to that of Fig. 7.38 resulted from the value of $\lambda = 0$, a uniaxial applied stress. This underscores the importance of the deviatoric stress component on controlling brittle crack initiation – as well as brittle consolidation – under compressive stresses.

Through Eq. 7.7 we observed that the stress intensity factor for a given pore was related to the macroscopically applied stress. Rearranging, we can solve for the mean indentation stress in terms of the other factors creating a link between the micromechanical failure and macroscopic driving force. Normalizing to create a unitless function we have:

$$\frac{P_m \cdot \sqrt{\pi l}}{K_1} = -\frac{4}{5(\xi P + 1)} \cdot \left\{ \frac{1.1(1 - 2.1\lambda)}{(1 + L)^{3.3}} - \lambda \right\}^{-1} \tag{7.8}$$

The critical indentation load to initiate quasi-ductility scales with the grain boundary fracture toughness, $K_1 = K_{1c}^{gb}$, is dependent on the amount and distribution of porosity reflected in the values of P and ξ. A range of values of Pmc are plotted in Fig. 7.41 for L = 0.1 to 0.3 and $K_{1c}^{gb} = 0.75$ MPa-m$^{1/2}$ for glass. The predictions of the critical mean indentation stress at 5% porosity for the LPS alumina lie with the range of flaw sizes covered. Given the many assumptions necessary to make these predictions the fit is reasonable. Fig. 7.42 contains the data for the pure alumina with $K_{1c}^{gb} = 3.25$ MPa-m$^{1/2}$ and the data was significantly higher which partially explains the ring cracking before the onset of quasi-ductility. However, quasi-ductility does form at significantly lower stresses than indicated – around 5 – 7 GPa for all porous pure alumina. Flaw size may contribute to this but it is more likely due to yielding by other mechanisms such as microtwinning or slip. This was suggested in the subsurface images of Fig. 6.17 and 6.19 for pure porous alumina that showed virtually no cracking near the yield stress and cracking when it did occur at higher load, appeared to be through the grains.

Although this investigation examined a narrow range of porosity, Latella (1997) studied PLPS alumina over a larger range of porosity. Included in his results were the stress-strain curves that showed significant variation in the yield stress (Fig. 7.43). In this case, yield stress is essentially equivalent to P_m, varying slightly with Poisson's ratio (Johnson, 1985). Microstructural information was not available for the materials used in Latella (1997) so the same values from our investigation were used to make the predictions. Thus L = 0.1, K_{Ic}^{gb} = 0.7 MPa-m$^{1/2}$, and ξ = 8.81 were used to predict P_{mc}.

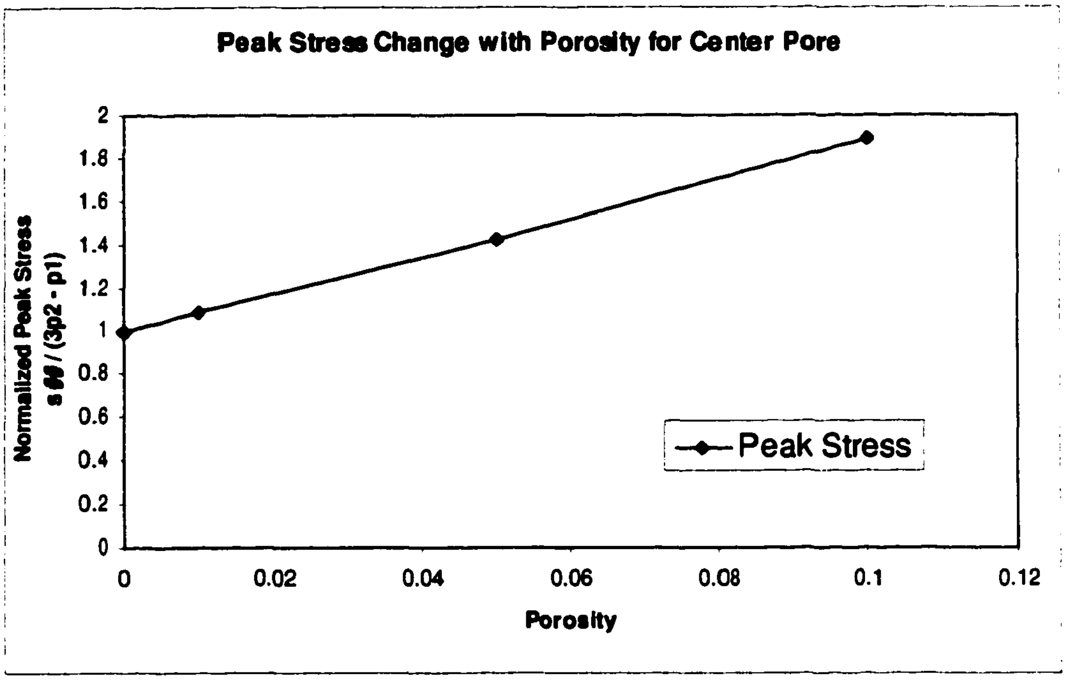

Figure 7. 38 Normalized peak tensile stress at the pore surface as a function of porosity. The slope of the regression analysis provided $\xi = 8.81$. This value was used in the magnification factor equation inserted into Eq. 7.7.

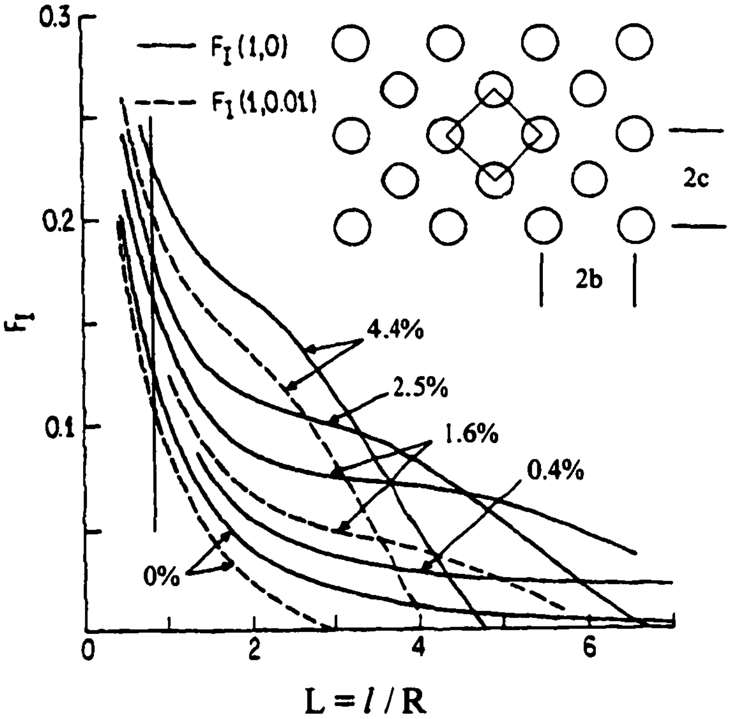

Figure 7. 39 Figure 2.22(b) showing the calculated stress concentration factor *f* by Isida and Nemat-Nasser (1987) for a tilted pore lattice. Extracted points from the graph for a short crack length at various porosity are plotted in Fig. 7.40.

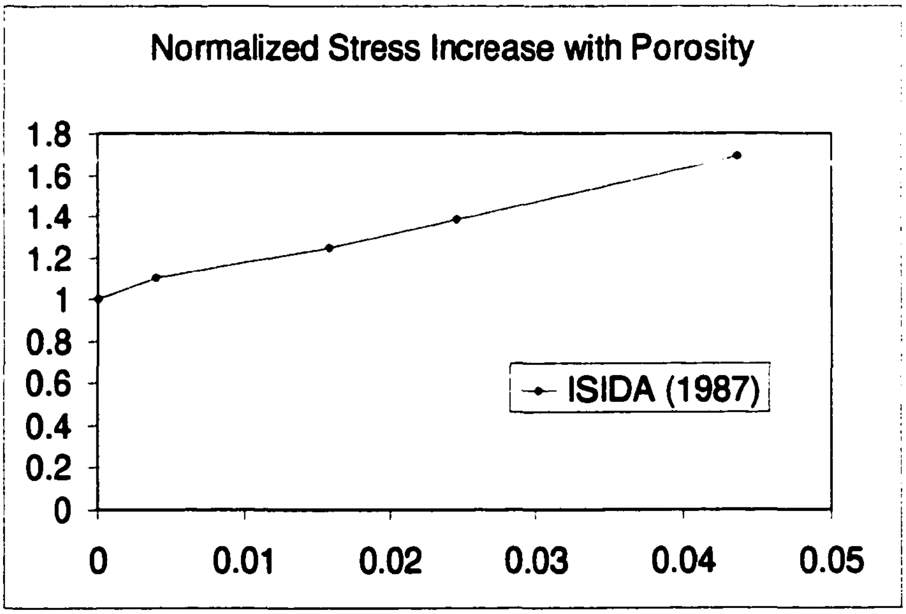

Figure 7. 40 A graph of the normalized stress magnification factor *f* for a tilted pore lattice taken from the plot shown in Fig. 7.39.

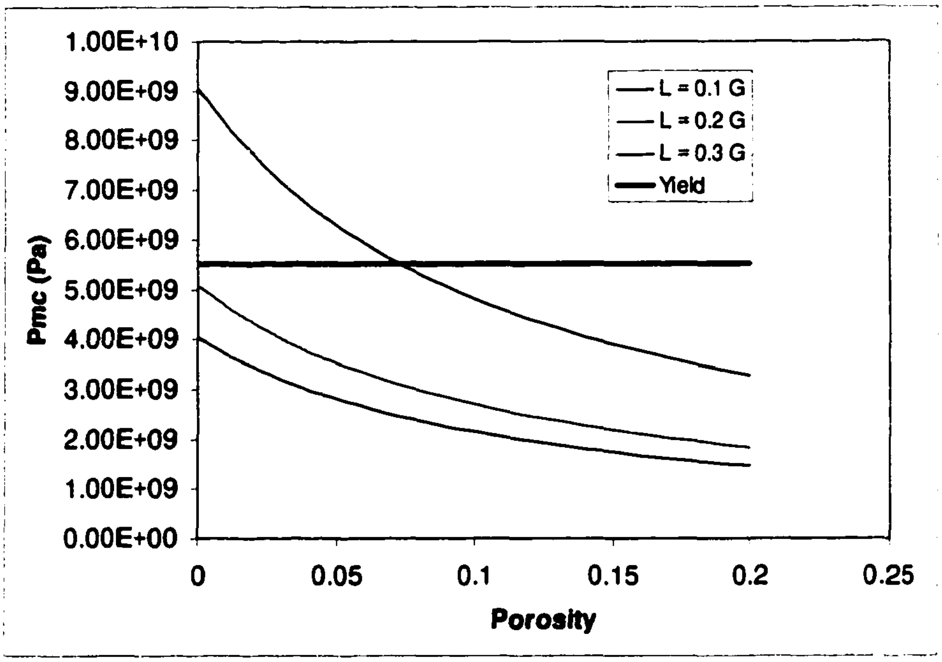

Figure 7. 41 Critical mean indentation stress predictions for a porous alumina with a glass phase at several values of L. The experimental value of P_{mc} is plotted for our LPS alumina with 5% porosity as the yield. The predictions for the alumina with glass lie between a flaw character of L = 0.1 and L = 0.2 for K1c of 0.75 MPa-m$^{1/2}$.

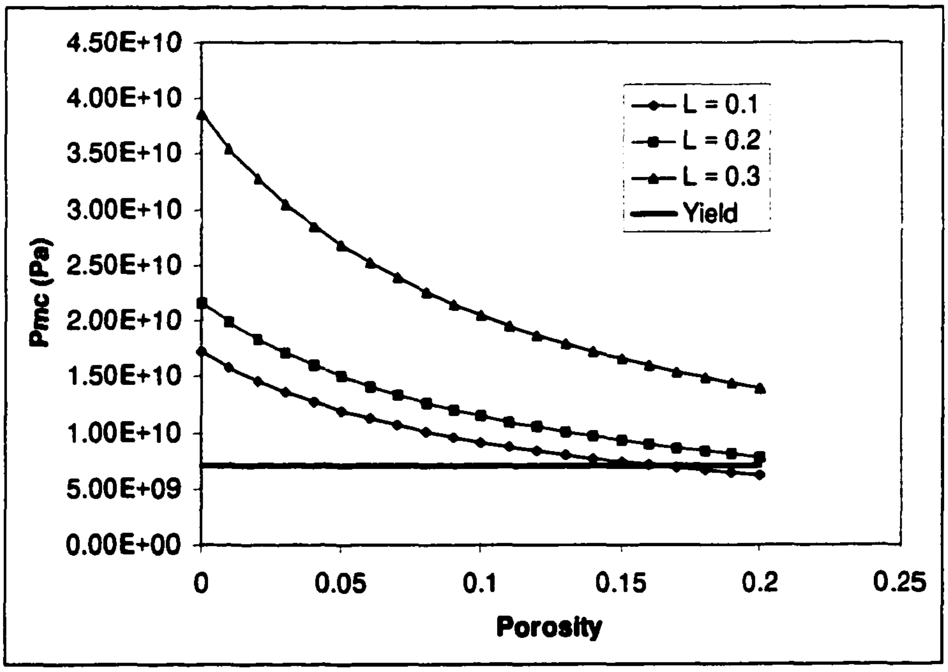

Figure 7. 42 Critical mean indentation stress predictions for pure porous alumina for several values of L. The higher values of L indicate that another mechanism may be controlling yield behavior.

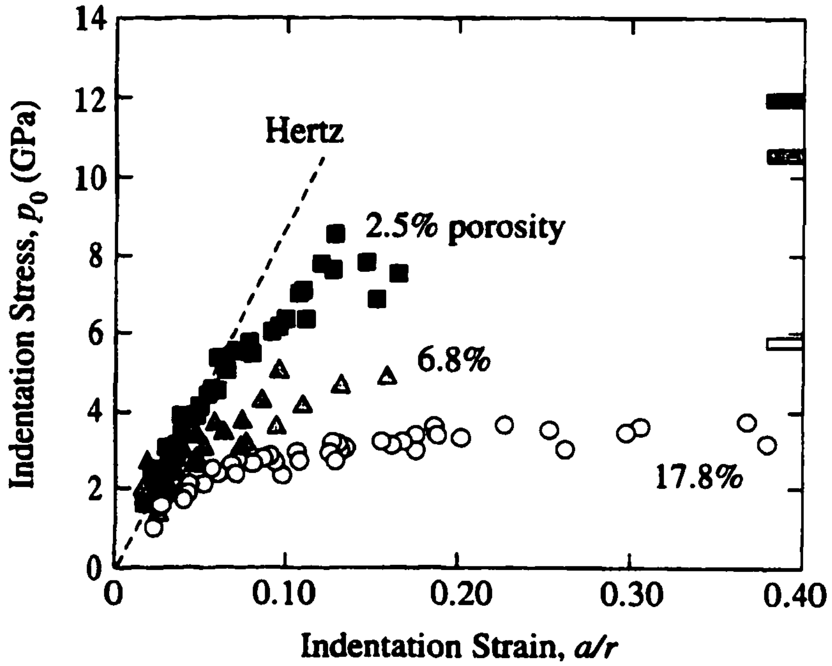

Figure 7. 43 Stress-strain curves of porous LPS alumina determined by Latella (1997). Although there is much scatter in the data, critical mean indentation stress was approximated from the point of deviation from the linear elastic behavior. These values are plotted in Fig. 7.44 and compared with predictions for the same material.

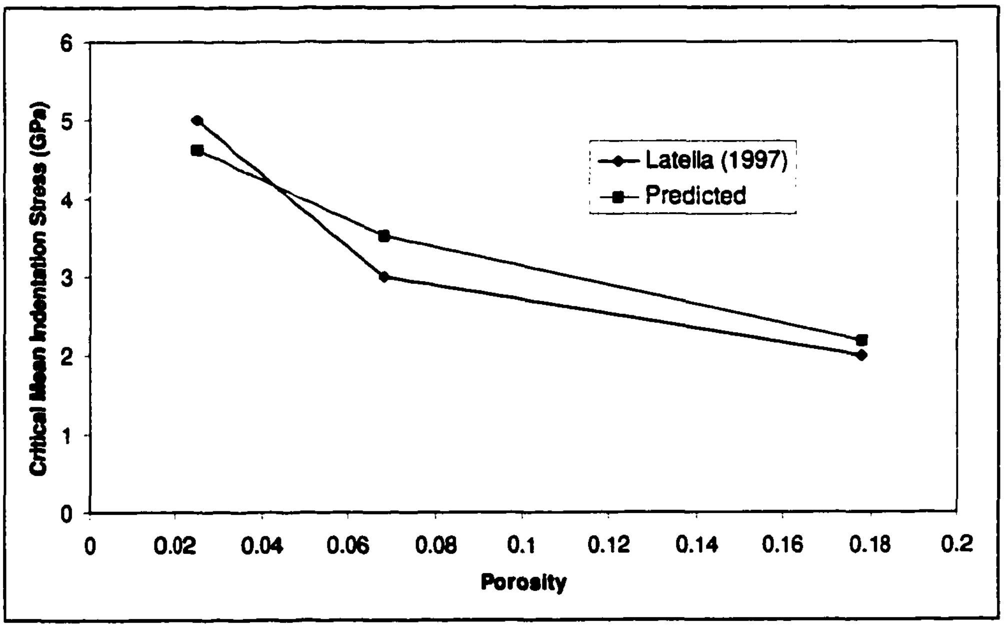

Figure 7. 44 Predicted critical mean indentation stress (L = 0.1) for the experimental data of Latella (1997). The comparison is good but the predictions rely on many approximations so the emphasis should be placed on the trend and not the exact values.

The ξ term was multiplied by 2/3 to account for the change from 2D to 3D (see Chapter 2) in the elastic stress solutions. The results are plotted in Fig. 7.44, with estimated values of P_{mc} from Latella's graph. Despite the many assumptions and the lack of detailed microstructural knowledge of Latella's material, the agreement was good. To a first order approximation, porosity was clearly the dominant failure mechanism under Hertzian contact in PLPS alumina. Again, these calculated results correlated with the observations that ring cracking was observed after subsurface deformation in the PLPS alumina measured optically and with the profilometer. In addition to porosity, failure will depend on plastic yield within an individual grain, axial splitting or cleavage within an individual grain, intergranular fracture, and intergranular friction/sliding.

We should briefly mention that compression dominated failure around pores has been observed in systems such as plaster of Paris (Vekinis, 1993; Lajitai & Lajitai, 1975) and assumed to control quasi-ductility in some porous sandstone (Hirth and Tullis, 1989). This failure mode, especially with the plaster materials, can be explained such that the grain size was very small with respect to the size of the holes. The holes were orders of magnitude larger than the grains and at low confining pressure, tensile cracking did dominate the failure process. However as the confining pressure increased, the compressive failure dominated with fractures occurring on conjugate shear planes at the sides of the hole perpendicular to the applied stress (Vekinis, 1993; Lajitai & Lajitai, 1975). With the very large number of grains around the hole, the compressive stress field approached a uniform condition with respect to the grain and flaw orientation. Failure could initiate from grains chipping out using the "persimmon seed" model by Adams and

Sines (1978). They describe a condition where dovetail-like chipping occurs from edges under uniform compressive stress. The result would be the initiation of failure by increasing the stress concentration at that point. Unlike the plaster models, the pores in the alumina were comprised of only a few grains - sometimes as few as three - and therefore were not likely to fail at the peak compressive stress point without crystalline plasticity.

Microtwinning or crystalline plasticity may be playing a small role in the deformation character under the indenter. Chapter 6 revealed apparent microtwinning in several grains of the LPS alumina after severe deformation. The compressive stresses under the indenter are high enough to cause slip in the alumina system (Bridgeman, 1952) and are exacerbated by the presence of porosity. Confirmation of crystalline plasticity would require a careful TEM investigation, which was not performed given the complexity of the technique.

7.6 CONCLUSIONS

- The peak tensile stress around a single hole was found to increase for a periodic array of holes under remotely applied compressive biaxial stresses where the NND was tilted at 45°; the increase was expressed as a stress magnification function (ξ P + 1) with a similar linearly increasing function being observed in previous literature.
- FEM results for peak stress behavior with increasing porosity in the orthogonal lattice orientation revealed similar trends to analytical calculations for a similar but more limited case of an infinite row of equal spaced holes.

- A lower modulus glassy grain boundary phase oriented in the plane of maximum shear stress magnified the peak tensile stress along the primary compressive stress loading axis indicating the glass may do more than simply provide a weak path for crack propagation.
- Although the largest unknown in the investigation was that of flaw size distribution within the pore, estimates of flaw sizes were sufficient to explain the occurrence of subsurface damage initiation prior to ring-cracking and vise versa for a range of similar normalized flaw sizes using normalized stress intensity factors.
- The stress magnification function determined by FEM in conjunction with the analytical description of stress concentration factor for a subsurface pore/flaw feature, allowed for reasonable predictions of macroscopic critical indentation stress in previously published work in LPS alumina.
- The influence of pore size was to increase the subsurface stress concentration factors when the flaw size remained fixed; similarly, the stress concentration factor was increased for small flaws with respect to a fixed pore size.
- Although the compressive stresses were often an order of magnitude higher than tensile stresses, the tensile stress dominated in the presence of the grain boundary liquid phase; the role of compressive stress may be more influential in pure materials where grain boundary fracture appeared less prevalent.

8. Summary

As we have discussed at various stages of this investigation, there were many ways for homogeneous damage to initiate in a brittle solid under multiaxial compression.

The damage mechanisms have been experimentally identified in two main areas: indentation of brittle ceramics and triaxial compression of geomaterials. They may be summarized as 1) Shear faulting - an existing crack plane or weak interface exists in a material whereby compressive stresses can overcome frictional forces to drive the two halves of the interface apart causing wing cracks to form at the fault extremities. 2) Twin faulting - very similar to shear faulting except that the fault forms along a twin boundary within the grain. Wing cracks formed at the edges of the shear fault and nucleation depended on grain size. 3) Crystalline plasticity - as a result of high pressure or increased temperature yield stress is accommodated by dislocation motion. Microtwinning was common in alumina under indentation at room temperature. 4) Pore collapse - in geomaterials the collapse of porosity has been associated with macroscopic quasi-ductile behavior. It is this last mechanism that we summarily ascribe to the observed quasi-ductility in the LPS alumina of this investigation. Experimentally we have demonstrated that the distributed microfracture was found only near the pores at loads just above the yield stress. Furthermore, cracking was almost exclusively through the grain boundary where the weaker glass phase existed. This result paralleled that of observations in geomechanics which found intergranular cracking to initiate prior to pore collapse in porous materials with weak cementing grain boundary phases.

Theoretically, we have identified the role of the pore as an individual stress concentrator. The subsurface stress intensity factor was increased for larger pores (fixed flaw size) and likewise for smaller flaw sizes (fixed pore size); the grain boundaries acting as nucleation points of fracture coupled with the weak glass phase at the grain boundary to enhance the failure process. FEM calculations placed further emphasis on the interaction of porosity on elastic stress concentration around a single pore. Moreover, the FEM results determined an orientation dependence of a periodic pore structure in a biaxial compressive stress field, which was correlated with published analytical calculations. Attempts at randomizing the pore structure corroborated the increasing stress trend. The generalized porosity interaction was incorporated with the fundamental stress intensity factor calculations to develop a predictive equation of the critical mean indentation load. Comparison to previously published data and those found in this investigation were in agreement with predictions. The stress intensity factor at the surface of the specimen under Hertzian contact was compared with the stress concentrating effects of the pore beneath the surface to determine the location and load for the onset of irreversible deformation. It was shown that the stress concentration factor of the porosity could explain the seemingly anomalous behavior of fine-grained alumina to larger grained alumina with and without a glass phase. We conclude that the porosity in the PLPS alumina was the microstructural mechanism responsible for the quasi-ductility observed beneath the Hertzian indenter and that this mechanism is valid for understanding distributed microfracture in all brittle materials under multiaxial compressive stresses.

8.1 Recommendations

Based on the results of this investigation, several suggestions can be made regarding the optimal microstructure to reduce contact related damage in commercial polycrystalline alumina. Obviously dense fine-grained materials have shown superior mechanical properties in past research (Evans and Langdon, 1976). If porosity must be incorporated into a microstructure, it follows that maximum resistance to quasi-ductility derives from smaller pores relative to the given internal flaw population. Unless porosity is controlled through artificial inclusions that burn out during firing, the grain size and sintering behavior will determine the final pore character (Zhao and Harmer, 1988) with smaller grains producing smaller pores (avoiding agglomeration of the powders). The same recommendation is made for LPS alumina: fine grain size or small pores with respect to the internal flaw population. The role of grain boundary microfracture through the glass phase suggests that residual compressive stresses at the grain boundary may help to reduce or delay the onset of quasi-ductility in the PLPS alumina as mentioned in Chapter 6. Further investigation is warranted.

9. SUGGESTIONS FOR FUTURE WORK

A hallmark of good research is the generation of more questions than answers. Certainly many pertinent questions remain with the results of this investigation. These areas will be highlighted below.

- Because the original investigation was not concerned with pore size – its true effect being revealed from a theoretical perspective – a controlled study of the pore size effect should follow. Polymer microspheres can be incorporated, as was done in the work of Zhao and Harmer (1988), to obtain a network of very spherical voids of a controlled size. This will simultaneously allow a study of the grain coordination effect on pore collapse, as it will control the flaw distribution.

- It follows that the internal flaw size distribution is clearly an important unknown in this investigation and an important parameter controlling deformation. With the equations provided and some careful statistics, one may back calculate the effective flaw size distributions, especially in conjunction with the polymer microsphere technique described earlier.

- As was brought up in the text, the pore/flaw initiation is not the only available deformation mechanism – especially at higher loads. Clearly, TEM work is required to ascertain the level of microtwinning or dislocation generation – if any – in the highly compressive region around the pore as it is often an order of magnitude higher than the tensile region.

- This entire investigation has relied on single-cycle indentation. Further studies with repeated or cyclic contact are necessary to understand fatigue effects on the damage behavior. Recall that Kubicki (1996) observed pore collapse in brittle metals under compressive fatigue. The PPI technique would prove invaluable for determining the difference between single-cycle and multi-cycle damage on the microstructure.

- We have only scratched the surface of the effects of second or multi-phased behavior. Experimentally, the next step should be to try to impart a residual compressive stress through recrystallization of the glassy grain boundary phase as Padture and Chan (1992) did with the low vol% anorthite alumina. Of course, this implies that reduced volume fractions of second phase could have a stronger influence than higher ones and should be investigated more closely. Theoretically, the FEM technique will be invaluable for studying multiple crack propagation under mixed mode loading conditions – analytically intractable problems – along with simultaneous application of residual compressive or tensile stress in the glass phase. Triple points should also be incorporated into the structure to assess their mechanical impact.

- The scope of the FEM work should be expanded to investigate inclusion effects as the applicability of the solutions will address composites as well. The inclusions can also be made elastic-plastic and thermal stresses add another dimension of commercial interest.

- Theoretically, for the same reasons described for the generalization of the FEM modeling, the effect of remotely applied *tensile* stress should be addressed. By considering tension, the commercial applications and relevant literature will increase an order of magnitude. This may be accomplished within the current framework of ideas with minimal effort.

- Macroscopically, several tests are necessary to verify the basic premise of the ideas in this dissertation and to address the viability of its results in making useful engineering predictions. A wear test – ball-on-disk or similar device – could easily be correlated with the mechanistic damage predictions as short crack toughness has been shown to control this effect (Lawn, 1998(a)). Very similar to wear testing is solid particle erosion. There has been clear evidence that microstructure plays an important role in erosion resistance, particle shape issues have been addressed by Hertzian and Vickers indenters, and there are a number of suitable industrial applications that consider solid particle erosion of brittle materials as shown the following references: Kamiya (1994); Anderson (1993); Hutchings (1992); Gochnour (1990); Rajendran and Kroupa (1989); Breder (1988(a)(b)); Wiederhorn and Hockey (1983); Evans (1978).

- Finally, the effect of the quasi-ductile damage on the overall strength of the bulk sample should be addressed. Similar to Lawn's (1998(b)) work in silicon nitride and micaceous glass-ceramics and that of Widjaja (1996) in alumina, tests should be performed to determine the effects of higher loading and repeated contacts on strength degradation.

REFERENCES

Adams, M. and G. Sines, "Crack Extension from Flaws in a Brittle Material Subjected to Compression," *Tectonophysics*, **49** 97-118 (1978)

Adler, T., "Elastic-Plastic Indentation of Hard, Brittle Materials with Spherical Indenters," *J. Am. Ceram. Soc.*, **77** [12] 3177-85 (1994)

Agarwal, B.D., Panizza, G. A., and L. J. Broutman, "Micromechanics Analysis of Porous and Filled Ceramic Composites," *J. Am. Ceram. Soc.*, **54** [12] p620-624 (1971)

Alves, J., "Effect of Liquid Phase on Coarsening Behavior in Porous Single-Phase and Duplex Microstructures," Ph.D. dissertation, Lehigh University (1997)

An, L., Chan, H.M., Padture, N. and Lawn, B., "Damage-Resistant Alumina-Based Layer Composites," *J. Mater. Res.*, **11** [1] 204-210 (1996)

Anderson, M., "Stress Distribution and Crack Initiation for an Elastic Contact Including Friction," *Int. J. Solids Structures*, **33** [25] 3673-3696 (1996)

Anderson, R.M., Adler, T.A. and J.A. Hawk, "Scale of Microstructure Effects on the Impact Resistance of Al_2O_3," *Wear*, **162-164** 1073-1080 (1993)

Ashby, M. and S. Hallam, "The Failure of Brittle Solids Containing Small Cracks under Compressive Stress States," *Acta met.*, **34** [3] 497-510 (1986)

Auerbach, F., "Measurement of Hardness," *Ann. Phys. Chem.*, **43** 61-100 (1891)

Bennison, S.J. and M. P. Harmer, "Swelling of Hot-Pressed Alumina," *J. Am. Ceram. Soc.*, **68** [11] 591-597 (1985)

Bennison, S.J. and M. P. Harmer, "Effect of MgO Solute on the Kinetics of Grain Growth in Al_2O_3," *J. Am. Ceram. Soc.*, **68** [11] p591-597 (1983)

Bickley, W.G., "The Distribution of Stress Round a Circular Hole in a Plate," *Phil. Trans. of the Roy. Soc., A.*, **226** 383-415 (1928)

Biot, M., "General Solutions of the Equations of Elasticity and Consolidation for a Porous Material," *J. App. Mech.*, **23** 91-96 (1956)

Biot, M., "General Theory of Three-Dimensional Consolidation," *J. App. Phys.*, **12** 155-164 (1941)

Boccaccini, A.R., "Comment on 'Effective Elastic Moduli of Porous Ceramic Materials," *J. Am. Ceram. Soc.*, **77** [10] 2779-81 (1994)

Boresi, A., Schmidt, R. and O. Sidebottom, "Advanced Mechanics of Materials," 5th ed., (John Wiley and Sons, New York, 1993)

Bouras, S. and B. Bouzabata, "Study of Hertzian Indentation on a Transparent Vitroceramic and on an Alumina," *Mat. Chem. Phys.*, **43** 127-134 (1996)

Bowie, O.L., "Analysis of an Infinite Plate Containing Radial Cracks originating at the Boudary of an Internal Circular Hole," *J. Math. Phys*, **35** 60-71 (1956)

Brace, W.F., Paulding, B.W. and C. Scholz, "Dilatancy in the Fracture of Crystalline Rocks," *J. Geophys. Res.*, **71** [16] 1966

Brada, M. and D. Clarke, "A Thermodynamic Approach to the Wetting and Dewetting of Grain Boundaries," *Acta Mater.*, **45** [6] 2501-08 (1997)

Breeder, K., De Portu, G., Ritter, J.E. and D. Dalle Fabbriche, "Erosion Damage and Strength Degradation of Zirconia-Toughened Alumina," J. Am. Ceram. Soc., **71** [9] 770-75 (1988)(a)

Breeder, K., Ritter, J.E. and K. Jakus, "Strength Degradation in Polycrystalline Alumina Due to Sharp-Particle Impact Damage," J. Am. Ceram. Soc., **71** [12] 1154-58 (1988)(b)

Bridgman, P. W., "Studies in Large Plastic Flow and Fracture," (McGraw-Hill, New York 1952)

Broek, D., "Elementary Engineering Fracture Mechanics," 4th ed., (Kluwer Academci Publishers, Boston, 1991)

Bruno, M.S. and R.B. Nelson, "Microstructural Analysis of the Inelastic Behavior of Sedimentary Rock," *Mech. Mat.*, **12** 95-118 (1991)

Byerlee, J.D., "Brittle-Ductile Transition in Rocks," *J. Geophys. Res.*, **73** [14] 4741-50 (1968)

Cai, H., Stevens Kalceff, M. A. and B. R. Lawn, "Deformation and Fracture of Mica-Containing Glass-Ceramics in Hertzian Contact," *J. Mater. Res.*, **9** [3] 762-770 (1994)(a)

Cai, H., Stevens Kalceff, M. A., Hooks, B. M., Lawn, B. R. and K. Chyung, "Cyclic Fatigue of a Mica-Containing Glass-Ceramic at Hertzian Contacts," *J. Mater. Res.*, **9** [10] 2654-61 (1994)(b)

Castaing, J, Cadoz, J. and S.H. Kirby, "Prismatic Slip of Al_2O_3 Single Crystals Below 1000°C in Compression Under Hydrostatic Pressure," *J. Am. Ceram. Soc.*, **64** [9] 504-511 (1981)

Chan, H. and B.R. Lawn, "Indentation Deformation and Fracture of Sapphire," *J. Am. Ceram. Soc.*, **71** [1] 29-35 (1988)

Chaudhri, M., "Subsurface Deformation Patterns Around Indentations in Work-Hardened Mild Steel," *Phil. Mag. A*, **67** [2] 107-115 (1993)

Chen, S., Farris, T. and S. Chandrasekar, "Contact Mechanics of Hertzian Cone Cracking," *Int. J. Solids Structures*, **32** [3/4] 329-40 (1995)

Chou, P.C. and M.J. Pagano, "Elasticity: Tensor, Dyadic, and Engineering Approaches," {Dover, New York, 1992} (org. publication: Van Nostrand, Princeton, 1967)

Clarke, D.R., "On the Equilibrium Thickness of Intergranular Glass Phases in Ceramic Materials," *J. Am. Ceram. Soc.*, **70** [1] 15-22 (1987)

Clarke, D.R. and G. Thomas, "Grain Boundary Phases in a Hot-Pressed MgO Fluxed Silicon Nitride," *J. Am. Ceram. Soc.*, **60** [11-12] 491-495 (1977)

Dai, D., Hills, D., Warren, P. and D. Nowell, " The Propulsion of Surface Flaws by Elastic Indentation Testing," *Acta metall. mater.*, **43** [3] 985-991 (1995)

DiGiovanni, A., Chan, H., and M. Harmer, "The Synergistic Effects of Glass and Porosity on Quasi-Ductility Under Hertzian Contact in LPS Alumina," *J. Am. Ceram. Soc.*, **82** [3] 749-752 (1999)

Dong, W., Jain, H. and M. Harmer, "Microstructure Evolution of Alumina in Liquid Phase Sintering," (1997); to be published

Du, Z.Z. and F.W. Zok, "Limit Stress Conditions for Weakly Bonded Fiber Composites Subject to Transverse Biaxial Tensile Loading," *Int. J. Solids Structures*, **35** [21] 2821-42 (1998)

Evans, A.G., "Perspective on the Development of High-Toughness Ceramics," *J. Am. Ceram. Soc.*, **73** [2] 197-206 (1990)

Evans, A.G. and R.M. Cannon, "Toughening of Brittle Solids by Martensitic Transformations: Overview No. 48," *Acta metall.*, **34** [5] 761-800 (1986)

Evans, A.G., Gulden, M.E. and M. Rosenblatt, "Impact Damage in Brittle Materials in the Elastic-Plastic Response Regime," *Proc. R. Soc. Lond. A.*, **361** 343-365 (1978)

Evans, A.G. and T. Langdon, "Structural Ceramics," Progress in Materials Science, **21** 171-441 (1976)

Evans, B., Fredrich, J.T. and T.F. Wong, "The Brittle-Ductile Transition in Rocks: Recent Experimental and Theoretical Progress," *Am. Geophys. Un. Geophys. Monogr.*, **56** 1-20 (1990)

Fabrikant, V. I., "Several Elliptical Punches on an Elastic Half Space," *J. of Appl. Mech.*, **53** 390-394 (1986)

Field, J. and M. Swain, "A Simple Predictive Model for Spherical Indentation," *J. Mat. Res.*, **8** [2] 297-306 (1993)

Fischer-Cripps, A., "Introduction to Contact Mechanics," Sydney, Australia (1998): *to be published*

Fischer-Cripps, A., "Predicting Hertzian Fracture," *J. Mat. Sci.*, **32** 1277-85 (1997)(a)

Fischer-Cripps, A., "Elastic-Plastic Behaviour in Materials Loaded with a Spherical Indenter," *J. Mat. Sci.*, **32** 727-736 (1997)(b)

Fischer-Cripps, A. and R. Collins, "The Probability of Hertzian Fracture," *J. Mat. Sci.*, **29** 2216-30 (1994)

Fischer-Cripps, A. and B. Lawn, "Stress Analysis of Contact Deformation in Quasi-Plastic Ceramics," *J. Am. Cer. Soc.*, **79** [10] 2609-18 (1996)(a)

Fischer-Cripps, A. and B. Lawn, "Indentation Stress-Strain Curves for "Quasi-Ductile" Ceramics," *Acta met.*, **44** [2] 519-527 (1996)(b)

Fleck, N., Otoyo, H. and A. Needleman, "Indentation of Porous Solids," *Int. J. Solids Structures*, **29** [13] 1613-36 (1992)

Follansbee, P. and G. Sinclair, "Quasi-Static Normal Indentation of an Elasto-Plastic Half-Space by a Rigid Sphere - I Analysis," *Int. J. Solids Structures*, **20** [1] 81-91 (1984)

Frank, F. and B. Lawn, "On the Theory of Hertzian Fracture," *Proc. Roy. Soc. Lond.*, **A299** 291-306 (1967)

Fredrich, J.T., Evans, B. and T.F. Wong, "Micromechanics of the Brittle to Plastic Transition in Carrara Marble," *J. Geophs. Res.*, **94** [B4] 4129-45 (1989)

Fuchs, S. "Hauptspannungstrajektorien bei der Berührung einer kugel mit einer Platte," *Physik. Zeitschr.*, **14** 1282-85 (1913)

Galin, L., "Contact Problems in the Theory of Elasticity," I. N. Sneddon (ed), North Carolina State College, Dept. Math. Engr. Res., Raleigh (1961)

Gere, J.M. and S.P. Timoshenko, "Mechanics of Materials," 2nd ed., (PWS-Kent, Boston, 1984)

Goodier, J., "Concentration of Stress Around Spherical and Cylindrical Inclusions and Flaws," Trans. ASME, *J. Appl. Mech.*, **55** 39-44 (1933)

Gouchnour, S., Bright, J.D., Shetty, D.K. and R.A. Cutler, "Solid Particle Erosion of SiC-Al_2OC Ceramics," *J. Mat. Sci.*, **25** 3229-35 (1990)

Greenwood, J., "Exact Formulae for Stresses Around Circular Holes and Inclusions," *Int. J. Mech. Sci.*, **31** [3] 219-227 (1989)

Griffith, A., "The Theory of Rupture," pp55-63, in Proc. 1st Int. Congress Appl. Mech., C. B. Biezeno and J. M. Burgers, eds., J. Waltman Jr., Delft (1924)

Griffith, A., "The Phenomena of Rupture and Flow in Solids," *Phil. Trans. Roy. Soc. of London*, **A221** 163-97 (1920)

Griggs, D.T., "Deformation of Rocks under High Confining Pressures," *J. Geol.*, **44** 541-577 (1936)

Guiberteau, F., Padture, N. P. and B. R. Lawn, "Effect of Grain Size on Hertzian Contact Damage in Alumina," *J. Am. Ceram. Soc.*, **77** [7] 1825-31 (1994)

Guiberteau, F., Padture, N. P., Cai, H. and B. R. Lawn, "Indentation Fatigue: A Simple Cyclic Hertzian Test for Measuring Damage Accumulation in Polycrystalline Ceramics," *Phil. Mag. A.*, **68** [5] 1003-1016 (1993)

Hadizadeh, J. and E. H. Rutter, "The Low Temperature Brittle-Ductile Transition in a Quartzite and the Occurrence of Cataclastic Flow in Nature," *Geologische Rundschau*, **72** [2] 493-509 (1983)

Hadizadeh, J. and E. H. Rutter, "Experimental Study of Cataclastic Deformation of a Quartzite," Issues in rock mechanics: Proceedings, 23rd Symposium on Rock Mechancis, the University of California, Berkeley, California, August 25-27, 1982, pp372-379

Hamilton, B. and H. Rawson, "The Determination of the Flaw Distributions on Various Glass Surfaces from Hertz Fracture Experiments," *J. Mech. Phys. Solids*, **18** 127-147 (1970)

Hanson, M.T. and I.W. Puja, "The Elastic Field Resulting from Elliptical Hertzian Contact of Transversely Isotropic Bodies: Closed-Form Solutions for Normal and Shear Loading," *J. Appl. Mech.*, **64** 457-465 (1997)

Hanson, M. T. and T. Johnson, "The Elastic Field for Spherical Hertzian Contact of Isotropic Bodies Revisted: Some Alternative Expressions," *J. of Tribology*, **115** 327-332 (1993)

Hardy, C., Baronet, C. and G. Tordion, "The Elasto-Plastic Indentation of a Half-Space by a Rigid Sphere," *Int. J. Num. Meth. Engr.*, **3** 451-462 (1971)

Harmer, M. P., "Use of Solid-Solution Additives in Ceramic Processing," pp. 679-696, in Advances in Ceramics, Structure and Properties of MgO and Al_2O_3 Ceramics," vol. 10, The American Ceramic Society, Westerville, OH (1985)

Hasselman, D.P.H., "On the Porosity Dependence of the Elastic Moduli of Polycrystalline Refractory Materials," *J. Am. Ceram. Soc.*, **45** [9] (1962)

Hertz, H., "Über die Berührung fester elastischer Körper," *J. Reine Angew. Math.*, **92** 156-171 (1881)

Hertz, H., "Miscellaneous papers," (Macmillan, London, Chs 5 and 6, 1896)

Hertzberg, R. "Deformation and Fracture Mechanics of Engineering Materials," 4th ed., (John Wiley & Sons, New York, 1996)

Hill, R., "The Mathematical Theory of Plasticity," (Clarendon Press, Oxford, U.K., 1950)

Hirth, G. and J. Tullis, "The Effects of Pressure and Porosity on the Micromechanics of the Brittle-Ductile Transition in Quartzite," *J. Geophys. Res.*, **94** [B12] 17825-38 (1989)

Howland, R.C.J., "Stresses in a Plate Containing an Infinite Row of Holes," *Proc. Roy. Soc. A*, **198** 471-491 (1935)

Huber, M., "Zur Theorie der Berührung fester elasticher Körper," *Ann. d. Phys.*, **14** 153-163 (1904)

Huber, M. and S. Fuchs, "Spannungsverteilung bei der Berührung zweier elasticher Zylinder," *Physik. Zeitschr.*, **15** 298-303 (1914)

Huber, N. and Ch. Tsakmakis, "A Finite Element Analysis of the Effect of Hardening Rules on the Indentation Test," *J. Engr. Mat. Tech.*, **120** 143-148 (1998)

Hutchings, I.M, "Ductile-Brittle Transitions and Wear Maps for the Erosion and Abrasion of Brittle Materials," *J. Phys. D: Appl. Phys.*, **25** A212-A221 (1992)

Irwin, G., *Trans. ASME, J. Appl. Mech.*, **24** 361 (1957)

Irwin, G. "Fracturing of Metals," (ASM, Cleveland, OH, 1949)

Isida, M. and Nemat-Nasser, S., "On Mechanics of Crack Growth and its Effects on the Overall Response of Brittle Porous Solids," *Acta metall.*, **35** [12] p2887-98 (1987)

Jaeger, J. and N. Cook, "Fundamentals of Rock Mechanics," (Chapman and Hall, New York 1969)

Johnson, K. L., "Contact mechanics" (Cambridge University Press, Cambridge 1985)

Kamiya, H. Sakakibara, Y.S. and G. Jimbo, "Erosion Wear Properties of Tetragonal ZrO_2 (Y_2O_3)-Toughened Al_2O_3 Composites," *J. Am. Ceram. Soc.*, **77** [3] 666-672 (1994)

Kármán, T. von "Festigkeitsversuche unter allseitegem Druck," *Z. Verein. Dtsch. Ing.*, **55** 1749-57 (1911)

Kaysser, W., Sprissler, M., Handwerker, C. and J. Blendell, "Effect of Liquid Phase on the Morphology of Grain Growth in Alumina," *J. Am. Ceram. Soc.*, **70** [5] 339-343 (1997)

Kirsch (1898): as referenced in "Strength of Materials: Part II, Advanced Theory and Problems," by S. Timoshenko, 2nd ed., (Van Nostrand, New York, 1951) p313

Knudsen, F.P., "Effect of Porosity on Young's Modulus of Alumina," *J. Am. Ceram. Soc.*, **45** [2] 94-95 (1962)

Kocer, C. and R. Collins, "The Angle of Hertzian Cone Cracks," *J. Am. Ceram. Soc.*, **91** [7] 1736-42 (1998)

Koval'chenko, M.S., "Mechanical Properties of Isotropic Porous Materials III. Strain-Hardening and Failure," *Poroshkovaya Metallurgiya*, No. 5, 64-70 (1993)

Krolevets, M.S., "A Critical Survey of Methods of Solving the Contact Problem of Elasticity Theory," *Prikladnaya Mekhanika*, **2** [11] 68-82 (1966)

Kubicki, B., "About Endurance Limit of Ductile Inhomogeneous Materials," *J. Mat. Sci.*, **31** 2475-79 (1996)

Kulhawy, F. H., "Stresses and Displacements around Openings in Homogeneous Rock," *Int. J. Rock Mech. Min. Sci. & Geomech. Abstr.*, **12** 43-57 (1975)(a)

Kulhawy, F. H., "Stresses and Displacements around Openings in Rock Containing an Elastic Discontinuity," *Int. J. Rock Mech. Min. Sci. & Geomech. Abstr.*, **12** 59-72 (1975)(b)

Kulhawy, F. H., "Stresses and Displacements around Openings in Rock Containing an Inelastic Discontinuity," *Int. J. Rock Mech. Min. Sci. & Geomech. Abstr.*, **12** 73-78 (1975)(c)

Lajtai, E.Z. and V.N. Lajtai, "The Collapse of Cavities," *Int. J. Rock Mech. Min. Sci. & Geomech. Abstr.*, **12** 81-86 (1975)

Lange, F.F., "Fabrication and Properties of Dense Polyphase Silicon Nitride," *J. Am. Ceram. Soc.*, **62** [12] 1369-74 (1983)

Latella, B., O'Connor, B. H., Padture, N. and B. Lawn, "Hertzian Contact Damage in Porous Alumina Ceramics," *J. Am. Ceram. Soc.*, **80** [4] 1027-31 (1997)

Laugier, M. "Hertzian Indentation of Sintered Alumina," *J. Mat. Sci.*, **19** 254-258 (1984)

Lawn, B. "Indentation of Ceramics with Spheres: A Century After Hertz," *J. Am. Ceram. Soc.*, **81** [9] 2394-2404 (1998)(a)

Lawn, B.R., Lee, S.K., Peterson, I.M. and S. Wuttiphan, "Model of Strength Degradation from Hertzian Contact Damage in Tough Ceramics," *J. Am. Ceram. Soc.*, **81** [6] 1509-20 (1998)(b)

Lawn, B. and D. Marshal, "Nonlinear Stress-Strain Curves for Solids Containing Closed Cracks with Friction," *J. Mech. Phys. Solids*, **46** [1] 85-113 (1998)

Lawn, B., Padture, N., Cai, H. and F. Guiberteau, "Making Ceramics 'Ductile'," *Science*, **263** 1114-16 (1994)(a)

Lawn, B., Padture, N., Guiberteau, F. and H. Cai, "A Model for Microcrack Initiation and Propagation Beneath Hertzian Contacts in Polycrystalline Ceramics," *Acta met. mat.*, **42** [5] 1683-93 (1994)(b)

Lawn, B., "Fracture of Brittle Solids," 2nd ed., (Cambridge University Press, Cambridge, 1993)

Lee, S.K. and B. R. Lawn, "Role of Microstructure in Hertzian Contact Damage in Silicon Nitride: II, Strength Degradation," *J. Am. Ceram. Soc.*, **81** [4] 997-1003 (1998)

Liu, H., Lawn, B. R. and S. M. Hsu, "Hertzian Contact Response of Tailored Silicon Nitride Multilayers," *J. Am. Ceram. Soc.*, **79** [4] 1009-14 (1996)

Love, A., "A Treatise on the Mathematical Theory of Elasticity," 4th ed., (Dover Publishing, New York, 1944)

Makino, H., Kamiya, N. and S. Wada, "Effects of Grain Size of Hot-Pressed Silicon Nitride on Contact Damage Morphology and Residual Strength," *J. Am. Ceram. Soc.*, **74** [8] (1991)

McColm, I., "Ceramic Hardness," (Plenum Press, New York, 1990)

Menendez, B., Zhu, W. and T.-F. Wong, "Micromechanics of Brittle Faulting and Cataclastic Flow in Berea Sandstone," *J. of Str. Geo.*, **18** [1] 1-16 (1996)

Milman, Y.V., Galanov, B.A. and S.I. Chugunova, "Plasticity Characteristic Obtained Through Hardness Measurement: Overview No. 107," *Acta metall. Mater.*, **41** [9] 2523-32 (1993)

Mogi, K., "Pressure Dependence of Rock Strength and Transition from Brittle Fracture to Ductile Flow," *Bull. Earthquake Res. Inst., Tokyo Univ.*, **44** 215-232 (1966)

Montmitonnet, P., Edlinger, M.L. and E. Felder, "Finite Element Analysis of Elastoplastic Indentation: Part 1 – Homogeneous Media," *J. Appl. Mech.*, **115** 10-14 (1993)

Morton, W.B. and L.J. Close, "Notes on Hertz's Theory of the Contact of Elastic Bodies," *Phil. Mag.*, **43** [254] 320-329 (1922)

Mulhearn, T., "The Deformation of Metals by Vickers-Type Pyramidal Indenters," *J. Mech. Phys. Solids*, **7** 86-96 (1959)

Nash, A., "Compressive Failure Modes of Alumina in Air and Physiological Media," *J. Mat. Sci.*, **18** 3571-77 (1983)

Nemat-Nasser, S. and H. Horii, "Compression-Induced Nonplanar Crack Extension with Application to Splitting, Exfoliation, and Rockburst," *J. Geophys. Res.*, **87** [B8] 6805-21 (1982)

Nemat-Nasser, S., Iwakuma, T. and M. Hejazi, "On Composites with Periodic Structure," *Mech. of Mat.*, **1** [3] 239-67 (1982)

Padture, N. and B. R. Lawn, "Contact Fatigue of a Silicon Carbide with a Heterogeneous Grain Structure," *J. Am. Ceram. Soc.*, **78** [6] 1431-38 (1995)(a)

Padture, N. and B. Lawn, "Fatigue in Ceramics with Interconnecting Weak Interfaces: A Study Using Cyclic Hertzian Contacts," *Acta met. mat.*, **43** [4] 1609-17 (1995)(b)

Padture, N. P. and H. M. Chan, "Improved Flaw Tolerance in Alumina Containing 1 vol% Anorthite via Crystallization of the Intergranular Glass," *J. Am. Ceram. Soc*, **75** [7] 1870-75 (1992)

Padture, N.P. and H. M. Chan, "Influence of Grain Size and Degree of Crystallization of Intergranular Glassy Phase on the Mechanical Behavior of a Debased Alumina," *J. Mat. Sci.*, **26** 2711-15 (1991)

Pajares, A., Guiberteau, F. and B. R. Lawn, "Hertzian Contact Damage in Magnesia-Partially-Stabilized Zirconia," *J. Am. Ceram. Soc.*, **78** [4] 1083-86 (1995)(a)

Pajares, A., Wei, L., Lawn, B. R. and D. B. Marshall, "Damage Accumulation and Cyclic Fatigue in Mg-PSZ at Hertzian Contacts," *J. Mater. Res.* **10** [10] 2613-25 (1995)(b)

Paterson, M. "Experimental Rock Deformation - The Brittle Field," (Springer, Berlin, 1978)

Pennings, E.C.M. and W. Grellner, "Precise Nondestructive Determination of the Density of Porous Ceramics," *J. Am. Ceram. Soc.*, **72** [2] 1268-70 (1989)

Powel-Dogan, C.A. and A.H. Heuer, "Microstruture of 96% Alumina Ceramics: I, Characterization of the As-Sintered Materials," *J. Am. Ceram. Soc.*, **73** [12] 3670-76 (1990)

Powel-Dogan, C.A. and A.H. Heuer, "Microstruture of 96% Alumina Ceramics: II, Crystallization of High-Magnesia Boundary Glasses," *J. Am. Ceram. Soc.*, **73** [12] 3677-83 (1990)

Powel-Dogan, C.A. and A.H. Heuer, "Microstruture of 96% Alumina Ceramics: III, Crystallization of High-Calcia Boundary Glasses," *J. Am. Ceram. Soc.*, **73** [12] 3684-91 (1990)

Rahaman, M. N. "Ceramic Processing and Sintering," (Marcel Dekker, Inc., New York, 1995)

Raj, R. "Morphology and Stability of the Glass Phase in Glass-Ceramic Systems," J. Am. Ceram. Soc., **64** [5] 245-248 (1981)

Rajendran, A.M. and J.L. Kroupa, "Impact Damage Model for Ceramic Materials," *J. Appl. Phys.*, **66** [8] 3560-3565 (1989)

Renner, J. and F. Rummel, "The Effect of Experimental and Microstructural Parameters on the Transition from Brittle Failure to Cataclastic Flow of Carbonate Rock," *Tectonophysics*, **258** 151-169 (1996)

Rice, R. W., "Porosity of Ceramics," (Marcel Dekker, New York, 1998)

Rice, R. W., "Limitations of Pore-Stress Concentrations on the Mechanical Properties of Porous Materials," *J. Mat. Sci.*, **32** 4731-36 (1997)

Richmond, O., Morrison, H. and M. Devenpeck, "Sphere Indentation with Application to the Brinell Hardness Test," *Int. J. Mech. Sci.*, **16** 75-82 (1974)

Rickerby, D. and N. Macmillan, "The Hardness of Cubic Single Crystals by Spherical Indentation," *Mat. Sci. Engr.*, **40** 251-259 (1979)

Rudnicki, J.W. and J.R. Rice, "Conditions for the Localization of Deformation in Pressure-Sensitive Dilatant Materials," *J. Mech. Phys. Solids,* **23** 371-394 (1975)

Rutter, E. and J. Hadizadeh, "On the Influence of Porosity on the Low-Temperature Brittle-Ductile Transition in Silicalstic Rocks," *J. Struct. Geo.*, **13** [5] 609-614 (1991)

Sackfield, A., Hills, D. A., and D. Nowell, "The Stress Field Induced by a General Elliptical Hertzian Contact," *J. of Tribology*, **115** 705-706 (1993)

Sackfield, A. and D.A. Hills, "Some Useful Results in the Classical Hertz Contact Problem," *J. of Str. Anal.*, **18** [2] 101-105 (1983)(a)

Sackfield, A. and D.A. Hills, "Some Useful Results in the Tangentially Loaded Hertzian Contact Problem," *J. of Str. Anal.*, **18** [2] 107-110 (1983)(b)

Sammis, C. and M. Ashby, "The Failure of Brittle Porous Solids under Compressive Stress States," *Acta met.*, **34** [3] 511-26 (1986)

Savin, G. N., "Stress Concentrations Around Holes," ed. W. Johnson, (Pergamon Press, New York, 1961)

Schieve, J., "Stress Intensity Factors of Hole Edge Cracks. Comparison Between One Crack and Two Symmetric Cracks," *Int. J. of Fract.*, **23** R111-R115 (1983)

Schmid, H. and M. Ruhle, "Structure of Special Grain Boundaries in SiAlON Ceramics," *J. Mat. Sci.*, **19** 615-628 (1984)

Scott, T. and K. Nielsen, "The Effects of Porosity on the Brittle-Ductile Transition in Sandstones," *J. Geophys. Res.*, **96** [B1] 405-414 (1991)

Sokolnikoff, I., "Mathematical Theory of Elasticity," (McGraw-Hill, New York, 1946)

Southwell, R. and H. Gough, "On the Concentration of Stress in the Neighborhood of a Small Spherical Flaw; and on the Propagation of Fatigue Fractures in 'Statically Isotropic' Materials," *Phil. Mag.*, **1** [1] 71-97 (1926)

Spriggs, R. M., "Effect of Open and Closed Pores on Elastic Moduli of Polycrystalline Alumina," J. Am. Ceram. Soc., 45 [9] 454 (1962)

Stearns, L.C., "Particle-Inhibited Grain Growth in Al_2O_3-SiC," Ph.D. dissertation, Lehigh University, (1995)

Storåkers, B., Biwa, S. and P-L. Larsson, "Similarity Analysis of Inelastic Contact," *Int. J. Solids Structures*, **34** [24] 3061-83 (1997)

Studman, C. and J. Field, "The Indentation Behaviour of Hard Metals," *J. Phys. D: Appl. Phys.*, **9** 857-867 (1976)

Susnitzky, D.W. and C.B. Carter, "Structure of Alumina Grain Boundaries Prepared with and without a Thin Amorphous Intergranular Film," *J. Am. Ceram. Soc.*, **73** [8] 2485-93 (1990)

Tabor, D., "The hardness of metals" (Clarendon Press, Oxford, 1951)

Tanaka, K. "Elastic/Plastic Indentation Hardness and Indentation Fracture Toughness: The Inclusion Core Model," *J. Mat. Sci.*, **22** 1501-1508 (1987)

Thomas, H.R. and V.A. Hoersch, "Stress Due to the Pressure of One Elastic Solid Upon Another," University of Illinois, Engineering Experimental Station, Bulletin No. 212 (1930)

Timoshenko, S. and J. Goodier, "Theory of Elasticity," 3rd Ed., (McGraw-Hill Inc., New York, 1970)

Tullis, J and R.A. Yund, "Experimental Deformation of Dry Westerly Granite," *J. Geophys. Res.*, **82** 5705-18 (1977)

Tweed, J. and D.P. Rooke, "The Distribution of Stress Near the Tip of a Radial Crack at the Edge of a Circular Hole," *Int. J. Engng. Sci.*, **11** 1185-95 (1973)

Twigg, P., Davidge, R., Riley, F., Franco, A. and S. Roberts, "Indentation-Induced Crack Interaction in Alumina Ceramics," *Phil. Mag. A*, **74** [5] 1245-52 (1996)

Underwood, E.E. "Quantitative Stereology," Addison-Wesley Publishing Co., Reading, MA, (1970)

Vardar, O., Finnie, I., Biswas, D. and R. Fulrath, "Effect of spherical pores on the strength of a polycrystalline ceramic," Int. J. Fract. 13 [2] p215-223 (1977)

Vekinis, G., Ashby, M. and P. Beaumont, "Plaster of Paris as a Model Material for Brittle Porous Solids," *J. of Mat. Sci.*, **28** 3221-27 (1993)

Vetrano, J.S., Kleebe, H.-J., Hampp, E. Hoffmann, M.J., Ruhle, M., and R.M. Cannon, "Yb_2O_3-Fluxed Sintered Silicon Nitride: Part 1 – Microstructure Characterization," *J. Mat. Sci.*, **28** [13] 3529-38 (1993)

Wagh, A.S., Poeppel, R.B. and J.P. Singh, "Open Pore Description of Mechanical Properties of Ceramics," *J. Mat. Sci.*, **26** 3862-68 (1991)

Wang, Y.H., Cheung, Y.K. and C.W. Woo, "The Stress Intensity Factor of a Crack Emanating from a Circular Hole in a Finite Plate by Boundary Collocation Method," *Int. J. Fract.*, **43** 97-108 (1990)

Warren, P. and D.A. Hills, "The Influence of Elastic Mismatch between Indenter and Substrate on Hertzian Fracture," *J. Mat. Sci.*, **29** 2860-66 (1994)(a)

Warren, P., Hills, D. and S. Roberts, "Surface Flaw Distributions in Brittle Materials and Hertzian Fracture," *J. Mater. Res.*, **9** [12] 3194-3202 (1994)(b)

Widjaja, S., Ritter, J.E. and K. Jakus, "Influence of R-Curve Behavior on Strength Degradation Due to Hertzian Indentation," *J. Mat. Sci.*, **31** 2379-84 (1996)

Wiederhorn, S.M. and B.J. Hockey, "Effect of Material Parameters on the Erosion Resistance of Brittle Materials," *J. Mat. Sci.*, **18** 766-780 (1983)

Wong, T.-F., "Mechanical Compaction and the Brittle-Ductile Transition in Porous Sandstones," Deformation Mechanisms, Rheology and Tectonics, Knipe, R. J. and Rutter, E. H. (eds), No. 54, 111-122 (1990)

Wong, T.-F., C. David and W. Zhu, "The Transition from Brittle Faulting to Cataclastic Flow in Porous Sandstones: Mechanical Deformation," *J. Geophys. Res.*, **102** [B2] 3009-3025 (1997)

Wong T.-F. and L.-C. Wu, "Tensile Stress Concentration and Compressive Failure in Cemented Granular Material," *Geophys. Res. Lett.*, **22** [13] 1649-52 (1995)

Wu, X.-R. and A.J. Carlsson, "Weight Functions and Stress Intensity Factor Solutions," (Pergamon Press, Oxford, U.K., 1991)

Wuttiphan, S. and B. Lawn, "Crack Suppression in Strongly Bonded Homogeneous/Heterogeneous Laminates: A Study on Glass/Glass-Ceramic Bilayers," *J. Am. Ceram.* Soc., **79** [3] 634-640 (1996)

Xu, H. H. K., Wei, L., Padture, N. P., Lawn, B. R. and R. L. Yeckley, "Effect of Microstructural Coarsening on Hertzian Contact Damage in Silicon Nitride," *J. Mater. Sci.*, **30** 869-878 (1995)

Yingzhi, L. and D. A. Hills, "The Hertzian Cone Crack," *J. Appl. Mech.*, **58** 120-127 (1991)

Yoffe, E., "Modified Hertz Theory for Spherical Indentation," *Phil. Mag. A*, **50** [6] 813-828 (1984)

Yoffe, E. "Elastic Stress Fields Caused by Indenting Brittle Materials," *Phil. Mag. A.*, **46** [4] 617-628 (1982)

Zang, A., "Finite Element Study on the Closure of Thermal Microcracks in Feldspar/Quartz-Rocks – I. Grain-Boundary Cracks," *Geophys. J. Int.*, **113** 17-31 (1993)

Zeng, K., Breder, K, D.J. Rowcliffe, and C. Herrström, "Elastic Modulus Determined by Hertzian Indentation," *J. Mat. Sci.*, **27** 3789-92 (1992)

Zeng, K., Breder, K. and D. Rowcliffe, "The Hertzian Stress Field and Formation of Cone Cracks - I. Theoretical Approach," *Acta metall. mater.*, **40** [10] 2595-2600 (1992)(a)

Zeng, K., Breder, K. and D. Rowcliffe, "The Hertzian Stress Field and Formation of Cone Cracks - II. Determination of Fracture Toughness," *Acta metall. mater.*, **40** [10] (1992)(b)

Zienkiewicz, O.C. and R.L. Taylor., "The Finite Element Method," 4th ed., (McGraw-Hill, New York, 1991)

Zhao, J. and M. Harmer, "Effect of Pore Distribution on Microstructure Development: I, Matrix Pores," *J. Am. Ceram. Soc.*, **71** [2] 113-20 (1988)

Zhao, J. and M. Harmer, "Effect of Pore Distribution on Microstructure Development: II, First- and Second-Generation Pores," *J. Am. Ceram. Soc.*, **71** [7] 530-39 (1988)

VITA

Anthony A. DiGiovanni was born February 9, 1969 to parents Albert and Rosemary. After graduating from high school in 1987, he enrolled in the University of Illinois, Chicago. In August of 1988, Anthony left the University of Illinois, Chicago to attend Harper College and simultaneously work part-time. Anthony enrolled at the University of Illinois, Urbana for the spring semester of 1990 in the Ceramic Engineering program. After one semester he began his first research job working for a graduate student in the polymer chemistry lab of Dr. Wool. Following one year at Illinois, Anthony left for an 8-month internship at Los Alamos National Laboratory as part of the DoE's SERS program. A two-week sabbatical from Los Alamos sent him to Lawrence Livermore National Lab to work with Roger Haas on a colliding-pulse mode-locked chemical dye laser for the Undergraduate Institute in Applied Science. He returned to Illinois to continue his studies and began working in the Payne-Viehland electroceramics group on superconductors and ferroelectrics. The next summer Anthony left for the University of Leeds, Holdsworth School of Materials to work with Tony Moulson. After returning from England, Anthony graduated with a B.S. in January 1993 and continued his work in the Payne-Viehland group until he left for Pacific Northwest National Laboratory to work on hazardous waste vitrification that summer. The fall of 1993 found Anthony in graduate school at Lehigh University under the guidance of Martin P. Harmer and Helen M. Chan. During his term at Lehigh, Anthony founded and was president of Lehigh's first student chapter of the Microelectronics Society (IMAPS). He won the materials science department's Conard Award for outstanding graduate student (1997), received an honorable mention in Lehigh University's graduate student leadership award (1997), and was recently awarded an IMAPS educational fellowship (1998).

Anthony was a co-author on two peer-reviewed publications as an undergraduate and has written two peer-reviewed papers as a graduate student. In addition, Anthony has given numerous presentations at national conferences – the first of which occurred as an undergraduate – since 1990. Having acquired a love of research early in his educational career, Anthony hopes to find postdoctoral research in the mechanics of materials after leaving Lehigh.

IMAGE EVALUATION TEST TARGET (QA-3)

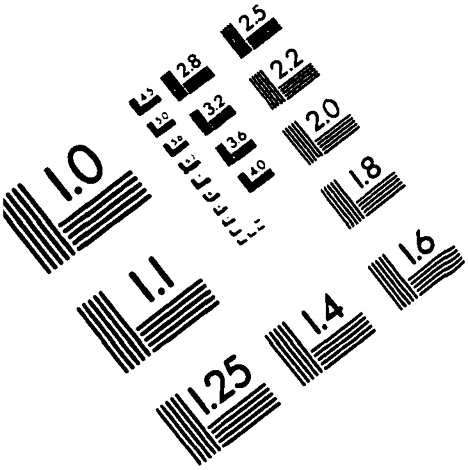

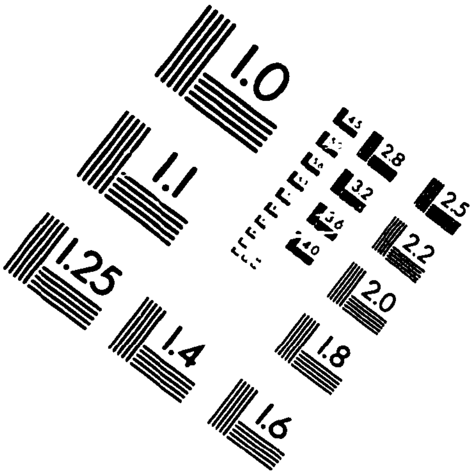

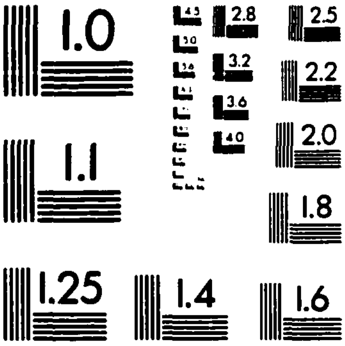

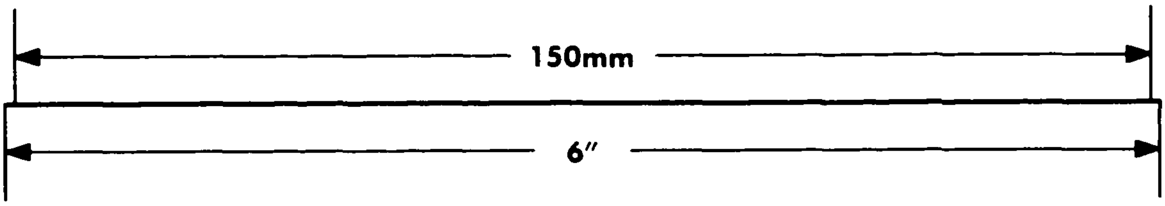

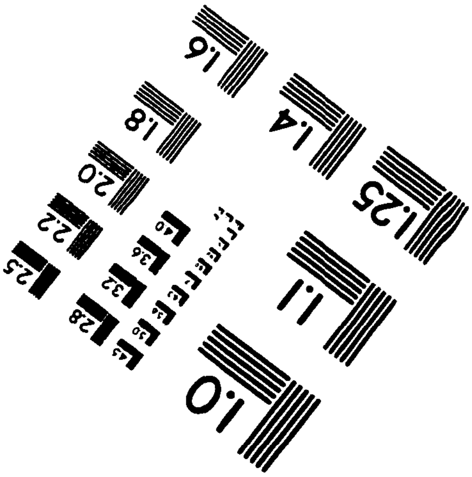

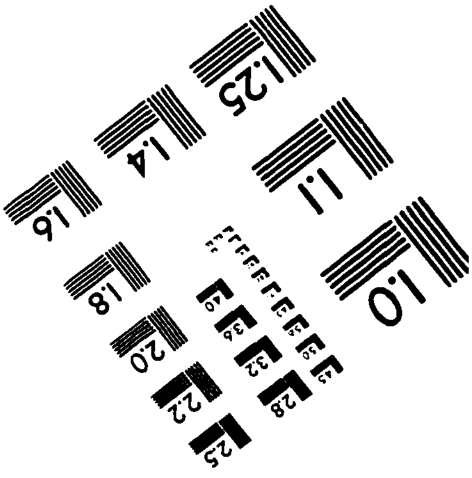

APPLIED IMAGE, Inc
1653 East Main Street
Rochester, NY 14609 USA
Phone: 716/482-0300
Fax: 716/288-5989